(4)

Radiation, Scattering and Guidance of Electromagnetic Fields by Arbitrarily Shaped Structures Embedded in Layered Media

Krzysztof A. Michalski

Final Technical Report
submitted to the
Office of Naval Research
Arlington, VA 22217-5000

Contract No.
N00014-90-J-1197

March 31, 1993

Electromagnetics & Microwave Laboratory
Department of Electrical Engineering
Texas A&M University

DISTRIBUTION STATEMENT A
Approved for public release;
Distribution Unlimited

164pp

Abstract

An integral equation approach based on the mixed-potential formulation is developed for the analysis of radiation, scattering and guidance of electromagnetic waves by arbitrarily shaped conducting objects in layered uniaxial media. This method is successfully applied to rigorously analyze coax- and waveguide-fed microstrip patch antennas of various shapes, as well as multiconductor transmission lines with conductors of various cross-section profiles, embedded in multilayered media. With the approach developed here, microstrip structures of various, possibly irregular shapes, embedded in multilayered isotropic or uniaxial substrates, may be investigated within one theoretical framework and using the same computer program.

Preface

This report comprises five technical papers written by the principal investigator and his collaborators. The unifying theme is the development and application of the mixed-potential integral equation (MPIE) formulation to the analysis of radiation, scattering and guidance of electromagnetic waves by conducting objects embedded in layered material media, with emphasis on non-planar structures having irregular or arbitrary shapes. The papers included here have been submitted for publication in scientific journals and, hence, are to a large degree self-contained. As a result, there is a certain amount of overlap in the material they cover.

Table of Contents

Formulation of Mixed-Potential Integral Equations for Arbitrarily Shaped Microstrip Structures with Uniaxial Substrates

Krzysztof A. Michalski

Electromagnetics & Microwave Laboratory
Department of Electrical Engineering
Texas A&M University
College Station, Texas 77843-3128, USA

Running head: Formulation of Mixed-Potential Integral Equations

Keywords: Microstrip, integral equation, layered medium, Green's function

Abstract—A systematic development is presented of three distinct mixed-potential integral equations for the analysis of printed circuits, microstrip resonators, and antennas embedded in multi-layered, planar, uniaxial media of infinite lateral extent, with emphasis on microstrip structures comprising non-planar conductors of irregular or arbitrary shapes.

1 Introduction

Most of the analysis methods presently available for the analysis of microstrip structures are either limited to or optimized for planar geometries with regular shapes. However, in view of the recent advances in the development of the monolithic microwave and millimeter-wave integrated circuits, it is increasingly important to have at one's disposal techniques, which would make it possible to accurately and efficiently analyze more complex microstrip geometries, comprising non-planar conductors. In this paper, we discuss an integral equation approach, which we have found to be especially suitable for this task. More specifically, we develop three distinct forms of the so-called mixed-potential integral equation (MPIE) [1], [2] for arbitrarily shaped conducting objects embedded in a planar, multi-layered, material medium of infinite lateral extent, which may be uniaxially anisotropic. The distinguishing feature of the MPIE formulations is that they employ vector and scalar potentials, which are expressed, respectively, in terms of the current and charge densities. They are preferable to other forms of the electric field integral equation (EFIE), because they involve less singular kernels and faster convergent spectral integrals (or series), and are amenable to the well-established method-of-moments (MOM) solution procedures, originally developed for arbitrarily shaped conducting scatterers in free space [3], [4], [5].

An MPIE was first used in the present context by Mosig and Gardiol [6], who applied it to analyze planar microstrip patch antennas of various shapes (see also [7], [8]). An extension of this approach to non-planar conductors in layered media was later proposed by Michalski [1]. More recently, Michalski and Zheng have developed three alternative MPIE formulations [9], referred to as Formulations A, B, and C, and applied Formulation C to analyze scatterers and antennas of various shapes partially buried in a material half-space [10], as well as microstrip transmission lines having conductors of arbitrary cross-section [11]. In the present paper, we extend the MPIE approach of [9] to the case of uniaxial media, which have important applications in modern microwave circuits [12], [13]. Although the approach presented here has successfully been applied to a number of structures in layered media [11], [14], [15], [16], [17], the details of the development have not yet appeared in the open literature.

The remainder of this paper is organized as follows. The problem statement is given in Section 2. In Section 3, we introduce the Fourier transform apparatus that considerably simplifies the following development, and express the electric dyadic Green's function of the layered uniaxial medium in terms of the voltage and current Green's functions of its transmission line network analog. For easy reference, the transmission line Green's functions pertinent to a multi-layered uniaxial medium are given in the appendix. The main result is given in Section 4, where we develop and discuss three distinct MPIE forms for non-planar conducting structures of arbitrary shape embedded in the layered medium, using the dyadic Green's function given in Section 3 as the point of departure. We close, in Section 5, with the summary and conclusions.

2 Problem Statement

We discuss the MPIE approach in the context of the general problem illustrated in Fig. 1, which shows an arbitrarily shaped conducting object embedded in a layered medium and excited by (presumably known) electric and magnetic currents, $\boldsymbol{J}^i$ and $\boldsymbol{M}^i$, respectively. The material layers are uniform and of infinite extent along the x and y axes, and may be uniaxially anisotropic, with the optic axis parallel to the z axis. The nth layer is characterized by the permittivity and permeability dyadics

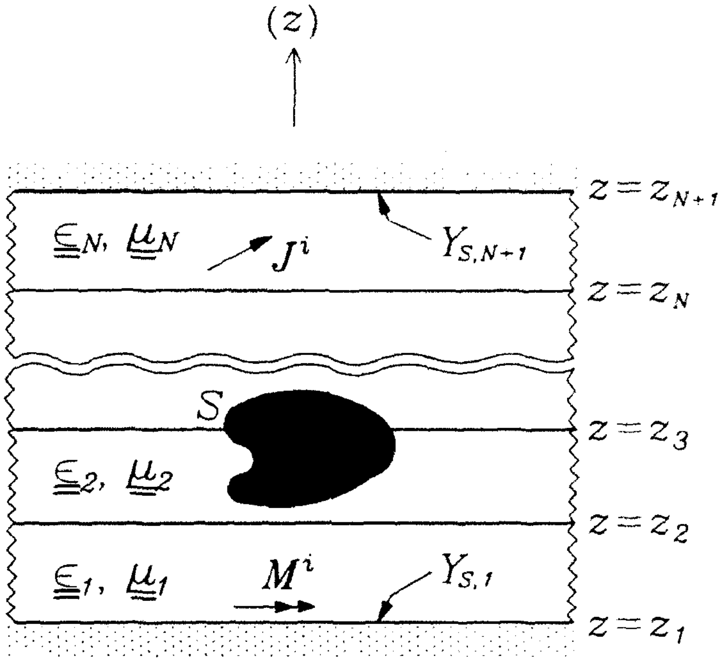

Figure 1: Arbitrarily shaped conducting object in a layered medium.

$$\underline{\underline{\epsilon}}_n = \underline{\underline{I}}_t \, \epsilon_{tn} + \hat{z}\hat{z} \, \epsilon_{zn} , \qquad \underline{\underline{\mu}}_n = \underline{\underline{I}}_t \, \mu_{tn} + \hat{z}\hat{z} \, \mu_{zn} \tag{1}$$

where $\underline{\underline{I}}_t$ is the unit dyadic transverse to z, and ϵ_{tn} (μ_{tn}) and ϵ_{zn} (μ_{zn}) denote, respectively, the transverse and longitudinal dielectric (magnetic) constants relative to free space. Observe that we distinguish dyadics by double underlines and unit vectors by carets. The free space permeability and permittivity will be denoted by μ_0 and ϵ_0, respectively. For each layer, we also introduce its electric and magnetic anisotropy ratios, ν_n^e and ν_n^h, respectively, given as

$$\nu_n^e = \frac{\epsilon_{zn}}{\epsilon_{tn}}, \qquad \nu_n^h = \frac{\mu_{zn}}{\mu_{tn}} \tag{2}$$

The top and bottom layers may be of infinite extent along the z axis or —as illustrated in Fig. 1—may be shielded by ground planes having specified surface admittances $Y_{S,N+1}$ and $Y_{S,1}$, respectively, where the latter are infinite for perfect electric conductors.

The original problem of Fig. 1 may be replaced by its equivalent [18, p. 106] shown in Fig. 2, where the conducting object has been removed and its effect replaced by an as yet unknown electric surface current with density $\boldsymbol{J}_S$, residing on a mathematical surface S. Because this current exists in the absence of the conducting object, the resulting electric field can be expressed as [19], [20]

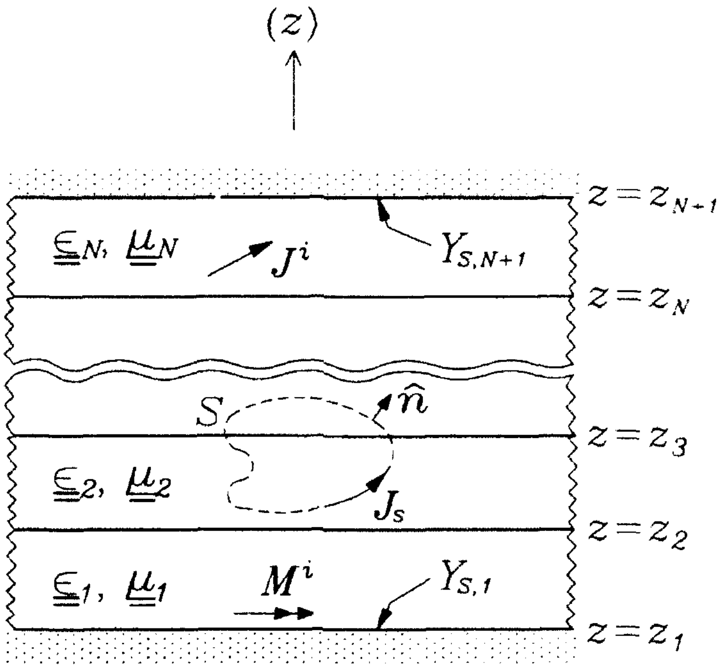

Figure 2: Problem equivalent to that in Fig. 1.

$$\boldsymbol{E}(\boldsymbol{r}) = \int \underline{\underline{\boldsymbol{G}}}^E(\boldsymbol{r}|\boldsymbol{r}') \cdot \boldsymbol{J}(\boldsymbol{r}')\, d\boldsymbol{r}' \tag{3}$$

where the integration is over the region occupied by $\boldsymbol{J}$ — the volume current density associated with $\boldsymbol{J}_S$, $\boldsymbol{r}$ and $\boldsymbol{r}'$ denote the position vectors associated with the field and source coordinates, respectively, and where $\underline{\underline{\boldsymbol{G}}}^E$ is the electric dyadic Green's function of the layered medium. This Green's dyadic will be developed in Section 3.

Although the equivalent current in Fig. 2 is not known, we may easily formulate an EFIE that $\boldsymbol{J}_S$ satisfies by imposing the impedance boundary condition [21, p. 18] on the surface S of the object. Hence, upon using (3), we obtain

$$Z_S \int_S \boldsymbol{\Lambda}_n(\boldsymbol{r})\cdot \boldsymbol{J}_S(\boldsymbol{r})\,dS - \int_S \boldsymbol{\Lambda}_n(\boldsymbol{r})\cdot \int_S \underline{\underline{\boldsymbol{G}}}^E(\boldsymbol{r}|\boldsymbol{r}')\cdot \boldsymbol{J}_S(\boldsymbol{r}')\,dS'\,dS = \int_S \boldsymbol{\Lambda}_n(\boldsymbol{r})\cdot \boldsymbol{E}^i(\boldsymbol{r})\,dS \tag{4}$$

where $\{\boldsymbol{\Lambda}_n\}$ is a suitable set of vector weight functions defined over and tangential to S, $\boldsymbol{E}^i$ is the 'incident' electric field due to $\boldsymbol{J}^i$ and $\boldsymbol{M}^i$ radiating in the layered medium of Fig. 2, and where Z_S is the surface impedance of the conducting object, given as

$$Z_S = \frac{1+j}{\sigma_c\delta_c}, \qquad \delta_c = \sqrt{\frac{2}{\omega\mu_0\sigma_c}} \tag{5}$$

in which σ_c denotes the conductivity and δ_c the skin depth of the conductor. In the case of strip-like structures, (5) is only applicable if $\delta_c << t_c$, where t_c is the strip thickness. If this condition is violated, the expression

$$Z_S = \frac{1}{\sigma_c t_c} \tag{6}$$

may be more appropriate [22]. In the above and throughout this paper, the $e^{j\omega t}$ time variation is assumed.

The EFIE (4) can, in principle at least, be solved for $\boldsymbol{J}_S$ by a MOM procedure, but the severe singularity of its kernel as $\boldsymbol{r}'$ approaches $\boldsymbol{r}$ on S makes it unsuitable for this purpose. A better approach is based on a mixed-potential representation of $\boldsymbol{E}$, given as

$$-\boldsymbol{E}(\boldsymbol{r}) = \boldsymbol{A}(\boldsymbol{r}) + \nabla\Phi(\boldsymbol{r}) \tag{7}$$

in which the vector and scalar potentials, $\boldsymbol{A}$ and Φ, respectively, are expressed as

$$\boldsymbol{A}(\boldsymbol{r}) = \int \underline{\underline{\boldsymbol{G}}}^{A}(\boldsymbol{r}|\boldsymbol{r}') \cdot \boldsymbol{J}(\boldsymbol{r}')\, d\boldsymbol{r}' \tag{8}$$

$$\begin{aligned}\Phi(\boldsymbol{r}) &= \int G^{\phi}(\boldsymbol{r}|\boldsymbol{r}')\boldsymbol{\nabla}'\cdot \boldsymbol{J}(\boldsymbol{r}')\, d\boldsymbol{r}' \\ &= -\int \boldsymbol{\nabla}' G^{\phi}(\boldsymbol{r}|\boldsymbol{r}')\cdot \boldsymbol{J}(\boldsymbol{r}')\, d\boldsymbol{r}' \end{aligned} \tag{9}$$

where $\underline{\underline{\boldsymbol{G}}}^{A}$ and G^{ϕ} are the vector and scalar potential kernels, and where $\boldsymbol{\nabla}'$ operates on the primed (source) coordinates. In view of the divergence theorem [23, p. 503], the above two forms of Φ are equivalent provided $\hat{\boldsymbol{n}}\cdot \boldsymbol{J}$ vanishes on the surface S of the object, where $\hat{\boldsymbol{n}}$ is a unit vector normal to S, and—if $\boldsymbol{J}$ penetrates a boundary between material layers, as illustrated in Fig. 2—provided G^{ϕ} is a continuous function of z' across the interface. Upon using (7) in conjunction with (8) and (9), instead of (3), in the impedance boundary condition on S, and applying the divergence theorem, we arrive at the MPIE

$$\begin{aligned} Z_S \int_S \boldsymbol{A}_n(\boldsymbol{r})\cdot \boldsymbol{J}_S(\boldsymbol{r})\, dS &+ \int_S \boldsymbol{A}_n(\boldsymbol{r})\cdot \int_S \underline{\underline{\boldsymbol{G}}}^{A}(\boldsymbol{r}|\boldsymbol{r}')\cdot \boldsymbol{J}_S(\boldsymbol{r}')\, dS'\, dS \\ &- \int_S \boldsymbol{\nabla}\cdot \boldsymbol{A}_n(\boldsymbol{r}) \int_S G^{\phi}(\boldsymbol{r}|\boldsymbol{r}')\boldsymbol{\nabla}'\cdot \boldsymbol{J}_S(\boldsymbol{r}')\, dS'\, dS = \int_S \boldsymbol{A}_n(\boldsymbol{r})\cdot \boldsymbol{E}^{i}(\boldsymbol{r})\, dS \end{aligned} \tag{10}$$

provided G^{ϕ} is a continuous function of z across any interface between dissimilar material layers the conducting object penetrates. Observe that in view of the equation of continuity, $\boldsymbol{\nabla}\cdot\boldsymbol{J}_S$ in the above is directly proportional to the surface charge density. Comparing the EFIE (4) with the MPIE (10), we note that in the latter the differential operator $\boldsymbol{\nabla}\boldsymbol{\nabla}'$ has in effect been extracted from $\underline{\underline{\boldsymbol{G}}}^{E}$ and transferred onto $\boldsymbol{A}_n$ and $\boldsymbol{J}_S$. As a consequence, the kernels $\underline{\underline{\boldsymbol{G}}}^{A}$ and G^{ϕ} appearing in (10) are less singular than $\underline{\underline{\boldsymbol{G}}}^{E}$, and the Sommerfeld-type integrals that arise converge more rapidly.

The form of (10) is not unique and leads to different MPIE formulations, depending on the choice of $\underline{\underline{\boldsymbol{G}}}^{A}$ and G^{ϕ}. In Section 4, we develop three distinct MPIE forms that have been found useful in MOM analyses of the radiation, scattering, and guidance of electromagnetic fields by arbitrarily shaped conducting structures in layered media.

The development is carried out in the spectral domain and it proceeds from the spectral electric dyadic Green's function of the layered medium, developed in the next section.

3 Preliminaries

Following Felsen and Marcuvitz [24, p. 188], we view the layered medium in Fig. 2 as a waveguide along the z axis and expand the electromagnetic fields and currents in terms of the waveguide modes. Because the waveguide cross section is of infinite extent along the x and y coordinates, the eigenvalues corresponding to the latter, k_x and k_y, respectively, form continuous spectra on the real axis. Consequently, the modal expansions may be expressed as the familiar double Fourier transforms, which prompts us to introduce the Fourier transform pair

$$\mathcal{F}\{f(\boldsymbol{\rho})\} \equiv \tilde{f}(\boldsymbol{k}_\rho) = \int_{-\infty}^{+\infty}\int_{-\infty}^{+\infty} f(\boldsymbol{\rho})\, e^{j\boldsymbol{k}_\rho\cdot\boldsymbol{\rho}}\, dx\, dy \tag{11}$$

$$\mathcal{F}^{-1}\left\{\tilde{f}(\boldsymbol{k}_\rho)\right\} \equiv f(\boldsymbol{\rho}) = \frac{1}{(2\pi)^2}\int_{-\infty}^{+\infty}\int_{-\infty}^{+\infty} \tilde{f}(\boldsymbol{k}_\rho)\, e^{-j\boldsymbol{k}_\rho\cdot\boldsymbol{\rho}}\, dk_x\, dk_y \tag{12}$$

where $\boldsymbol{k}_\rho = \hat{\boldsymbol{x}}k_x + \hat{\boldsymbol{y}}k_y$ is the spectral domain counterpart of $\boldsymbol{\rho} = \hat{\boldsymbol{x}}x + \hat{\boldsymbol{y}}y$. If we now write $\boldsymbol{E}(\boldsymbol{r})$ as $\boldsymbol{E}(\boldsymbol{\rho}; z)$, its Fourier transform may be expressed as $\tilde{\boldsymbol{E}}(\boldsymbol{k}_\rho; z)$, and similarly for the other field quantities. We also note that in the spectral domain the operator nabla becomes $\tilde{\boldsymbol{\nabla}} = -j\boldsymbol{k}_\rho + \hat{\boldsymbol{z}}\partial/\partial z$, which suggests that we introduce a rotated spectral domain coordinate system based on $\boldsymbol{k}_\rho$, as illustrated in Fig. 3, where (cf. [25], [26], [27], [28])

$$\hat{\boldsymbol{u}} = \frac{\boldsymbol{k}_\rho}{k_\rho}, \quad \hat{\boldsymbol{v}} = \frac{\hat{\boldsymbol{z}} \times \boldsymbol{k}_\rho}{k_\rho}, \quad k_\rho = \sqrt{k_x^2 + k_y^2} \tag{13}$$

When the Fourier-transformed Maxwell's equations are projected on this coordinate system, it is found that the spectral domain electromagnetic field may efficiently and elegantly be expressed in terms of the voltages and currents on two transmission lines along the z axis, with the propagation wavenumbers and characteristic admittances

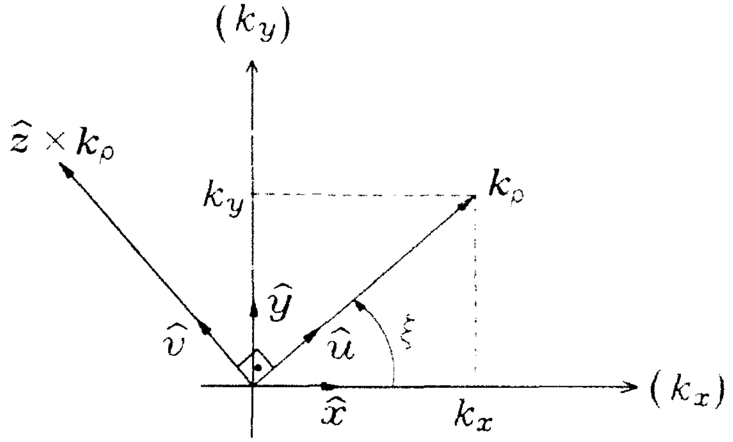

Figure 3: Rotated spectral domain coordinate system.

given as

$$k_z^e = \sqrt{k_0^2 \mu_t \epsilon_t - k_\rho^2/\nu^e}\,, \qquad Y^e \equiv \frac{1}{Z^e} = \frac{k_0 \epsilon_t}{\eta_0 k_z^e} \tag{14}$$

and

$$k_z^h = \sqrt{k_0^2 \mu_t \epsilon_t - k_\rho^2/\nu^h}\,, \qquad Y^h \equiv \frac{1}{Z^h} = \frac{k_z^h}{\eta_0 k_0 \mu_t} \tag{15}$$

respectively, where $k_0 = \omega\sqrt{\mu_0\epsilon_0}$ is the wavenumber and $\eta_0 = \sqrt{\mu_0/\epsilon_0}$ the intrinsic impedance of free space. Observe that at this stage of the development, the permeability and permittivity (and thus also the anisotropy ratios) of the medium may vary arbitrarily with z and are not necessarily restricted to be piecewise-constant, as is the case in Fig. 2. The voltage V^e and current I^e on the line with the propagation wavenumber and characteristic admittance given in (14) specify the transverse-magnetic (TM) partial field, while the voltage V^h and current I^h on the line with the propagation wavenumber and characteristic admittance given in (15) specify the transverse-electric (TE) part of the field. For the following development, it will be convenient to also introduce transmission line Green's functions, which represent the voltage or current excited by a unit-strength voltage or current point source. Hence, let $V_i^p(z|z')$ and $I_i^p(z|z')$, where the superscript p stands for e or h, denote the voltage and current, respectively, at a point z due to a 1 A current source located at z' on the corresponding transmission line (cf. [27], [29]). It then follows that these Green's functions are governed by the coupled equations

$$\frac{d}{dz}V_i^p(z|z') = -jk_z^p Z^p I_i^p(z|z') \tag{16}$$

$$\frac{d}{dz}I_i^p(z|z') = -jk_z^p Y^p V_i^p(z|z') + \delta(z-z') \tag{17}$$

where $\delta(z-z')$ is the Dirac delta. Similarly, let $V_v^p(z|z')$ and $I_v^p(z|z')$ denote the voltage and current, respectively, at z due to a 1 V voltage source at z'. It is then found that these Green's functions satisfy equations dual to (16)–(17), which are obtained from the latter by making the substitutions $V_i^p \rightarrow I_v^p$, $I_i^p \rightarrow V_v^p$, $Z^p \rightarrow Y^p$, and $Y^p \rightarrow Z^p$. From their governing equations, it can also be shown that the four transmission line Green's functions possess the symmetry and reciprocity properties [21, p. 194]

$$V_i^p(z|z') = V_i^p(z'|z)\,, \quad I_v^p(z|z') = I_v^p(z'|z)\,, \quad V_v^p(z|z') = -I_i^p(z'|z) \tag{18}$$

Once the transmission line Green's functions are determined, the voltage and current at any point on the transmission line, excited by an arbitrary, distributed voltage v^p and current i^p may be expressed in terms of the superposition relations (cf. [30, p. 63], [24, p. 193])

$$V^p(z) = \int V_v^p(z|z')\,v^p(z')\,dz' + \int V_i^p(z|z')\,i^p(z')\,dz' \tag{19}$$

$$I^p(z) = \int I_v^p(z|z')\,v^p(z')\,dz' + \int I_i^p(z|z')\,i^p(z')\,dz' \tag{20}$$

In view of the uniformity of the medium of Fig. 2 along the x and y axes, the dyadic Green's function in (3) possesses a translational symmetry with respect to the transverse coordinates. Consequently, we may write $\underline{\underline{G}}^E(\boldsymbol{r}|\boldsymbol{r}') = \underline{\underline{G}}^E(\boldsymbol{\rho}-\boldsymbol{\rho}'; z|z')$, where $\underline{\underline{G}}^E(\boldsymbol{\rho}; z|z')$ may be given as

$$\underline{\underline{G}}^E(\boldsymbol{\rho}; z|z') = \mathcal{F}^{-1}\left\{\underline{\underline{Q}}^T(\xi)\cdot\underline{\underline{\tilde{G}}}^E(\boldsymbol{k}_\rho; z|z')\cdot\underline{\underline{Q}}(\xi)\right\} \tag{21}$$

Here, $\underline{\underline{\tilde{G}}}^E$ is the spectral domain counterpart of $\underline{\underline{G}}^E$, expressed in the rotated coordinate system of Fig. 3, and the dyadic operator

$$\underline{\underline{\boldsymbol{Q}}}(\xi) = (\hat{\boldsymbol{u}}\hat{\boldsymbol{x}} + \hat{\boldsymbol{v}}\hat{\boldsymbol{y}})\cos\xi + (\hat{\boldsymbol{u}}\hat{\boldsymbol{y}} - \hat{\boldsymbol{v}}\hat{\boldsymbol{x}})\sin\xi + \hat{\boldsymbol{z}}\hat{\boldsymbol{z}} \qquad (22)$$

and its transpose, $\underline{\underline{\boldsymbol{Q}}}^T(\xi)$, are employed to directly transform $\underline{\underline{\tilde{\boldsymbol{G}}}}^E$ from the rotated spectral domain coordinate system to the space domain. Upon using the superposition relations (19)-(20) in the Fourier-transformed Maxwell's equations, we find that $\underline{\underline{\tilde{\boldsymbol{G}}}}^E$ may be expressed in terms of the voltage and current transmission line Green's functions as

$$\begin{aligned} -\underline{\underline{\tilde{\boldsymbol{G}}}}^E(\boldsymbol{k}_\rho; z|z') = {} & \hat{\boldsymbol{u}}\hat{\boldsymbol{u}}\, V_i^e(k_\rho; z|z') + \hat{\boldsymbol{v}}\hat{\boldsymbol{v}}\, V_i^h(k_\rho; z|z') - \hat{\boldsymbol{u}}\hat{\boldsymbol{z}}\, \frac{\eta_0 k_\rho}{k_0 \epsilon_z'}\, V_v^e(k_\rho; z|z') \\ & - \hat{\boldsymbol{z}}\hat{\boldsymbol{u}}\, \frac{\eta_0 k_\rho}{k_0 \epsilon_z}\, I_i^e(k_\rho; z|z') + \hat{\boldsymbol{z}}\hat{\boldsymbol{z}} \left[\left(\frac{\eta_0 k_\rho}{k_0} \right)^2 \frac{I_v^e(k_\rho; z|z')}{\epsilon_z \epsilon_z'} + \frac{\eta_0}{j k_0 \epsilon_z'}\, \delta(z - z') \right] \qquad (23) \end{aligned}$$

where the primed and unprimed parameters are evaluated at z' and z, respectively—a convention that will be in effect throughout this paper, unless the layer index is explicitly stated. Observe that in the above we explicitly indicate the dependence of the transmission line Green's functions on the transverse spectral wavenumber k_ρ. The isotropic medium form of $\underline{\underline{\tilde{\boldsymbol{G}}}}^E$ was previously given by Kastner et al. [27].

In view of the fact that no assumptions have so far been made regarding the dependence of the media parameters on z, the spectral dyadic Green's function given in (23) is valid, in particular, for the layered medium of Fig. 2, where the permeability and permittivity are piecewise-constant. The corresponding transmission line network is illustrated in Fig. 4. Observe that the original vector problem has thus been reduced to a much simpler equivalent network problem, in which the individual material layers are viewed as uniform transmission line sections, where the nth section has the propagation constant k_{zn}^p and characteristic admittance Y_n^p. This network analog actually comprises two networks—one associated with the TM and the other with the TE partial fields—which have identical configurations, but differ in the characteristic admittances and propagation constants. In the case of an unshielded structure, where the top (or bottom) layer is of infinite extent along the z axis, the

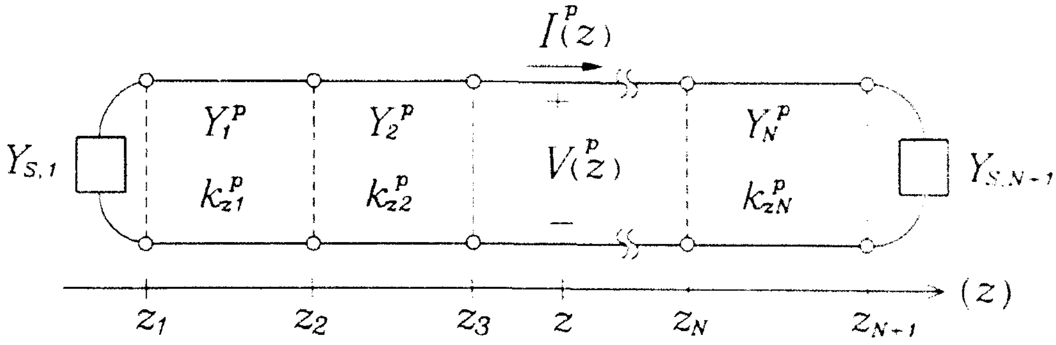

Figure 4: Transmission line network analog of the layered medium.

corresponding transmission line section in the network analog of Fig. 4 also extends to infinity, where it is terminated into a matched load. The voltage and current Green's functions for the network of Fig. 4 are easily found for any number of layers, as discussed in the appendix.

We note that in view of (14)-(15), the transmission line Green's functions appearing in (23) depend on the spectral variables k_x and k_y exclusively through k_ρ. As a consequence, when the double spectral integrations in (21) are performed in the polar system (k_ρ, ξ) illustrated in Fig. 3, the ξ-integrals can be evaluated in closed form. More specifically, we find that

$$\mathcal{F}^{-1}\left\{ \begin{matrix}\sin\\ \cos\end{matrix}\, n\xi\, f(k_\rho)\right\} = (-j)^n \begin{matrix}\sin\\ \cos\end{matrix}\, n\varphi\, \mathcal{S}_n\left\{f(k_\rho)k_\rho^{-n}\right\}, \quad n = 0, 1, 2 \tag{24}$$

where we have introduced the notation

$$\mathcal{S}_n\{f(k_\rho)\} = \frac{1}{2\pi}\int_0^\infty dk_\rho\, f(k_\rho)k_\rho^{n+1} J_n(k_\rho \rho) \tag{25}$$

In the above, (ρ, φ) are the configuration space polar coordinates and J_n is the Bessel function of order n. In this fashion, the space domain dyadic $\underline{\underline{\mathbf{G}}}^E(\boldsymbol{\rho}; z|z')$ may be expressed in terms of the Sommerfeld-type integrals (25). To obtain $\underline{\underline{\mathbf{G}}}^E(\boldsymbol{\rho}-\boldsymbol{\rho}'; z|z')$ required in (3), we replace φ and ρ in (24)-(25) by ϑ and ϱ, respectively, where

$$\vartheta = \arctan\left(\frac{y-y'}{x-x'}\right), \qquad \varrho = \sqrt{(x-x')^2+(y-y')^2} \tag{26}$$

Since only $\tilde{\underline{\underline{\boldsymbol{G}}}}^E$ will be needed in the following development, in the interest of brevity we do not list the explicit form of its space domain counterpart.

4 Development of the MPIE Formulations

Because (3) has the form of a convolution in the transverse plane, its Fourier transform becomes

$$\tilde{\boldsymbol{E}}(\boldsymbol{k}_\rho; z) = \int \tilde{\underline{\underline{\boldsymbol{G}}}}^E(\boldsymbol{k}_\rho; z|z')\cdot \tilde{\boldsymbol{J}}(\boldsymbol{k}_\rho; z')\, dz' \tag{27}$$

with $\tilde{\underline{\underline{\boldsymbol{G}}}}^E$ given in (23). Similarly, the spectral domain counterpart of (7) is found as

$$-\tilde{\boldsymbol{E}}(\boldsymbol{k}_\rho; z) = \tilde{\boldsymbol{A}}(\boldsymbol{k}_\rho; z) + \boldsymbol{\nabla}\tilde{\Phi}(\boldsymbol{k}_\rho; z) \tag{28}$$

in which

$$\tilde{\boldsymbol{A}}(\boldsymbol{k}_\rho; z) = \int \tilde{\underline{\underline{\boldsymbol{G}}}}^A(\boldsymbol{k}_\rho; z|z')\cdot \tilde{\boldsymbol{J}}(\boldsymbol{k}_\rho; z')\, dz' \tag{29}$$

$$\tilde{\Phi}(\boldsymbol{k}_\rho; z) = -\int \tilde{\boldsymbol{\nabla}}'\tilde{G}^\phi(\boldsymbol{k}_\rho; z|z')\cdot \tilde{\boldsymbol{J}}(\boldsymbol{k}_\rho; z')\, dz' \tag{30}$$

where $\tilde{\boldsymbol{\nabla}}' = j\boldsymbol{k}_\rho + \hat{\boldsymbol{z}}\partial/\partial z'$. Comparing (27) and (28), we arrive at the relation

$$-\tilde{\underline{\underline{\boldsymbol{G}}}}^E(\boldsymbol{k}_\rho; z|z') = \tilde{\underline{\underline{\boldsymbol{G}}}}^A(\boldsymbol{k}_\rho; z|z') - \tilde{\boldsymbol{\nabla}}\tilde{\boldsymbol{\nabla}}'\tilde{G}^\phi(\boldsymbol{k}_\rho; z|z') \tag{31}$$

which will serve as the point of departure in the development of $\tilde{\underline{\underline{\boldsymbol{G}}}}^A$ and $\tilde{G}^\phi$ from $\tilde{\underline{\underline{\boldsymbol{G}}}}^E$. In what follows, we continue to use the rotated spectral domain coordinate system of Fig. 3, in which four of the nine components of $\tilde{\underline{\underline{\boldsymbol{G}}}}^E$ are zero, as is evident from (23). This and the fact that $\tilde{\boldsymbol{\nabla}}$ and $\tilde{\boldsymbol{\nabla}}'$ are orthogonal to the v axis greatly simplifies the development. Hence, we immediately find from (31) and (23) that

$$\tilde{G}^A_{vu} = \tilde{G}^A_{uv} = \tilde{G}^A_{zv} = \tilde{G}^A_{vz} = 0 \tag{32}$$

and that the nonzero elements of $\tilde{\underline{\underline{\boldsymbol{G}}}}^A$ and $\tilde{G}^\phi$ are related by

$$-\tilde{G}^E_{uu} = \tilde{G}^A_{uu} - k_\rho^2\tilde{G}^\phi \tag{33}$$

$$-\tilde{G}^E_{vv} = \tilde{G}^A_{vv} \tag{34}$$

$$-\tilde{G}^E_{uz} = \tilde{G}^A_{uz} + jk_\rho \frac{\partial \tilde{G}^\phi}{\partial z'} \tag{35}$$

$$-\tilde{G}^E_{zu} = \tilde{G}^A_{zu} - jk_\rho \frac{\partial \tilde{G}^\phi}{\partial z} \tag{36}$$

$$-\tilde{G}^E_{zz} = \tilde{G}^A_{zz} - \frac{\partial^2 \tilde{G}^\phi}{\partial z \partial z'} \tag{37}$$

For notational simplicity, we omit in the above and in some equations that follow the arguments of the spectral domain kernels. Observe that the system (33)–(37) is underdetermined, because there are six unknowns, viz. the five components of

$$\underline{\underline{\tilde{\boldsymbol{G}}}}^A = \hat{\boldsymbol{u}}\hat{\boldsymbol{u}}\tilde{G}^A_{uu} + \hat{\boldsymbol{v}}\hat{\boldsymbol{v}}\tilde{G}^A_{vv} + \hat{\boldsymbol{u}}\hat{\boldsymbol{z}}\tilde{G}^A_{uz} + \hat{\boldsymbol{z}}\hat{\boldsymbol{u}}\tilde{G}^A_{zu} + \hat{\boldsymbol{z}}\hat{\boldsymbol{z}}\tilde{G}^A_{zz} \tag{38}$$

and $\tilde{G}^\phi$, and only five equations. Consequently, we are free to impose an additional constraint on (38)—for instance, we may choose one of the elements of $\underline{\underline{\tilde{\boldsymbol{G}}}}^A$ to be zero. Note, however, that there is no flexibility in choosing $\tilde{G}^A_{vv}$. In fact, it immediately follows from (34) and (23) that

$$\tilde{G}^A_{vv}(k_\rho; z|z') = V_i^h(k_\rho; z|z') \tag{39}$$

Below, we introduce three different constraints on the remaining four elements of $\underline{\underline{\tilde{\boldsymbol{G}}}}^A$ and explore the resulting MPIE formulations, which will be referred to as Formulations A, B, and C, following the terminology introduced in [9].

4.1 Formulation A

To arrive at Formulation A, we set

$$\tilde{G}^A_{zu}(k_\rho; z|z') = 0 \tag{40}$$

It then follows from (36) that

$$\frac{\partial \tilde{G}^{\varphi}}{\partial z} = -\frac{j\eta_0}{k_0\epsilon_z} I_i^e \tag{41}$$

which, in view of (16), leads to

$$\tilde{G}^{\varphi}(k_\rho; z|z') = \frac{V_i^e(k_\rho; z|z')}{\nu^e (k_z^e)^2} \tag{42}$$

provided the field point is within a homogeneous material layer. Upon using the above in (33), we arrive at

$$\tilde{G}^A_{uu}(k_\rho; z|z') = \frac{k_0^2\mu_t\epsilon_t}{(k_z^e)^2} V_i^e(k_\rho; z|z') \tag{43}$$

Similarly, from (42) and (35), we find

$$\tilde{G}^A_{uz} = -\frac{\eta_0 k_\rho}{k_0\epsilon_z'} V_v^e - \frac{jk_\rho}{\nu^e (k_z^e)^2}\frac{\partial V_i^e}{\partial z'} \tag{44}$$

which, in view of (16) and (18), may be reduced to

$$\tilde{G}^A_{uz}(k_\rho; z|z') = k_0\eta_0\mu_t'\left(1 - \frac{\mu_t\epsilon_z}{\mu_t'\epsilon_z'}\right)\frac{k_\rho V_v^e(k_\rho; z|z')}{\nu^e (k_z^e)^2} \tag{45}$$

Finally, from (37) and (42), we obtain

$$\tilde{G}^A_{zz} = \left(\frac{\eta_0 k_\rho}{k_0}\right)^2 \frac{I_v^e}{\epsilon_z\epsilon_z'} + \frac{\eta_0}{jk_0\epsilon_z'}\delta(z-z') + \frac{1}{\nu^e (k_z^e)^2}\frac{\partial^2 V_i^e}{\partial z\partial z'} \tag{46}$$

which, upon using (16), (18), and the equation dual to (17), simplifies to

$$\tilde{G}^A_{zz}(k_\rho; z|z') = \eta_0^2\frac{\mu_t'}{\epsilon_z} I_v^e(k_\rho; z|z') \tag{47}$$

We have thus determined all elements of $\underline{\underline{\tilde{\boldsymbol{G}}}}^A$ in (38), as well as the corresponding $\tilde{G}^{\varphi}$. To obtain the space domain counterpart of $\underline{\underline{\tilde{\boldsymbol{G}}}}^A$, we subject the latter to the inverse

Fourier transform in the manner of (21) and use (24), with the result

$$\underline{\underline{\boldsymbol{G}}}^A(\boldsymbol{\rho}; z|z') = \frac{1}{2}\underline{\underline{\boldsymbol{I}}}_t\, \mathcal{S}_0\left\{ V_i^h(k_\rho; z|z') + \frac{k_0^2\mu_t\epsilon_t}{(k_z^e)^2}\, V_i^e(k_\rho; z|z') \right\}$$
$$+ \frac{1}{2}[(\hat{\boldsymbol{x}}\hat{\boldsymbol{x}} - \hat{\boldsymbol{y}}\hat{\boldsymbol{y}})\cos 2\varphi + (\hat{\boldsymbol{x}}\hat{\boldsymbol{y}} + \hat{\boldsymbol{y}}\hat{\boldsymbol{x}})\sin 2\varphi]\, \mathcal{S}_2\left\{ \frac{V_i^h(k_\rho; z|z')}{k_\rho^2} - \frac{k_0^2\mu_t\epsilon_t}{(k_z^e)^2}\, \frac{V_i^e(k_\rho; z|z')}{k_\rho^2} \right\}$$
$$- (\hat{\boldsymbol{x}}\hat{\boldsymbol{z}}\cos\varphi + \hat{\boldsymbol{y}}\hat{\boldsymbol{z}}\sin\varphi)\, jk_0\eta_0\mu_t'\left(1 - \frac{\mu_t\epsilon_z}{\mu_t'\epsilon_z'}\right) \mathcal{S}_1\left\{ \frac{V_i^e(k_\rho; z|z')}{\nu^e(k_z^e)^2} \right\}$$
$$+ \hat{\boldsymbol{z}}\hat{\boldsymbol{z}}\, \eta_0^2\, \frac{\mu_t'}{\epsilon_z}\, \mathcal{S}_0\{ I_v^e(k_\rho; z|z') \} \tag{48}$$

Similarly, the space domain counterpart of $\tilde{G}^\phi$ is readily found as

$$G^\phi(\boldsymbol{\rho}; z|z') = \mathcal{S}_0\left\{ \frac{V_i^e(k_\rho; z|z')}{\nu^e(k_z^e)^2} \right\} \tag{49}$$

Finally, in order to obtain $\underline{\underline{\boldsymbol{G}}}^A(\boldsymbol{\rho}-\boldsymbol{\rho}'; z|z')$ and $G^\phi(\boldsymbol{\rho}-\boldsymbol{\rho}'; z|z')$ required in the MPIE (10), we make the replacements $\varphi \rightarrow \vartheta$ and $\rho \rightarrow \varrho$ in (48) and (49), with ϑ and ϱ given in (26). Observe that when the source and field points are within the same material layer, $\tilde{\underline{\underline{\boldsymbol{G}}}}^A$ becomes a diagonal dyadic and the xz and yz components of $\underline{\underline{\boldsymbol{G}}}^A$ vanish, thus resulting in a significant simplification of this MPIE formulation. Note, however, that G^ϕ in this formulation is a discontinuous function of z across any interface between dissimilar material layers.

4.2 Formulation B

To obtain Formulation B, we set

$$\tilde{G}_{uz}^A(k_\rho; z|z') = 0 \tag{50}$$

It then follows from (35) that

$$\frac{\partial \tilde{G}^\phi}{\partial z'} = \frac{j\eta_0}{k_0\epsilon_z'}\, V_v^e \tag{51}$$

which, in view of (16), leads to

$$\tilde{G}^{\phi}(k_\rho;z|z') = \frac{V_i^e(k_\rho;z|z')}{\nu^{e\prime}(k_z^{e\prime})^2} \tag{52}$$

provided the source point is within a homogeneous material layer. Upon using the above in (33), we arrive at

$$\tilde{G}^A_{uu}(k_\rho;z|z') = \frac{k_0^2\mu_t'\epsilon_t'}{(k_z^{e\prime})^2}\, V_i^e(k_\rho;z|z') \tag{53}$$

Similarly, from (52) and (36), we find

$$\tilde{G}^A_{zu} = -\frac{\eta_0 k_\rho}{k_0\epsilon_z}\, I_i^e + \frac{jk_\rho}{\nu^{e\prime}(k_z^{e\prime})^2}\,\frac{\partial V_i^e}{\partial z} \tag{54}$$

which, in view of (16) and (18), may be reduced to

$$\tilde{G}^A_{zu}(k_\rho;z|z') = k_0\eta_0\mu_t\left(1-\frac{\mu_t'\epsilon_z'}{\mu_t\epsilon_z}\right)\frac{k_\rho I_i^e(k_\rho;z|z')}{\nu^{e\prime}(k_z^{e\prime})^2} \tag{55}$$

Finally, from (52) and (37), we obtain

$$\tilde{G}^A_{zz} = \left(\frac{\eta_0 k_\rho}{k_0}\right)^2\frac{I_v^e}{\epsilon_z\epsilon_z'} + \frac{\eta_0}{jk_0\epsilon_z'}\,\delta(z-z') + \frac{1}{\nu^{e\prime}(k_z^{e\prime})^2}\,\frac{\partial^2 V_i^e}{\partial z\partial z'} \tag{56}$$

which, upon using (16), (18), and the equation dual to (17), simplifies to

$$\tilde{G}^A_{zz}(k_\rho;z|z') = \eta_0^2\,\frac{\mu_t}{\epsilon_z'}\, I_v^e(k_\rho;z|z') \tag{57}$$

The elements of $\underline{\underline{\tilde{G}}}^A$, as well as the corresponding $\tilde{G}^\phi$, have thus been determined. Their space domain counterparts are found in the same manner as in Formulation A, and take the form

$$\underline{\underline{G}}^A(\boldsymbol{\rho};z|z') = \frac{1}{2}\underline{\underline{I}}_t\,\mathcal{S}_0\left\{V_i^h(k_\rho;z|z') + \frac{k_0^2\mu_t'\epsilon_t'}{(k_z^{e\prime})^2}\,V_i^e(k_\rho;z|z')\right\}$$

$$+\frac{1}{2}[(\hat{\boldsymbol{x}}\hat{\boldsymbol{x}}-\hat{\boldsymbol{y}}\hat{\boldsymbol{y}})\cos 2\varphi+(\hat{\boldsymbol{x}}\hat{\boldsymbol{y}}+\hat{\boldsymbol{y}}\hat{\boldsymbol{x}})\sin 2\varphi]\,\mathcal{S}_2\left\{\frac{V_i^h(k_\rho;z|z')}{k_\rho^2}-\frac{k_0^2\mu_t'\epsilon_t'}{(k_z^{e\prime})^2}\,\frac{V_i^e(k_\rho;z|z')}{k_\rho^2}\right\}$$

$$-\,(\hat{\boldsymbol{z}}\hat{\boldsymbol{x}}\cos\varphi+\hat{\boldsymbol{z}}\hat{\boldsymbol{y}}\sin\varphi)\,jk_0\eta_0\mu_t\left(1-\frac{\mu_t'\epsilon_z'}{\mu_t\epsilon_z}\right)\mathcal{S}_1\left\{\frac{I_i^e(k_\rho;z|z')}{\nu^{e\prime}(k_z^{e\prime})^2}\right\}$$

$$+\,\hat{\boldsymbol{z}}\hat{\boldsymbol{z}}\,\eta_0^2\,\frac{\mu_t}{\epsilon_z'}\,\mathcal{S}_0\{I_v^e(k_\rho;z|z')\} \tag{58}$$

and

$$G^\varphi(\boldsymbol{\rho};z|z')=\mathcal{S}_0\left\{\frac{V_i^e(k_\rho;z|z')}{\nu^{e\prime}(k_z^{e\prime})^2}\right\} \tag{59}$$

The remark following (49) also applies in the present case. Observe that when the source and field points are within the same material layer, $\underline{\underline{\boldsymbol{G}}}^A$ becomes a diagonal dyadic and the zx and zy components of $\underline{\underline{\boldsymbol{G}}}^A$ vanish, thus resulting in a significant simplification of this MPIE formulation. Note, however, that G^φ in this formulation is a discontinuous function of z' across any interface between dissimilar material layers.

4.3 Formulation C

To arrive at Formulation C, we set

$$\tilde{G}_{uu}^A(k_\rho;z|z')=\tilde{G}_{vv}^A(k_\rho;z|z')=V_i^h(k_\rho;z|z') \tag{60}$$

where we have used (39). It then follows from (33) that

$$\tilde{G}^\phi(k_\rho;z|z')=\frac{1}{k_\rho^2}[V_i^h(k_\rho;z|z')-V_i^e(k_\rho;z|z')] \tag{61}$$

Upon using the above in (35), we obtain

$$\tilde{G}_{uz}^A=-\frac{\eta_0 k_\rho}{k_0\epsilon_z'}V_v^e-\frac{j}{k_\rho}\frac{\partial}{\partial z'}\left(V_i^h-V_i^e\right) \tag{62}$$

which, in view of (16) and (18), may be reduced to

$$\tilde{G}_{uz}^A(k_\rho;z|z')=\frac{k_0\eta_0\mu_t'}{k_\rho}\left[V_v^h(k_\rho;z|z')-V_v^e(k_\rho;z|z')\right] \tag{63}$$

Similarly, upon using (61) in (36), we obtain

$$\tilde{G}^A_{zu} = -\frac{\eta_0 k_\rho}{k_0 \epsilon_z} I_i^e + \frac{j}{k_\rho}\frac{\partial}{\partial z}\left(V_i^h - V_i^e\right) \tag{64}$$

which, in view of (16), may be reduced to

$$\tilde{G}^A_{zu}(k_\rho; z|z') = \frac{k_0 \eta_0 \mu_t}{k_\rho}\left[I_i^h(k_\rho; z|z') - I_i^e(k_\rho; z|z')\right] \tag{65}$$

Finally, from (61) and (37), we obtain

$$\tilde{G}^A_{zz} = \left(\frac{\eta_0 k_\rho}{k_0}\right)^2 \frac{I_v^e}{\epsilon_z \epsilon_z'} + \frac{\eta_0}{j k_0 \epsilon_z'}\,\delta(z-z') + \frac{1}{k_\rho^2}\frac{\partial^2}{\partial z \partial z'}\left(V_i^h - V_i^e\right) \tag{66}$$

which, upon using (16), (18), and the equation dual to (17), may be expressed as

$$\tilde{G}^A_{zz}(k_\rho; z|z') = \eta_0^2 \mu_t \mu_t' \left\{\left(\frac{k_0}{k_\rho}\right)^2 I_v^h(k_\rho; z|z') + \left[\frac{1}{\mu_t \epsilon_z} + \frac{1}{\mu_t' \epsilon_z'} - \left(\frac{k_0}{k_\rho}\right)^2\right] I_v^e(k_\rho; z|z')\right\} \tag{67}$$

The elements of $\tilde{\underline{\underline{\boldsymbol{G}}}}^A$, as well as the corresponding $\tilde{G}^\phi$, have thus been determined. Their space domain counterparts are found in the same manner as in Formulation A, and take the form

$$\begin{aligned}
\underline{\underline{\boldsymbol{G}}}^A(\boldsymbol{\rho}; z|z') = {} & \underline{\underline{\boldsymbol{I}}}_t\, \mathcal{S}_0\left\{V_i^h(k_\rho; z|z')\right\} \\
& - (\hat{\boldsymbol{z}}\hat{\boldsymbol{x}}\cos\varphi + \hat{\boldsymbol{z}}\hat{\boldsymbol{y}}\sin\varphi)\, j k_0 \eta_0 \mu_t\, \mathcal{S}_1\left\{\frac{I_i^h(k_\rho; z|z') - I_i^e(k_\rho; z|z')}{k_\rho^2}\right\} \\
& - (\hat{\boldsymbol{x}}\hat{\boldsymbol{z}}\cos\varphi + \hat{\boldsymbol{y}}\hat{\boldsymbol{z}}\sin\varphi)\, j k_0 \eta_0 \mu_t'\, \mathcal{S}_1\left\{\frac{V_v^h(k_\rho; z|z') - V_v^e(k_\rho; z|z')}{k_\rho^2}\right\} \\
& + \hat{\boldsymbol{z}}\hat{\boldsymbol{z}}\, \eta_0^2 \mu_t \mu_t'\, \mathcal{S}_0\left\{\left(\frac{k_0}{k_\rho}\right)^2 I_v^h(k_\rho; z|z') + \left[\frac{1}{\mu_t \epsilon_z} + \frac{1}{\mu_t' \epsilon_z'} - \left(\frac{k_0}{k_\rho}\right)^2\right] I_v^e(k_\rho; z|z')\right\}
\end{aligned} \tag{68}$$

and

$$G^\phi(\boldsymbol{\rho}; z|z') = \mathcal{S}_0\left\{\frac{V_i^h(k_\rho; z|z') - V_i^e(k_\rho; z|z')}{k_\rho^2}\right\} \tag{69}$$

The remark following (49) also applies in the present case. Observe that G^{ϕ} in this formulation is a continuous function of both z and z' across any interface between dissimilar material layers.

5 Summary and Conclusions

We present a systematic derivation of three distinct mixed-potential integral equation (MPIE) formulations, referred to as Formulations A, B, and C, for arbitrarily shaped non-planar conducting objects embedded in a medium comprising any number of planar material layers of infinite lateral extent, which may be uniaxially anisotropic. The development is carried out in the spectral domain, which effectively reduces the original vector problem to a much simpler, scalar transmission line problem. The spectral domain vector and scalar potential kernels of the three formulations have explicitly been expressed in terms of the voltage and current Green's functions of the transmission line network analog of the layered medium. It is found that the three MPIE formulations are of similar complexity for arbitrarily shaped structures, but for strictly planar microstrip geometries, Formulation C is the simplest and thus the most efficient one. This formulation is also recommended when the conductor penetrates an interface between dissimilar material layers, in which case Formulations A and B are not applicable, unless the MPIE (10) is augmented by additional contour integral terms, as discussed by Michalski and Zheng [9], [10]. However, when the conducting structure is confined to a single material layer, Formulations A and B become attractive, because in that case two off-diagonal components of their vector potential kernels vanish, which results in considerable savings in the computational effort. The reader is referred to [9], [10] for a more detailed discussion of the properties of the three formulations.

The advantage of the MPIE approach presented here is that it involves kernels which are less singular and comprise faster converging spectral integrals than the kernels encountered in the standard electric field integral equation (EFIE) formulation. Although the MPIE is more complex than the EFIE, it is amenable to well-established numerical solution procedures originally developed for scatterers of arbitrary shape in homogeneous media [4], [5]. The MPIE approach may not be the most efficient one to use in the case of planar structures with simple, regular shapes, but it offers the flexibility and accuracy that make it well suited for the analysis of nonplanar and/or irregularly shaped microstrip transmission lines and antennas frequently encountered in modern microwave and millimeter-wave systems. The MPIE is also a promising candidate for use in hybrid formulations, which combine differential and integral equation methods [31], [32].

A Transmission Line Green's Functions

Consider a transmission line section corresponding to the nth material layer of Fig. 2, characterized by the parameters (1). Let this line section comprise a unit-strength current source i at z', as illustrated in Fig. 5. It then follows that the voltage V_i^p and current I_i^p at any point z within this section obey the equations (16)-(17), in which $k_z^p = k_{zn}^p$ and $Y^p = Y_n^p$. From these equations, we find that V_i^p may be expressed in

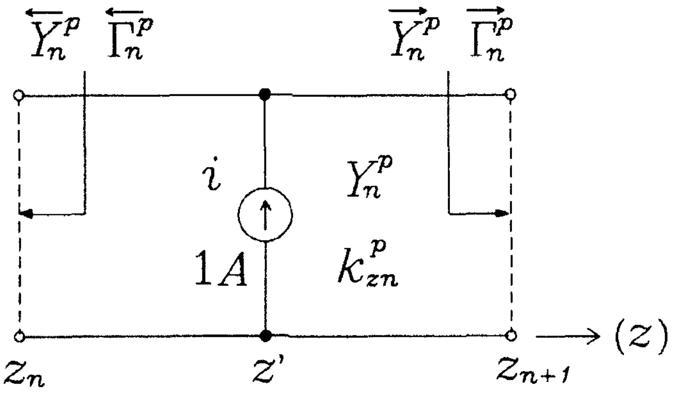

Figure 5: Transmission line section comprising a unit-strength current source.

the traveling-wave form (cf. [24, p. 213])

$$V_i(z|z') = \frac{e^{-jk_{zn}|z-z'|}}{2Y_n} \frac{\left[1+ \overleftarrow{\Gamma}_n(z_0)e^{-j2k_{zn}(z_<-z_0)}\right]\left[1+ \overrightarrow{\Gamma}_n(z_0)e^{j2k_{zn}(z_>-z_0)}\right]}{1- \overleftarrow{\Gamma}_n(z_0)\overrightarrow{\Gamma}_n(z_0)} \tag{70}$$

where $z_< = \min(z, z')$, $z_> = \max(z, z')$, z_0 is an arbitrary reference point within the nth section (which is usually set to z_n or z_{n+1}, whichever is more convenient), and $\overleftarrow{\Gamma}_n(z_0)$ and $\overrightarrow{\Gamma}_n(z_0)$ are the reflection coefficients 'looking to the left' and 'looking to the right,' respectively, at z_0. By means of the translation formula

$$\overset{\rightleftarrows}{\Gamma}_n(z) = \overset{\rightleftarrows}{\Gamma}_n(z_0)\, e^{\pm j2k_{zn}(z-z_0)} \tag{71}$$

where the upper and lower signs correspond to the right and left arrows, respectively, these reflection coefficients can be expressed in terms of the respective terminal reflection coefficients $\overleftarrow{\Gamma}_n$ and $\overrightarrow{\Gamma}_n$, which are related to the corresponding terminal admittances $\overleftarrow{Y}_n$ and $\overrightarrow{Y}_n$ (see Fig. 5) as

$$\overset{\rightleftarrows}{\Gamma}_n = \frac{Y_n - \overset{\rightleftarrows}{Y}_n}{Y_n + \overset{\rightleftarrows}{Y}_n}, \qquad \overset{\rightleftarrows}{Y}_n = Y_n\, \frac{1 - \overset{\rightleftarrows}{\Gamma}_n}{1 + \overset{\rightleftarrows}{\Gamma}_n} \tag{72}$$

For a transmission line section of a finite length d_n, a particularly convenient form of (70) is

$$V_i(z|z') = \frac{e^{-jk_{zn}|z-z'|}}{2Y_n}\, \frac{\left[1 + \overleftarrow{\Gamma}_n\, e^{-j2k_{zn}(z_< - z_n)}\right]\left[1 + \overrightarrow{\Gamma}_n\, e^{-j2k_{zn}(z_{n+1} - z_>)}\right]}{1 - \overleftarrow{\Gamma}_n \overrightarrow{\Gamma}_n\, e^{-j2k_{zn}d_n}} \tag{73}$$

which is obtained by letting $z_0 = z_n$ and using (71).

The remaining transmission line Green's functions can be derived from (73). Hence, $I_v(z|z')$, which is dual to $V_i(z|z')$, is obtained when Y_n is replaced by Z_n in (73) (which causes the reflection coefficients to change signs), $I_i(z|z')$ follows from (16) and (73), and $V_v(z|z')$ may then be obtained from the reciprocity relation given in (18).

The voltage and current on the nth transmission line section that is source-free satisfy (16)-(17) with the delta function absent. From these equations, the voltage at any point z within the line section may be expressed in terms of the voltage $V(z_0)$

across one of its terminal pairs. The result is

$$V(z) = V(z_0) \frac{e^{-jk_{zn}|z-z'|}}{1+ \overset{\rightleftarrows}{\Gamma}_n e^{-j2k_{zn}d_n}} \left[1+ \overset{\leftrightarrows}{\Gamma}_n e^{-j2k_{zn}|z-z_0|}\right] \tag{74}$$

where $z_0 = z_n$ or $z_0 = z_{n+1}$ (see Fig. 5), depending on whether the source is located to the left or to the right, respectively, of the line section, and where the upper (lower) arrow corresponds to $z > z_0$ ($z < z_0$). We have omitted the subscript of V in (74), because the latter applies irrespective of the nature of the source, and dropped z' from its argument, because (74) only implicitly depends on the source location, which is outside the nth line section. The current $I(z)$ corresponding to (74) may be obtained by substituting the latter into (16).

Finally, we note that (71)-(72) are easily implemented in a recursive computer routine to determine the leftward- and rightward-looking reflection coefficients needed in (73) and (74). The computations proceed from the outward-looking reflection coefficients in the top and bottom transmission line sections (see Fig. 4), where they vanish for unshielded structures or otherwise are easily determined, provided the surface admittances $Y_{S,1}$ and $Y_{S,N+1}$ are known. Observe that the exponential functions encountered in (71), (73), and (74) have nonincreasing magnitudes, so there is no danger of overflow. When the nth transmission line section extends to positive (negative) infinity along the z axis, the reflection coefficient $\overrightarrow{\Gamma}_n$ ($\overleftarrow{\Gamma}_n$) is set to zero in (73) and (74).

Acknowledgments

The author is indebted to Drs. Joseph R. Mautz and Chung-I G. Hsu for their constructive criticism of the original manuscript. This work was supported in part by the Office of Naval Research under Contract N00014-90-J-1197.

References

[1] K. A. Michalski, "The mixed-potential electric field integral equation for objects in layered media," *Arch. Elek. Übertragung.*, vol. 39, pp. 317–322, Sept.–Oct. 1985.

[2] J. R. Mosig, "Arbitrarily shaped microstrip structures and their analysis with a mixed potential integral equation," *IEEE Trans. Microwave Theory Tech.*, vol. 36, pp. 314–323, Feb. 1988.

[3] R. F. Harrington, *Field Computation by Moment Methods*. New York: Macmillan, 1968. Reprinted by Krieger Publishing Co., Melbourne, FL, 1982.

[4] A. W. Glisson and D. R. Wilton, "Simple and efficient numerical methods for problems of electromagnetic radiation and scattering from surfaces," *IEEE Trans. Antennas Propagat.*, vol. AP-28, pp. 593–603, Sept. 1980.

[5] S. M. Rao, D. R. Wilton, and A. W. Glisson, "Electromagnetic scattering by surfaces of arbitrary shape," *IEEE Trans. Antennas Propagat.*, vol. AP-30, pp. 409–418, May 1982.

[6] J. R. Mosig and F. E. Gardiol, "A dynamical radiation model for microstrip structures," in *Adv. Electron. Electron Phys.* (P. W. Hawkes, ed.), vol. 59, pp. 139–237, New York: Academic Press, 1982.

[7] J. R. Mosig, "Integral equation technique," in *Numerical Techniques for Microwave and Millimeter-Wave Passive Structures* (T. Itoh, ed.), pp. 133–213, New York: Wiley, 1989.

[8] J. R. Mosig, R. C. Hall, and F. E. Gardiol, "Numerical analysis of microstrip patch antennas," in *Handbook of Microstrip Antennas* (J. R. James and P. S. Hall, eds.), pp. 391–453, London: Peter Peregrinus, 1989.

[9] K. A. Michalski and D. Zheng, "Electromagnetic scattering and radiation by surfaces of arbitrary shape in layered media, Part I: Theory," *IEEE Trans. Antennas Propagat.*, vol. 38, pp. 335–344, Mar. 1990.

[10] K. A. Michalski and D. Zheng, "Electromagnetic scattering and radiation by surfaces of arbitrary shape in layered media, Part II: Implementation and results for contiguous half-spaces," *IEEE Trans. Antennas Propagat.*, vol. 38, pp. 345-352, Mar. 1990.

[11] K. A. Michalski and D. Zheng, "Rigorous analysis of open microstrip lines of arbitrary cross section in bound and leaky regimes," *IEEE Trans. Microwave Theory Tech.*, vol. 37, pp. 2005-2010, Dec. 1989.

[12] N. G. Alexopoulos, "Integrated-circuit structures on anisotropic substrates," *IEEE Trans. Microwave Theory Tech.*, vol. MTT-33, pp. 847-881, Oct. 1985.

[13] D. M. Pozar, "Radiation and scattering from a microstrip patch on a uniaxial substrate," *IEEE Trans. Antennas Propagat.*, vol. AP-35, pp. 613-621, June 1987.

[14] N. W. Montgomery and D. R. Wilton, "Analysis of arbitrary conducting periodic structures embedded in layered media," in *Digest IEEE AP-S Int. Symp.*, (London, Ontario), pp. 1889–1892, June 1991.

[15] D. Zheng and K. A. Michalski, "Analysis of coaxially fed microstrip antennas of arbitrary shape with thick substrates," *J. Electromagn. Waves Appl.*, vol. 5, no. 12, pp. 1303–1327, 1991.

[16] K. A. Michalski and D. Zheng, "Analysis of microstrip resonators of arbitrary shape," *IEEE Trans. Antennas Propagat.*, vol. 40, pp. 112–119, Jan. 1992.

[17] C.-I. G. Hsu, R. F. Harrington, K. A. Michalski, and D. Zheng, "Analysis of a multiconductor transmission lines of arbitrary cross-section in multilayered uniaxial media," *IEEE Trans. Microwave Theory Tech.*, vol. 41, Jan. 1993 (to appear).

[18] R. F. Harrington, *Time-Harmonic Electromagnetic Field.* New York: McGraw-Hill, 1961.

[19] T. Sphicopoulos, V. Teodoridis, and F. E. Gardiol, "Dyadic Green function for the electromagnetic field in multilayered isotropic media: An operator approach," *IEE Proc., Pt. H*, vol. 132, pp. 329–334, Aug. 1985.

[20] W. S. Weiglhofer, "Dyadic Green's functions for general uniaxial media," *IEE Proc., Pt. H*, vol. 137, pp. 5–10, Feb. 1990.

[21] R. E. Collin and F. J. Zucker, eds., *Antenna Theory - Part I*. New York: McGraw-Hill, 1969.

[22] J. M. Pond, C. M. Krowne, and W. L. Carter, "On the application of complex resistive boundary conditions to model transmission lines consisting of very thin superconductors," *IEEE Trans. Antennas Propagat.*, vol. 37, pp. 181–190, Jan. 1989.

[23] J. Van Bladel, *Electromagnetic Fields*. New York: Hemisphere, 1985.

[24] L. B. Felsen and N. Marcuvitz, *Radiation and Scattering of Waves*. Englewood Cliffs, N.J.: Prentice Hall, 1973.

[25] T. Itoh, "Spectral-domain immittance approach for dispersion characteristics of generalized printed transmission lines," *IEEE Trans. Microwave Theory Tech.*, vol. MTT-28, pp. 733–736, July 1980.

[26] L. Vegni, R. Cicchetti, and P. Capece, "Spectral dyadic Green's function formulation for planar integrated structures," *IEEE Trans. Antennas Propagat.*, vol. 36, pp. 1057–1065, Aug. 1988.

[27] R. Kastner, E. Heyman, and A. Sabban, "Spectral domain iterative analysis of single- and double-layered microstrip antennas using the conjugate gradient algorithm," *IEEE Trans. Antennas Propagat.*, vol. 36, pp. 1204–1212, Sept. 1988.

[28] L. Beyne and D. De Zutter, "Green's function for layered lossy media with special application to microstrip antennas," *IEEE Trans. Microwave Theory Tech.*, vol. 36, pp. 875–881, May 1988.

[29] M. Davidovitz and Y. T. Lo, "Rigorous analysis of a circular patch antenna excited by a microstrip transmission line," *IEEE Trans. Antennas Propagat.*, vol. 37, pp. 949–958, Aug. 1989.

[30] P. E. Mayes, *Electromagnetics for Engineers*. Dept. of Electrical and Computer Eng., Univ. of Illinois, Urbana, IL: P. E. Mayes, 1965.

[31] Z. Gong and A. W. Glisson, "A hybrid equation approach for the solution of electromagnetic scattering problems involving two-dimensional inhomogeneous dielectric cylinders," *IEEE Trans. Antennas Propagat.*, vol. 38, pp. 60–68, Jan. 1990.

[32] X. Yuan, D. R. Lynch, and J. W. Strohbehn, "Coupling of finite element and moment methods for electromagnetic scattering from inhomogeneous objects," *IEEE Trans. Antennas Propagat.*, vol. 38, pp. 386–393, Mar. 1990.

Mixed-Potential Integral Equation (MPIE) Formulation for Non-Planar Microstrip Structures of Arbitrary Shape in Multi-Layered Uniaxial Media

Krzysztof A. Michalski

Electromagnetics & Microwave Laboratory, Department of Electrical
Engineering, Texas A&M University, College Station, Texas 77843

Abstract

A straightforward derivation is presented of three distinct mixed-potential integral equations (MPIEs) that are well-suited for the analysis of arbitrarily shaped, planar or non-planar microstrip structures in multi-layered, planar, uniaxially anisotropic media of infinite lateral extent.

1 Introduction

The integral equation–method of moments (IE–MOM) approach, implemented either in the spectrum or space domain, continues to be the method of choice for the analysis of open microstrip structures (see [1] and [2] for recent examples of the application of these techniques). The spectral and space domain IE formulations, both being based on the rigorous Green's function of the background medium, are formally identical, and only differ in the order in which the integrals that arise are performed. When applied to planar geometries, the spectral domain approach (SDA) results in very simple expressions for the MOM matrix elements, which, however, comprise slowly convergent double spectral integrals. Consequently, to make this technique practical, a considerable effort is required to accelerate these integrals, and the initial simplicity of the formulation is lost in the process [3], [4], [5]. Although the SDA can in principle be extended to non-planar conductors, the space domain integrals that must be analytically evaluated involve in that case the layered medium Green's function, and the development is tedious and results in several spectral integrals for each matrix element, thus further complicating the acceleration procedure.

The space domain IE is usually first transformed into a mixed-potential form, in which the electric field is expressed in terms of the vector and scalar potentials, before it is subjected to the MOM [6]. The resulting IE, which is often referred to in the literature as the mixed-potential integral equation (MPIE) [7], [8], has a more complicated form than its spectral domain counterpart, but has many advantages, making it very attractive, particularly for non-planar and arbitrarily shaped microstrip structures. First, the MPIE potential kernels are less singular when the source and observation points coincide on the surface of the object than the dyadic kernel of the standard electric field integral equation (EFIE) (in the SDA implementation of the EFIE, the severe kernel singularity of the latter is manifested by a divergent behavior of the double spectral integrals). Second, the MPIE is amenable to well-established numerical solution procedures [6], [9], [10], [11] and—in contrast to the SDA—it only requires single spectral integrals of the Sommerfeld type [12, p. 240], which are independent of the testing and basis functions employed in the MOM procedure. Third, these Sommerfeld integrals are amenable to various approximation methods, such as the interpolation and table look-up scheme [13] (see also [14], [15]), or the complex-image representation [16], [17], which drastically reduce the computational effort.

In a layered medium, different MPIE formulations are possible, as a result of the non-uniqueness of the potentials. There are at least three possible useful choices of the magnetic vector potential (or electric Hertz vector) associated with a horizontal time-harmonic dipole [18], which also lead to different scalar potentials. Of the three vector potential choices, the classical Sommerfeld's form [12, p. 258] (termed 'traditional' in [19]) has been and remains the most popular and useful. Another form, termed 'alternative,' has been shown to have some advantages over the traditional one in the MPIE formulation [19]. As was first pointed out by Mosig and Gardiol [13], the scalar potential kernel of the MPIE may be interpreted as the potential of a single point charge associated with a time-harmonic dipole. In a layered medium, the potentials associated with the horizontal and vertical dipoles are different [19], which poses a difficulty in the case of arbitrarily shaped, non-planar objects, because only one scalar potential appears in the standard form of the MPIE. A method to overcome this difficulty was first proposed by Michalski [7]. The two forms of the vector potential (traditional and alternative) and two scalar potentials (horizontal and vertical) lead to three distinct MPIE formulations, which were first developed and explored in detail by Michalski and Zheng [20], [21].

The MPIE approach was first applied to planar microstrip structures with isotropic substrates by Mosig and Gardiol [13]. Their formulation was later adopted by others [22], [23], [24], [25], [26], [27] and was extended to multi-layered media [14], [15] and to electrically uniaxial media [28]. One of the MPIE forms developed in [20], referred to as Formulation C (which corresponds to the 'traditional formulation' of [19]), has recently been employed to analyze coax-fed microstrip patch antennas of arbitrary shape [29], [30], [31], as well as microstrip transmission lines of arbitrary cross-section [32], [33]. This formulation, which is based on the Sommerfeld's form of the vector potential and the scalar potential associated with a horizontal dipole, reduces for planar microstrip structures with isotropic substrates to that originally developed by Mosig and Gardiol [13] (see also [15], [14]). A modification of Formulation C was adopted by Montgomery and Wilton [34] (see also [35]) for the analysis of arbitrary conducting periodic structures embedded in layered media. For microstrip geometries that only comprise planar and vertical components, such as coax probe-fed microstrip patch antennas, hybrid MPIE formulations have been developed, which utilize two scalar potential kernels (associated with the horizontal and vertical dipoles) and, as a result, require a point charge at the probe-to-patch junction [36], [37], [38], [39], [40]. A still different MPIE formulation has recently been introduced by Vandenbosch and Van de Capelle [41].

The purpose of this paper is to present a new, straightforward development of three distinct MPIE formulations (corresponding to Formulations A, B, and C of [20]), that are suitable for arbitrarily shaped, non-planar, microstrip structures embedded multi-layered, planar, uniaxial media of infinite lateral extent.

2 Preliminaries

Consider a medium comprising N planar, uniaxially anisotropic layers of infinite lateral extent, as illustrated in Fig. 1. The nth layer is characterized by the permittivity and permeability dyadics, $\underline{\underline{\epsilon}}_n$ and $\underline{\underline{\mu}}_n$, of the form

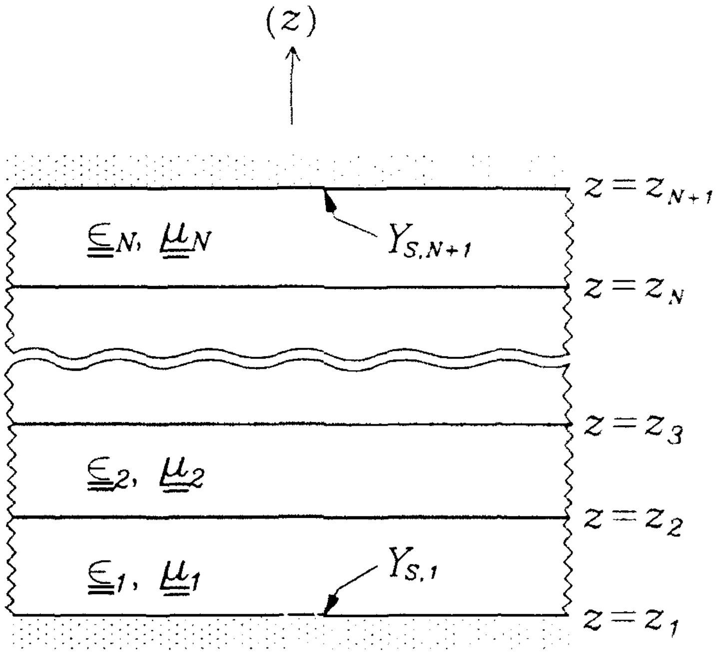

Figure 1: Medium comprising N planar, uniaxially anisotropic layers.

$$\underline{\underline{\epsilon}}_n = \underline{\underline{I}}_t \, \epsilon_{tn} + \hat{z}\hat{z} \, \epsilon_{zn} , \qquad \underline{\underline{\mu}}_n = \underline{\underline{I}}_t \, \mu_{tn} + \hat{z}\hat{z} \, \mu_{zn} \tag{1}$$

where ϵ_{tn} (μ_{tn}) and ϵ_{zn} (μ_{zn}) denote, respectively, the transverse and longitudinal dielectric (magnetic) constants relative to free space, and $\underline{\underline{I}}_t$ is the unit dyadic transverse to z. Observe that we distinguish dyadics by double underlines and unit vectors by carets. The free space permeability and permittivity will be denoted by μ_0 and ϵ_0, respectively. For each layer, we also introduce its electric and magnetic anisotropy ratios, ν_n^e and ν_n^h, respectively, given as

$$\nu_n^e = \frac{\epsilon_{zn}}{\epsilon_{tn}} , \qquad \nu_n^h = \frac{\mu_{zn}}{\mu_{tn}} \tag{2}$$

The top and bottom layers may be of infinite extent along the z axis or as illustrated in Fig. 1—may be shielded by ground planes having specified surface admittances $Y_{S,N+1}$ and $Y_{S,1}$, respectively, where the latter are infinite for perfect electric conductors (PEC).

Let an arbitrarily shaped PEC object, whose surface S may be open or closed, be embedded in the layered medium of Fig. 1. Furthermore, let $\boldsymbol{E}^i$ denote the impressed (primary) time-harmonic (the $e^{j\omega t}$ time convention is adopted here) electric field that exists in the layered medium in the absence of the object. With the object present, this field excites on S the surface current $\boldsymbol{J}_S$, which is the source of the scattered (secondary) electric field. The latter may be expressed as

$$\begin{aligned} \boldsymbol{E}(\boldsymbol{r}) &= \int_S \underline{\underline{\boldsymbol{G}}}^E(\boldsymbol{\rho}-\boldsymbol{\rho}'; z|z') \cdot \boldsymbol{J}_S(\boldsymbol{r}')\, dS' \\ &\equiv \langle \underline{\underline{\boldsymbol{G}}}^E ; \boldsymbol{J}_S \rangle'_S \end{aligned} \tag{3}$$

where $\underline{\underline{\boldsymbol{G}}}^E$ is the dyadic Green's function of the layered medium, $\boldsymbol{r}$ and $\boldsymbol{\rho}$ denote, respectively, the position vector and its projection on the xy plane, and where primes are used to distinguish source coordinates. For later convenience, we have introduced in (3) the shorthand notation $\langle\, ; \rangle$ for an integral of a product of two functions separated by the comma. The dot over the comma signifies a 'dot product' of vector arguments and the prime over $\rangle$ indicates that the integration is over the primed (source) coordinates, while the subscript S designates the domain of integration.

The dyadic Green's function in (3) may be expressed as the inverse Vector Fourier Transform (cf. [42]) of its spectral domain counterpart, $\tilde{\underline{\underline{\boldsymbol{G}}}}^E$, of the form

$$\begin{aligned} \underline{\underline{\boldsymbol{G}}}^E(\boldsymbol{\rho}-\boldsymbol{\rho}'; z|z') &= \mathcal{F}^{-1}\left\{ \underline{\underline{\boldsymbol{Q}}}^T(\xi) \cdot \tilde{\underline{\underline{\boldsymbol{G}}}}^E(\boldsymbol{k}_\rho; z|z') \cdot \underline{\underline{\boldsymbol{Q}}}(\xi) \right\} \\ &\equiv \frac{1}{(2\pi)^2} \int_{-\infty}^{+\infty}\int_{-\infty}^{+\infty} \underline{\underline{\boldsymbol{Q}}}^T(\xi) \cdot \tilde{\underline{\underline{\boldsymbol{G}}}}^E(\boldsymbol{k}_\rho; z|z') \cdot \underline{\underline{\boldsymbol{Q}}}(\xi)\, e^{-j\boldsymbol{k}_\rho\cdot(\boldsymbol{\rho}-\boldsymbol{\rho}')}\, dk_x\, dk_y \end{aligned} \tag{4}$$

Here, k_x and k_y are the spectral domain counterparts of x and y, respectively, and $\boldsymbol{k}_\rho = \hat{\boldsymbol{x}} k_x + \hat{\boldsymbol{y}} k_y$ is the radial wave vector. Based on $\boldsymbol{k}_\rho$, we introduce the rotated spectral domain coordinate system illustrated in Fig. 2, where the unit vectors $\hat{\boldsymbol{u}}$ and $\hat{\boldsymbol{v}}$ are

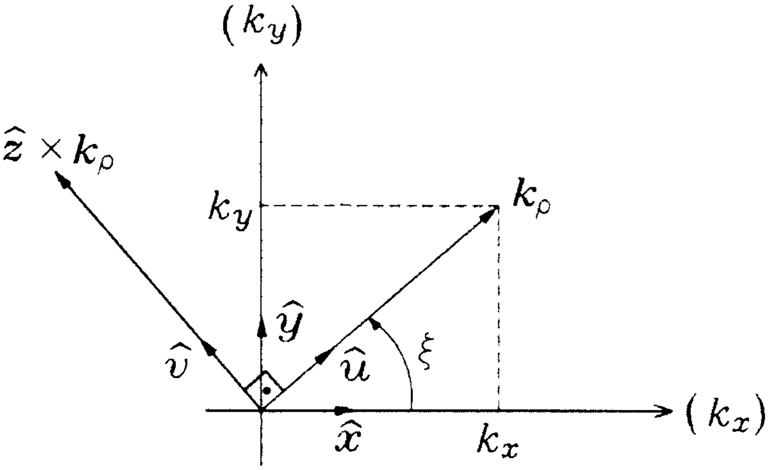

Figure 2: Rotated spectral domain coordinate system.

given as (cf. [43], [44], [45], [46])

$$\hat{\boldsymbol{u}} = \frac{\boldsymbol{k}_\rho}{k_\rho}, \qquad \hat{\boldsymbol{v}} = \frac{\hat{\boldsymbol{z}} \times \boldsymbol{k}_\rho}{k_\rho}, \qquad k_\rho = \sqrt{k_x^2 + k_y^2} \tag{5}$$

In (4), the dyadic operator

$$\underline{\underline{\boldsymbol{Q}}}(\xi) = (\hat{\boldsymbol{u}}\hat{\boldsymbol{x}} + \hat{\boldsymbol{v}}\hat{\boldsymbol{y}})\cos\xi + (\hat{\boldsymbol{u}}\hat{\boldsymbol{y}} - \hat{\boldsymbol{v}}\hat{\boldsymbol{x}})\sin\xi + \hat{\boldsymbol{z}}\hat{\boldsymbol{z}} \tag{6}$$

and its transpose, $\underline{\underline{\boldsymbol{Q}}}^T(\xi)$, are employed to directly transform $\grave{\underline{\underline{\boldsymbol{G}}}}^E$ from the rotated spectrum space to the configuration space. Upon projecting Fourier-transformed Maxwell's equations on the rotated coordinates of Fig. 2, we find that these equations split into two independent sets comprising, respectively, fields that are transverse-magnetic (TM) and transverse-electric (TE) to z. Furthermore, it is found that these partial fields may efficiently be expressed in terms of the voltages and currents on two transmission lines along the z axis, with the propagation wavenumbers and characteristic admittances given as

$$k_z^e = \sqrt{k_0^2 \mu_t \epsilon_t - k_\rho^2 / \nu^e}, \qquad Y^e \equiv \frac{1}{Z^e} = \frac{k_0 \epsilon_t}{\eta_0 k_z^e} \tag{7}$$

and

$$k_z^h = \sqrt{k_0^2\mu_t\epsilon_t - k_\rho^2/\nu^h}\,, \qquad Y^h \equiv \frac{1}{Z^h} = \frac{k_z^h}{\eta_0 k_0 \mu_t} \tag{8}$$

respectively, where $k_0 = \omega\sqrt{\mu_0\epsilon_0}$ is the wavenumber and $\eta_0 = \sqrt{\mu_0/\epsilon_0}$ the intrinsic impedance of free space. Observe that at this stage of the development, the permeability and permittivity (and thus also the anisotropy ratios) of the medium may vary arbitrarily with z and are not necessarily restricted to be piecewise-constant, as is the case in Fig. 1. In the above we have adopted the convention that the quantities associated with the TM and TE transmission lines are distinguished by superscripts e and h, respectively. For the following development, it will be convenient to also introduce transmission line Green's functions, which represent the voltage or current excited by a unit-strength voltage or current point source. Hence, let $V_i^p(z|z')$ and $I_i^p(z|z')$, where the superscript p stands for e or h, denote the voltage and current, respectively, at a point z due to a 1 A current source located at z' on the corresponding transmission line (cf. [47], [46]). These Green's functions are governed by the coupled equations

$$\begin{aligned} \frac{d}{dz}V_i^p(z|z') &= -jk_z^p Z^p\, I_i^p(z|z') && (9)\\ \frac{d}{dz}I_i^p(z|z') &= -jk_z^p Y^p\, V_i^p(z|z') + \delta(z-z') && (10) \end{aligned}$$

where $\delta(z-z')$ is the Dirac delta. Similarly, let $V_v^p(z|z')$ and $I_v^p(z|z')$ denote the voltage and current, respectively, at z due to a 1 V voltage source at z'. It then follows that these Green's functions satisfy equations dual to (9)-(10), which are obtained from the latter by making the substitutions $V_i^p \to I_v^p$, $I_i^p \to V_v^p$, $Z^p \to Y^p$, and $Y^p \to Z^p$. From their governing equations, it can also be shown that the four transmission line Green's functions possess the symmetry and reciprocity properties [48, p. 194]

$$V_i^p(z|z') = V_i^p(z'|z)\,, \quad I_v^p(z|z') = I_v^p(z'|z)\,, \quad V_v^p(z|z') = -I_i^p(z'|z) \tag{11}$$

In the rotated coordinate system of Fig. 2, the spectral domain dyadic $\underline{\underline{\tilde{G}}}^E$ in (4) may be expressed in terms of the transmission line Green's functions as (see also

Kastner et al. [47])

$$
\begin{aligned}
-\underline{\underline{\tilde{\boldsymbol{G}}}}^{E}(\boldsymbol{k}_\rho;z|z') = {} & \hat{\boldsymbol{u}}\hat{\boldsymbol{u}}\, V_i^e(k_\rho;z|z') + \hat{\boldsymbol{v}}\hat{\boldsymbol{v}}\, V_i^h(k_\rho;z|z') \\
& - \hat{\boldsymbol{z}}\hat{\boldsymbol{u}}\,\frac{\eta_0 k_\rho}{k_0\epsilon_z}\, I_i^e(k_\rho;z|z') - \hat{\boldsymbol{u}}\hat{\boldsymbol{z}}\,\frac{\eta_0 k_\rho}{k_0\epsilon_z'}\, V_v^e(k_\rho;z|z') \\
& + \hat{\boldsymbol{z}}\hat{\boldsymbol{z}}\left[\left(\frac{\eta_0 k_\rho}{k_0}\right)^2 \frac{I_v^e(k_\rho;z|z')}{\epsilon_z\epsilon_z'} + \frac{\eta_0}{jk_0\epsilon_z'}\,\delta(z-z')\right]
\end{aligned}
\tag{12}
$$

where δ is the Dirac delta function, and where the primed and unprimed media parameters are evaluated at z' and z, respectively—a convention that will also be in effect throughout the remainder of this paper, unless the layer index is explicitly stated. Observe that in the above we explicitly indicate the dependence of the transmission line Green's functions on the transverse spectral wavenumber k_ρ. Since no assumptions have so far been made regarding the dependence of the media parameters on z, the spectral dyadic Green's function given in (12) is valid, in particular, for the layered medium of Fig. 1, where the permeability and permittivity are piecewise-constant. The voltage and current Green's functions of its transmission line network analog are easily found for any number of layers, as discussed in the appendix.

We note that the transmission line Green's functions appearing in (12) depend on the spectral variables k_x and k_y exclusively through k_ρ. As a consequence, when the double spectral integration in (4) is performed in the polar system (k_ρ,ξ) shown in Fig. 2, the ξ-integrals can be evaluated in closed form. More specifically, we find that

$$
\mathcal{F}^{-1}\left\{\begin{matrix}\sin\\ \cos\end{matrix}\, n\xi\, f(k_\rho)\right\} = (-j)^n \begin{matrix}\sin\\ \cos\end{matrix}\, n\vartheta\, \mathcal{S}_n\left\{f(k_\rho)k_\rho^{-n}\right\}, \qquad n = 0,1,2 \tag{13}
$$

where we have introduced the notation

$$
\mathcal{S}_n\{f(k_\rho)\} = \frac{1}{2\pi}\int_0^\infty dk_\rho\, f(k_\rho)k_\rho^{n+1} J_n(k_\rho\varrho) \tag{14}
$$

In the above,

$$
\vartheta = \arctan\left(\frac{y-y'}{x-x'}\right), \qquad \varrho = \sqrt{(x-x')^2+(y-y')^2} \tag{15}
$$

and J_n is the Bessel function of order n. In this fashion, the space domain dyadic $\underline{\underline{\boldsymbol{G}}}^E$ may be expressed in terms of the Sommerfeld-type integrals (14). Its explicit form is easily found with the help of (4) and (13), but will not be required in the following development, and is not listed here in the interest of brevity.

With $\underline{\underline{\boldsymbol{G}}}^E$ determined, the electric field scattered by the conducting object may be found from (3), provided the surface current $\boldsymbol{J}_S$ is given. When the latter is not known a priori as is usually the case, we may use (3) to formulate an IE for $\boldsymbol{J}_S$ by enforcing the condition that the total tangential electric field must vanish at S. As a result, we obtain the EFIE

$$-\left\langle \boldsymbol{A}_k ; \langle \underline{\underline{\boldsymbol{G}}}^E ; \boldsymbol{J}_S \rangle'_S \right\rangle_S = \langle \boldsymbol{A}_k ; \boldsymbol{E}^i \rangle_S \tag{16}$$

where $\{\boldsymbol{A}_k\}$ is a suitably chosen complete set of linearly independent vector weight (testing) functions defined over and tangential to S. This EFIE, however, is not suitable for a direct application of the MOM [6] because the dyadic kernel $\underline{\underline{\boldsymbol{G}}}^E$ exhibits a severe singularity when the source and observation points coincide on S and the Sommerfeld-type integrals that arise are slowly convergent.

When the spectral representation of $\underline{\underline{\boldsymbol{G}}}^E$ given in (4) is substituted into (16) and the order of the spectral and space integrals reversed, the latter may be evaluated analytically, provided the testing functions $\{\boldsymbol{A}_k\}$ and the basis functions used to represent $\boldsymbol{J}_S$ are Fourier-transformable in closed form. This procedure leads to the previously mentioned SDA, which has been popular in the analysis of planar microstrip structures. Unfortunately, the double spectral integrals associated with this approach suffer from an extremely slow convergence and—except for simple, regular geometries, for which the MOM matrix has a small size—the method is inefficient.

The difficulties encountered when the MOM is applied to the EFIE may be alleviated if the secondary electric field (3) is expressed as

$$-\boldsymbol{E}(\boldsymbol{r}) = \langle \underline{\underline{\boldsymbol{G}}}^A ; \boldsymbol{J}_S \rangle'_S + \nabla \langle G^\Phi , \nabla' \cdot \boldsymbol{J}_S \rangle'_S \tag{17}$$

in which ∇' operates on source coordinates, and where $\underline{\underline{\boldsymbol{G}}}^A$ and G^Φ are referred to, respectively, as the vector and scalar potential kernels. Because both potentials appear in (17), the latter is termed the mixed-potential representation of the electric field [7], [49]. Upon using (17), instead of (3), in the procedure that led to the EFIE (16), and applying a Gauss' theorem [50, p. 503], we arrive at the MPIE

$$\left\langle \boldsymbol{A}_k ; \langle \underline{\underline{\boldsymbol{G}}}^A ; \boldsymbol{J}_S \rangle'_S \right\rangle_S - \left\langle \boldsymbol{\nabla} \cdot \boldsymbol{A}_k , \langle G^\phi , \boldsymbol{\nabla}' \cdot \boldsymbol{J}_S \rangle'_S \right\rangle_S = \langle \boldsymbol{A}_k ; \boldsymbol{E}^i \rangle_S \qquad (18)$$

provided G^ϕ is a continuous function of z across any interface between dissimilar material layers the object penetrates. Comparing the EFIE (16) with the MPIE (18), we note that in the latter the differential operator $\boldsymbol{\nabla}\boldsymbol{\nabla}'$ has in effect been extracted from $\underline{\underline{\boldsymbol{G}}}^E$ and transferred onto $\boldsymbol{A}_k$ and $\boldsymbol{J}_S$ [35]. As a consequence, the kernels $\underline{\underline{\boldsymbol{G}}}^A$ and G^ϕ appearing in the MPIE (18) are less singular (or 'less discontinuous' [50, p. 195]) than $\underline{\underline{\boldsymbol{G}}}^E$, and the resulting Sommerfeld-type integrals converge more rapidly. Clearly, for this equation to be applicable, the testing functions and the basis functions used to represent $\boldsymbol{J}_S$ must be at least once differentiable—a requirement that can easily be accommodated [10]. Finally, we note that (18) may readily be extended to imperfect conductors via the surface impedance concept [8], [38].

In the next section, we employ the spectral dyadic $\tilde{\underline{\underline{\boldsymbol{G}}}}^E$ given in (12) as the point of departure in the development of the vector and scalar potential kernels, $\underline{\underline{\boldsymbol{G}}}^A$ and G^ϕ, respectively, associated with three distinct MPIE formulations, for multi-layered, planar, uniaxial media of infinite lateral extent.

3 MPIE Development

The development is carried out in the spectral domain and it proceeds from the spectral electric dyadic Green's function $\tilde{\underline{\underline{\boldsymbol{G}}}}^E$ given in (12). First, we add to and subtract from (12) the term $\hat{\boldsymbol{u}}\hat{\boldsymbol{u}}\, V_i^h(k_\rho; z|z')$ and recognize that $\hat{\boldsymbol{u}}\hat{\boldsymbol{u}} + \hat{\boldsymbol{v}}\hat{\boldsymbol{v}} = \underline{\underline{\boldsymbol{I}}}_t$. Next, we observe that $\tilde{\boldsymbol{\nabla}}_t = -jk_\rho \hat{\boldsymbol{u}}$, where $\tilde{\boldsymbol{\nabla}}_t$ is the spectral domain counterpart of $\boldsymbol{\nabla}_t$ —the transverse (to z) part of the operator nabla, and that $\tilde{\boldsymbol{\nabla}}'_t = jk_\rho \hat{\boldsymbol{u}}$. As a results of these steps, we obtain

$$-\tilde{\underline{\underline{\boldsymbol{G}}}}^E(\boldsymbol{k}_\rho; z|z') = \underline{\underline{\boldsymbol{I}}}_t\, V_i^h(k_\rho; z|z') - \tilde{\boldsymbol{\nabla}}_t \tilde{\boldsymbol{\nabla}}'_t \left[\frac{V_i^h(k_\rho; z|z') - V_i^e(k_\rho; z|z')}{k_\rho^2} \right]$$

$$- \hat{z}\tilde{\nabla}_t' \frac{\eta_0}{jk_0\epsilon_z} I_i^e(k_\rho;z|z') + \tilde{\nabla}_t\hat{z} \frac{\eta_0}{jk_0\epsilon_z'} V_v^e(k_\rho;z|z')$$
$$+ \hat{z}\hat{z}\left[\left(\frac{\eta_0 k_\rho}{k_0}\right)^2 \frac{I_v^e(k_\rho;z|z')}{\epsilon_z\epsilon_z'} + \frac{\eta_0}{jk_0\epsilon_z'}\delta(z-z')\right] \qquad (19)$$

Next, we use the properties of the transmission line Green's functions in conjunction with the identity

$$\tilde{\nabla}\tilde{\nabla}' = \tilde{\nabla}_t\tilde{\nabla}_t' + \tilde{\nabla}_t\hat{z}\frac{\partial}{\partial z'} + \hat{z}\frac{\partial}{\partial z}\tilde{\nabla}_t' + \hat{z}\hat{z}\frac{\partial}{\partial z}\frac{\partial}{\partial z'} \qquad (20)$$

to express $\underline{\underline{\tilde{G}}}^E$ in the form

$$-\underline{\underline{\tilde{G}}}^E(\boldsymbol{k}_\rho;z|z') = \underline{\underline{\tilde{G}}}^A(\boldsymbol{k}_\rho;z|z') - \tilde{\nabla}\tilde{\nabla}'\tilde{G}^\Phi(\boldsymbol{k}_\rho;z|z') \qquad (21)$$

which in the space domain becomes

$$-\underline{\underline{G}}^E(\boldsymbol{\rho}-\boldsymbol{\rho}';z|z') = \underline{\underline{G}}^A(\boldsymbol{\rho}-\boldsymbol{\rho}';z|z') - \nabla\nabla'G^\Phi(\boldsymbol{\rho}-\boldsymbol{\rho}';z|z') \qquad (22)$$

Upon using the above in (3) and appealing to the divergence theorem [50, p. 503], we arrive at the mixed-potential representation of $\boldsymbol{E}$ given in (17)—provided G^Φ is a continuous function of z' across any interface between dissimilar material layers the object penetrates, which then leads to the desired MPIE (18).

The decomposition of $\underline{\underline{\tilde{G}}}^E$ according to (21) is not unique and leads to different MPIE forms, depending on the choice of $\underline{\underline{\tilde{G}}}^A$ and $\tilde{G}^\Phi$. Below, we develop three distinct MPIE formulations that have been found useful in MOM analyses of the radiation, scattering, and guidance of electromagnetic fields by arbitrarily shaped conducting structures in layered media. In the interest of brevity, some details of the derivations—which repeatedly invoke the equations (9)–(10) and their duals, as well as the reciprocity and symmetry properties (11) of the transmission line Green's functions—are omitted.

Formulation A

By invoking the properties of the transmission line Green's functions, we may express (19) as

$$-\tilde{\underline{\underline{G}}}^E(\boldsymbol{k}_\rho;z|z') = \underline{\underline{I}}_t\,V_i^h(k_\rho;z|z') - \tilde{\boldsymbol{\nabla}}_t\tilde{\boldsymbol{\nabla}}_t'\left[\frac{V_i^h(k_\rho;z|z') - V_i^e(k_\rho;z|z')}{k_\rho^2}\right]$$
$$+\,\tilde{\boldsymbol{\nabla}}_t\hat{\boldsymbol{z}}\,\frac{\eta_0}{jk_0\epsilon_z'}\,V_v^e(k_\rho;z|z') + \hat{\boldsymbol{z}}\hat{\boldsymbol{z}}\,\eta_0^2\frac{\mu_t'}{\epsilon_z}\,I_v^e(k_\rho;z|z')$$
$$-\left(\hat{\boldsymbol{z}}\frac{\partial}{\partial z}\tilde{\boldsymbol{\nabla}}_t' + \hat{\boldsymbol{z}}\hat{\boldsymbol{z}}\frac{\partial}{\partial z}\frac{\partial}{\partial z'}\right)\frac{V_i^e(k_\rho;z|z')}{\nu^e(k_z^e)^2} \qquad (23)$$

provided the field point is within a homogeneous material layer. The form of the above suggests that we may choose

$$\tilde{G}^\Phi(\boldsymbol{k}_\rho;z|z') = \frac{V_i^e(k_\rho;z|z')}{\nu^e(k_z^e)^2} \qquad (24)$$

as the spectral domain scalar potential kernel (this choice corresponds to Formulation A of [20]). Next, we make use of the identity (20) and combine terms in (23) to arrive at (21), in which

$$\tilde{\underline{\underline{G}}}^A(\boldsymbol{k}_\rho;z|z') = \underline{\underline{I}}_t\,V_i^h(k_\rho;z|z')$$
$$-\,\tilde{\boldsymbol{\nabla}}_t\tilde{\boldsymbol{\nabla}}_t'\left[\frac{V_i^h(k_\rho;z|z')}{k_\rho^2} - \frac{k_0^2\mu_t\epsilon_t}{(k_z^e)^2}\,\frac{V_i^e(k_\rho;z|z')}{k_\rho^2}\right]$$
$$+\,\tilde{\boldsymbol{\nabla}}_t\hat{\boldsymbol{z}}\,jk_0\eta_0\mu_t'\left(1-\frac{\mu_t\epsilon_z}{\mu_t'\epsilon_z'}\right)\frac{V_v^e(k_\rho;z|z')}{\nu^e(k_z^e)^2} + \hat{\boldsymbol{z}}\hat{\boldsymbol{z}}\,\eta_0^2\frac{\mu_t'}{\epsilon_z}\,I_v^e(k_\rho;z|z') \qquad (25)$$

The space domain counterparts of (25) and (24) are found as

$$\underline{\underline{G}}^A(\boldsymbol{\rho}-\boldsymbol{\rho}';z|z') = \frac{1}{2}\underline{\underline{I}}_t\,\mathcal{S}_0\left\{V_i^h(k_\rho;z|z') + \frac{k_0^2\mu_t\epsilon_t}{(k_z^e)^2}\,V_i^e(k_\rho;z|z')\right\}$$
$$+\,\frac{1}{2}[(\hat{\boldsymbol{x}}\hat{\boldsymbol{x}}-\hat{\boldsymbol{y}}\hat{\boldsymbol{y}})\cos 2\vartheta + (\hat{\boldsymbol{x}}\hat{\boldsymbol{y}}+\hat{\boldsymbol{y}}\hat{\boldsymbol{x}})\sin 2\vartheta]\,\mathcal{S}_2\left\{\frac{V_i^h(k_\rho;z|z')}{k_\rho^2} - \frac{k_0^2\mu_t\epsilon_t}{(k_z^e)^2}\,\frac{V_i^e(k_\rho;z|z')}{k_\rho^2}\right\}$$
$$-\,(\hat{\boldsymbol{x}}\hat{\boldsymbol{z}}\cos\vartheta + \hat{\boldsymbol{y}}\hat{\boldsymbol{z}}\sin\vartheta)\,jk_0\eta_0\mu_t'\left(1-\frac{\mu_t\epsilon_z}{\mu_t'\epsilon_z'}\right)\mathcal{S}_1\left\{\frac{V_v^e(k_\rho;z|z')}{\nu^e(k_z^e)^2}\right\}$$

$$+ \,\hat{\boldsymbol{z}}\hat{\boldsymbol{z}}\, \eta_0^2 \frac{\mu_t'}{\epsilon_z} \mathcal{S}_0 \{ I_v^e(k_\rho; z|z') \} \tag{26}$$

and

$$G^\Phi(\boldsymbol{\rho} - \boldsymbol{\rho}'; z|z') = \mathcal{S}_0 \left\{ \frac{V_i^e(k_\rho; z|z')}{\nu^e (k_z^e)^2} \right\} \tag{27}$$

respectively, where we have used the notation introduced in (13)–(15). Observe that when the source and field points are within the same material layer, the xz and yz components of $\underline{\underline{\boldsymbol{G}}}^A$ vanish, thus resulting in a significant simplification of this MPIE formulation. Note, however, that G^Φ in this formulation is a discontinuous function of z across any interface between dissimilar material layers.

Formulation B

Upon using the properties of the transmission line Green's functions, we may also express (19) as

$$\begin{aligned} -\,\underline{\underline{\tilde{\boldsymbol{G}}}}^E(\boldsymbol{k}_\rho; z|z') = {} & \underline{\underline{\boldsymbol{I}}}_t\, V_i^h(k_\rho; z|z') - \tilde{\boldsymbol{\nabla}}_t \tilde{\boldsymbol{\nabla}}_t' \left[\frac{V_i^h(k_\rho; z|z') - V_i^e(k_\rho; z|z')}{k_\rho^2} \right] \\ & - \hat{\boldsymbol{z}} \tilde{\boldsymbol{\nabla}}_t' \frac{\eta_0}{j k_0 \epsilon_z} I_i^e(k_\rho; z|z') + \hat{\boldsymbol{z}}\hat{\boldsymbol{z}}\, \eta_0^2 \frac{\mu_t}{\epsilon_z'} I_v^e(k_\rho; z|z') \\ & - \left(\tilde{\boldsymbol{\nabla}}_t \hat{\boldsymbol{z}} \frac{\partial}{\partial z'} + \hat{\boldsymbol{z}}\hat{\boldsymbol{z}} \frac{\partial}{\partial z} \frac{\partial}{\partial z'} \right) \frac{V_i^e(k_\rho; z|z')}{\nu^{e\prime} (k_z^{e\prime})^2} \end{aligned} \tag{28}$$

provided the source point is within a homogeneous material layer. The form of the above suggests that we may choose

$$\tilde{G}^\Phi(\boldsymbol{k}_\rho; z|z') = \frac{V_i^e(k_\rho; z|z')}{\nu^{e\prime} (k_z^{e\prime})^2} \tag{29}$$

as the spectral domain scalar potential kernel (this choice corresponds to Formulation B of [20]). Next, we make use of the identity (20) and combine terms in (28) to obtain (21), in which

$$\underline{\underline{\tilde{\boldsymbol{G}}}}^A(\boldsymbol{k}_\rho; z|z') = \underline{\underline{\boldsymbol{I}}}_t\, V_i^h(k_\rho; z|z')$$

$$- \tilde{\boldsymbol{\nabla}}_t \tilde{\boldsymbol{\nabla}}_t' \left[\frac{V_i^h(k_\rho; z|z')}{k_\rho^2} - \frac{k_0^2 \mu_t' \epsilon_t'}{(k_z^{e\prime})^2} \frac{V_i^e(k_\rho; z|z')}{k_\rho^2} \right]$$
$$- \hat{\boldsymbol{z}} \tilde{\boldsymbol{\nabla}}_t' \, j k_0 \eta_0 \mu_t \left(1 - \frac{\mu_t' \epsilon_z'}{\mu_t \epsilon_z} \right) \frac{I_i^e(k_\rho; z|z')}{\nu^{e\prime} (k_z^{e\prime})^2} + \hat{\boldsymbol{z}} \hat{\boldsymbol{z}} \, \eta_0^2 \frac{\mu_t}{\epsilon_z'} I_v^e(k_\rho; z|z') \qquad (30)$$

In the space domain, (30) and (29) become

$$\underline{\underline{\boldsymbol{G}}}^A(\boldsymbol{\rho} - \boldsymbol{\rho}'; z|z') = \frac{1}{2} \underline{\underline{\boldsymbol{I}}}_t \, \mathcal{S}_0 \left\{ V_i^h(k_\rho; z|z') + \frac{k_0^2 \mu_t' \epsilon_t'}{(k_z^{e\prime})^2} V_i^e(k_\rho; z|z') \right\}$$
$$+ \frac{1}{2} [(\hat{\boldsymbol{x}}\hat{\boldsymbol{x}} - \hat{\boldsymbol{y}}\hat{\boldsymbol{y}}) \cos 2\vartheta + (\hat{\boldsymbol{x}}\hat{\boldsymbol{y}} + \hat{\boldsymbol{y}}\hat{\boldsymbol{x}}) \sin 2\vartheta] \, \mathcal{S}_2 \left\{ \frac{V_i^h(k_\rho; z|z')}{k_\rho^2} - \frac{k_0^2 \mu_t' \epsilon_t'}{(k_z^{e\prime})^2} \frac{V_i^e(k_\rho; z|z')}{k_\rho^2} \right\}$$
$$- (\hat{\boldsymbol{z}}\hat{\boldsymbol{x}} \cos \vartheta + \hat{\boldsymbol{z}}\hat{\boldsymbol{y}} \sin \vartheta) \, j k_0 \eta_0 \mu_t \left(1 - \frac{\mu_t' \epsilon_z'}{\mu_t \epsilon_z} \right) \mathcal{S}_1 \left\{ \frac{I_i^e(k_\rho; z|z')}{\nu^{e\prime} (k_z^{e\prime})^2} \right\}$$
$$+ \hat{\boldsymbol{z}} \hat{\boldsymbol{z}} \, \eta_0^2 \frac{\mu_t}{\epsilon_z'} \mathcal{S}_0 \{ I_v^e(k_\rho; z|z') \} \qquad (31)$$

and

$$G^\phi(\boldsymbol{\rho} - \boldsymbol{\rho}'; z|z') = \mathcal{S}_0 \left\{ \frac{V_i^e(k_\rho; z|z')}{\nu^{e\prime} (k_z^{e\prime})^2} \right\} \qquad (32)$$

respectively. Observe that when the source and field points are within the same material layer, the zx and zy components of $\underline{\underline{\boldsymbol{G}}}^A$ vanish, thus resulting in a significant simplification of this MPIE formulation. Note, however, that G^ϕ in this formulation is a discontinuous function of z' across any interface between dissimilar material layers.

Formulation C

The form of (19) suggests that we may also choose

$$\tilde{G}^\phi(\boldsymbol{k}_\rho; z|z') = \frac{V_i^h(k_\rho; z|z') - V_i^e(k_\rho; z|z')}{k_\rho^2} \qquad (33)$$

as the spectral scalar potential kernel (this choice, which was previously used in [28] for a planar microstrip geometry, corresponds to Formulation C of [20]). Next, we make use of the identity (20) and combine terms in (19) to obtain (21), in which

$$\begin{aligned}\underline{\underline{\tilde{\boldsymbol{G}}}}^{A}(\boldsymbol{k}_\rho; z|z') &= \underline{\underline{\boldsymbol{I}}}_t\, V_i^h(k_\rho; z|z') \\ &- \hat{\boldsymbol{z}}\tilde{\boldsymbol{\nabla}}_t'\, jk_0\eta_0\mu_t \left[\frac{I_i^h(k_\rho; z|z') - I_i^e(k_\rho; z|z')}{k_\rho^2}\right] \\ &+ \tilde{\boldsymbol{\nabla}}_t\hat{\boldsymbol{z}}\, jk_0\eta_0\mu_t' \left[\frac{V_v^h(k_\rho; z|z') - V_v^e(k_\rho; z|z')}{k_\rho^2}\right] \\ &+ \hat{\boldsymbol{z}}\hat{\boldsymbol{z}}\, \eta_0^2\mu_t\mu_t' \left\{\left(\frac{k_0}{k_\rho}\right)^2 I_v^h(k_\rho; z|z') + \left[\frac{1}{\mu_t\epsilon_z} + \frac{1}{\mu_t'\epsilon_z'} - \left(\frac{k_0}{k_\rho}\right)^2\right] I_v^e(k_\rho; z|z')\right\} \qquad (34)\end{aligned}$$

The space domain counterparts of (34) and (33) are found as

$$\begin{aligned}\underline{\underline{\boldsymbol{G}}}^{A}(\boldsymbol{\rho}-\boldsymbol{\rho}'; z|z') &= \underline{\underline{\boldsymbol{I}}}_t\, \mathcal{S}_0\left\{V_i^h(k_\rho; z|z')\right\} \\ &- (\hat{\boldsymbol{z}}\hat{\boldsymbol{x}}\cos\vartheta + \hat{\boldsymbol{z}}\hat{\boldsymbol{y}}\sin\vartheta)\, jk_0\eta_0\mu_t\, \mathcal{S}_1\left\{\frac{I_i^h(k_\rho; z|z') - I_i^e(k_\rho; z|z')}{k_\rho^2}\right\} \\ &- (\hat{\boldsymbol{x}}\hat{\boldsymbol{z}}\cos\vartheta + \hat{\boldsymbol{y}}\hat{\boldsymbol{z}}\sin\vartheta)\, jk_0\eta_0\mu_t'\, \mathcal{S}_1\left\{\frac{V_v^h(k_\rho; z|z') - V_v^e(k_\rho; z|z')}{k_\rho^2}\right\} \\ &+ \hat{\boldsymbol{z}}\hat{\boldsymbol{z}}\, \eta_0^2\mu_t\mu_t'\, \mathcal{S}_0\left\{\left(\frac{k_0}{k_\rho}\right)^2 I_v^h(k_\rho; z|z') + \left[\frac{1}{\mu_t\epsilon_z} + \frac{1}{\mu_t'\epsilon_z'} - \left(\frac{k_0}{k_\rho}\right)^2\right] I_v^e(k_\rho; z|z')\right\} \qquad (35)\end{aligned}$$

and

$$G^{\Phi}(\boldsymbol{\rho}-\boldsymbol{\rho}'; z|z') = \mathcal{S}_0\left\{\frac{V_i^h(k_\rho; z|z') - V_i^e(k_\rho; z|z')}{k_\rho^2}\right\} \qquad (36)$$

respectively. Observe that G^{Φ} in this formulation is a continuous function of both z and z' across any interface between dissimilar material layers.

Discussion

Although the three MPIE formulations are of similar complexity for arbitrarily shaped conductors, Formulation C is the simplest (and thus the most efficient) one for strictly planar microstrip geometries. This formulation is also recommended when the conductor penetrates an interface between dissimilar material layers, in which case Formulations A and B are not applicable, unless the MPIE (18) is augmented by additional contour integral terms, as discussed by Michalski and Zheng [20]. However, when the microstrip structure is confined to a single material layer (as is often the case), Formulations A and B become attractive, because in that case two off-diagonal components of their vector potential kernels vanish, which may result in significant savings in the computational effort. The reader is referred to [20], [21] for a more detailed discussion of the properties of the three formulations.

4 Conclusion

A new, straightforward development has been presented of three distinct mixed-potential integral equation (MPIE) formulations for non-planar, arbitrarily shaped microstrip structures embedded in planar, laterally open, multi-layered, uniaxial media. These MPIEs may be used in conjunction with the method of moments to analyze three-dimensional microstrip discontinuities, such as transitions between printed traces on different levels, vias, air-bridges, bond-wires, etc., as well as microstrip patch antennas with shorting pins and coaxial probe feeds.

A Transmission Line Green's Functions

The transmission line analog of the layered medium invoked in Section 2 comprises two transmission line networks—having identical configurations, but different propagation wavenumbers and characteristic admittances—associated with the TM and TE partial fields. In each of these two networks, a homogeneous material layer of the medium of Fig. 1 is represented by a uniform transmission line section. In the case of an unshielded structure, where the top (or bottom) layer is of infinite extent along the z axis, the corresponding transmission line section also extends to infinity, where it is terminated into a matched load.

Consider a transmission line section corresponding to the nth material layer, characterized by the parameters (1). Let this line section comprise a unit-strength current source i at z', as illustrated in Fig. 3. It then follows that the voltage V_i^p and current I_i^p at any point z within this section are governed by (9)–(10), in which $k_z^p = k_{zn}^p$

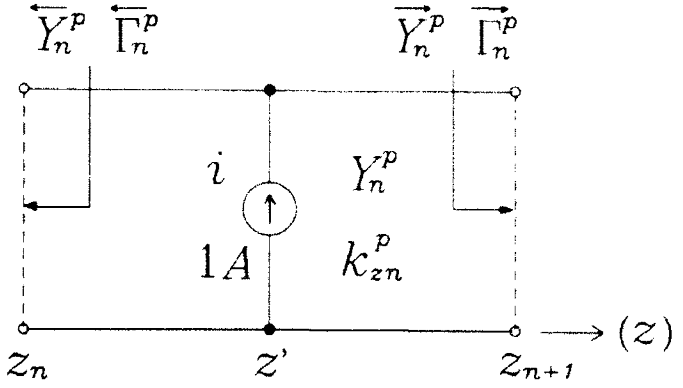

Figure 3: Transmission line section comprising a unit-strength current source.

and $Y^p = Y_n^p$, where the latter are obtained by substituting the material parameters of the layer into (7)-(8). From (9)-(10), we find that V_i^p may be expressed in the traveling-wave form (cf. [48, p. 213])

$$V_i(z|z') = \frac{\epsilon^{-jk_{zn}|z-z'|}}{2Y_n} \frac{\left[1+ \overleftarrow{\Gamma}_n(z_0)\epsilon^{-j2k_{zn}(z_< - z_0)}\right]\left[1+ \overrightarrow{\Gamma}_n(z_0)\epsilon^{j2k_{zn}(z_> - z_0)}\right]}{\left[1- \overleftarrow{\Gamma}_n(z_0)\overrightarrow{\Gamma}_n(z_0)\right]} \tag{37}$$

where $z_< = \min(z, z')$, $z_> = \max(z, z')$, z_0 is an arbitrary reference point within the nth section (which is usually set to z_n or z_{n+1}, whichever is more convenient), and $\overleftarrow{\Gamma}_n(z_0)$ and $\overrightarrow{\Gamma}_n(z_0)$ are the reflection coefficients 'looking to the left' and 'looking to the right,' respectively, at z_0. In the above and in what follows, we omit the superscript p for notational simplicity. By means of the translation formula

$$\overset{\rightleftarrows}{\Gamma}_n(z) = \overset{\rightleftarrows}{\Gamma}_n(z_0)\,\epsilon^{\pm j2k_{zn}(z-z_0)} \tag{38}$$

where the upper and lower signs correspond to the right and left arrows, respectively, these reflection coefficients can be expressed in terms of the respective terminal reflection coefficients $\overleftarrow{\Gamma}_n$ and $\overrightarrow{\Gamma}_n$, which are related to the corresponding terminal admittances $\overleftarrow{Y}_n$ and $\overrightarrow{Y}_n$ (see Fig. 3) as

$$\overset{\rightleftarrows}{\Gamma}_n = \frac{Y_n - \overset{\rightleftarrows}{Y}_n}{Y_n + \overset{\rightleftarrows}{Y}_n}, \qquad \overset{\rightleftarrows}{Y}_n = Y_n\,\frac{1 - \overset{\rightleftarrows}{\Gamma}_n}{1 + \overset{\rightleftarrows}{\Gamma}_n} \tag{39}$$

For a transmission line section of a finite length d_n, a particularly convenient form of (37) is

$$V_i(z|z') = \frac{e^{-jk_{zn}|z-z'|}}{2Y_n} \frac{\left[1+ \overleftarrow{\Gamma}_n \, e^{-j2k_{zn}(z_< - z_n)}\right]\left[1+ \overrightarrow{\Gamma}_n \, e^{-j2k_{zn}(z_{n+1} - z_>)}\right]}{\left[1- \overleftarrow{\Gamma}_n \overrightarrow{\Gamma}_n \, e^{-j2k_{zn}d_n}\right]} \tag{40}$$

which is obtained by letting $z_0 = z_n$ and using (38).

The remaining Green's functions can easily be derived from (40). Hence, $I_i(z|z')$, which is dual to $V_i(z|z')$, is obtained when Y_n is replaced by Z_n in (40) (which causes the reflection coefficients to change signs). $I_i(z|z')$ follows from (40) and (9), and $V_v(z|z')$ may then be obtained from the reciprocity relation given in (11).

The voltage and current on the nth transmission line section that is source-free satisfy (9)-(10) with the delta function absent. From these equations, the voltage at any point z within the line section may be expressed in terms of the voltage $V(z_0)$ across one of its terminal pairs. The result is

$$V(z) = V(z_0) \frac{e^{-jk_{zn}|z-z'|}}{1+ \overset{\rightleftarrows}{\Gamma}_n \, e^{-j2k_{zn}d_n}} \left[1+ \overset{\rightleftarrows}{\Gamma}_n \, e^{-j2k_{zn}|z-z_0|}\right] \tag{41}$$

where $z_0 = z_n$ or $z_0 = z_{n+1}$ (see Fig. 3), depending on whether the source is located to the left or to the right, respectively, of the line section, and where the upper (lower) arrow corresponds to $z > z_0$ ($z < z_0$). We have omitted the subscript of V in (41), because the latter applies irrespective of the nature of the source, and dropped z' from its argument, because (41) only implicitly depends on the source location, which is outside the nth line section. The current $I(z)$ corresponding to (41) may be obtained by substituting the latter into (9).

Finally, we note that (38)-(39) are easily implemented in a recursive computer routine to determine the leftward- and rightward-looking reflection coefficients needed in (40) and (41). The computations proceed from the outward-looking reflection coefficients in the top and bottom transmission line sections, where they vanish for unshielded structures or otherwise are easily determined, provided the surface admittances $Y_{S,1}$ and $Y_{S,N+1}$ are known. Observe that the exponential functions encountered in (38), (40), and (41) have nonincreasing magnitudes, so there is no danger of overflow. When the nth transmission line section extends to positive (negative) infinity along the z axis, the reflection coefficient $\overrightarrow{\Gamma}_n$ ($\overleftarrow{\Gamma}_n$) is set to zero in (40) and (41).

Acknowledgments

The author wishes to thank David R. Jackson for inviting him to write this paper. The research reported here was supported in part by the Office of Naval Research under Contract N00014-90-J-1197.

References

[1] T.-S. Horng, N. G. Alexopoulos, S.-C. Wu, and H.-Y. Yang, "Full-wave spectral analysis for open microstrip discontinuities of arbitrary shape including radiation and surface-wave losses," *Int. J. Microwave Millimeter-Wave Computer-Aided Eng.*, vol. 2, no. 4, pp. 224–240, 1992.

[2] L. Barlatey, H. Smith, and J. Mosig, "Printed radiating structures and transitions in multilayered substrates," *Int. J. Microwave Millimeter-Wave Computer-Aided Eng.*, vol. 2, no. 4, pp. 273–285, 1992.

[3] D. M. Pozar, "Improved computational efficiency for the moment method solution of printed dipoles and patches," *Electromagn.*, vol. 3, no. 3–4, pp. 299–309, 1983.

[4] J. P. Damiano, "Computation of input impedance in microstrip antennas. Graphic representation and numerical integration of oscillating functions," *IEE Proc., Pt. H*, vol. 134, pp. 456–466, Oct. 1987. Correction: *ibid.*, vol. 134, p. 501, Dec. 1987.

[5] K. A. Michalski and D. Zheng, "Analysis of planar microstrip structures of arbitrary shape—To be, or not to be in the spectral domain?," in *Proc. Symp.*

on Antenna Techn. and Appl. Electromagn., (Winnipeg, Canada), pp. 240–245, Aug. 1990.

[6] R. F. Harrington, *Field Computation by Moment Methods*. New York: Macmillan, 1968. Reprinted by Krieger Publishing Co., Melbourne, FL, 1982.

[7] K. A. Michalski, "The mixed-potential electric field integral equation for objects in layered media," *Arch. Elek. Übertragung.*, vol. 39, pp. 317–322, Sept.–Oct. 1985.

[8] J. R. Mosig, "Arbitrarily shaped microstrip structures and their analysis with a mixed potential integral equation," *IEEE Trans. Microwave Theory Tech.*, vol. 36, pp. 314–323, Feb. 1988.

[9] A. W. Glisson and D. R. Wilton, "Simple and efficient numerical methods for problems of electromagnetic radiation and scattering from surfaces," *IEEE Trans. Antennas Propagat.*, vol. AP-28, pp. 593–603, Sept. 1980.

[10] S. M. Rao, D. R. Wilton, and A. W. Glisson, "Electromagnetic scattering by surfaces of arbitrary shape," *IEEE Trans. Antennas Propagat.*, vol. AP-30, pp. 409–418, May 1982.

[11] W. A. Johnson, D. R. Wilton, and R. M. Sharpe, "Modeling scattering from and radiation by arbitrarily shaped objects with the electric field integral equation triangular surface patch code," *Electromagn.*, vol. 10, no. 1-2, pp. 41–63, 1990.

[12] A. Sommerfeld, *Partial Differential Equations*. New York: Academic Press, 1949.

[13] J. R. Mosig and F. E. Gardiol, "A dynamical radiation model for microstrip structures," in *Adv. Electron. Electron Phys.* (P. W. Hawkes, ed.), vol. 59, pp. 139–237, New York: Academic Press, 1982.

[14] J. R. Mosig, "Integral equation technique," in *Numerical Techniques for Microwave and Millimeter-Wave Passive Structures* (T. Itoh, ed.), pp. 133–213, New York: Wiley, 1989.

[15] J. R. Mosig, R. C. Hall, and F. E. Gardiol, "Numerical analysis of microstrip patch antennas," in *Handbook of Microstrip Antennas* (J. R. James and P. S. Hall, eds.), pp. 391–453, London: Peter Peregrinus, 1989.

[16] Y. L. Chow, J. J. Yang, D. G. Fang, and G. E. Howard, "A closed-form spatial Green's function for the thick microstrip substrate," *IEEE Trans. Microwave Theory Tech.*, vol. 39, pp. 588–592, Mar. 1991.

[17] M. I. Aksun and R. Mittra, "Derivation of closed-form Green's functions for a general microstrip geometry," *IEEE Trans. Microwave Theory Tech.*, vol. 40, pp. 2055–2062, Nov. 1992.

[18] A. Erteza and B. K. Park, "Nonuniqueness of resolution of Hertz vector in presence of a boundary, and the horizontal dipole problem," *IEEE Trans. Antennas Propagat.*, vol. AP-17, pp. 376–378, May 1969.

[19] K. A. Michalski, "On the scalar potential of a point charge associated with a time-harmonic dipole in a layered medium," *IEEE Trans. Antennas Propagat.*, vol. AP-35, pp. 1299–1301, Nov. 1987.

[20] K. A. Michalski and D. Zheng, "Electromagnetic scattering and radiation by surfaces of arbitrary shape in layered media, Part I: Theory," *IEEE Trans. Antennas Propagat.*, vol. 38, pp. 335–344, Mar. 1990.

[21] K. A. Michalski and D. Zheng, "Electromagnetic scattering and radiation by surfaces of arbitrary shape in layered media. Part II: Implementation and results for contiguous half-spaces," *IEEE Trans. Antennas Propagat.*, vol. 38, pp. 345–352, Mar. 1990.

[22] P. Pichon, J. R. Mosig, and A. Papiernik, "Input impedance of arbitrarily shaped microstrip antennas," *Electron. Lett.*, vol. 24, pp. 1214–1215, Sept. 1988.

[23] K.-L. Wu, J. Litva, R. Fralich, and C. Wu, "Full-wave analysis of arbitrarily shaped line-fed microstrip antennas using triangular finite-element method," *IEE Proc., Pt. H*, vol. 138, pp. 421–428, Oct. 1991.

[24] T. K. Sarkar, P. Midya, Z. A. Maricevic, M. Kahrizi, S. M. Rao, and A. R. Djordjevic, "Analysis of arbitrarily shaped microstrip patch antennas using the Sommerfeld formulation," *Int. J. Microwave Millimeter-Wave Computer-Aided Eng.*, vol. 2, no. 3, pp. 168–178, 1992.

[25] F. A. Monferrer, A. A. Kishk, and A. W. Glisson, "Green's function analysis of planar circuits in a two-layer grounded medium," *IEEE Trans. Antennas Propagat.*, vol. 40, pp. 690–696, June 1992.

[26] A. Hoorfar, J. X. Zheng, and D. C. Chang, "Numerical modeling of crossover and other junction discontinuities in two-layer microstrip circuits," *Int. J. Microwave Millimeter-Wave Computer-Aided Eng.*, vol. 2, no. 4, pp. 261–272, 1992.

[27] D. C. Chang and J. X. Zheng, "Electromagnetic modeling of passive circuit elements in MMIC," *IEEE Trans. Microwave Theory Tech.*, vol. 40, pp. 1741–1747, Sept. 1992.

[28] K. A. Michalski and D. Zheng, "Analysis of microstrip resonators of arbitrary shape," *IEEE Trans. Antennas Propagat.*, vol. 40, pp. 112–119, Jan. 1992.

[29] D. Zheng and K. A. Michalski, "Analysis of arbitrarily shaped coax-fed microstrip antennas with thick substrates," *Electron. Lett.*, vol. 26, no. 12, pp. 794–795, 1990.

[30] D. Zheng and K. A. Michalski, "Analysis of coaxially fed microstrip antennas of arbitrary shape with thick substrates," *J. Electromagn. Waves Appl.*, vol. 5, no. 12, pp. 1303–1327, 1991.

[31] K. A. Michalski and C.-I. G. Hsu, "RCS computation of coax-loaded microstrip patch antennas of arbitrary shape," *Electromagn.*, vol. 13, 1993 (to appear).

[32] K. A. Michalski and D. Zheng, "Rigorous analysis of open microstrip lines of arbitrary cross section in bound and leaky regimes," *IEEE Trans. Microwave Theory Tech.*, vol. 37, pp. 2005–2010, Dec. 1989.

[33] C.-I. G. Hsu, R. F. Harrington, K. A. Michalski, and D. Zheng, "Analysis of a multiconductor transmission lines of arbitrary cross-section in multilayered uniaxial media," *IEEE Trans. Microwave Theory Tech.*, vol. 41, Jan. 1993 (to appear).

[34] N. W. Montgomery and D. R. Wilton, "Analysis of arbitrary conducting periodic structures embedded in layered media," in *Digest IEEE AP-S Int. Symp.*, (London, Ontario), pp. 1889–1892, June 1991.

[35] D. R. Wilton, "Review of current status and trends in the use of integral equations in computational electromagnetics," *Electromagn.*, vol. 12, pp. 287–341, July-Dec. 1992.

[36] R. C. Hall and J. R. Mosig, "The analysis of coaxially fed microstrip antennas with electrically thick substrates," *Electromagn.*, vol. 9, no. 4, pp. 367–384, 1989.

[37] L. Barlatey, J. R. Mosig, and T. Sphicopoulos, "Analysis of stacked microstrip patches with a mixed potential integral equation," *IEEE Trans. Antennas Propagat.*, vol. 38, pp. 608–615, May 1990.

[38] A. Skrivervik and J. R. Mosig, "Impedance matrix of multiport microstrip discontinuities including radiation effects," *Arch. Elek. Übertragung.*, vol. 25, no. 4, pp. 193–196, 1990.

[39] D. Zheng and K. A. Michalski, "Analysis of arbitrarily shaped coax-fed microstrip antennas—A hybrid mixed-potential integral equation approach," *Microwave & Opt. Technol. Lett.*, vol. 3, pp. 200–203, June 1990.

[40] H. Legay, R. Gillard, J. Citerne, and G. Piton, "Via-hole effects on radiation characteristics of a patch microstrip antenna coaxially fed through the ground plane," *Ann. Télécommun.*, vol. 46, no. 7-8, pp. 367–381, 1991.

[41] G. A. E. Vandenbosch and A. R. Van de Capelle, "Mixed-potential integral expression formulation of the electric field in a stratified dielectric medium—

Application to the case of a probe current source," *IEEE Trans. Antennas Propagat.*, vol. 40, pp. 806–817, July 1992.

[42] W. C. Chew and Q. Liu, "Resonance frequency of a rectangular microstrip patch," *IEEE Trans. Antennas Propagat.*, vol. 36, pp. 1045–1056, Aug. 1988.

[43] T. Itoh, "Spectral-domain immittance approach for dispersion characteristics of generalized printed transmission lines," *IEEE Trans. Microwave Theory Tech.*, vol. MTT-28, pp. 733–736, July 1980.

[44] L. Vegni, R. Cicchetti, and P. Capece, "Spectral dyadic Green's function formulation for planar integrated structures," *IEEE Trans. Antennas Propagat.*, vol. 36, pp. 1057–1065, Aug. 1988.

[45] L. Beyne and D. De Zutter, "Green's function for layered lossy media with special application to microstrip antennas," *IEEE Trans. Microwave Theory Tech.*, vol. 36, pp. 875–881, May 1988.

[46] M. Davidovitz and Y. T. Lo, "Rigorous analysis of a circular patch antenna excited by a microstrip transmission line," *IEEE Trans. Antennas Propagat.*, vol. 37, pp. 949–958, Aug. 1989.

[47] R. Kastner, E. Heyman, and A. Sabban, "Spectral domain iterative analysis of single- and double-layered microstrip antennas using the conjugate gradient algorithm," *IEEE Trans. Antennas Propagat.*, vol. 36, pp. 1204–1212, Sept. 1988.

[48] L. B. Felsen and N. Marcuvitz, *Radiation and Scattering of Waves.* Englewood Cliffs, N.J.: Prentice Hall, 1973.

[49] M. J. Cloud and D. P. Nyquist, "A note on the mixed potential representation of electric fields in layered media," *IEEE Trans. Microwave Theory Tech.*, vol. 37, pp. 1150–1152, July 1989.

[50] J Van Bladel, *Electromagnetic Fields.* New York: Hemisphere, 1985.

RCS COMPUTATION OF COAX-LOADED MICROSTRIP PATCH ANTENNAS OF ARBITRARY SHAPE

Krzysztof A. Michalski, *Electromagnetics & Microwave Laboratory*
Department of Electrical Engineering
Texas A&M University
College Station, Texas 77843-3128, USA

Chung-I G. Hsu, *Department of Electrical Engineering*
Dai-Yeh Institute of Technology
Dah-Tsuen Hsiang
Chang-Hwa County, Taiwan 51505, ROC

Abstract

A space-domain mixed-potential integral equation approach is applied in conjunction with the method of moments to compute the radar cross-section (RCS) of coax-loaded microstrip patch antennas having arbitrary or irregular shapes. The effects of the substrate—which may be electrically thick and may consist of any number of planar, possibly uniaxially anisotropic dielectric layers, backed by a ground plane—are rigorously incorporated in the analysis by means of the vector and scalar potential Green's functions. The latter are expressed in terms of the voltages and currents on transmission line analogs of the layered medium, associated with TM and TE partial fields. The current distribution on the microstrip patch is approximated using vector basis functions defined over triangular elements and the coax probe current is expanded in terms of piecewise-linear subdomain basis functions. A simple probe-to-patch attachment mode, compatible with the triangular element model of the microstrip patch, is used to enforce current continuity at the junction, and the coax aperture is modeled by a magnetic current frill. The far zone fields are found by the stationary phase method, and are expressed in terms of the Fourier-transformed basis functions and the transmission line voltages and currents evaluated at the stationary phase point value of the transverse wavenumber. Computed RCS results are presented for several loaded and unloaded microstrip patch antennas of various shapes and are shown to be in agreement with published measured data and with computed results obtained by specialized techniques, which—unlike the method presented here—are not easily extendable to arbitrary shapes.

1 Introduction

The radar cross-section (RCS) of rectangular microstrip patch antennas was first studied by Newman and Forrai [1], who used a spectral domain integral equation method and validated it by measurements. Pozar [2] used a similar approach, extended to the case of a uniaxial substrate and combined with an idealized feed model, to compute the RCS of both loaded and unloaded rectangular patch antennas. Jackson [3] investigated the superstrate effects on the RCS of rectangular microstrip patches, also using a spectral domain integral equation method. Aberle et al. [4] computed the RCS of loaded and unloaded rectangular and circular patch antennas using a spectral domain integral equation technique incorporating a rigorous feed model, and corroborated their analysis by measurements. More recently, King and Bow [5] used a similar approach to compute the RCS of finite arrays of rectangular microstrip patch antennas. The RCS of cavity backed, loaded and unloaded microstrip patch antennas and antenna arrays was studied by Jin and Volakis [6] using a hybrid approach combining finite-element differential and integral formulations.

In this paper, we present an RCS analysis of coax-loaded microstrip patch antennas of arbitrary or irregular shape, residing in a grounded dielectric substrate of infinite lateral extent. The analysis is based on the mixed-potential integral equation formulation in conjunction with the method of moments (MOM) [7] utilizing a triangular element model of the patch. In this approach, which was pioneered by Pichon et al. [8] and adopted by others [9], [10], [11], [12], [13], [14], [15], [16], [17], the effects of the substrate and superstrate (if present) are rigorously taken into account by means of the vector and scalar potential Green's functions. The latter are expressed in terms of the voltages and currents on transmission line analogs of the layered medium, associated with TM and TE partial fields. The current distribution on the microstrip patch, which may have an arbitrary or irregular shape, is approximated in terms of vector basis functions defined over triangular subdomains [18]. The substrate and the cover layer (if present) may be electrically thick and uniaxially anisotropic. The current on the coax probe is expanded in terms of piecewise linear subdomain basis functions and the coax aperture is modeled by a magnetic current frill [19], [12]. A simple probe-to-patch attachment mode [11], compatible with the triangular element model of the microstrip patch, is implemented to enforce current continuity at the junction. The far zone fields are found by the stationary phase method, and are expressed in terms of the Fourier-transformed basis functions and the transmission line voltages and currents evaluated at the stationary phase point value of the transverse wavenumber.

The remainder of this paper is organized as follows. In Section 2, a coupled set of mixed-potential integral equations for the currents induced on a coax-loaded microstrip patch antenna is formulated. Also, the coax load model is developed and the formulas for the far fields and RCS are stated. The formulation consistently employs a transmission line analog of the layered medium and is thus directly applicable to antennas with any number of layers. The relevant details of the transmission line analysis are enclosed for easy reference in Appendix A. The numerical procedures are described in considerable detail in Section 3, including the coax probe-to-patch junction treatment. The approach relies heavily on concepts developed by the finite elements community to efficiently organize the computations and the assembly of the resulting matrix equation. The Fourier transforms of the shape functions encountered in the far fields computation are given in closed form, with the details of the development relegated to Appendix B. In Section 4, sample computed RCS results are presented for several loaded and unloaded rectangular and circular microstrip patch antennas and are shown to be in agreement with published measured data and with computed results obtained by specialized techniques, which—unlike the method presented here—are not easily extendable to patches of arbitrary shape. New RCS results are also included for a coax-loaded pentagonal microstrip patch antenna designed to radiate circularly polarized field from a single feed. Finally, the summary and conclusion are given in Section 5.

2 Formulation

A. Problem statement and assumptions

The geometry of the problem under consideration is illustrated in Fig. 1, where the

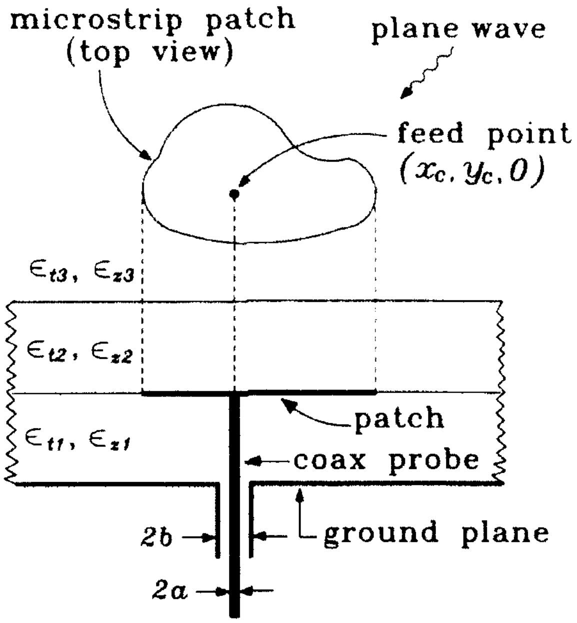

Figure 1: Geometry of a coax-fed microstrip patch antenna.

dielectric layers, which are assumed to be nonmagnetic, are characterized by their transverse and longitudinal dielectric constants, ϵ_{tn} and ϵ_{zn}, respectively, relative to free space, and anisotropy ratios $\nu_n = \epsilon_{zn}/\epsilon_{tn}$. If dielectric losses are present, ϵ_{tn} and ϵ_{zn} are multiplied by $(1 - j\tan\delta_n)$, where $\tan\delta_n$ is the loss tangent of the nth layer. (Here and throughout this paper, the $e^{j\omega t}$ time convention is implied.) The layered medium, which may consist of an arbitrary number of planar layers, and the ground plane are assumed to be of infinite lateral extent. The coaxial probe, which has the inner and outer radii a and b, respectively, is centered at (x_c, y_c). The patch, the ground plane, and the probe are assumed to be perfectly conducting.

By invoking the equivalence principle [20], the original problem of Fig. 1 may be replaced by its equivalent, shown in Fig. 2. In the latter, the conducting patch and the coax probe are replaced by equivalent electric currents, $\boldsymbol{J}_s$ and I, respectively. Also, an equivalent magnetic current frill, $\boldsymbol{M}_s$, is placed over the coax aperture, which is shorted. To simplify the analysis, we assume that the distribution of the aperture electric field is that of the TEM coax mode. We further assume that the coax probe current is z-directed and is azimuthally invariant on its circumference. The strength

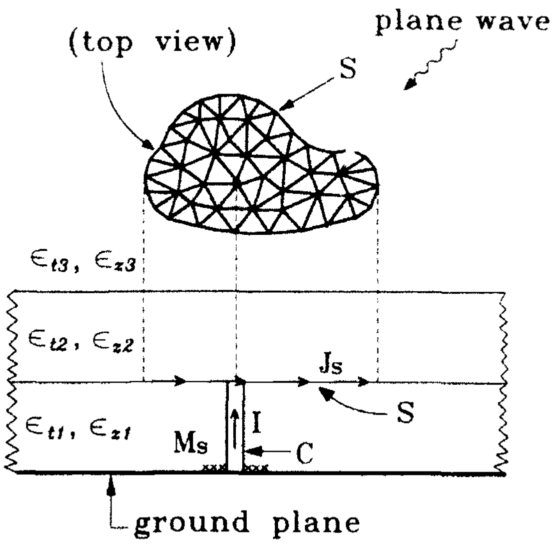

Figure 2: Problem equivalent to that in Fig. 1.

of the magnetic current will be related to the load impedance, Z_L, and to the value of I at the base of the coax probe. As a result, the patch current, $\boldsymbol{J}_s$, which resides on the surface S and represents the vector sum of the currents that exist on the bottom and top sides of the microstrip patch, and the total z-directed coax probe current, I, which is uniformly distributed on the perimeter of the cylindrical surface C, remain the basic unknowns of the problem. Once these currents are found, other quantities of interest, such as the far fields and the RCS of the antenna, are readily determined.

B. Integral equations

Since Green's functions for the layered medium of Fig. 2 are available, the electric field produced by the coax-fed patch may be expressed in terms of integrals over the as yet unknown currents $\boldsymbol{J}_s$ and I, weighted by the appropriate kernel functions. The fields excited by the plane wave and $\boldsymbol{M}_s$ can also be easily determined. A coupled set of integral equations for $\boldsymbol{J}_s$ and I may then be obtained from the condition that the total tangential electric field must vanish on the patch and the probe. On the coax probe, since I is assumed to be azimuthally invariant, we only enforce the vanishing of the z component of the electric field, *averaged* over the probe circumference. In what follows, we use the following notation: $\boldsymbol{r}$ is the position vector of an arbitrary point with respect to the global coordinate origin, $\boldsymbol{\rho}$ is the projection of $\boldsymbol{r}$ on the xy plane, $\boldsymbol{\rho}_c$ is the radial position vector of the coax probe axis, primes denote source coordinates, unit vectors are distinguished by carets, and the subscript s denotes components tangential to S.

Upon using the procedure described above, we arrive at a coupled set of integral equations for $\boldsymbol{J}_s$ and I, which may be expressed as (the details of the derivation are omitted here due to lack of space)

$$\begin{aligned}\int_S G_A(\boldsymbol{r}|\boldsymbol{r}')\boldsymbol{J}_s(\boldsymbol{\rho}')\,dS' + \boldsymbol{\nabla}_s\int_S G_\phi(\boldsymbol{r}|\boldsymbol{r}')\boldsymbol{\nabla}_s'\cdot\boldsymbol{J}_s(\boldsymbol{\rho}')\,dS' \\ + \hat{\boldsymbol{\varrho}}_c\int_C K_{\varrho z}(\boldsymbol{r}|z')I(z')\,dz' + \boldsymbol{\nabla}_s\int_C K_\phi(\boldsymbol{r}|z')\,\frac{dI(z')}{dz'}\,dz' \\ - \hat{\boldsymbol{\varrho}}_c\,E_\varrho^c(\boldsymbol{r}) = \boldsymbol{E}_s^i(\boldsymbol{r}), \quad \boldsymbol{r}\in S\end{aligned} \tag{1}$$

$$\begin{aligned}\int_S \mathcal{G}_{z\varrho}(z|\boldsymbol{r}')\hat{\boldsymbol{\varrho}}_c'\cdot\boldsymbol{J}_s(\boldsymbol{\rho}')\,dS' + \frac{d}{dz}\int_S \mathcal{G}_\phi(z|\boldsymbol{r}')\boldsymbol{\nabla}_s'\cdot\boldsymbol{J}_s(\boldsymbol{\rho}')\,dS' \\ + \int_C \mathcal{K}_{zz}(z|z')I(z')\,dz' + \frac{d}{dz}\int_C \mathcal{K}_\phi(z|z')\,\frac{dI(z')}{dz'}\,dz' \\ - \mathcal{E}_z^c(z) = \mathcal{E}_z^i(z), \quad z\in C\end{aligned} \tag{2}$$

where $\boldsymbol{\varrho}_c = \boldsymbol{\rho} - \boldsymbol{\rho}_c$, $\boldsymbol{\varrho}_c' = \boldsymbol{\rho}_c - \boldsymbol{\rho}'$, and where the script symbols are used for quantities averaged over the coax probe circumference. The kernel functions in (1)–(2) may be expressed as

$$G_A(\boldsymbol{r}|\boldsymbol{r}') = \frac{1}{2\pi}\int_0^\infty V_i^h(k_\rho; z|z')J_0(k_\rho|\boldsymbol{\rho}-\boldsymbol{\rho}'|)\,k_\rho\,dk_\rho \tag{3}$$

$$G_\phi(\boldsymbol{r}|\boldsymbol{r}') = \frac{1}{2\pi}\int_0^\infty P(k_\rho; z|z')J_0(k_\rho|\boldsymbol{\rho}-\boldsymbol{\rho}'|)\,\frac{dk_\rho}{k_\rho} \tag{4}$$

$$K_{\varrho z}(\boldsymbol{r}|z') = \frac{k_0\eta_0}{2\pi j}\int_0^\infty Q(k_\rho; z|z')J_0(k_\rho a)J_1(k_\rho|\boldsymbol{\rho}-\boldsymbol{\rho}_c|)\,dk_\rho \tag{5}$$

$$K_\phi(\boldsymbol{r}|z') = \frac{1}{2\pi}\int_0^\infty P(k_\rho; z|z')J_0(k_\rho a)J_0(k_\rho|\boldsymbol{\rho}-\boldsymbol{\rho}_c|)\,\frac{dk_\rho}{k_\rho} \tag{6}$$

$$\mathcal{G}_{z\varrho}(z|\boldsymbol{r}') = \frac{k_0\eta_0}{2\pi j}\int_0^\infty R(k_\rho; z|z')J_0(k_\rho a)J_1(k_\rho|\boldsymbol{\rho}_c-\boldsymbol{\rho}'|)\,dk_\rho \tag{7}$$

$$\mathcal{G}_{\phi}(z|\mathbf{r}') = \frac{1}{2\pi}\int_0^\infty P(k_\rho; z|z')J_0(k_\rho a)J_0(k_\rho|\boldsymbol{\rho}-\boldsymbol{\rho}'|)\,\frac{dk_\rho}{k_\rho} \tag{8}$$

$$\mathcal{K}_{zz}(z|z') = \frac{\eta_0^2}{2\pi}\int_0^\infty S(k_\rho; z|z')J_0^2(k_\rho a)\,k_\rho\,dk_\rho \tag{9}$$

$$\mathcal{K}_{\phi}(z|z') = \frac{1}{2\pi}\int_0^\infty P(k_\rho; z|z')J_0^2(k_\rho a)\,\frac{dk_\rho}{k_\rho} \tag{10}$$

in which J_n denotes the Bessel function of order n, k_ρ is the spectral wavenumber variable corresponding to ρ, and where $\eta_0=\sqrt{\mu_0/\epsilon_0}$ and $k_0=\omega\sqrt{\mu_0\epsilon_0}$ are the intrinsic impedance and wavenumber of free space. The $J_0(k_\rho a)$ factor appearing in the above equations is the result of averaging of the respective integral kernel over the coax probe circumference and the application of Graf's addition theorem [21, p. 363]. In (4)-(10), we have introduced the auxiliary functions

$$P(k_\rho; z|z') = V_i^h(k_\rho; z|z') - V_i^e(k_\rho; z|z') \tag{11}$$

$$Q(k_\rho; z|z') = V_v^h(k_\rho; z|z') - V_v^e(k_\rho; z|z') \tag{12}$$

$$R(k_\rho; z|z') = I_i^h(k_\rho; z|z') - I_i^e(k_\rho; z|z') \tag{13}$$

$$S(k_\rho; z|z') = \left(\frac{k_0}{k_\rho}\right)^2 I_v^h(k_\rho; z|z') + \left[\frac{\epsilon_z+\epsilon_z'}{\epsilon_z\epsilon_z'} - \left(\frac{k_0}{k_\rho}\right)^2\right] I_v^e(k_\rho; z|z') \tag{14}$$

where ϵ_z and ϵ_z' denote the longitudinal dielectric constants of the observation and source layers, respectively. This convention is in effect throughout this paper, unless the layer index is explicitly shown.

It is important to note that the integral equations (1)-(2) are in the mixed-potential form [22], [23], [24], [25], which is amenable to the existing numerical solution procedures developed for scatterers of arbitrary shape residing in a free space [18], [26].

C. Transmission line network analog of the layered medium

As an aid in deriving (3)-(10), we have employed a transmission line network analog of the layered medium, in which each layer is represented by a transmission line section, as illustrated in Fig. 3. This analog comprises two networks, which arise from the decomposition of the electromagnetic field into partial fields that are transverse-

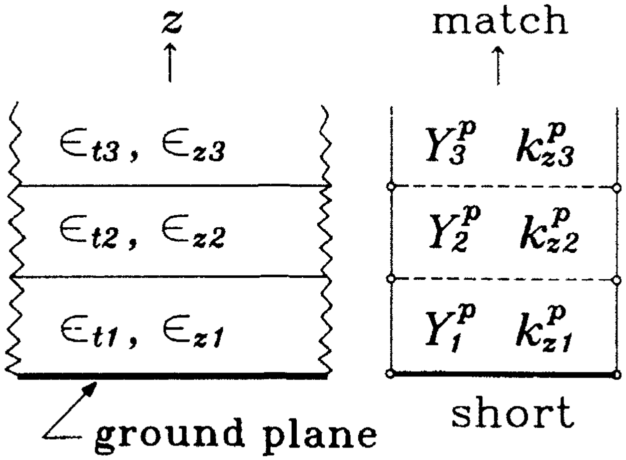

Figure 3: Transmission line network analog of the layered medium.

magnetic (TM) and transverse-electric (TE) to z [27, pp. 185-217]. The quantities corresponding to the TM and TE networks are distinguished by the superscripts e and h, respectively. The characteristic admittance and propagation constant of the nth section of the TE and TM transmission lines are given, respectively, as

$$Y_n^h = \frac{k_{zn}^h}{k_0\eta_0}, \qquad k_{zn}^h = \sqrt{k_0^2\epsilon_{tn} - k_\rho^2} \tag{15}$$

and

$$Y_n^e = \frac{k_0\epsilon_{tn}}{\eta_0 k_{zn}^e}, \qquad k_{zn}^e = \sqrt{k_0^2\epsilon_{tn} - k_\rho^2/\nu_n} \tag{16}$$

where the branch of the square root function is determined by the condition that k_{zn}^p be positive when it is real-valued, or that $\Im\{k_{zn}^p\} < 0$ otherwise. Here and in what follows, the superscript p stands for e or h. For each transmission line network, we introduce the Green's functions $V_i^p(k_\rho; z|z')$ and $I_i^p(k_\rho; z|z')$, which represent the voltage and current, respectively, at a point z, excited by a unit-strength shunt current source located at z'. We also introduce the Green's functions $V_v^p(k_\rho; z|z')$ and $I_v^p(k_\rho; z|z')$, which represent the voltage and current, respectively, at a point z, excited by a unit-strength series voltage source located at z'. These four transmission line Green's functions, which can easily be derived by network theory methods, are discussed in more detail in Appendix A.

Note that the integral equations (1)–(2) are valid for a medium with an arbitrary number of layers, provided the appropriate transmission line Green's functions are used in (3)–(10). Also, it can be shown that the kernel functions appearing in (1)–(2) exhibit only mild singularities when the source and observation points coincide on S and C, which makes these equations particularly amenable to numerical solution procedures.

D. Coax load model

We assume that the aperture field in the problem of Fig. 1 is that of a TEM coax mode with a voltage

$$V_L = Z_L I_L \tag{17}$$

where Z_L is the load impedance presented to the antenna by the coaxial transmission line and I_L is the load current. In view of this assumption, with respect to a polar coordinate system (ϱ, ϑ) centered at (x_c, y_c), the magnetic surface current $\boldsymbol{M}_s$ in Fig. 2 has only a ϑ component, given as [20, p. 112]

$$M_\vartheta(\varrho) = -I_L \frac{K}{\varrho}, \qquad K = \frac{Z_L}{\ln(b/a)} \tag{18}$$

in which $a < \varrho < b$. The electric field excited by this magnetic current frill embedded at $z = z'$ in the layered medium, which appears in (1)–(2), can be expressed as

$$E_\varrho^c(\boldsymbol{r}) = I_L T(\boldsymbol{\rho}; z), \qquad \mathcal{E}_z^c(z) = I_L \mathcal{U}(z) \tag{19}$$

where, for notational convenience, we have introduced the auxiliary functions

$$T(\boldsymbol{\rho}; z) = K \int_0^\infty V_v^e(k_\rho; z|z') \Big[J_0(k_\rho a) - J_0(k_\rho b) \Big] J_1(k_\rho |\boldsymbol{\rho} - \boldsymbol{\rho}_c|)\, dk_\rho \tag{20}$$

$$\mathcal{U}(z) = \frac{K\eta_0}{jk_0\epsilon_z} \int_0^\infty I_v^e(k_\rho; z|z') \Big[J_0(k_\rho a) - J_0(k_\rho b) \Big] J_0(k_\rho a)\, k_\rho\, dk_\rho \tag{21}$$

The second $J_0(k_\rho a)$ factor in (21) results from the averaging of E_z^c over the coax probe circumference In the case of a short-circuit load ($Z_L = 0$) the magnetic current frill is absent. In the other extreme, when the antenna terminals are open-circuited

$(Z_L = \infty)$, the frill is absent as well, but we impose the condition $I_L = 0$ in the solution procedure. For any other load, I_L is not known a priori and must be computed together with $\boldsymbol{J}_s$ and I. Note that (20)–(21) are in a general form applicable to a medium with an arbitrary number of layers, provided the appropriate transmission line Green's functions V_v^p and I_v^e are employed (see Appendix A).

E. Incident field

The structure of Fig. 1 is excited by a plane wave field

$$\boldsymbol{E}^{inc}(\boldsymbol{r}) = \left(\hat{\boldsymbol{\theta}}_i E_\theta^{inc} + \hat{\boldsymbol{\varphi}}_i E_\varphi^{inc}\right) e^{jk_0[\rho \sin\theta_i \cos(\varphi-\varphi_i)+(z-d)\cos\theta_i]} \tag{22}$$

incident from the direction (θ_i, φ_i) on the grounded layered medium from the upper half-space, which is assumed to have free-space parameters. Observe that in (22) the phase reference point is chosen on the z axis at $z = d$, where d specifies the location of the uppermost interface. The plane wave (22) is the source of the 'incident' field appearing in (1)–(2), which may be expressed as

$$\boldsymbol{E}_s^i(\boldsymbol{r}) = \left[\hat{\boldsymbol{\rho}}_i\, V^e(k_\rho^i; z|d) + \hat{\boldsymbol{\varphi}}_i\, V^h(k_\rho^i; z|d)\right] e^{j\boldsymbol{k}_\rho^i \cdot \boldsymbol{\rho}} \tag{23}$$

$$\mathcal{E}_z^i(z) = -\frac{\eta_0}{\epsilon_z} \sin\theta_i\, I^e(k_\rho^i; z|d)\, J_0(k_\rho^i a)\, e^{j\boldsymbol{k}_\rho^i \cdot \boldsymbol{\rho}_c} \tag{24}$$

where the direction of the unit vectors $\hat{\boldsymbol{\rho}}_i$ and $\hat{\boldsymbol{\varphi}}_i$, and $\boldsymbol{k}_\rho^i = \hat{\boldsymbol{\rho}}_i k_\rho^i$, with $k_\rho^i = k_0 \sin\theta_i$, are specified by the direction of arrival of the plane wave. In the above, V^p and I^p denote, respectively, the voltage and current on the corresponding transmission line network analog of the layered medium (see Fig. 3), excited in the uppermost section by the incident voltage waves

$$V_-^e(z) = \cos\theta_i\, E_\theta^{inc}\, e^{jk_0(z-d)\cos\theta_i} \tag{25}$$

$$V_-^h(z) = E_\varphi^{inc}\, e^{jk_0(z-d)\cos\theta_i} \tag{26}$$

propagating in the $-z$ direction. In (23)–(24), we explicitly indicate in the arguments of V^p and I^p their dependence on k_ρ^i and on the phase reference point $(z = d)$ of the plane wave field. (Although similar notation is used, V^p and I^p appearing in (23)-(24) should not be confused with the transmission line Green's functions introduced earlier.) The $J_0(k_\rho^i a)$ factor in (24) is the result of the averaging of E_z^i over the coax probe circumference. Observe that (23)-(24) are in a general form applicable to a medium with any number of layers, provided the appropriate transmission line voltages and current are employed (see Appendix A).

F. Far fields and RCS

The 'scattered' far-zone field radiated by the patch and probe currents can be determined by the stationary-phase method [28]. It is then found that the patch contribution to the far field in the direction (θ_o, φ_o) is

$$E_\theta^s \sim \frac{k_0}{2\pi j r}\, e^{-jk_0(r-d\cos\theta_o)}\, V_i^e(k_\rho^o; d|z')\, \hat{\boldsymbol{\rho}}_o \cdot \int_S \boldsymbol{J}_s(\boldsymbol{\rho}')\, e^{j\boldsymbol{k}_\rho^o\cdot\boldsymbol{\rho}'}\, dS' \tag{27}$$

$$E_\varphi^s \sim \frac{k_0}{2\pi j r}\, e^{-jk_0(r-d\cos\theta_o)}\, \cos\theta_o\, V_i^h(k_\rho^o; d|z')\, \hat{\boldsymbol{\varphi}}_o \cdot \int_S \boldsymbol{J}_s(\boldsymbol{\rho}')\, e^{j\boldsymbol{k}_\rho^o\cdot\boldsymbol{\rho}'}\, dS' \tag{28}$$

where the orientation of the unit vectors $\hat{\boldsymbol{\rho}}_o$ and $\hat{\boldsymbol{\varphi}}_o$, and $\boldsymbol{k}_\rho^o = \hat{\boldsymbol{\rho}}_o k_\rho^o$, with $k_\rho^o = k_0 \sin\theta_o$ are specified by (θ_o, φ_o). It is assumed in the above that the layered medium and the radiating structure are confined to the region $z < d$. The contribution of the coax probe to the far field is found by a similar procedure, with the result

$$E_\theta^s \sim -\frac{k_0}{2\pi j r}\, e^{-jk_0(r-d\cos\theta_o)} J_0(k_\rho^o a)\, e^{jk_0\rho_c\sin\theta_o\cos(\varphi_o-\varphi_c)} \cdot \sin\theta_o\cos\theta_o\, \frac{\eta_0^2}{\epsilon_z'} \int_C I(z')\, I_v^e(k_\rho^o; d|z')\, dz' \tag{29}$$

where (ρ_c, φ_c) are the polar coordinates of the probe. Analogous expressions for the far field of the magnetic frill current can also be given, but are omitted here because the contribution of the coax aperture—which is assumed to be electrically small—to the total radiated field has been found to be negligible. We note that (27)-(29) are applicable to multilayered media, provided the appropriate transmission line Green's functions are employed (see Appendix A). However, these simple expressions lose validity near the horizon ($\theta_o \approx 90°$), in which case the stationary phase point approaches a branch point singularity in the k_ρ-plane, and guided wave phenomena dominate the far field.

If the plane wave field incident in the upper half-space is polarized in the u direction and the v component of the scattered field is considered, where u and v stand for θ or φ, the RCS of the antenna is given as [29, p. 48]

$$\sigma_{uv} = 4\pi r^2 \frac{|E_v^s|^2}{|E_u^{inc}|^2} \tag{30}$$

It should be noted that the scattered field in the above does not include the plane wave (geometrical optics) field reflected by the layered medium.

3 Numerical Method

A. Weak form of the integral equations

The MOM is applied to the weak forms of (1) and (2), which are obtained by 'testing' them with suitably selected weight functions $\{\boldsymbol{\Lambda}_k\}$ and $\{N_k\}$, respectively, where the former are defined over S and the latter over C. As a result, upon using Gauss' theorem [30, p. 503] and integrating by parts, we obtain (cf. [31])

$$\begin{aligned}\Big\langle \boldsymbol{\Lambda}_k ; \Big\langle G_A, \boldsymbol{J}_s \Big\rangle'_S \Big\rangle_S - \Big\langle \boldsymbol{\nabla}_s \cdot \boldsymbol{\Lambda}_k, \Big\langle G_\phi, \boldsymbol{\nabla}_s \cdot \boldsymbol{J}_s \Big\rangle'_S \Big\rangle_S \\ + \Big\langle \boldsymbol{\Lambda}_k \cdot \hat{\boldsymbol{\varrho}}_c, \Big\langle K_{\varrho z}, I \Big\rangle'_C \Big\rangle_S - \Big\langle \boldsymbol{\nabla}_s \cdot \boldsymbol{\Lambda}_k, \Big\langle K_\phi, \frac{dI}{dz} \Big\rangle'_C \Big\rangle_S \\ - \Big\langle \boldsymbol{\Lambda}_k \cdot \hat{\boldsymbol{\varrho}}_c, E_\varrho^c \Big\rangle_S = \Big\langle \boldsymbol{\Lambda}_k ; \boldsymbol{E}_s^i \Big\rangle_S\end{aligned} \tag{31}$$

$$\begin{aligned}\Big\langle N_k, \Big\langle \mathcal{G}_{z\varrho}, \hat{\boldsymbol{\varrho}}'_c \cdot \boldsymbol{J}_s \Big\rangle'_S \Big\rangle_C - \Big\langle \frac{dN_k}{dz}, \Big\langle \mathcal{G}_\phi, \boldsymbol{\nabla}_s \cdot \boldsymbol{J}_s \Big\rangle'_S \Big\rangle_C \\ + \Big\langle N_k, \Big\langle \mathcal{K}_{zz}, I \Big\rangle'_C \Big\rangle_C - \Big\langle \frac{dN_k}{dz}, \Big\langle \mathcal{K}_\phi, \frac{dI}{dz} \Big\rangle'_C \Big\rangle_C - \Big\langle N_k, \mathcal{E}_z^c \Big\rangle_C = \Big\langle N_k, \mathcal{E}_z^i \Big\rangle_C\end{aligned} \tag{32}$$

where we have introduced the notation $\langle\, ; \rangle$ for an integral of a product of two functions separated by the comma. The dot over the comma signifies a 'dot product' of vector arguments and the prime over $\int$ indicates that the integration is over the primed (source) coordinates, while the subscript S or C designates the domain of integration (i.e., the surface of the patch or the length of the coax probe—see Fig. 2). For simplicity, the arguments of the integrand functions are omitted in (31)-(32).

B. Patch current expansion

The microstrip patch is modeled by triangular elements, as indicated in Fig. 2. The probe-to-patch junction can be located anywhere on the patch, including edges and corners, but must coincide with a node of the triangular element mesh. The nodes of each triangular element are assigned indices i, j, and k in a counterclockwise direction, as illustrated in Fig. 4. We adopt here a local indexing scheme, in which these indices assume the values 1, 2, or 3, in a cyclic manner. The sides of a triangle with an area A are formed by three edge vectors, $\boldsymbol{\ell}_i$, $\boldsymbol{\ell}_j$, and $\boldsymbol{\ell}_k$, where $\boldsymbol{\ell}_i$ is oriented from node j to node k. The position of the ith node with respect to the global coordinate origin is specified by the vector $\boldsymbol{r}_i$, whose projection on the xy plane is $\boldsymbol{\rho}_i$. Since the microstrip patch lies in a $z=$constant plane with z known, the location of an arbitrary point $\boldsymbol{r}$ within an element may also be uniquely specified by its radial position vector $\boldsymbol{\rho} = \boldsymbol{\rho}_i + \boldsymbol{\varrho}_i$, where $\boldsymbol{\varrho}_i$ is the local position vector originating at the ith node of the

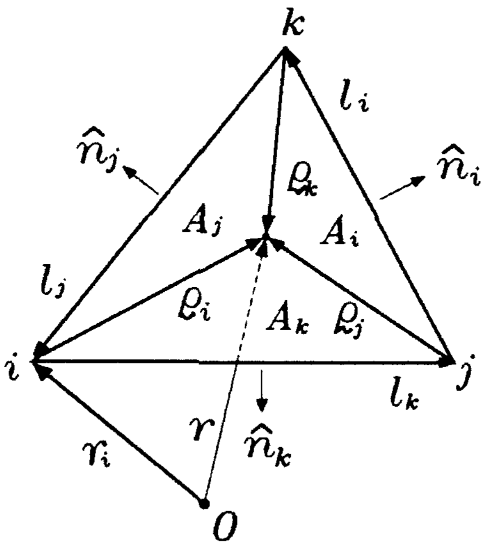

Figure 4: Local coordinates associated with a triangular element.

element. As indicated in Fig. 4, the three local position vectors further divide the element into three triangles, where the area of the triangle opposite node i is denoted by A_i. To facilitate the integrations over irregularly shaped triangles encountered in (31)-(32), we introduce for each triangle a 'natural' coordinate system (L_i, L_j, L_k), where L_i is known as the 'area coordinate' or 'shape function' associated with node i of the element [32, p. 110], and is defined as

$$L_i = \frac{A_i}{A}, \qquad \sum_{i=1}^{3} L_i = 1 \tag{33}$$

In terms of the area coordinates, the local position vector $\boldsymbol{\varrho}_i$ may be expressed as

$$\boldsymbol{\varrho}_i = \boldsymbol{\ell}_k L_j - \boldsymbol{\ell}_j L_k \tag{34}$$

To represent the patch current on each triangular element, we introduce a vector basis function $\boldsymbol{\Lambda}_i$, given as (cf. [18])

$$\boldsymbol{\Lambda}_i = \frac{\boldsymbol{\varrho}_i}{2A} \tag{35}$$

Noting that [33]

$$\boldsymbol{\nabla}_s L_i = -\hat{\boldsymbol{n}}_i \frac{\ell_i}{2A} \tag{36}$$

where $\hat{\boldsymbol{n}}_i$ is a unit vector normal to edge i in the plane and pointing out of the triangular element (see Fig. 4), we find the divergence of $\boldsymbol{\Lambda}_i$ as

$$\boldsymbol{\nabla}_s \cdot \boldsymbol{\Lambda}_i = \frac{1}{A} \tag{37}$$

We also find that $\hat{\boldsymbol{n}}_i \cdot \boldsymbol{\Lambda}_i$ is constant on edge i, which makes it easy to enforce the continuity of the normal component of $\boldsymbol{J}_s$ between the elements that share this edge. The patch current density and its divergence on each element may now be approximated as

$$\boldsymbol{J}_s = \sum_{i=1}^{3} I_i \boldsymbol{\Lambda}_i, \qquad \boldsymbol{\nabla}_s \cdot \boldsymbol{J}_s = \sum_{i=1}^{3} \frac{I_i}{A} \tag{38}$$

where I_i is the current leaving the element through edge i.

C. Probe current expansion

The coaxial probe is modeled by a number of non-overlapping line segment elements. The end points of a segment with length h are assigned local indices i and j, which assume the values 1 or 2 in a cyclic manner. The global coordinates of these points are specified by z_i and z_j. As indicated in Fig. 5, the distance of a point z within an element from node j is denoted by h_i. For each element, we introduce a pair of linear shape functions (N_i, N_j), defined as (cf. [34, p. 99])

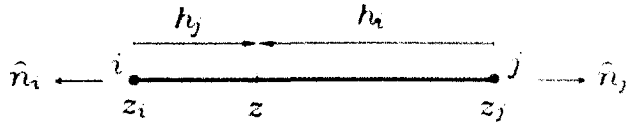

Figure 5: Local coordinates associated with a line segment element.

$$N_i = \frac{h_i}{h}, \qquad \sum_{i=1}^{2} N_i = 1 \tag{39}$$

The location of a point z on an element may now be specified as

$$z = z_i + c_j h N_j, \qquad c_i = \hat{\boldsymbol{z}} \cdot \hat{\boldsymbol{n}}_i \tag{40}$$

where $\hat{\boldsymbol{n}}_i$ is a unit vector pointing out of the element at node i. Observe that the value of c_i is either +1 or −1, and that $c_i = -c_j$. From (40), it follows that

$$\frac{d}{dz} N_i = \frac{c_i}{h} \tag{41}$$

The axial probe current and its derivative on an element may now be approximated by the expansions

$$I = \sum_{i=1}^{2} I_i c_i N_i, \qquad \frac{d}{dz} I = \sum_{i=1}^{2} \frac{I_i}{h} \tag{42}$$

where I_i is the current leaving the element through node i.

D. Attachment mode

The current expansion (38) is not suitable for a patch element having the probe to-patch junction point as one of its nodes. To represent the current distribution on such 'junction elements,' a special 'attachment mode' is required, which is superposed on the non-junction part of the current, represented by (38). Let there be N_J junction elements attached to a junction node, where the total current I_J enters the microstrip patch (see Fig. 6, where only one patch junction element is shown for simplicity). Also, let the junction node of each junction element be assigned a local index i, and

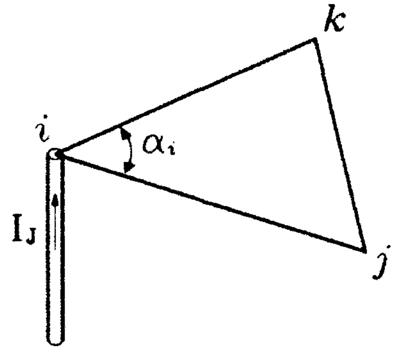

Figure 6: Geometry of the probe-to-patch junction.

let the angle between the element edges that meet at this node be designated α_i. Furthermore, let the sum of the junction vertex angles be denoted by α. (Clearly, $\alpha = 2\pi$, unless the junction node is on the edge of the microstrip patch.) To represent the junction part of the current on an element whose node i is the junction node, we use the basis function [12]

$$\boldsymbol{\Pi}_i = -\frac{\alpha_i}{2\alpha}(\boldsymbol{\Lambda}_j + \boldsymbol{\Lambda}_k) \tag{43}$$

The junction current density and its divergence on this element may then be expressed as

$$\boldsymbol{J}_s = I_J\,\boldsymbol{\Pi}_i, \qquad \boldsymbol{\nabla}_s \cdot \boldsymbol{J}_s = -\,I_J\,\frac{\alpha_i}{\alpha A} \tag{44}$$

where the second expression follows from (43) and (37). The union of the currents represented by (44), which only exist on the patch elements adjacent to the junction node, form the patch part of the attachment mode. As mentioned above, this attachment mode exists in addition to the non-junction part of the patch current, represented by (38). The coax probe part of the attachment mode, which extends over the line segment adjacent to the junction node, is simply given as

$$I = I_J N_i , \qquad \frac{d}{dz} I = \frac{I_J}{h} \tag{45}$$

where it is assumed that the junction node has a local index i. We note that this attachment current is easily incorporated in the expansion (42), by setting $I_i = I_J$ on the junction line segment. We also note that the current given by (44) does not enter the patch through the junction node; rather, it enters through the element edges that meet at that node. Consequently, unlike some more rigorous attachment modes [35], [36], (44) does not correctly model the diverging current behavior near the junction. Nevertheless, the current continuity at the junction is satisfied in a global sense, i.e., the total current entering the N_J junction patch elements is equal to the current I_J leaving the coax probe, and the net charge associated with (44)-(45) is zero. This attachment mode is easily implemented in the MOM procedure because it comprises regular basis functions already used to expand the non-junction part of the current.

E. Global MOM matrix assembly and solution procedure

The testing functions in the integral equations (31)-(32) are drawn from the same sets as the basis functions used to represent the current on the patch and on the coax probe. Hence, $\{\boldsymbol{\Lambda}_k\}$ consists of $\boldsymbol{\Lambda}_i^{(n)}$, with $i = 1, 2$, and 3, and $n = 1, \ldots, N_S$, where N_S is the total number of triangular patch elements. Similarly, $\{N_k\}$ consists of $c_i^{(n)} N_i^{(n)}$, with $i = 1, 2$, and $n = 1, \ldots, N_C$, where N_C is the total number of line segment elements on the coax probe. In addition, (31) is tested with the patch part of the attachment mode, comprising the union of the basis functions $\boldsymbol{\Pi}_i^{(n)}$, where $n = 1, 2, \ldots, N_J$. The resulting equation is then combined with the equation that results from the testing of (32) with the coax part of the attachment mode, $N_i^{(n)}$, where the nth probe element is assumed to be adjacent to the junction. As before, we assume here that the local index of the junction node is i. In the above, it was necessary to introduce the superscript (n) to distinguish the local basis functions associated with element n. In what follows, where there is no danger of confusion, this element superscript will be omitted for notational simplicity.

When the expansions (38), (42), and (44)-(45) are substituted into the integral equations (31)–(32), the coefficients $I_i^{(n)}$ are constrained by the boundary conditions, which require continuity of the normal components of $\boldsymbol{J}_s$ across the edges shared by adjacent elements, or their vanishing at the boundary edges of S, as well as continuity of the coax probe current between adjacent segments. On the uppermost probe segment, if the junction node has a local index i, $I_i^{(n)}$ is set to I_J, which explicitly enforces the continuity of the attachment mode current at the probe-to-patch junction. Similarly, on the line segment at the base of the coax probe, if the load node has a local index i, $I_i^{(n)}$ is set to I_L. In general, I_J and I_L are not known a priori and must be computed together with the other current expansion coefficients. In the unloaded case (when $Z_L = \infty$), [illegible] is set to zero. If the number of the non-boundary triangle element edges is denoted by N_E and the total number of the unknown current coefficients by N, then $N = N_E + N_C + 1$ (or one less that number, if $Z_L = \infty$). As a result of this procedure, the coupled integral equations (31)-(32) are converted into an algebraic system

$$[Z_{mn}][I_n] = [V_m] \tag{46}$$

where $[Z_{mn}]$ is the N-by-N global MOM matrix (also referred to as the global impedance matrix), $[I_n]$ is the N-by-1 global vector of the sought after current expansion coefficients, and $[V_m]$ is the N-by-1 global voltage excitation vector.

To assemble the global system (46), we consider one source element-test element pair at a time. Let the global indices of these elements be n and m, respectively. Then, for each such pair we assemble a local system

$$[Z_{ii'}^{(mn)}][I_{i'}^{(n)}] = [V_i^{(m)}] \tag{47}$$

where $[Z_{ii'}^{(mn)}]$ is the local impedance matrix and $[V_i^{(m)}]$ is the local voltage excitation vector. Here, the primed local source element indices i', j', and (in case of a triangular element) k' follow the same cyclic convention as the unprimed ones. Observe that there exists a unique mapping between the local coefficients $\{I_i^{(n)}\}$ of each element and the global current coefficients $\{I_n\}$, where the reference directions of the latter are specified by the order in which the element nodes appear in the input geometry data. This mapping determines to which entries of the global system (46) should the elements of (47) be added, and with what signs.

Consider first a test element, S_m, on the microstrip patch. Then, if the source element, S_n, is also on the patch, the entries of the resulting 3-by-3 local impedance matrix are found as

$$Z_{ii'}^{(mn)} = \left\langle \boldsymbol{\Lambda}_i; \left\langle G_A, \boldsymbol{\Lambda}_{i'} \right\rangle'_{S_n} \right\rangle_{S_m} - \left\langle \frac{1}{A}, \left\langle G_\phi, \frac{1}{A} \right\rangle'_{S_n} \right\rangle_{S_m} \tag{48}$$

If, on the other hand, the source element, C_n, is on the coax probe, there results a 3-by-2 local impedance matrix with the entries given as

$$Z_{ii'}^{(mn)} = \left\langle \boldsymbol{\Lambda}_i \cdot \hat{\boldsymbol{\varrho}}_c, \left\langle K_{\varrho z}, c_{i'} N_{i'} \right\rangle'_{C_n} \right\rangle_{S_m} - \left\langle \frac{1}{A}, \left\langle K_\phi, \frac{1}{h} \right\rangle'_{C_n} \right\rangle_{S_m} \tag{49}$$

In addition, when C_n is the line segment at the base of the probe and L is the local index of the load node, this matrix is augmented by the load contributions

$$Z_{iL}^{(mn)} = -\left\langle \boldsymbol{\Lambda}_i \cdot \hat{\boldsymbol{\varrho}}_c, T \right\rangle_{S_m} \tag{50}$$

which only affect the column of (49) corresponding to the load node. Finally, the elements of the 3-by-1 local voltage excitation vector resulting from testing over S_m are found as

$$V_i^{(m)} = \left\langle \boldsymbol{\Lambda}_i; \boldsymbol{E}_s^i \right\rangle_{S_m} \tag{51}$$

Next, consider a test element, C_m, on the coax probe. Then, if the source element, S_n, is on the patch, there results a local 2-by-3 impedance matrix with the entries given as

$$Z_{ii'}^{(mn)} = \left\langle c_i N_i, \left\langle \mathcal{G}_{z\varrho}, \hat{\boldsymbol{\varrho}}'_c \cdot \boldsymbol{\Lambda}_{i'} \right\rangle'_{S_n} \right\rangle_{C_m} - \left\langle \frac{1}{h}, \left\langle \mathcal{G}_\phi, \frac{1}{A} \right\rangle'_{S_n} \right\rangle_{C_m} \tag{52}$$

If, on the other hand, the source element, C_n, is also on the coax probe, the entries of the resulting the 2-by-2 local impedance matrix are found as

$$Z_{ii'}^{(mn)} = \left\langle c_i N_i, \left\langle \mathcal{K}_{zz}, c_{i'} N_{i'} \right\rangle'_{C_n} \right\rangle_{C_m} - \left\langle \frac{1}{h}, \left\langle \mathcal{K}_{\phi}, \frac{1}{h} \right\rangle'_{C_n} \right\rangle_{C_m} \tag{53}$$

In addition, when C_n is the line segment at the base of the probe and L is the local index of the load node, this matrix is augmented by the load contributions

$$Z_{iL}^{(mn)} = -\left\langle c_i N_i, \mathcal{U} \right\rangle_{C_m} \tag{54}$$

which only affect the column of (53) corresponding to the load node. Finally, the elements of the 2-by-1 local voltage excitation vector resulting from testing over C_m are given as

$$V_i^{(m)} = \left\langle c_i N_i, \mathcal{E}_z^i \right\rangle_{C_m} \tag{55}$$

The local impedance matrices given above must be further modified to include the contribution of the patch part of the attachment mode. Hence, let J be the local index of the junction node on the coax probe. Then, for every patch junction element S_n, whose junction node is assumed to have a local index i', the entries of (49) are augmented by

$$\begin{aligned} Z_{iJ}^{(mn)} = & - \left\langle \boldsymbol{\Lambda}_i; \left\langle G_A, \frac{\alpha_{i'}}{2\alpha} \boldsymbol{\Lambda}_{j'} \right\rangle'_{S_n} \right\rangle_{S_m} - \left\langle \boldsymbol{\Lambda}_i; \left\langle G_A, \frac{\alpha_{i'}}{2\alpha} \boldsymbol{\Lambda}_{k'} \right\rangle'_{S_n} \right\rangle_{S_m} \\ & + \left\langle \frac{1}{A}, \left\langle G_\phi, \frac{\alpha_{i'}}{\alpha A} \right\rangle'_{S_n} \right\rangle_{S_m} \end{aligned} \tag{56}$$

and the entries of (53) are augmented by

$$\begin{aligned} Z_{iJ}^{(mn)} = & - \left\langle c_i N_i, \left\langle \mathcal{G}_{z\varrho}, \frac{\alpha_{i'}}{2\alpha} \hat{\boldsymbol{\varrho}}'_c \cdot \boldsymbol{\Lambda}_{j'} \right\rangle'_{S_n} \right\rangle_{C_m} - \left\langle c_i N_i, \left\langle \mathcal{G}_{z\varrho}, \frac{\alpha_{i'}}{2\alpha} \hat{\boldsymbol{\varrho}}'_c \cdot \boldsymbol{\Lambda}_{k'} \right\rangle'_{S_n} \right\rangle_{C_m} \\ & + \left\langle \frac{1}{h}, \left\langle \mathcal{G}_\phi, \frac{\alpha_{i'}}{\alpha A} \right\rangle'_{S_n} \right\rangle_{C_m} \end{aligned} \tag{57}$$

Note that (56) and (57) only affect the column of the respective impedance matrix corresponding to the junction node. Furthermore, for every patch junction element

S_m, whose junction node is assumed to have a local index i, the impedance matrix given by (52) is augmented by

$$Z_{Ji'}^{(mn)} = -\left\langle \frac{\alpha_i}{2\alpha}\boldsymbol{A}_j ; \left\langle G_A , \boldsymbol{A}_{i'} \right\rangle'_{S_n} \right\rangle_{S_m} - \left\langle \frac{\alpha_i}{2\alpha}\boldsymbol{A}_k ; \left\langle G_A , \boldsymbol{A}_{i'} \right\rangle'_{S_n} \right\rangle_{S_m} + \left\langle \frac{\alpha_i}{\alpha A} , \left\langle G_\phi , \frac{1}{A} \right\rangle'_{S_n} \right\rangle_{S_m} \tag{58}$$

In addition, the element $Z_{JJ}^{(mn)}$ of (53) is augmented by the attachment mode 'self-term'

$$\begin{aligned} Z_{JJ}^{(mn)} = {} & \left\langle \frac{\alpha_i}{2\alpha}\boldsymbol{A}_j ; \left\langle G_A , \frac{\alpha_{i'}}{2\alpha}\boldsymbol{A}_{j'} \right\rangle'_{S_n} \right\rangle_{S_m} + \left\langle \frac{\alpha_i}{2\alpha}\boldsymbol{A}_j ; \left\langle G_A , \frac{\alpha_{i'}}{2\alpha}\boldsymbol{A}_{k'} \right\rangle'_{S_n} \right\rangle_{S_m} \\ & + \left\langle \frac{\alpha_i}{2\alpha}\boldsymbol{A}_k ; \left\langle G_A , \frac{\alpha_{i'}}{2\alpha}\boldsymbol{A}_{j'} \right\rangle'_{S_n} \right\rangle_{S_m} + \left\langle \frac{\alpha_i}{2\alpha}\boldsymbol{A}_k ; \left\langle G_A , \frac{\alpha_{i'}}{2\alpha}\boldsymbol{A}_{k'} \right\rangle'_{S_n} \right\rangle_{S_m} \\ & - \left\langle \frac{\alpha_i}{\alpha A} , \left\langle G_\phi , \frac{\alpha_{i'}}{\alpha A} \right\rangle'_{S_n} \right\rangle_{S_m} \end{aligned} \tag{59}$$

in which i' is the local junction node index on element S_n. Similarly, for every patch junction element S_m, whose junction node has a local index i, the impedance matrix given by (53) is further augmented by

$$Z_{Ji}^{(mn)} = -\left\langle \frac{\alpha_i}{2\alpha}\boldsymbol{A}_i \cdot \hat{\boldsymbol{\varrho}}_z , \left\langle K_{\varrho z} , c_{i'} N_{i'} \right\rangle'_{C_n} \right\rangle_{S_m} - \left\langle \frac{\alpha_i}{2\alpha}\boldsymbol{A}_k \cdot \hat{\boldsymbol{\varrho}}_z , \left\langle K_{\varrho z} , c_{i'} N_{i'} \right\rangle'_{C_n} \right\rangle_{S_m} + \left\langle \frac{\alpha_i}{\alpha A} , \left\langle K_\phi , \frac{1}{h} \right\rangle'_{C_n} \right\rangle_{S_m} \tag{60}$$

and by

$$Z_{JL}^{(mn)} = \left\langle \frac{\alpha_i}{2\alpha}\boldsymbol{A}_j \cdot \hat{\boldsymbol{\varrho}}_z , T \right\rangle_{S_m} + \left\langle \frac{\alpha_i}{2\alpha}\boldsymbol{A}_k \cdot \hat{\boldsymbol{\varrho}}_z , T \right\rangle_{S_m} \tag{61}$$

in which L is the local index of the load node on the coax probe. Also, the voltage excitation vector given in (55) is augmented by

$$V_J^{(m)} = -\left\langle \frac{\alpha_i}{2\alpha}\boldsymbol{A}_j ; \boldsymbol{E}_s^i \right\rangle_{S_m} - \left\langle \frac{\alpha_i}{2\alpha}\boldsymbol{A}_k ; \boldsymbol{E}_s^i \right\rangle_{S_m} \tag{62}$$

Note that (58)-(62) affect only the row of the respective local system (47) corresponding to the junction node on the coax probe.

It can be shown, by using the reciprocity properties of the transmission line Green's functions (see Appendix A), that—apart from the load terms—the local impedance matrices defined above posses symmetry properties, which may be exploited to nearly halve the computational effort involved in filling the global impedance matrix in (46). The integrals over the source coordinates, which appear in the impedance matrices above, involve kernels that are singular when the test and source elements coincide. These singularities are extracted and integrated analytically [38], leaving well-behaved integrals over triangular and line segment elements, which are numerically evaluated by Gaussian quadratures (see, e g., [32, p. 113] regarding Gaussian rules for triangular domains). On the other hand, the testing (exterior) integrals have regular and slowly varying integrands, and may thus be approximated using one-point quadrature rules [18]. For example, the integral in (51) is approximated as

$$\left\langle \boldsymbol{\Lambda}_i ; \boldsymbol{E}_s^i \right\rangle_{S_m} \approx \frac{1}{2}\boldsymbol{\varrho}_i^{cm} \cdot \boldsymbol{E}_s^i(\boldsymbol{r}^{cm}) \qquad (63)$$

where $\boldsymbol{\varrho}_i^{cm}$ and $\boldsymbol{r}^{cm}$ denote, respectively, the local (with respect to node i—see Fig. 4) and global position vectors of the centroid of element S_m. This procedure results in significant savings in the computational effort, even though it sacrifices the symmetry properties of the impedance matrices.

Once the complex-valued matrix equation (46) is assembled and solved, which is accomplished by standard procedures (LU factorization with partial pivoting, followed by a forward and back substitution [37, p. 160]), the current density within each microstrip patch element may be obtained from (38) (and (44), in the case of a junction element). Similarly, the current within each coax probe element may be found from (42). The resonant frequencies and Q-factors of a microstrip antenna may be found as zeros in the complex frequency plane of the determinant of the global impedance matrix (this is accomplished by means of the Müller's search procedure [37, p. 120]). The corresponding modal currents may then be obtained from (46) with the excitation voltage vector set to zero.

F. Computation of spectral integrals

For the solution procedure described above to be practical, the spectral integrals that occur in (3)-(10) and in (20)-(21) must be efficiently evaluated. To accomplish that, these integrals are accelerated by asymptotic integrand subtraction and the method of averages [39], [40], [41]. In addition to these techniques, an interpolation and table look-up scheme is implemented to further reduce the computation time [39], [40], [41]. The integration path is properly deformed to avoid the integrand singularities, which occur on or near the real axis in the k_ρ plane [14].

G. Far field and RCS computation

Once the coefficients I_i are found for each element, the current expansions (38), (42), and (44) are substituted into (27)-(29) to determine the far fields. The integrals encountered in (27)-(28) are then recognized as Fourier transforms of the vector basis functions (35), evaluated at $\boldsymbol{k}_\rho = \boldsymbol{k}_\rho^o$. In view of (35) and (34), the Fourier transform of $\boldsymbol{\Lambda}_i$ associated with a triangular element S_n may be expressed as

$$\begin{aligned} \tilde{\boldsymbol{\Lambda}}_i &= \left\langle \boldsymbol{\Lambda}_i, e^{j\boldsymbol{k}_\rho\cdot\boldsymbol{\rho}'} \right\rangle'_{S_n} \\ &= \frac{1}{2A}\left(\boldsymbol{\ell}_k \tilde{L}_j - \boldsymbol{\ell}_j \tilde{L}_k\right) \end{aligned} \tag{64}$$

where $\tilde{L}_i$ denotes the Fourier transformed shape function L_i. Upon using the procedure of Appendix B, we may express $\tilde{L}_i$ as

$$\begin{aligned} \tilde{L}_i = & -\frac{b_i}{2Ak_\rho^2}\sum_{\nu=1}^{3} b_\nu j_0(a_\nu k_\rho/2)\, e^{j\boldsymbol{k}_\rho\cdot\boldsymbol{\rho}_{c\nu}} \\ & + \frac{b_j}{2k_\rho}\Big[j_1(a_j k_\rho/2) - j j_0(a_j k_\rho/2)\Big]\, e^{j\boldsymbol{k}_\rho\cdot\boldsymbol{\rho}_{cj}} \\ & - \frac{b_k}{2k_\rho}\Big[j_1(a_k k_\rho/2) + j j_0(a_k k_\rho/2)\Big]\, e^{j\boldsymbol{k}_\rho\cdot\boldsymbol{\rho}_{ck}} \end{aligned} \tag{65}$$

where $\boldsymbol{\rho}_{ci}$ is a position vector of the midpoint of edge i of the element, $a_i = \hat{\boldsymbol{u}}\cdot\boldsymbol{\ell}_i$, $b_i = \hat{\boldsymbol{v}}\cdot\boldsymbol{\ell}_i$, and j_n denotes the spherical Bessel function of order n. We note that although (65) can be put in a simpler form, this is counterproductive because it introduces removable singularities, which occur when $\boldsymbol{k}_\rho$ happens to be orthogonal to any of the three edges of the element, i.e., when $a_i = 0$ for $i = 1, 2,$ or 3. In contrast, the expression for $\grave{L}_i$ given in (65) is clearly nonsingular, unless $k_\rho = 0$. Even in the latter case, it can be shown that (65) approaches a finite limit $A/3$ as $k_\rho \rightarrow 0$. We also note that when (65) is evaluated for $\boldsymbol{k}_\rho = \boldsymbol{k}_\rho^o$, as is required in (27)-(28), then $k_\rho = k_\rho^o$, $\hat{\boldsymbol{u}} = \hat{\boldsymbol{\rho}}_o$, and $\hat{\boldsymbol{v}} = \hat{\boldsymbol{\varphi}}_o$.

The integrals that arise when the probe current expansion (42) is substituted into (29) depend on the form of the transmission line Green's function $I_v^e(k_\rho; d|z')$. Let us suppose that the coax probe extends over layer l of thickness d_l, between the z-axis coordinates z_l and z_{l+1}, where $z_{l+1} \leq d$. Consequently, $I_v^e(k_\rho; d|z')$ can be expressed as a constant factor times $I_v^e(k_\rho; z_{l+1}|z')$. Using the traveling-wave form of the latter (see Appendix A), we then find that the integrals over a line segment element C_n within layer l, required to evaluate (29), are given as

$$\begin{aligned}\left\langle c_i N_i,\ I_v^e(k_\rho; z_{l+1}|z')\right\rangle_{C_n}^{\prime} &= \frac{Y_l^{\prime e}\left(1 - \overrightarrow{\Gamma}_l^{e}\right)}{1 - \overleftarrow{\Gamma}_l^{e}\,\overrightarrow{\Gamma}_l^{e}\,e^{-j2k_{zl}^e d_l}} \\ &\cdot \frac{h}{4}\left\{e^{jk_{zl}^e z_c}\left[c_i j_0(hk_{zl}^e/2) + j j_1(hk_{zl}^e/2)\right]\right. \\ &\left. - \overleftarrow{\Gamma}_l^{e}\,e^{-jk_{zl}^e(2d_l+z_c)}\left[c_i j_0(hk_{zl}^e/2) - j j_1(hk_{zl}^e/2)\right]\right\} \qquad (66)\end{aligned}$$

where h is the length and z_c the midpoint coordinate of the element, c_i is defined in (40), k_{zl}^e and $Y_l^{\prime e}$ are given in (16), and where the terminal reflection coefficients $\overleftarrow{\Gamma}_l^{e}$ and $\overrightarrow{\Gamma}_l^{e}$ are found from (71). When used in (29), the above is evaluated for $k_\rho = k_\rho^o$.

Once the microstrip patch and coax probe contributions to the far zone fields are determined, the RCS is readily obtained from (30).

4 Sample Results

The techniques developed in the previous sections have been implemented in a FORTRAN computer code. In this section, we present sample computed monostatic (i.e., $\theta_o = \theta_i$, $\varphi_o = \varphi_i$) RCS results for loaded and unloaded, coax-fed rectangular, circular and pentagonal microstrip patch antennas (see Fig. 7), and—where possible—

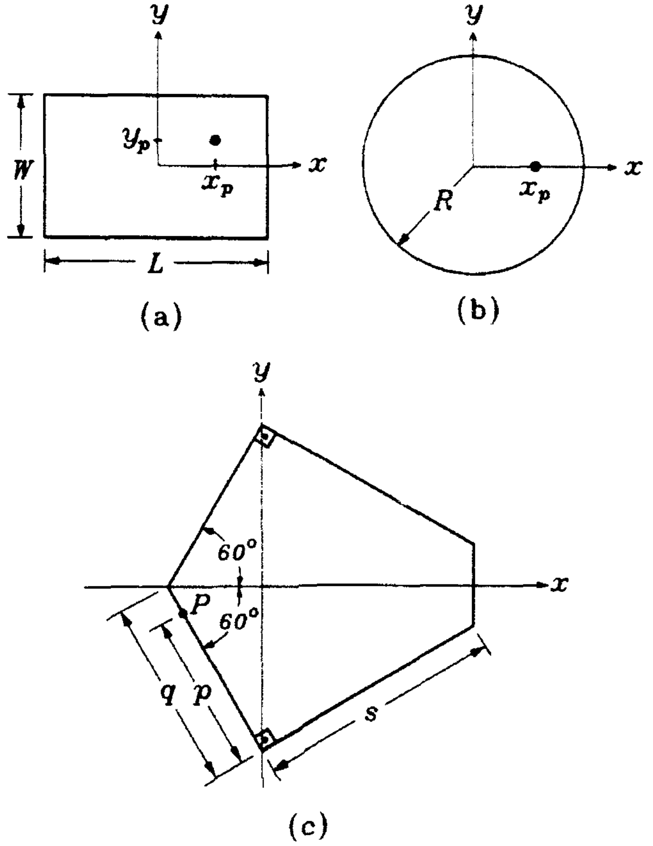

Figure 7: Geometries of probe-fed (*a*) rectangular, (*b*) circular, and (*c*) pentagonal microstrip patch antennas.

compare them with available published data. In all cases included here the patch resides on a single-layer substrate of varying thickness h, without a cover layer (see Fig. 1). The incident field is θ-polarized, with the electric field amplitude $E_\theta^{inc} = 1$ V/m. All RCS results are plotted vs. the frequency f, and are referred to 1 m^2 and given in dBsm ('decibels above a square meter') [29, p. 160].

The results shown in Fig. 8 are for an unloaded ($Z_L = \infty$) rectangular patch antenna (see Fig. 7*a*) on an isotropic substrate characterized by $\epsilon_r(1 - j\tan\delta)$, with ϵ_r and $\tan\delta$ specified in the figure caption. Newman and Forrei's [1] and Pozar's [2] results for this antenna are included for comparison.

In Fig. 9 we show results for a coax-fed rectangular patch antenna (see Fig. 7*a*, where (x_p, y_p) are the feed point coordinates) on a lossless uniaxial substrate. Three sets of data are presented, corresponding to $Z_L = \infty$ (no load), $Z_L = 50\,\Omega$ (matched load), and $Z_L = 0$ (short-circuit load). For the first two cases, our results are compared with those of Pozar [2]. We note that, as expected, the first and, to a lesser degree, the second RCS peak are suppressed by a matched load, and that the shorting pin causes the RCS peaks to shift up in frequency.

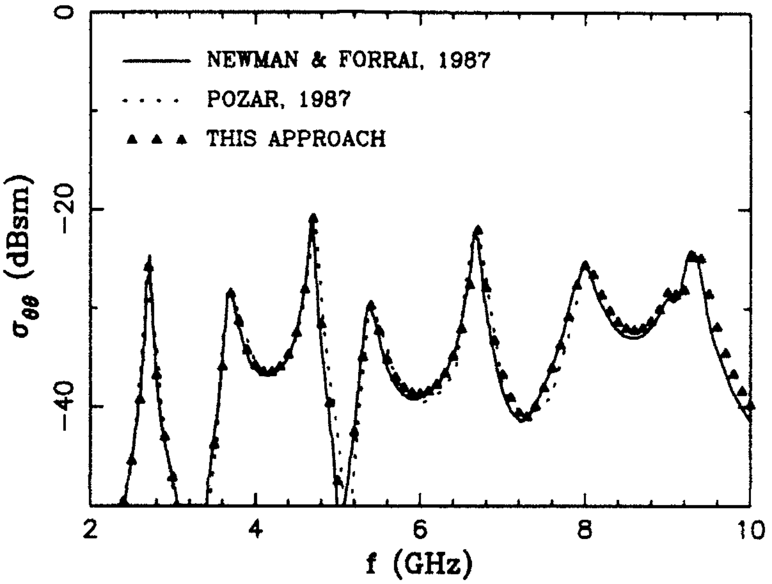

Figure 8: RCS of an unloaded rectangular microstrip patch antenna. The parameters are: $L = 36.6\,\text{mm}$, $W = 26\,\text{mm}$, $h = 1.58\,\text{mm}$, $\epsilon_r = 2.17$, $\tan\delta = 0.001$, $\varphi_i = 45°$, and $\theta_i = 60°$.

The results shown in Figs. 10 and 11 are for coax-fed circular microstrip patch antennas (see Fig. 7*b*, where x_p specifies the feed point location) on isotropic substrates, with the loads $Z_L = \infty$, 50, and $0\,\Omega$. In Fig. 10 we also show for comparison Aberle's [42] computed results, and in Fig. 11 we include the results computed and measured by Aberle et al. [4] for $Z_L = \infty$ and $50\,\Omega$. In reference to Fig. 11, it is of interest to note that our results are closer to the computed, rather than the measured data of Aberle et al. [4].

Finally, in Figs. 12 and 13 we show results for a coax-fed pentagonal microstrip patch antenna (see Fig. 7*c*, where P denotes the feed point) on an isotropic substrate.

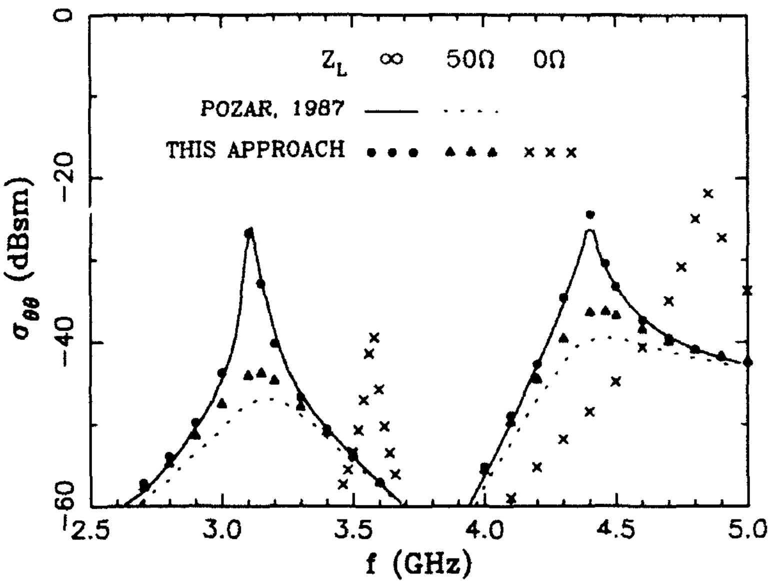

Figure 9: RCS of a rectangular microstrip patch antenna for $Z_L = \infty$, 50, and 0 Ω. The parameters are: $L = 10\,\mathrm{mm}$, $W = 15\,\mathrm{mm}$, $x_p = -L/4$, $y_p = -W/4$, $h = 1.27\,\mathrm{mm}$, $\epsilon_t = 13$, $\epsilon_z = 10.2$, $a = 0.432\,\mathrm{mm}$, $b = 1.397\,\mathrm{mm}$, $\varphi_i = 45°$, and $\theta_i = 0°$.

With the dimensions given in the caption of Fig. 12 (which correspond to a case considered in [43, p. 245]) and no load attached, the first three excitation-free modes of this antenna were found at the resonant frequencies $f_{r1} = 1.123\,\mathrm{GHz}$, $f_{r2} = 1.194\,\mathrm{GHz}$, and $f_{r3} = 2.184\,\mathrm{GHz}$, respectively. The modal currents of the first two modes, which resonate at very close frequencies, are orthogonal to one another. With a properly selected feed location, these two modes are excited with equal amplitudes, resulting in a circularly polarized (CP) radiation field at a frequency that lies between f_{r1} and f_{r2} [43]. The coax feed is used to minimize the degradation of ellipticity by unwanted radiation from the feed network. In the case of Fig. 12*a*, where $\varphi_i = 0°$, the polarization of the incident field is such that it excites the first mode of the antenna, but is orthogonal to the second mode. As a result, the co-polarized RCS component, $\sigma_{\theta\theta}$, dominates the cross-polarized component, $\sigma_{\theta\varphi}$, except near the CP frequency, at which the first and second modes are coupled through the loaded coax feed, and the value of $\sigma_{\theta\varphi}$ approaches that of $\sigma_{\theta\theta}$. The second peak in the plot of $\sigma_{\theta\varphi}$ corresponds to the third mode of the antenna. In the case of Fig. 12*b*, where $\varphi_i = 45°$, the incident

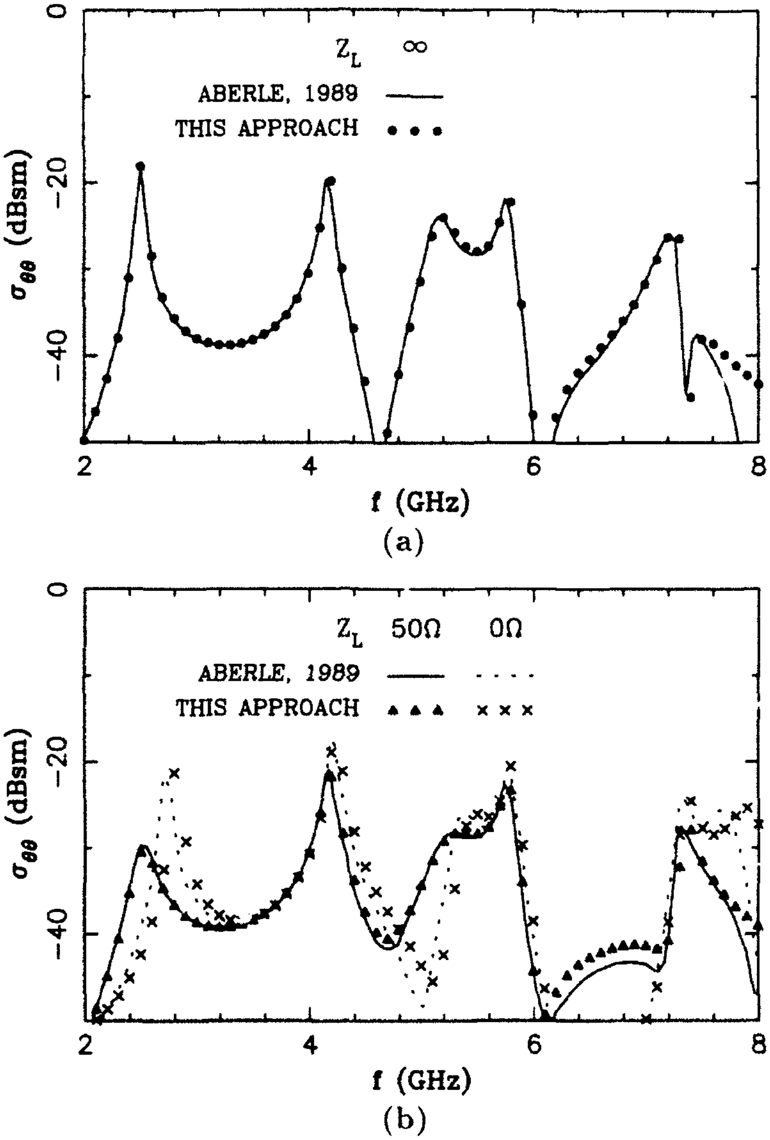

Figure 10: RCS of a circular microstrip patch antenna. (*a*) $Z_L = \infty$. (*b*) $Z_L = 50$ and 0 Ω. The parameters are: $R = 23\,\text{mm}$, $x_p = 9.2\,\text{mm}$, $h = 1.58\,\text{mm}$, $\epsilon_r = 2.2$, $\tan\delta = 0.0009$, $a = 0.432\,\text{mm}$, $b = 1.397\,\text{mm}$, $\varphi_i = 0°$, and $\theta_i = 60°$.

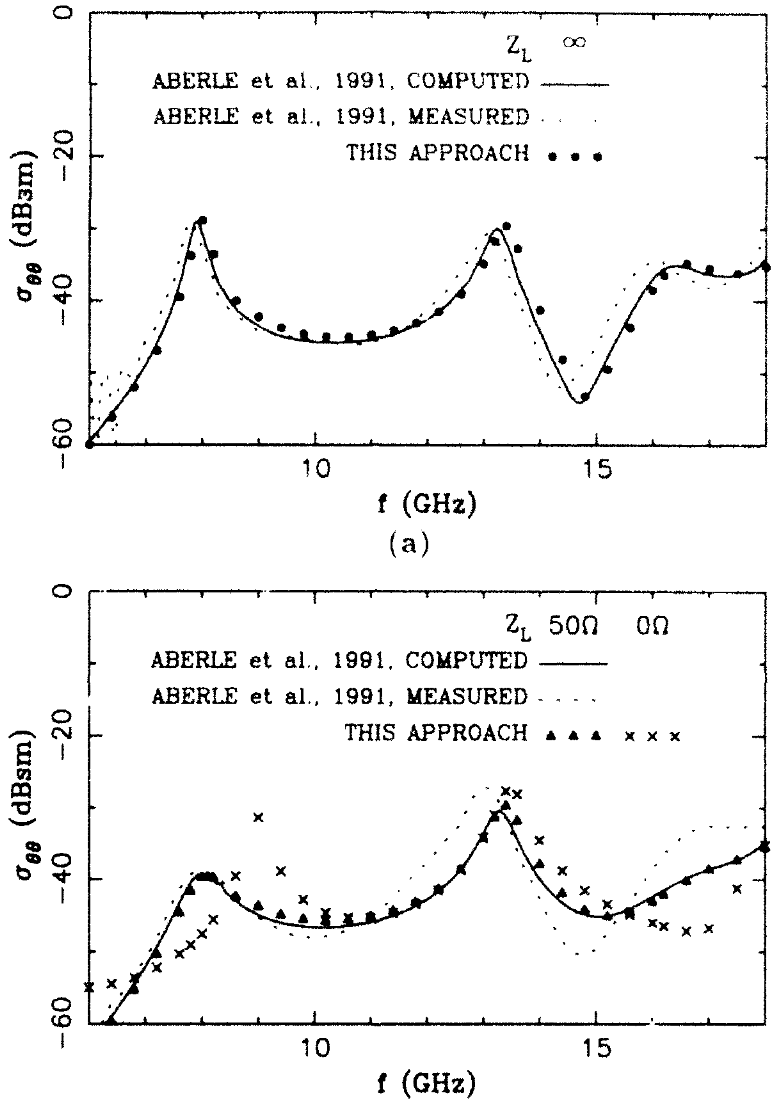

(a)

(b)

Figure 11: RCS of a circular microstrip patch antenna. (a) $Z_L = \infty$. (b) $Z_L = 50$ and $0\,\Omega$. The parameters are: $R = 7.1$ mm, $x_p = 2.5$ mm, $h = 0.787$ mm, $\epsilon_r = 2.2$, $\tan\delta = 0.0009$, $a = 0.432$ mm, $b = 1.397$ mm, $\varphi_i = 0°$, and $\theta_i = 63°$.

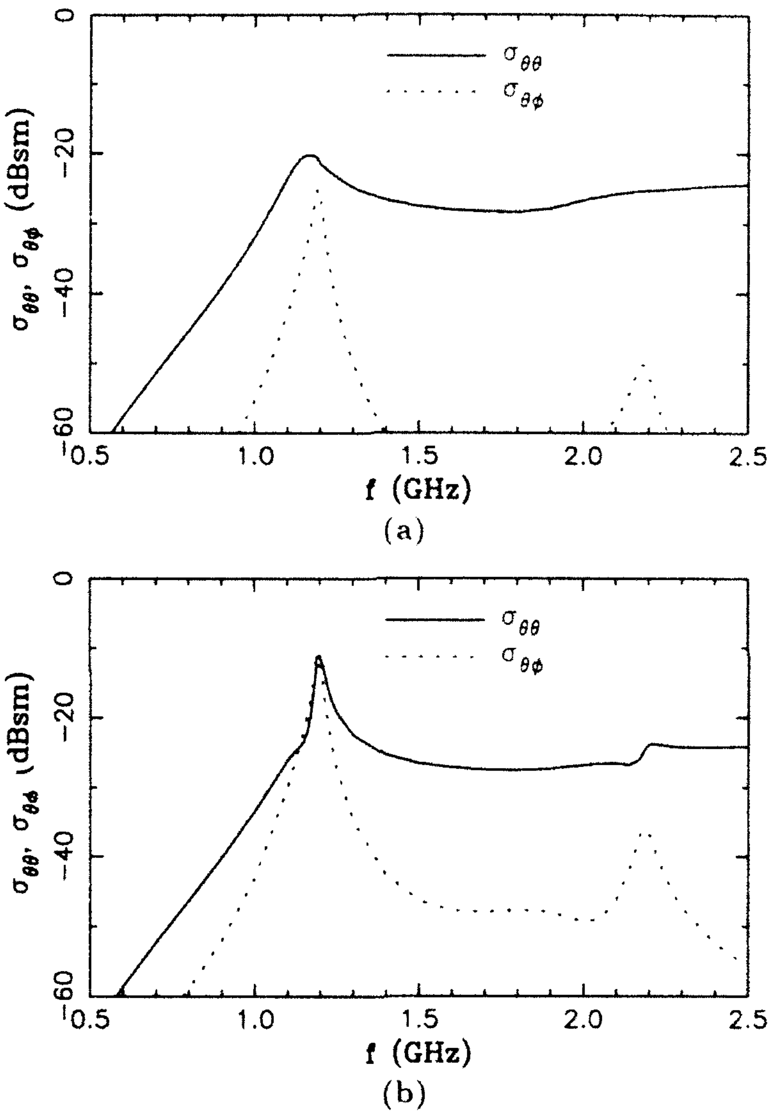

Figure 12: RCS of a pentagonal microstrip patch antenna for $Z_L = 50\,\Omega$ and $\theta_i = 0°$. (a) $\varphi_i = 0°$. (b) $\varphi_i = 45°$. The parameters are: $s = 80.13\,\mathrm{mm}$, $q = 61.22\,\mathrm{mm}$, $p =$ .57 mm, $h = 3.2\,\mathrm{mm}$, $\epsilon_r = 2.55$, $\tan\delta = 0.0018$, $a = 0.635\,\mathrm{mm}$, $b = 2.095\,\mathrm{mm}$.

field couples approximately equally to the first two modes. In Fig. 13 we show vector plots of the real and imaginary parts of the patch current density for the case of Fig. 12*a*, at a frequency $f = 1.194\,\text{GHz}$, which corresponds to the first peak of the $\sigma_{\theta\theta}$ curve. We note that near the coax probe the imaginary part of the current density is directed towards the feed point, as expected.

The results presented in Figs. 12 and 13 were obtained using a 156-element model of the pentagonal patch (which can be seen in Fig. 13) and a three-element model of the coax probe. The resulting size of the global impedance matrix in (46) was 220-by-220. The computation time was under 10 minutes per frequency point on an *i*486 PC running at 25 MHz.

5 Conclusion

We have developed an elegant and efficient integral equation approach for the RCS computation of coax-loaded microstrip patch antennas of arbitrary shape with substrates that may be electrically thick. The method has been validated for rectangular and circular patch antennas, for which results are available in the literature. New RCS results have also been presented for a pentagonal microstrip patch antenna designed to radiate a circularly polarized field from a single coax feed. With the approach presented here, microstrip patch antennas of various, possibly irregular shapes, embedded in a multilayered uniaxial substrate, may be analyzed within a single theoretical framework, using the same computer code.

A limitation inherent in this approach is the assumption of a laterally infinite substrate and ground plane. Although the patch current distribution is rather insensitive to the finite substrate and ground plane effects (assuming that $\theta_i < 90°$), the same cannot be said of the scattered field (and RCS), especially for θ_s approaching 90°, where the diffracted field from the edges of the substrate and ground plane may be the dominant contribution to the far field of the antenna. Also, the back lobes of the radiation pattern obviously cannot be predicted based on the infinite ground plane assumption. One way to remedy this is by using hybrid techniques, which combine the infinite-substrate integral equation method with the geometrical theory of diffraction

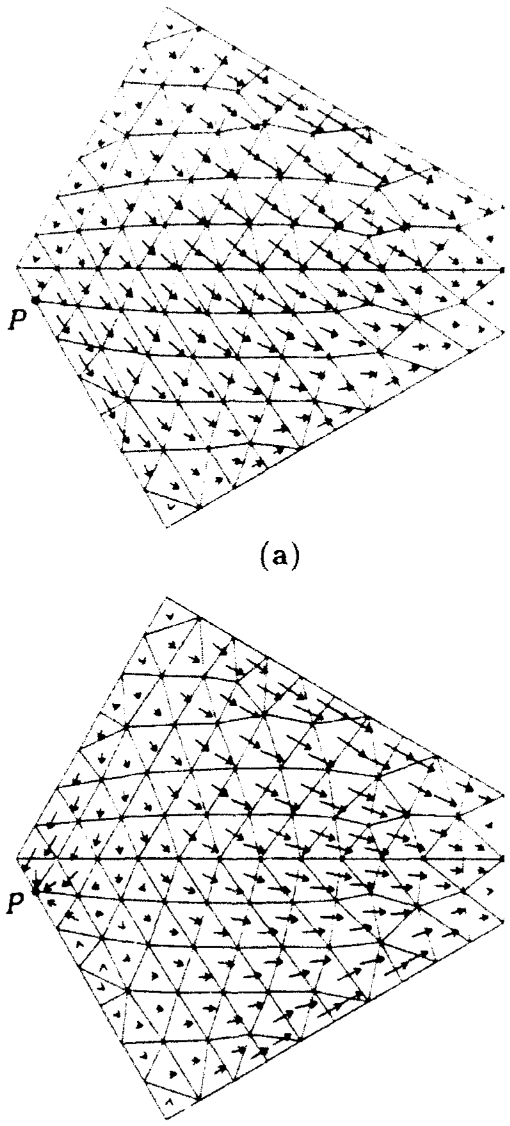

(a)

(b)

Figure 13: Vector plots of the current density on the pentagonal patch antenna for the case of Fig. 12*a*, at the frequency $f = 1.194\,\text{GHz}$. (*a*) Real part. (*b*) Imaginary part.

(GTD) [44] or the Fast Fourier Transform (FFT) method [45].

A Transmission Line Green's Functions

The voltage V_i and current I_i at a point z in the nth transmission line section containing a unit-strength current source i at z', as illustrated in Fig. 14, obey the equations [27, pp. 747]

$$\frac{d}{dz}V_i(z|z') = -jk_{zn}Z_n\, I_i(z|z') \tag{67}$$

$$\frac{d}{dz}I_i(z|z') = -jk_{zn}Y_n\, V_i(z|z') + \delta(z-z') \tag{68}$$

where k_{zn} is the propagation constant, Y_n (Z_n) is the characteristic admittance (impedance), and δ denotes the delta function. For notational simplicity, we omit here the

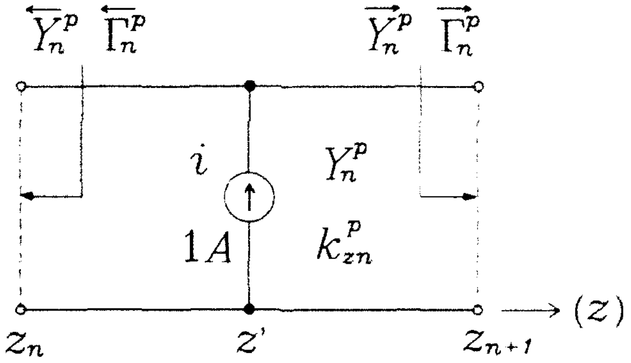

Figure 14: Transmission line section comprising a unit-strength current source.

superscript p (which stands for e or h), and we do not explicitly indicate the dependence of the voltage and current on the transverse wavenumber k_ρ, which determines k_{zn} through (15)-(16). From (67)-(68), $V_i(z|z')$ within the nth transmission line section containing a source may be expressed in the traveling-wave form

$$V_i(z|z') = \frac{e^{-jk_{zn}|z-z'|}}{2Y_n}\frac{\left[1+\overleftarrow{\Gamma}_n(z_0)e^{-j2k_{zn}(z_<-z_0)}\right]\left[1+\overrightarrow{\Gamma}_n(z_0)e^{j2k_{zn}(z_>-z_0)}\right]}{1-\overleftarrow{\Gamma}_n(z_0)\overrightarrow{\Gamma}_n(z_0)} \tag{69}$$

where $z_< = \min(z, z')$, $z_> = \max(z, z')$, z_0 is an arbitrary reference point within the nth section (which is usually set to z_n or z_{n+1}, whichever is more convenient), and $\overleftarrow{\Gamma}_n(z_0)$ and $\overrightarrow{\Gamma}_n(z_0)$ are the reflection coefficients 'looking to the left' and 'looking to the right,' respectively, at z_0. By means of the translation formula

$$\overset{\rightleftarrows}{\Gamma}_n(z) = \overset{\rightleftarrows}{\Gamma}_n(z_0)\, e^{\pm j2k_{zn}(z-z_0)} \tag{70}$$

where the upper and lower signs correspond to the right and left arrows, respectively, these reflection coefficients can be expressed in terms of the respective terminal reflection coefficients $\overleftarrow{\Gamma}_n$ and $\overrightarrow{\Gamma}_n$, which are related to the corresponding terminal admittances $\overleftarrow{Y}_n$ and $\overrightarrow{Y}_n$ (see Fig. 14) as

$$\overset{\rightleftarrows}{\Gamma}_n = \frac{Y_n - \overset{\rightleftarrows}{Y}_n}{Y_n + \overset{\rightleftarrows}{Y}_n}, \qquad \overset{\rightleftarrows}{Y}_n = Y_n \frac{1 - \overset{\rightleftarrows}{\Gamma}_n}{1 + \overset{\rightleftarrows}{\Gamma}_n} \tag{71}$$

For a transmission line section of a finite length d_n, a particularly convenient form of (69) is

$$V_i(z|z') = \frac{e^{-jk_{zn}|z-z'|}}{2Y_n} \frac{\left[1 + \overleftarrow{\Gamma}_n\, e^{-j2k_{zn}(z_< - z_n)}\right]\left[1 + \overrightarrow{\Gamma}_n\, e^{-j2k_{zn}(z_{n+1} - z_>)}\right]}{1 - \overleftarrow{\Gamma}_n \overrightarrow{\Gamma}_n\, e^{-j2k_{zn}d_n}} \tag{72}$$

which is obtained by letting $z_0 = z_n$ and using (70).

The voltage V_v and current I_v, excited by a unit-strength voltage source v, satisfy equations dual to (67)–(68), which are obtained from the latter by making the substitutions: $V_i \rightarrow I_v$, $I_i \rightarrow V_v$, $Z_n \rightarrow Y_n$, and $Y_n \rightarrow Z_n$. Furthermore, it can be shown that the following symmetry and reciprocity relations hold (cf. [16, p. 74], [27, p. 194])

$$V_i(z|z') = V_i(z'|z), \; I_v(z|z') = I_v(z'|z), \; V_v(z|z') = -I_i(z'|z) \tag{73}$$

As a result, $I_v(z|z')$ can be obtained from (72) by replacing in the latter Y_n by its inverse (which causes the reflection coefficients to change signs). $I_i(z|z')$ follows from (67) and (72), and $V_v(z|z')$ may then be obtained from the last relation in (73).

The voltage and current on the nth transmission line section that is source-free satisfy the homogeneous form of (67)-(68). From these equations, the voltage at any point z within the line section may be expressed in terms of the voltage $V(z_0)$ across one of its terminal pairs. The result is

$$V(z) = V(z_0)\,\frac{e^{-jk_{zn}|z-z'|}}{1+\overset{\rightleftarrows}{\Gamma}_n\,e^{-j2k_{zn}d_n}}\left[1+\overset{\rightleftarrows}{\Gamma}_n\,e^{-j2k_{zn}\,\text{[illegible]}}\right] \qquad (74)$$

where $z_0 = z_n$ or $z_0 = z_{n+1}$ (see Fig. 11), depending on whether the source is located to the left or to the right, respectively, of the line section, and where the upper (lower) arrow corresponds to $z > z_0$ ($z < z_0$). We have omitted the subscript of V in (74), because the latter applies irrespective of the nature of the source, and dropped z' from its argument, because (74) only implicitly depends on the source location, which is outside the nth line section. The current $I(z)$ corresponding to (74) may be obtained by substituting the latter into (67).

Finally, we note that (70)-(71) are easily implemented in a recursive computer routine to determine the leftward and rightward reflection coefficients needed in (72) and (74). The computations proceed from the outward-looking reflection coefficients in the top and bottom transmission line sections (see Fig. 3). Observe that the exponential functions encountered in (70), (72), and (74) have nonincreasing magnitudes, so there is no danger of overflow. When the nth transmission line section extends to positive (negative) infinity along the z axis, the reflection coefficient $\overrightarrow{\Gamma}_n$ ($\overleftarrow{\Gamma}_n$) is set to zero in (72) and (74).

B Fourier Transform of a Triangle Shape Function

The Fourier transform of a shape function L_i associated with a triangular element S_n is given as

$$\tilde{L}_i = \int_{S_n} L_i\, e^{j\boldsymbol{k}_\rho\cdot\boldsymbol{\rho}}\, dS \qquad (75)$$

where $\boldsymbol{k}_\rho = \hat{\boldsymbol{u}}k_\rho$. To evaluate the integral in (75), it is helpful to first convert it to a line integral around the boundary contour, ∂S_n, of S_n (cf. [17], [18], [19]). This is most easily accomplished by noting that [50]

$$e^{j\mathbf{k}_\rho\cdot\boldsymbol{\rho}} = \nabla_s\cdot\left(\hat{\boldsymbol{u}}\frac{e^{j\mathbf{k}_\rho\cdot\boldsymbol{\rho}}}{jk_\rho}\right) \tag{76}$$

and by making use of the divergence theorem. As a result, when $k_\rho \neq 0$, we obtain

$$\dot{L}_i = -\frac{1}{2Ak_\rho^2}\oint_{\partial S_n}(2jk_\rho A L_i + \hat{\boldsymbol{v}}\cdot\boldsymbol{\ell}_i)\,e^{j\mathbf{k}_\rho\cdot\boldsymbol{\rho}}\,\hat{\boldsymbol{u}}\cdot\hat{\boldsymbol{n}}\,d\ell \tag{77}$$

where $\hat{\boldsymbol{v}} = \hat{\boldsymbol{z}}\times\hat{\boldsymbol{u}}$ and $\hat{\boldsymbol{n}}$ denotes a unit vector normal to ∂S_n at ℓ in the plane and pointing out of S_n. The integral in (77) is easily evaluated in the local coordinates, if one notes that when ℓ is on edge i, $\hat{\boldsymbol{n}} = \hat{\boldsymbol{n}}_i$, $0 \leq L_k \leq 1$, $L_i = 0$, $L_j = 1 - L_k$, and $d\ell = \ell_i dL_k$ (see Fig. 4). Also, in that case $\boldsymbol{\rho} = \boldsymbol{\rho}_j + \boldsymbol{\varrho}_j$, where $\boldsymbol{\varrho}_j$ is a vector from node j to the point ℓ on edge i of the element. The resulting closed-form expression for $\dot{L}_i$ is given in (65).

Acknowledgments

The authors are indebted to Dr. Dalian Zheng for his contributions during the early stages of this work, to Mr. Min-Hua Ho for his help in the preparation of the figures, to Dr. James T. Aberle for providing in a computer-readable form his RCS results included in Fig. 11, and to Dr. John L. Volakis for inviting them to write this paper. This work was supported in part by the Office of Naval Research under Contract N00014-90-J-1197.

References

[1] E. H. Newman and D. Forrai, "Scattering from a microstrip patch," *IEEE Trans. Antennas Propagat.*, vol. AP-35, pp. 245–251, Mar. 1987.

[2] D. M Pozar, "Radiation and scattering from a microstrip patch on a uniaxial substrate," *IEEE Trans. Antennas Propagat.*, vol. AP-35, pp. 613–621, June

1987.

[3] D. R. Jackson, "The RCS of a rectangular microstrip patch in a substrate-superstrate geometry," *IEEE Trans. Antennas Propagat.*, vol. 38, pp. 1-8, Jan. 1990.

[4] J. T. Aberle, D. M. Pozar, and C. R. Birtcher, "Evaluation of input impedance and radar cross section of probe-fed microstrip patch elements using an accurate feed model," *IEEE Trans. Antennas Propagat.*, vol. 39, pp. 1691-1696, Dec. 1991.

[5] A. S. King and W. J. Bow, "Scattering from a finite array of microstrip patches," *IEEE Trans. Antennas Propagat.*, vol. 40, pp. 770-771, July 1992.

[6] J.-M. Jin and J. L. Volakis, "A hybrid finite element method for scattering and radiatio: by microstrip patch antennas and arrays residing in a cavity," *IEEE Trans. Antennas Propagat.*, vol. 39, pp. 1598-1604, Nov. 1991.

[7] R. F. Harrington, *Field Computation by Moment Methods*. New York: Macmillan, 1968. Reprinted by Krieger Publishing Co., Melbourne, FL, 1982.

[8] P. Pichon, J. R. Mosig, and A. Papiernik, "Input impedance of arbitrarily shaped microstrip antennas," *Electron. Lett.*, vol. 24, pp. 1214-1215, Sept. 1988.

[9] M. J. Notter and C. G. Parini, "Modelling of arbitrary shaped M/S patch antennas in multiple substrate media," *Electron. Lett.*, vol. 26, pp. 50-52, 1990.

[10] D. Zheng and K. A. Michalski, "Analysis of arbitrarily shaped coax-fed microstrip antennas—A hybrid mixed-potential integral equation approach," *Microwave & Opt. Technol. Lett.*, vol. 3, pp. 200-203, June 1990.

[11] D. Zheng and K. A. Michalski, "Analysis of arbitrarily shaped coax-fed microstrip antennas with thick substrates," *Electron. Lett.*, vol. 26, no. 12, pp. 794-795, 1990.

[12] D. Zheng and K. A. Michalski, "Analysis of coaxially fed microstrip antennas of arbitrary shape with thick substrates," *J. Electromagn. Waves Appl.*, vol. 5, no. 12, pp. 1303–1327, 1991.

[13] K.-L. Wu, J. Litva, R. Fralich, and C. Wu, "Full-wave analysis of arbitrarily shaped line-fed microstrip antennas using triangular finite-element method," *IEE Proc., Pt. H*, vol. 138, pp. 421–428, Oct. 1991.

[14] K. A. Michalski and D. Zheng, "Analysis of microstrip resonators of arbitrary shape," *IEEE Trans. Antennas Propagat.*, vol. 40, pp. 112–119, Jan. 1992.

[15] T. K. Sarkar, P. Midya, Z. A. Maricevic, M. Kahrizi, S. M. Rao, and A. R. Djordjevic, "Analysis of arbitrarily shaped microstrip patch antennas using the Sommerfeld formulation," *Int. J. Microwave Millimeter-Wave Computer-Aided Eng.*, vol. 2, no. 3, pp. 168–178, 1992.

[16] F. A. Monferrer, A. A. Kishk, and A. W. Glisson, "Green's function analysis of planar circuits in a two-layer grounded medium," *IEEE Trans. Antennas Propagat.*, vol. 40, pp. 690–696, June 1992.

[17] D. C. Chang and J. X. Zheng, "Electromagnetic modeling of passive circuit elements in MMIC," *IEEE Trans. Microwave Theory Tech.*, vol. 40, pp. 1741–1747, Sept. 1992.

[18] S. M. Rao, D. R. Wilton, and A. W. Glisson, "Electromagnetic scattering by surfaces of arbitrary shape," *IEEE Trans. Antennas Propagat.*, vol. AP-30, pp. 409–418, May 1982.

[19] R. C. Hall and J. R. Mosig, "The analysis of coaxially fed microstrip antennas with electrically thick substrates," *Electromagn.*, vol. 9, no. 4, pp. 367–384, 1989.

[20] R. F. Harrington, *Time-Harmonic Electromagnetic Field*. New York: McGraw-Hill, 1961.

[21] M. Abramowitz and I. A. Stegun, eds., *Handbook of Mathematical Functions*. New York: Dover, 1965.

[22] K. A. Michalski, "The mixed-potential electric field integral equation for objects in layered media," *Arch. Elek. Übertragung.*, vol. 39, pp. 317–322, Sept.-Oct. 1985.

[23] J. R. Mosig, "Arbitrarily shaped microstrip structures and their analysis with a mixed potential integral equation," *IEEE Trans. Microwave Theory Tech.*, vol. 36, pp. 314–323, Feb. 1988.

[24] K. A. Michalski and D. Zheng, "Electromagnetic scattering and radiation by surfaces of arbitrary shape in layered media, Part I: Theory," *IEEE Trans. Antennas Propagat.*, vol. 38, pp. 335–344, Mar. 1990.

[25] K. A. Michalski and D. Zheng, "Electromagnetic scattering and radiation by surfaces of arbitrary shape in layered media. Part II: Implementation and results for contiguous half-spaces," *IEEE Trans. Antennas Propagat.*, vol. 38, pp. 345–352, Mar. 1990.

[26] W. A. Johnson, D. R. Wilton, and R. M. Sharpe, "Modeling scattering from and radiation by arbitrarily shaped objects with the electric field integral equation triangular surface patch code," *Electromagn.*, vol. 10, no. 1-2, pp. 41–63, 1990.

[27] L. B. Felsen and N. Marcuvitz, *Radiation and Scattering of Waves.* Englewood Cliffs, N.J.: Prentice Hall, 1973.

[28] W. C. Chew, "A quick way to approximate a Sommerfeld-Weyl-type integral," *IEEE Trans. Antennas Propagat.*, vol. 36, pp. 1654–1657, Nov. 1988.

[29] E. F. Knott, J. F. Shaeffer, and M. T. Tuley, *Radar Cross Section: Its Prediction, Measurement and Reduction.* Norwood, MA: Artech House, 1985.

[30] J. Van Bladel, *Electromagnetic Fields.* New York: Hemisphere, 1985.

[31] D. R. Wilton, "Review of current status and trends in the use of integral equations in computational electromagnetics," *Electromagn.*, vol. 12, pp. 287–341, July-Dec. 1992.

[32] L. Lapidus and G. F. Pinder, *Numerical Solution of Partial Differential Equations in Science and Engineering.* New York: Wiley, 1982.

[33] D. R. Tanner and A. F. Peterson, "Vector expansion functions for the numerical solution of Maxwell's equations," *Microwave & Opt. Technol. Lett.*, vol. 2, pp. 331–334, Sept. 1989.

[34] O. C. Zienkiewicz and K. Morgan, *Finite Elements and Approximation.* New York: Wiley, 1983.

[35] M. F. Costa and R. F. Harrington, "Minimization of radiation from computer system," in *Proc. Int'l Electrical Electronics Conference and Exposition*, (Toronto, Canada), pp. 660–665, Sept. 1983.

[36] S. U. Hwu, D. R. Wilton, and S. M. Rao, "Electromagnetic scattering and radiation by arbitrary conducting wire surface configurations," in *Digest IEEE AP-S Int. Symp.*, (Syracuse, NY), pp. 890–893, June 1988.

[37] S. D. Conte and C. de Boor, *Elementary Numerical Analysis: An Algorithmic Approach.* New York: McGraw-Hill, 1980.

[38] D. R. Wilton, S. M. Rao, A. W. Glisson, D. H. Schaubert, O. M. Al-Bundak, and C. M. Butler, "Potential integrals for uniform and linear source distributions on polygonal and polyhedral domains," *IEEE Trans. Antennas Propagat.*, vol. AP-32, pp. 276–281, Mar. 1984.

[39] J. R. Mosig and F. E. Gardiol, "A dynamical radiation model for microstrip structures," in *Adv. Electron. Electron Phys.* (P. W. Hawkes, ed.), vol. 59, pp. 139–237, New York: Academic Press, 1982.

[40] J. R. Mosig, "Integral equation technique," in *Numerical Techniques for Microwave and Millimeter-Wave Passive Structures* (T. Itoh, ed.), pp. 133–213, New York: Wiley, 1989.

[41] J. R. Mosig, R. C. Hall, and F. E. Gardiol, "Numerical analysis of microstrip patch antennas," in *Handbook of Microstrip Antennas* (J. R. James and P. S. Hall, eds.), pp. 391–453, London: Peter Peregrinus, 1989.

[42] J. T. Aberle, *Analysis of probe-fed circular microstrip antennas*. PhD thesis, Univ. of Massachussetts, Amherst, MA, 1989.

[43] M. Haneishi and Y. Suzuki, "Circular polarization and bandwidth," in *Handbook of Microstrip Antennas* (J. R. James and P. S. Hall, eds.), pp. 219–274, London: Peter Peregrinus, 1989.

[44] S. A. Bokhari, J. R. Mosig, and F. E. Gardiol, "Hybrid approach to compute radiation pattern of finite microstrip antennas," *Electron. Lett.*, vol. 27, pp. 2091–2093, Oct. 1991.

[45] S. A. Bokhari, J. R. Mosig, and F. E. Gardiol, "Radiation pattern computation of microstrip antennas on finite size ground planes," *IEE Proc., Pt. H*, vol. 139, pp. 278–286, June 1992.

[46] P. E. Mayes, *Electromagnetics for Engineers*. Dept. of Electrical and Computer Eng., Univ. of Illinois, Urbana, IL: P. E. Mayes, 1965.

[47] B. Houshmand, W. C. Chew, and S. W. Lee, "Fourier transform of a linear distribution with triangular support and its applications in electromagnetics," *IEEE Trans. Antennas Propagat.*, vol. 39, pp. 252–254, Feb. 1991.

[48] K. McInturff and P. S. Simon, "The Fourier transform of linearly varying functions with polygonal support," *IEEE Trans. Antennas Propagat.*, vol. 39, pp. 1441–1443, Sept. 1991.

[49] T.-S. Horng, N. G. Alexopoulos, S.-C. Wu, and H.-Y. Yang, "Full-wave spectral analysis for open microstrip discontinuities of arbitrary shape including radiation and surface-wave losses," *Int. J. Microwave Millimeter-Wave Computer-Aided Eng.*, vol. 2, no. 4, pp. 224–240, 1992.

[50] D. R. Wilton, private communication.

WAVEGUIDE EXCITED MICROSTRIP PATCH ANTENNA - THEORY AND EXPERIMENT

M.-H. Ho, K. A. Michalski, and K. Chang

Electromagnetics & Microwave Laboratory
Department of Electrical Engineering
Texas A&M University
College Station, Texas 77843-3128, USA

ABSTRACT

An arbitrarily shaped microstrip patch antenna excited through an arbitrarily shaped aperture in the mouth of a rectangular waveguide is investigated theoretically and experimentally. The metallic patch resides on a dielectric substrate grounded by the waveguide flange, and may be covered by a dielectric superstrate. The substrate (and superstrate, if present) consists of one or more planar, homogeneous layers, which may exhibit uniaxial anisotropy. The analysis is based on the space domain integral equation approach. More specifically, the Green's functions for the layered medium and the waveguide are used to formulate a coupled set of integral equations for the patch current and the aperture electric field. The layered medium Green's function is expressed in terms of Sommerfeld-type integrals and the waveguide Green's function in terms of Floquet series, which are accelerated to reduce the computational effort. The coupled integral equations are solved by the method of moments using vector basis functions defined over triangular subdomains. The dominant mode reflection coefficient in the waveguide and the far field radiation patterns are then found from the computed aperture field and patch current distributions. The radar cross section (RCS) of a plane-wave excited structure is obtained in a like manner. Sample numerical results are presented and are found to be in good agreement with measurements and with published data.

1 Introduction

Microstrip patch antennas, which belong to a large class of printed circuit antennas, are widely used in the microwave frequency range, both as single elements and (more often) in array configurations. Their advantages are well known: low cost, conformity, ease of fabrication and integration, reproducibility, ruggedness, light weight, and low profile [1], [2]. In recent years, the utilization of millimeterwave systems, with smaller, lighter components and antennas, has provided a wider bandwidth, and consequently higher data rate communication and better resolution than microwave systems [3], [4]. However, the feed structures that operate well at microwave frequencies are not always viable in the millimeterwave range. For example, microstrip line losses become significant and coaxial feed components are not available above about 50 GHz, which renders the direct feed techniques impractical in this frequency range. On the other hand, since the waveguide bulkiness becomes less of a factor, while its losses remain smaller than those of a microstrip line [5], the indirect waveguide feed becomes an attractive option for millimeterwave antennas and antenna arrays [6]. Moreover, in some applications the aluminum waveguide may also serve as a heat sink and support for active devices that may be integrated with the antenna. Another antenna configuration that possesses the advantages listed above is a waveguide-fed slot antenna. Its gain, however, is significantly lower than that of a waveguide-excited microstrip patch.

In this paper, we present a rigorous integral equation analysis of a waveguide-fed microstrip patch antenna, as illustrated in Fig. 1. The arbitrarily shaped microstrip patch is coupled to the rectangular waveguide through an aperture, which may also be of arbitrary shape. The dielectric medium above the ground plane may consist of one or more planar, homogeneous layers, which may exhibit uniaxial anisotropy. The nth layer is characterized by the permittivity and permeability dyadics

$$\underline{\underline{\boldsymbol{\epsilon}}}_n = \underline{\underline{\boldsymbol{I}}}_t \epsilon_{tn} + \hat{\boldsymbol{z}}\hat{\boldsymbol{z}}\epsilon_{zn} \qquad \underline{\underline{\boldsymbol{\mu}}}_n = \underline{\underline{\boldsymbol{I}}}_t \mu_{tn} + \hat{\boldsymbol{z}}\hat{\boldsymbol{z}}\mu_{zn} \tag{1}$$

where $\underline{\underline{\boldsymbol{I}}}_t$ is the unit dyadic transverse to z, and ϵ_{tn} (μ_{tn}) and ϵ_{zn} (μ_{zn}) denote, respectively, the transverse and longitudinal dielectric (magnetic) constants relative to free

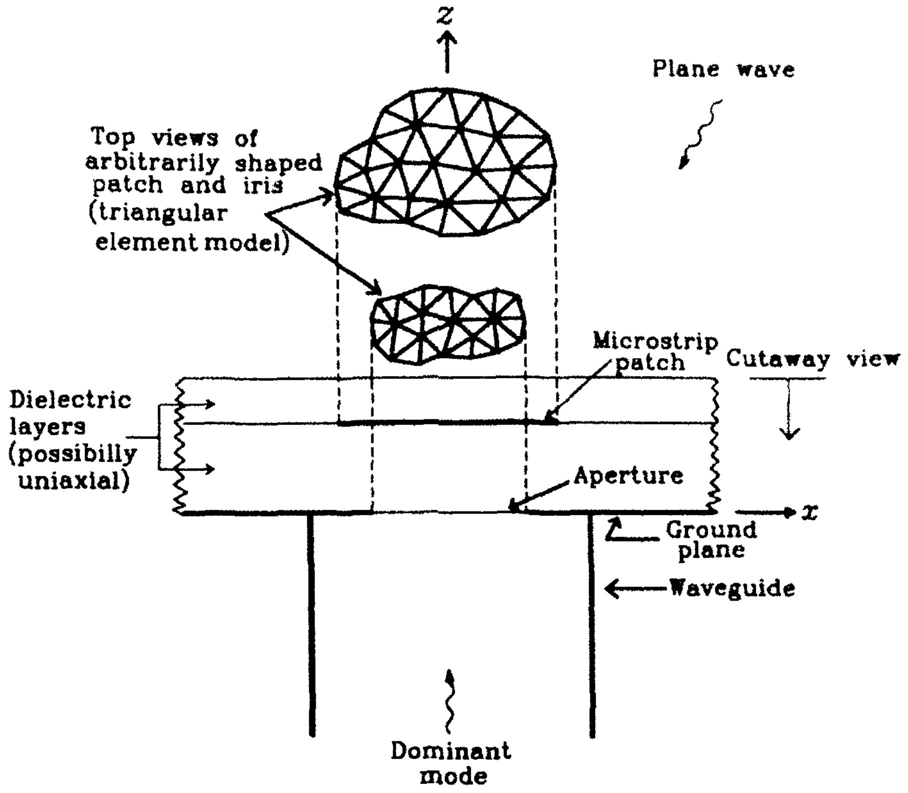

Figure 1: Geometry of a waveguide-fed microstrip patch antenna.

space. Observe that we distinguish dyadics by double underlines and unit vectors by carets. The free space permeability and permittivity will be denoted by μ_o and ϵ_o, respectively. For each layer, we also introduce its electric and magnetic anisotropy ratios, ν_n^e and ν_n^h, respectively, given as

$$\nu_n^e = \frac{\epsilon_{zn}}{\epsilon_{tn}}, \qquad \nu_n^h = \frac{\mu_{zn}}{\mu_{tn}} \tag{2}$$

The structure is excited either by the dominant (TE_{10}) waveguide mode or by a plane wave incident in the upper-half space. The primary quantities to be computed are the aperture field and patch current distributions. From these, other quantities of interest will be found, including the dominant mode reflection coefficient, the far field radiation patterns, and the radar cross section (RCS). Although attention is limited to a single antenna element, it is expected that the results of this study will also be useful in the analysis, by an approximate technique, of finite waveguide-fed antenna arrays.

The remainder of this paper is organized as follows. In Sec. 2 we formulate coupled integral equations for the patch current and the aperture electric field, where the latter is represented by an equivalent magnetic current. The kernels of these integral equations are expressed in terms of the voltage and current Green's functions of a transmission line network analog of the layered medium, which is discussed in Appendix A. In Sec. 3 we give the numerical procedure for the solution of the integral equations, and in Sec. 4 we describe the experimental verification of the theory. We present sample computed and measured results in Sec. 5, and give conclusions in Sec. 6.

2 Formulation

2.1 Integral equations

To facilitate the analysis of the structure shown in Fig. 1, we invoke the *equivalence* principle [7] to in effect decouple the original problem into two simpler ones, referred to as the 'interior' (inside the shorted waveguide) and 'exterior' (above the ground plane) problems, as illustrated in Fig. 2. This decoupling is achieved by first shorting the aperture S_a through which the two regions interact, and then placing over it an equivalent magnetic current $\boldsymbol{M}_S$, which represents the tangential electric field in the aperture. The negative of $\boldsymbol{M}_S$ is placed on the opposite side of the shorted aperture, thus explicitly enforcing the continuity of the tangential electric field across S_a. In the equivalent problem, the effect of the metallic patch S_p is replaced by an equivalent electric current $\boldsymbol{J}_S$.

The conditions of vanishing tangential electric field on the patch (which is assumed to be perfectly conducting) and continuity of the tangential magnetic field across the aperture may now be stated as

$$\hat{\boldsymbol{z}} \times \left[\boldsymbol{E}^s_+(\boldsymbol{r}) + \boldsymbol{E}^i_+(\boldsymbol{r})\right] = \boldsymbol{O}, \quad \boldsymbol{r} \in S_p \tag{3}$$

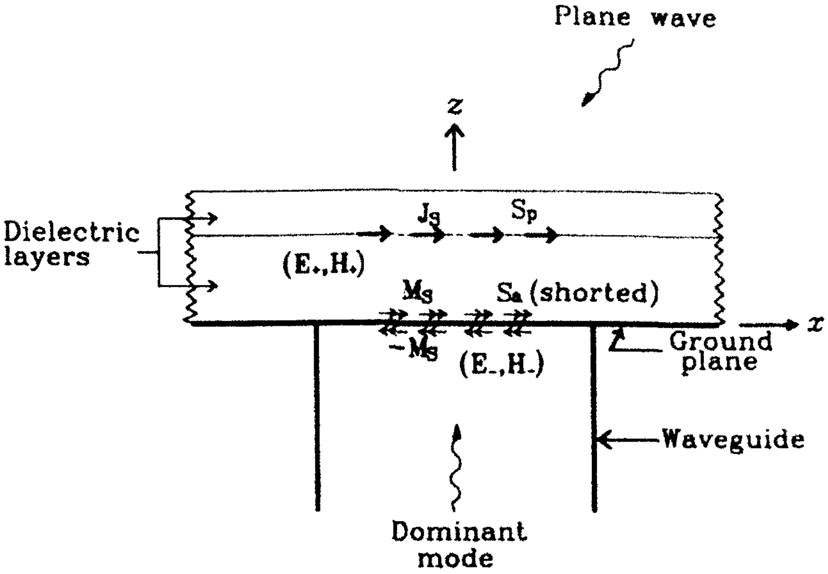

Figure 2: Problem equivalent to that in Fig. 1.

$$\hat{\boldsymbol{z}} \times \left[\boldsymbol{H}^s_+(\boldsymbol{r}) + \boldsymbol{H}^i_+(\boldsymbol{r})\right] = \hat{\boldsymbol{z}} \times \left[\boldsymbol{H}^s_-(\boldsymbol{r}) + \boldsymbol{H}^i_-(\boldsymbol{r})\right], \quad \boldsymbol{r} \in S_a \tag{4}$$

where the subscripts + and − refer to, respectively, the exterior and the interior regions, $\boldsymbol{r}$ is the position vector, $(\boldsymbol{E}^i, \boldsymbol{H}^i)$ are the the 'short-circuit' electric and magnetic fields of known sources, computed in the absence of the patch and with the aperture shorted [8], and $(\boldsymbol{E}^s, \boldsymbol{H}^s)$ are the 'scattered' fields produced by $\boldsymbol{J}_S$ and $\boldsymbol{M}_S$. Rearranging (3) and (4), we obtain

$$-\hat{\boldsymbol{z}} \times \boldsymbol{E}^s_+(\boldsymbol{r}) = \hat{\boldsymbol{z}} \times \boldsymbol{E}^i_+(\boldsymbol{r}), \quad \boldsymbol{r} \in S_p \tag{5}$$

$$-\hat{\boldsymbol{z}} \times \left[\boldsymbol{H}^s_+(\boldsymbol{r}) - \boldsymbol{H}^s_-(\boldsymbol{r})\right] = \hat{\boldsymbol{z}} \times \left[\boldsymbol{H}^i_+(\boldsymbol{r}) - \boldsymbol{H}^i_-(\boldsymbol{r})\right], \quad \boldsymbol{r} \in S_a \tag{6}$$

The scattered fields in (5)–(6) can be expressed in terms of the dyadic and scalar kernels of the exterior and interior problem as [9]

$$\begin{aligned} \boldsymbol{E}^s_+(\boldsymbol{r}) &= -\int_{S_p} \underline{\underline{\boldsymbol{G}}}^A(\boldsymbol{r}\,|\,\boldsymbol{r}')\cdot \boldsymbol{J}_S(\boldsymbol{\rho}')\,dS' - \boldsymbol{\nabla}\int_{S_p} G^{\phi}(\boldsymbol{r}\,|\,\boldsymbol{r}')\boldsymbol{\nabla}'\cdot \boldsymbol{J}_S(\boldsymbol{\rho}')\,dS' \\ &\quad + \int_{S_a} \underline{\underline{\boldsymbol{G}}}^{EM}(\boldsymbol{r}\,|\,\boldsymbol{r}')\cdot \boldsymbol{M}_S(\boldsymbol{\rho}')dS' \end{aligned} \tag{7}$$

$$\boldsymbol{H}^s_+(\boldsymbol{r}) = \int_{S_p} \underline{\underline{\boldsymbol{G}}}^{HJ}(\boldsymbol{r}\,|\,\boldsymbol{r}')\cdot \boldsymbol{J}_S(\boldsymbol{\rho}')\,dS' - \int_{S_a} \underline{\underline{\boldsymbol{G}}}^{F+}(\boldsymbol{r}\,|\,\boldsymbol{r}')\cdot \boldsymbol{M}_S(\boldsymbol{\rho}')\,dS'$$

$$- \nabla \int_{S_a} G^{\vartheta +}(\boldsymbol{r}\,|\,\boldsymbol{r}')\,\nabla'\cdot \boldsymbol{M}_S(\boldsymbol{\rho}')\,dS' \tag{8}$$

$$\begin{aligned} \boldsymbol{H}^s_-(\boldsymbol{r}) &= \int_{S_a} \underline{\underline{\boldsymbol{G}}}^{F-}(\boldsymbol{r}\,|\,\boldsymbol{r}')\cdot \boldsymbol{M}_S(\boldsymbol{\rho}')dS' \\ &\quad + \nabla \int_{S_a} G^{\vartheta -}(\boldsymbol{r}\,|\,\boldsymbol{r}')\,\nabla'\cdot \boldsymbol{M}_S(\boldsymbol{\rho}')\,dS' \end{aligned} \tag{9}$$

where primes indicate source coordinates and $\boldsymbol{\rho}$ is the projection of $\boldsymbol{r}$ on the xy plane. Upon substituting (7)–(9) into (5)–(6), we obtain a coupled set of integral equations for the unknown equivalent currents $\boldsymbol{J}_S$ and $\boldsymbol{M}_S$, given as

$$\left\langle \underline{\underline{\boldsymbol{G}}}_t^{A} \,;\, \boldsymbol{J}_S \right\rangle'_{S_p} + \nabla_t \left\langle G^{\phi} \,,\, \nabla'_t\cdot \boldsymbol{J}_S \right\rangle'_{S_p} - \left\langle \underline{\underline{\boldsymbol{G}}}_t^{EM} \,;\, \boldsymbol{M}_S \right\rangle'_{S_a} = \boldsymbol{E}^i_{t,+}(\boldsymbol{r}), \quad \boldsymbol{r} \in S_p \tag{10}$$

$$\begin{aligned} &\left\langle \underline{\underline{\boldsymbol{G}}}_t^{HJ} \,;\, \boldsymbol{J}_S \right\rangle'_{S_p} - \left\langle \underline{\underline{\boldsymbol{G}}}_t^{F+} + \underline{\underline{\boldsymbol{G}}}_t^{F-} \,;\, \boldsymbol{M}_S \right\rangle'_{S_a} \\ &- \nabla_t \left\langle G^{\vartheta +} + G^{\vartheta -} \,,\, \nabla'_t\cdot \boldsymbol{M}_S \right\rangle'_{S_a} = \boldsymbol{H}^i_{t,+}(\boldsymbol{r}) - \boldsymbol{H}^i_{t,-}(\boldsymbol{r}), \quad \boldsymbol{r} \in S_a \end{aligned} \tag{11}$$

Here, we have introduced the notation $\langle\,;\,\rangle$ for an integral of a product of functions separated by the comma. The dot over the comma signifies a 'dot product' of vector arguments, while the prime over $\rangle$ indicates that the integration is over the primed coordinates. The subscript t distinguishes components transverse to $\hat{\boldsymbol{z}}$, and the subscripts S_p and S_a indicate the integration domains (see Fig. 2). The dyadic kernels in (10)–(11) are given as [9]

$$\underline{\underline{\boldsymbol{G}}}_t^{A}(\boldsymbol{r}\,|\,\boldsymbol{r}') = \underline{\underline{\boldsymbol{I}}}_t G^{A}_{xx}(\boldsymbol{r}\,|\,\boldsymbol{r}') \tag{12}$$

$$\begin{aligned} \underline{\underline{\boldsymbol{G}}}_t^{EM}(\boldsymbol{r}\,|\,\boldsymbol{r}') &= (\hat{\boldsymbol{x}}\hat{\boldsymbol{x}} - \hat{\boldsymbol{y}}\hat{\boldsymbol{y}})G^{EM}_{xx}(\boldsymbol{r}\,|\,\boldsymbol{r}') \\ &\quad + \hat{\boldsymbol{x}}\hat{\boldsymbol{y}}G^{EM}_{xy}(\boldsymbol{r}\,|\,\boldsymbol{r}') + \hat{\boldsymbol{y}}\hat{\boldsymbol{x}}G^{EM}_{yx}(\boldsymbol{r}\,|\,\boldsymbol{r}') \end{aligned} \tag{13}$$

$$\begin{aligned} \underline{\underline{\boldsymbol{G}}}_t^{HJ}(\boldsymbol{r}\,|\,\boldsymbol{r}') &= (-\hat{\boldsymbol{x}}\hat{\boldsymbol{x}} + \hat{\boldsymbol{y}}\hat{\boldsymbol{y}})G^{EM}_{xx}(\boldsymbol{r}'\,|\,\boldsymbol{r}) \\ &\quad - \hat{\boldsymbol{x}}\hat{\boldsymbol{y}}G^{EM}_{yx}(\boldsymbol{r}'\,|\,\boldsymbol{r}) - \hat{\boldsymbol{y}}\hat{\boldsymbol{x}}G^{EM}_{xy}(\boldsymbol{r}'\,|\,\boldsymbol{r}) \end{aligned} \tag{14}$$

$$\underline{\underline{\boldsymbol{G}}}_t^{F+}(\boldsymbol{r}\,|\,\boldsymbol{r}') = \underline{\underline{\boldsymbol{I}}}_t G^{F+}_{xx}(\boldsymbol{r}\,|\,\boldsymbol{r}') \tag{15}$$

$$\underline{\underline{G}}_t^{F-}(\boldsymbol{r}\,|\,\boldsymbol{r}') = \hat{\boldsymbol{x}}\hat{\boldsymbol{x}}G_{xx}^{F-}(\boldsymbol{r}\,|\,\boldsymbol{r}') + \hat{\boldsymbol{y}}\hat{\boldsymbol{y}}G_{yy}^{F-}(\boldsymbol{r}\,|\,\boldsymbol{r}') \tag{16}$$

where

$$G_{xx}^{A}(\boldsymbol{r}\,|\,\boldsymbol{r}') = S_0\left\{V_i^h(k_\rho; z\,|\,z')\right\} \tag{17}$$

$$G_{xx}^{EM}(\boldsymbol{r}\,|\,\boldsymbol{r}') = -\frac{\sin 2\zeta}{2}S_2\left\{\frac{V_v^e(k_\rho; z\,|\,z') - V_v^h(k_\rho; z\,|\,z')}{k_\rho^2}\right\} \tag{18}$$

$$\begin{aligned} G_{xy}^{EM}(\boldsymbol{r}\,|\,\boldsymbol{r}') \; &= \; \frac{\cos 2\zeta}{2}S_2\left\{\frac{V_v^e(k_\rho; z\,|\,z') - V_v^h(k_\rho; z\,|\,z')}{k_\rho^2}\right\} \\ &\quad + \frac{1}{2}S_0\left\{V_v^e(k_\rho; z\,|\,z') + V_v^h(k_\rho; z\,|\,z')\right\} \end{aligned} \tag{19}$$

$$\begin{aligned} G_{yx}^{EM}(\boldsymbol{r}\,|\,\boldsymbol{r}') \; &= \; \frac{\cos 2\zeta}{2}S_2\left\{\frac{V_v^e(k_\rho; z\,|\,z') - V_v^h(k_\rho; z\,|\,z')}{k_\rho^2}\right\} \\ &\quad - \frac{1}{2}S_0\left\{V_v^e(k_\rho; z\,|\,z') + V_v^h(k_\rho; z\,|\,z')\right\} \end{aligned} \tag{20}$$

$$G_{xx}^{F_+}(\boldsymbol{r}\,|\,\boldsymbol{r}') = S_0\left\{I_v^e(k_\rho; z\,|\,z')\right\} \tag{21}$$

$$G_{xx}^{F_-}(\boldsymbol{r}\,|\,\boldsymbol{r}') = \left[\mathcal{F}_{mn}^{\binom{x'}{y'}} - \mathcal{F}_{mn}^{\binom{a-x'}{y'}} - \mathcal{F}_{mn}^{\binom{a-x'}{b-y'}} + \mathcal{F}_{mn}^{\binom{x'}{b-y'}}\right]\left\{I_v^e(k_\rho; z\,|\,z')\right\} \tag{22}$$

$$G_{yy}^{F_-}(\boldsymbol{r}\,|\,\boldsymbol{r}') = \left[\mathcal{F}_{mn}^{\binom{x'}{y'}} + \mathcal{F}_{mn}^{\binom{a-x'}{y'}} - \mathcal{F}_{mn}^{\binom{a-x'}{b-y'}} - \mathcal{F}_{mn}^{\binom{x'}{b-y'}}\right]\left\{I_v^e(k_\rho; z\,|\,z')\right\} \tag{23}$$

and the scalar kernels are given as

$$G^{\phi}(\boldsymbol{r}\,|\,\boldsymbol{r}') = S_0\left\{\frac{V_i^h(k_\rho; z\,|\,z') - V_i^e(k_\rho; z\,|\,z')}{k_\rho^2}\right\} \tag{24}$$

$$G^{\vartheta_+}(\boldsymbol{r}\,|\,\boldsymbol{r}') = S_0\left\{\frac{I_v^e(k_\rho; z\,|\,z') - I_v^h(k_\rho; z\,|\,z')}{k_\rho^2}\right\} \tag{25}$$

$$G^{\vartheta_-}(\boldsymbol{r}\,|\,\boldsymbol{r}') = \left[\mathcal{F}_{mn}^{\binom{x'}{y'}} + \mathcal{F}_{mn}^{\binom{a-x'}{y'}} + \mathcal{F}_{mn}^{\binom{a-x'}{b-y'}} + \mathcal{F}_{mn}^{\binom{x'}{b-y'}}\right]\left\{\frac{I_v^e(k_\rho; z\,|\,z') - I_v^h(k_\rho; z\,|\,z')}{k_\rho^2}\right\} \tag{26}$$

In the above, we have introduced the Sommerfeld integral notation

$$S_n\left\{f(k_\rho)\right\} = \frac{1}{2\pi}\int_0^\infty f(k_\rho)J_n(k_\rho\xi)k_\rho^{n+1}dk_\rho\,, \quad n = 0,\ 1,\ 2 \tag{27}$$

$$\xi = \sqrt{(x-x')^2+(y-y')^2}, \quad \zeta = \arctan\left(\frac{y-y'}{x-x'}\right) \tag{28}$$

where J_n is the Bessel function of order n, and the Floquet series notation

$$\mathcal{F}_{mn}^{\binom{x'}{y'}}\{f(k_\rho)\} = \frac{1}{A_w}\sum_{m=-\infty}^{+\infty}\sum_{n=-\infty}^{+\infty} f(k_{\rho_{mn}})\, e^{-j[\boldsymbol{k}_{\rho mn}\cdot(\boldsymbol{\rho}-x'\hat{\boldsymbol{x}}-y'\hat{\boldsymbol{y}})]} \tag{29}$$

with

$$\boldsymbol{k}_{\rho mn} = k_{x_m}\hat{\boldsymbol{x}} + k_{y_n}\hat{\boldsymbol{y}}, \quad k_{\rho_{mn}} = \sqrt{k_{x_m}^2+k_{y_n}^2}, \quad k_{x_m} = \frac{m\pi}{d_x}, \quad k_{y_n} = \frac{n\pi}{d_y} \tag{30}$$

Here, $A_w = d_x d_y$, with $d_x = 2a$ and $d_y = 2b$, where a and b are the inner waveguide dimensions along the x and y directions, respectively. The symbols V_α^p and I_α^p in (17)-(26), where p stands for e (E mode) or h (H mode) and α stands for i (current source) or v (voltage source), denote, respectively, the voltage and current transmission-line Green's functions discussed in Appendix A. The four series in (22)-(23) and (26) arise from the multiple images of a transverse magnetic dipole in the walls of a rectangular waveguide.

Once the current distributions $\boldsymbol{J}_S$ and $\boldsymbol{M}_S$ are determined, the secondary quantities of interest, such as the waveguide dominant mode reflection coefficient at the aperture, the far zone field radiation pattern and the RCS, can be found with little extra effort.

2.2 Short-circuit incident fields

In the driven antenna analysis, the incident electric field in the air-filled waveguide is taken to be that of the dominant TE$_{10}$ mode (we assume that $a \geq b$), and is given as

$$\boldsymbol{E}_{-}^{inc}(\boldsymbol{r}) = V_o\boldsymbol{e}_{10}(\boldsymbol{\rho})e^{-jk_{z10}z} \tag{31}$$

with

$$\boldsymbol{e}_{10}(\boldsymbol{\rho}) = \hat{\boldsymbol{y}}\sqrt{\frac{2}{ab}}\cos\left(\frac{\pi x}{a}\right), \quad k_{z10} = \sqrt{k_o^2-\left(\frac{\pi}{a}\right)^2} \tag{32}$$

where $k_o = \sqrt{\mu_o\epsilon_o}$ is the free space wavenumber. This incident wave excites the short-circuit magnetic field, whose transverse component is

$$\boldsymbol{H}_{t,-}^{i}(\boldsymbol{r}) = Y_{10}V_o\boldsymbol{h}_{10}\left[1-\overrightarrow{\Gamma}_{10}(z)\right]e^{-jk_{z10}z} \tag{33}$$

with

$$\boldsymbol{h}_{10}(\boldsymbol{\rho}) = \hat{\boldsymbol{z}} \times \boldsymbol{e}_{10}, \qquad Y_{10} = \frac{k_{z10}}{k_o \eta_o} \tag{34}$$

where $\eta_o = \sqrt{\mu_o/\epsilon_o}$ is the free space intrinsic impedance. In (33), $\overleftarrow{\Gamma}_{10}(z)$ is the dominant mode reflection coefficient in the short-circuited waveguide, which assumes the value -1 at $z = 0$.

In the RCS analysis, the structure is illuminated by a uniform plane wave field

$$\boldsymbol{E}_{+}^{inc}(\boldsymbol{r}) = \left(\hat{\boldsymbol{\theta}}_i E_{\theta}^{i} + \hat{\boldsymbol{\varphi}}_i E_{\varphi}^{i}\right) e^{jk_o[\rho \sin\theta_i \cos(\varphi - \varphi_i) + (z-d)\cos\theta_i]} \tag{35}$$

impinging from the direction (θ_i, φ_i) on the grounded layered medium from the upper half-space, which is assumed to have free space parameters. Observe that in (35) the phase reference point is chosen at $(0, 0, d)$, where d is the $z-$coordinate of the uppermost interface. This plane wave is the source of the short-circuit electric field, whose transverse part is given as

$$\boldsymbol{E}_{t,+}^{i}(\boldsymbol{r}) = \left[\hat{\boldsymbol{\rho}}_i V^{e}(k_{\rho}^{i}; z \,|\, d) + \hat{\boldsymbol{\varphi}}_i V^{h}(k_{\rho}^{i}; z \,|\, d)\right] e^{j\boldsymbol{k}_{\rho}^{i} \cdot \boldsymbol{\rho}} \tag{36}$$

where $\boldsymbol{k}_{\rho}^{i} = \hat{\boldsymbol{\rho}}_i k_{\rho}^{i}$, with $k_{\rho}^{i} = k_o \sin\theta_i$. In the above, $V^{p}(k_{\rho}^{i}; z \,|\, d)$ denotes the voltage on the respective transmission line analog of the layered medium, excited in the uppermost section by the voltage waves

$$V_{-}^{e}(k_{\rho}^{i}; z \,|\, d) = \cos\theta_i \, E_{\theta}^{i} \, e^{jk_o(z-d)\cos\theta_i} \tag{37}$$

$$V_{-}^{h}(k_{\rho}^{i}; z \,|\, d) = E_{\varphi}^{i} e^{jk_o(z-d)\cos\theta_i} \tag{38}$$

propagating in the $-z$ direction. The transverse short-circuit magnetic field associated with (36) may be expressed as

$$\boldsymbol{H}_{t,+}^{i}(\boldsymbol{r}) = -\left[\hat{\boldsymbol{\rho}}_i I^{h}(k_{\rho}^{i}; z \,|\, d) - \hat{\boldsymbol{\varphi}}_i I^{e}(k_{\rho}^{i}; z \,|\, d)\right] e^{j\boldsymbol{k}_{\rho}^{i} \cdot \boldsymbol{\rho}} \tag{39}$$

The voltages and currents in (36) and (39) can easily be found in any transmission line section, as discussed in Appendix A.

2.3 Secondary quantities

From the equivalent currents $\boldsymbol{J}_S$ and $\boldsymbol{M}_S$, other quantities of interest may easily be obtained. Hence, for the driven antenna we compute the dominant mode aperture reflection coefficient Γ and the corresponding normalized aperture admittance Y, given as

$$\Gamma = -\frac{1}{V_o}\langle \boldsymbol{M}_S\,;\,\boldsymbol{h}_{10}\rangle_{S_a} - 1\,, \qquad Y = \frac{1-\Gamma}{1+\Gamma} \tag{40}$$

For the plane-wave excited structure we also compute the dominant mode aperture transmission coefficient, given as

$$T = -\frac{\langle \boldsymbol{M}_S\,;\,\boldsymbol{h}_{10}\rangle_{S_a}}{\sqrt{|\,E^i_\theta\,|^2 + |\,E^i_\varphi\,|^2}} \tag{41}$$

For either excitation, the far zone fields in the direction (θ_o,φ_o) are obtained as

$$\begin{aligned} E^s_\theta \sim\; & -\frac{jk_o}{2\pi r}e^{-jk_o(r-d\cos\theta_o)}\left\{V^e_i(k^o_\rho;d\,|\,h)\hat{\boldsymbol{\rho}}_o\cdot\left\langle \boldsymbol{J}_S(\boldsymbol{\rho}')\,,\,e^{j\boldsymbol{k}^o_\rho\cdot\boldsymbol{\rho}'}\right\rangle'_{S_p}\right. \\ & \left. +\eta_o\cos\theta_o\,I^e_v(k^o_\rho;d\,|\,0)\hat{\boldsymbol{\varphi}}_o\cdot\left\langle \boldsymbol{M}_S(\boldsymbol{\rho}')\,,\,e^{j\boldsymbol{k}^o_\rho\cdot\boldsymbol{\rho}'}\right\rangle'_{S_a}\right\} \end{aligned} \tag{42}$$

$$\begin{aligned} E^s_\varphi \sim\; & -\frac{jk_o}{2\pi r}e^{-jk_o(r-d\cos\theta_o)}\left\{\cos\theta_o V^h_i(k^o_\rho;d\,|\,h)\hat{\boldsymbol{\varphi}}_o\cdot\left\langle \boldsymbol{J}_S(\boldsymbol{\rho}')\,,\,e^{j\boldsymbol{k}^o_\rho\cdot\boldsymbol{\rho}'}\right\rangle'_{S_p}\right. \\ & \left. -\eta_o I^h_v(k^o_\rho;d\,|\,0)\hat{\boldsymbol{\rho}}_o\cdot\left\langle \boldsymbol{M}_S(\boldsymbol{\rho}')\,,\,e^{j\boldsymbol{k}^o_\rho\cdot\boldsymbol{\rho}'}\right\rangle'_{S_a}\right\} \end{aligned} \tag{43}$$

where $\hat{\boldsymbol{\rho}}_o$ and $\hat{\boldsymbol{\varphi}}_o$ are the radial and azimuthal unit vectors evaluated at (θ_o,φ_o), and $\boldsymbol{k}^o_\rho = \hat{\boldsymbol{\rho}}_o k^o_\rho$, with $k^o_\rho = k_o\sin\theta_o$. It is assumed in (42)-(43) that the aperture is in the $z=0$ plane and the patch resides on a substrate with thickness h. Observe that (42)-(43) include contributions both from the patch and the aperture.

For the plane-wave excited antenna we also compute its monostatic RCS. Hence, if the incident field in the upper half-space is polarized in the u direction and the v component of the scattered field is considered, the RCS of the antenna is given as [9]

$$\sigma_{uv} = 4\pi r^2\frac{|\,E^s_v\,|^2}{|\,E^{inc}_{u,+}\,|^2} \tag{44}$$

It should be noted that the scattered field in the above does not include the plane wave (geometrical optics) field reflected by the layered medium.

3 Numerical Procedure

3.1 Weak form of the integral equations

The method of moments (MOM) is applied to the weak forms of (10) and (11), which are obtained by testing them with suitably selected weight functions $\{\boldsymbol{\Lambda}_m\}$ defined over S_p and S_a. As a result, upon using the Gauss theorem [10, p. 503], we obtain

$$\begin{aligned}\left\langle \boldsymbol{\Lambda}_m ; \left\langle G^A_{xx} , \boldsymbol{J}_S \right\rangle'_{S_p} \right\rangle_{S_p} - \left\langle \boldsymbol{\nabla}_t \cdot \boldsymbol{\Lambda}_m , \left\langle G^\phi , \boldsymbol{\nabla}'_t \cdot \boldsymbol{J}_S \right\rangle'_{S_p} \right\rangle_{S_p} \\ - \left\langle \boldsymbol{\Lambda}_m ; \left\langle \underline{\underline{\boldsymbol{G}}}^{EM}_t ; \boldsymbol{M}_S \right\rangle'_{S_a} \right\rangle_{S_p} = \left\langle \boldsymbol{\Lambda}_m ; \boldsymbol{E}^i_{t,+} \right\rangle_{S_p}\end{aligned} \tag{45}$$

$$\begin{aligned}\left\langle \boldsymbol{\Lambda}_m ; \left\langle \underline{\underline{\boldsymbol{G}}}^{HJ}_t ; \boldsymbol{J}_S \right\rangle'_{S_p} \right\rangle_{S_a} - \left\langle \boldsymbol{\Lambda}_m ; \left\langle G^{F+}_{xx} \underline{\underline{\boldsymbol{I}}}_t + \underline{\underline{\boldsymbol{G}}}^{F-}_t ; \boldsymbol{M}_S \right\rangle'_{S_a} \right\rangle_{S_a} \\ + \left\langle \boldsymbol{\nabla}_t \cdot \boldsymbol{\Lambda}_m , \left\langle G^{\vartheta +} + G^{\vartheta -} , \boldsymbol{\nabla}'_t \cdot \boldsymbol{M}_S \right\rangle'_{S_a} \right\rangle_{S_a} \\ = \left\langle \boldsymbol{\Lambda}_m ; \boldsymbol{H}^i_{t,+} - \boldsymbol{H}^i_{t,-} \right\rangle_{S_a}\end{aligned} \tag{46}$$

Here, the incident fields $\boldsymbol{E}^i_{t,+}$ and $\boldsymbol{H}^i_{t,+}$ are absent when the waveguide aperture reflection coefficient is calculated, and $\boldsymbol{H}^i_{t,-}$ is zero in RCS computations.

3.2 Patch and aperture current expansions

As indicated in Fig. 1, we model the microstrip patch S_p and the aperture S_a by triangular elements. The nodes of each triangular element are assigned indices i, j, and k in a counterclockwise direction, as illustrated in Fig. 3. The sides of a triangle are formed by three edge vectors, $\boldsymbol{\ell}_i$, $\boldsymbol{\ell}_j$, and $\boldsymbol{\ell}_k$, where $\boldsymbol{\ell}_i$ is oriented from node j to node k. The position of the ith node with respect to the global coordinate origin is specified by the vector $\boldsymbol{r}_i$, whose projection on the xy plane is $\boldsymbol{\rho}_i$. Since the microstrip patch and the aperture each lie in a z = constant plane with z known, the location of an arbitrary point within an element may uniquely be specified by its radial vector $\boldsymbol{\rho} = \boldsymbol{\rho}_i + \boldsymbol{\varrho}_i$, where $\boldsymbol{\varrho}_i$ is the local position vector originating at the ith node of the element. As indicated in Fig. 3, the three local position vectors further divide the

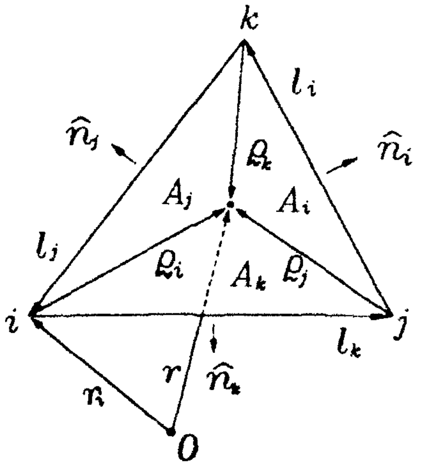

Figure 3: Local coordinates associated with a triangular element

element into three triangles, where the area of the triangle opposite node i is denoted by A_i. To facilitate the integration over triangular domains, encountered in (45)–(46), we introduce for each triangle a 'natural' coordinate system (L_i, L_j, L_k), where L_i is known as the 'area coordinate' or 'shape function' associated with node i of the element [11, p. 110], and is defined as

$$L_i = \frac{A_i}{A}, \qquad \sum_{i=1}^{3} L_i = 1 \tag{47}$$

where A is the triangle area. In terms of the area coordinates, the local position vector $\boldsymbol{\varrho}_i$ may be expressed as

$$\boldsymbol{\varrho}_i = \boldsymbol{\ell}_k L_j - \boldsymbol{\ell}_j L_k \tag{48}$$

To represent the patch and aperture currents on each triangular element, we introduce a vector basis function $\boldsymbol{A}_i$, given as (cf. [12])

$$\boldsymbol{A}_i = \frac{\boldsymbol{\varrho}_i}{2A} \tag{49}$$

Noting that the gradient of the shape function is

$$\boldsymbol{\nabla}_t L_i = -\hat{\boldsymbol{n}}_i \frac{\ell}{2A} \tag{50}$$

where $\hat{\boldsymbol{n}}_i$ is a unit vector perpendicular to edge i in the plane and pointing out of the triangle element (see Fig. 3), we find the divergence of $\boldsymbol{A}_i$ as

$$\nabla_t \cdot \boldsymbol{A}_i = \frac{1}{A} \tag{51}$$

We also find that $\hat{\boldsymbol{n}}_i \cdot \boldsymbol{A}_i$ is constant on edge i, which makes it easy to enforce the continuity of the normal component of current density between the elements that share this edge. The patch current density and its divergence on each element may now be approximated as

$$\boldsymbol{J}_S = \sum_{i=1}^{3} I_i \boldsymbol{A}_i, \quad \nabla_t \cdot \boldsymbol{J}_S = \sum_{i=1}^{3} \frac{I_i}{A} \tag{52}$$

where I_i is the electric current leaving the element through edge i. Similarly, the aperture current density and its divergence on each element are approximated as

$$\boldsymbol{M}_S = \sum_{i=1}^{3} K_i \boldsymbol{A}_i, \quad \nabla_t \cdot \boldsymbol{M}_S = \sum_{i=1}^{3} \frac{K_i}{A} \tag{53}$$

where K_i is the magnetic current leaving the element through edge i.

3.3 Global system assembly and solution procedure

The testing functions in the integral equations (45)-(46) are drawn from the same sets as the basis functions used to represent the patch and aperture currents. Hence, $\{\boldsymbol{A}_m\}$ consists of $\boldsymbol{A}_i^{(n)}$, with $i = 1, 2$, and 3, and $n = 1, \cdots, N_s$, where N_s is the total number of triangular elements of S_p and S_a. In the above, it was necessary to introduce the superscript n to distinguish the local basis functions associated with element n. In what follows, where there is no danger of confusion, this element superscript will be omitted for notational simplicity.

When the expansions (52)-(53) are substituted into the integral equations (45)-(46), the coefficients $I_i^{(n)}$ and $K_i^{(n)}$ are constrained by the boundary conditions, which require the continuity of the normal components of $\boldsymbol{J}_S$ and $\boldsymbol{M}_S$ across the edges shared by adjacent elements, or their vanishing at the boundary edges of S_p and S_a, respectively. If the numbers of the non-boundary triangle element edges on the patch and the aperture are denoted by N_p and N_a, respectively, and the total number of the unknown current expansion coefficients by N, then $N = N_p + N_a$. As a result of this procedure, the coupled integral equations (45)–(46) are converted into an algebraic system

$$\begin{bmatrix} [Z_{mn}] & [T_{mn}] \\ [D_{mn}] & [Y_{mn}] \end{bmatrix} \begin{bmatrix} [I_n] \\ [K_n] \end{bmatrix} = \begin{bmatrix} [V_m] \\ [H_m] \end{bmatrix} \tag{54}$$

Here, the N-by-N system matrix consists of four submatrices, where $[Z_{mn}]$ is the N_p-by-N_p global impedance matrix, $[T_{mn}]$ is the N_p-by-N_a global coupling matrix, $[D_{mn}] = -[T_{mn}]^T$, where the superscript T indicates the matrix transpose, and $[Y_{mn}]$ is the N_a-by-N_a global admittance matrix. The N-by-1 vector of the unknown current expansion coefficients in (54) comprises the N_p-by-1 global vector $[I_n]$ of patch current coefficients and the N_a-by-1 global vector $[K_n]$ of aperture current coefficients. The N-by-1 global excitation vector consists of the N_p-by-1 global patch voltage excitation vector $[V_m]$ and the N_a-by-1 global aperture current excitation vector $[H_m]$.

To assemble the global system (54), we consider one source element-test element pair at a time. Each such pair will in general contribute to nine elements of the global system matrix. It is convenient to view these contributions as the entries of a local 3-by-3 system matrix corresponding to the element pair. Furthermore, each element will in general contribute to three entries of the global excitation vector, and these contributions may be assembled into a local 3-by-1 excitation vector. To be more specific, let the global indices of the source and test elements be n and m, respectively. Also, suppose that both elements are on the microstrip patch. Then, the associated local system will take the form

$$\left[Z_{ii'}^{(mn)}\right]\left[I_{i'}^{(n)}\right] = \left[V_i^{(m)}\right] \tag{55}$$

where $[Z_{ii'}^{(mn)}]$ is the local impedance matrix, $[I_{i'}^{(n)}]$ is the local vector of current coefficients, and $[V_{i'}^{(m)}]$ is the local voltage excitation vector. Here, the primed local source element indices i', j', and k' follow the same cyclic convention as the unprimed ones. Observe that there exists a unique mapping between the local coefficients $\{I_i^{(n)}\}$ of each element and the global current coefficients $\{I_n\}$, where the reference directions of the latter are specified by the order in which the element nodes appear in the input geometry data. This mapping determines to which entries of the global system (54) should the elements of (55) be added, and with what signs. Local systems similar to (55) arise when both the source and test elements are in the aperture, and when one of them is on the patch and the other in the aperture. Below, we describe these local systems in more detail.

Consider first a test element, S_p^m, on the patch. Then, if the source element, S_p^n, is also on the patch, the entries of the resulting local impedance matrix are found as

$$Z_{ii'}^{(mn)} = \left\langle \boldsymbol{A}_i \, ; \left\langle G_{xx}^{A} \, , \, \boldsymbol{A}_{i'} \right\rangle_{S_p^n}' \right\rangle_{S_p^m} - \left\langle \frac{1}{A} \, , \left\langle G^{\varphi} \, , \, \frac{1}{A} \right\rangle_{S_p^n}' \right\rangle_{S_p^m} \tag{56}$$

If, on the other hand, the source element, S_a^n, is in the aperture, there results a local coupling matrix, with the entries given as

$$T_{ii'}^{(mn)} = \left\langle \boldsymbol{A}_i \, ; \left\langle \underline{\underline{\boldsymbol{G}}}_t^{EM} \, ; \, \boldsymbol{A}_{i'} \right\rangle_{S_a^n}' \right\rangle_{S_p^m} \tag{57}$$

Each patch element also contributes a local voltage excitation vector, whose entries are

$$V_i^{(m)} = \left\langle \boldsymbol{A}_i \, ; \, \boldsymbol{E}_{t,+}^{i} \right\rangle_{S_p^m} \tag{58}$$

Next, consider a test element, S_a^m, in the aperture. Then, if the source element, S_p^n, is on the patch, there arises a local coupling matrix, which may be shown (from reciprocity considerations [7, pp. 116–120]) to be the negative transpose of the coupling matrix given by (57). If, on the other hand, the source element, S_a^n, is also in the aperture, there arises a local admittance matrix, whose entries are given as

$$Y_{ii'}^{(mn)} = Y_{ii',+}^{(mn)} + Y_{ii',-}^{(mn)} \tag{59}$$

$$Y_{ii',+}^{(mn)} = \left\langle \boldsymbol{A}_i \, ; \left\langle G_{xx}^{F+} \, , \, \boldsymbol{A}_{i'} \right\rangle_{S_a^n}' \right\rangle_{S_a^m} - \left\langle \frac{1}{A} \, , \left\langle G^{\vartheta+} \, , \, \frac{1}{A} \right\rangle_{S_a^n}' \right\rangle_{S_a^m} \tag{60}$$

$$Y_{ii',-}^{(mn)} = \left\langle \boldsymbol{A}_i \, ; \left\langle \underline{\underline{\boldsymbol{G}}}^{F-} \, ; \, \boldsymbol{A}_{i'} \right\rangle_{S_a^n}' \right\rangle_{S_a^m} - \left\langle \frac{1}{A} \, ; \left\langle G^{\vartheta-} \, , \, \frac{1}{A} \right\rangle_{S_a^n}' \right\rangle_{S_a^m} \tag{61}$$

Finally, each aperture element also contributes a local current excitation vector, with the entries

$$\Pi_i^{(m)} = \left\langle \boldsymbol{A}_i \, ; \, \boldsymbol{H}_{t,+}^{i} - \boldsymbol{H}_{t,-}^{i} \right\rangle_{S_a^m} \tag{62}$$

The integrals over source coordinates in (56) and (60) (61) involve kernels that are singular when the test and source elements coincide. These singularities are extracted and integrated analytically [13], leaving well-behaved integrals over triangular elements, which are numerically evaluated by a Gaussian quadrature [11, p. 113]. On the other hand, the testing (exterior) integrals in (56) and (60) (61), as well as the integrals in the excitation terms (58) and (62), have regular and slowly-varying integrands, and may thus be approximated using a one-point quadrature rule [12]. For example, the integral in (56) is approximated as

$$\left\langle \boldsymbol{\Lambda}_i ; \left\langle G_{xx}^A , \boldsymbol{\Lambda}_{i'} \right\rangle'_{S_p^n} \right\rangle_{S_p^m} \approx \frac{\boldsymbol{\varrho}_{ci}^{(m)}}{2} \cdot \left\langle G_{xx}^A(\boldsymbol{r}_c^{(m)} | \boldsymbol{r}') , \boldsymbol{\Lambda}_{i'}(\boldsymbol{\rho}') \right\rangle'_{S_p^n} \tag{63}$$

where $\boldsymbol{\varrho}_{ci}^{(m)}$ and $\boldsymbol{r}_c^{(m)}$ denote, respectively, the local (with respect to node i—see Fig. 3) and global position vectors of the centroid of element S_p^m. This one-point approximation results in significant savings in the computational effort, even though it sacrifices the symmetry properties of the impedance and admittance matrices. The integrals appearing in (57) have regular, but rapidly varying kernels (which represent electric field, rather than potentials), especially when the substrate between the microstrip patch and the aperture is electrically thin. For this reason, both the interior and exterior integrals in (57) are evaluated by Gaussian quadratures without further approximations.

Once the complex-valued matrix equation (54) is assembled and solved, which is accomplished by standard procedures (LU factorization with partial pivoting, followed by a forward and back substitution [11, p. 120]), the current density within each triangular element may be obtained from (52) or (53).

3.4 Evaluation of spectral integrals and Floquet series

For the solution procedure described above to be practical, the Sommerfeld-type spectral integrals that occur in (17)-(21) and (24)-(25), as well as the Floquet series that appear in (22)-(23) and (26), must be efficiently evaluated. To accomplish that, the Sommerfeld integrals are accelerated by asymptotic integrand subtraction and the method of averages [14]. In addition to these techniques, an interpolation and table look-up scheme is implemented to further reduce the computation time [15]. The integration path is properly deformed to avoid the integrand singularities, which occur on or near the real axis in the k_ρ plane [16].

The Floquet series are accelerated as well, by a combination of the Kummer and Poisson transformations [17]. As a result of this procedure, the original slowly convergent Floquet series is converted into the sum of an accelerated spectral series and an exponentially convergent spatial series. Observe that in (61) these series are integrated against the basis functions over the source and test triangular elements. The source element integrals are introduced inside the spectral sums and evaluated analytically [17, pp. 107–114], thus further accelerating the convergence of these series. The same integrals over the spatial series are evaluated by a Gaussian quadrature, as discussed in Sec. 3.3.

3.5 Far field and RCS computation

Once the coefficients I_i and K_i are found for each element, the current expansions (52)–(53) are substituted into (42)–(43) to determine the far zone fields. The integrals encountered in (42)–(43) are then recognized as Fourier transforms of the vector basis functions (49), evaluated at $\boldsymbol{k}_\rho = \boldsymbol{k}_\rho^o$. In view of (49) and (48), the Fourier transform of $\boldsymbol{\Lambda}_i$ associated with a triangular element S_n may be expressed as

$$\begin{aligned} \tilde{\boldsymbol{\Lambda}}_i &= \left\langle \boldsymbol{\Lambda}_i \, , \, e^{-j\boldsymbol{k}_\rho \cdot \boldsymbol{\rho}'} \right\rangle'_{S_n} \\ &= \frac{1}{2A} \left(\boldsymbol{\ell}_k \tilde{L}_j - \boldsymbol{\ell}_j \tilde{L}_k \right) \end{aligned} \tag{64}$$

where the $\tilde{L}_i$ denotes the Fourier transformed shape function L_i. Upon using the procedure of Appendix B, we may express $\tilde{L}_i$ as

$$\begin{aligned} \tilde{L}_i &= -\frac{b_i}{2Ak_\rho^2} \sum_{\nu=1}^{3} b_\nu j_o(a_\nu k_\rho/2) e^{-\boldsymbol{k}_\rho \cdot \boldsymbol{\rho}_{c\nu}} \\ &\quad + \frac{b_j}{2k_\rho} \left[j_1(a_j k_\rho/2) - j j_o(a_j k_\rho/2) \right] e^{j\boldsymbol{k}_\rho \cdot \boldsymbol{\rho}_{cj}} \end{aligned}$$

$$-\frac{b_k}{2k_\rho}\left[j_1(a_k k_\rho/2) + j j_0(a_k k_\rho/2)\right] e^{j\boldsymbol{k}_\rho\cdot\boldsymbol{\rho}_{ck}} \qquad (65)$$

where $\boldsymbol{\rho}_{ci}$ is a position vector of the midpoint of edge i of the element, $a_i = \hat{\boldsymbol{u}}\cdot\boldsymbol{\ell}_i$, $b_i = \hat{\boldsymbol{v}}\cdot\boldsymbol{\ell}_i$, and j_n denotes the spherical Bessel function of order n. We note that (65) is evaluated for $\boldsymbol{k}_\rho = \boldsymbol{k}_\rho^o$, as is required in (42)-(43), then $k_\rho = k_\rho^o$, $\hat{\boldsymbol{u}} = \hat{\boldsymbol{\rho}}_o$, and $\hat{\boldsymbol{v}} = \hat{\boldsymbol{\varphi}}_o$. It can be shown that (65) approaches a finite limit $A/3$ as $k_\rho \to 0$.

Once the microstrip patch and the waveguide aperture contributions to the far zone fields are determined, the RCS is readily obtained from (44).

4 Experimental Setup and Measurement Procedures

The experiment was done in X-band, rather than in the millimeterwave range, to reduce the effect of fabrication tolerances on the results. The components of the measured structure are shown in Fig. 4. Circular and rectangular microstrip patch antennas were investigated, each excited through a waveguide-backed concentric rectangular slot, as illustrated in Figs. 5a and 5b, respectively. The substrate and superstrate materials used in the experiment (and also in the numerical examples presented in Sec. 5) are non-magnetic and isotropic. Therefore, the nth layer may conveniently be characterized by a complex number $\epsilon_n(1 - j\tan\delta_n)$, where ϵ_n is the real relative dielectric and $\tan\delta_n$ is the loss tangent. The substrate used in antennas of Fig. 5 has $\epsilon_1 = 2.2$, $\tan\delta_1 = 0.001$, and thickness $h = 3.15\,\mathrm{mm}$. The cover layer, if present, is made of the same material with thickness $t = 1.57\,\mathrm{mm}$. The microstrip antennas were mounted on the waveguide flange using plastic screws (see Fig. 4).

The dominant mode reflection coefficient Γ, referred to the aperture plane, was measured using the HP-8510B network analyzer. Prior to the measurement, the thru-reflect-line (TRL) two-port calibration method [18] was used to eliminate the systematic errors due to the coax-to-waveguide adapter and to establish the measurement reference plane (MRP) at the aperture location. In order to implement the TRL calibration procedure, three sets of measurements, referred to as thru, reflect,

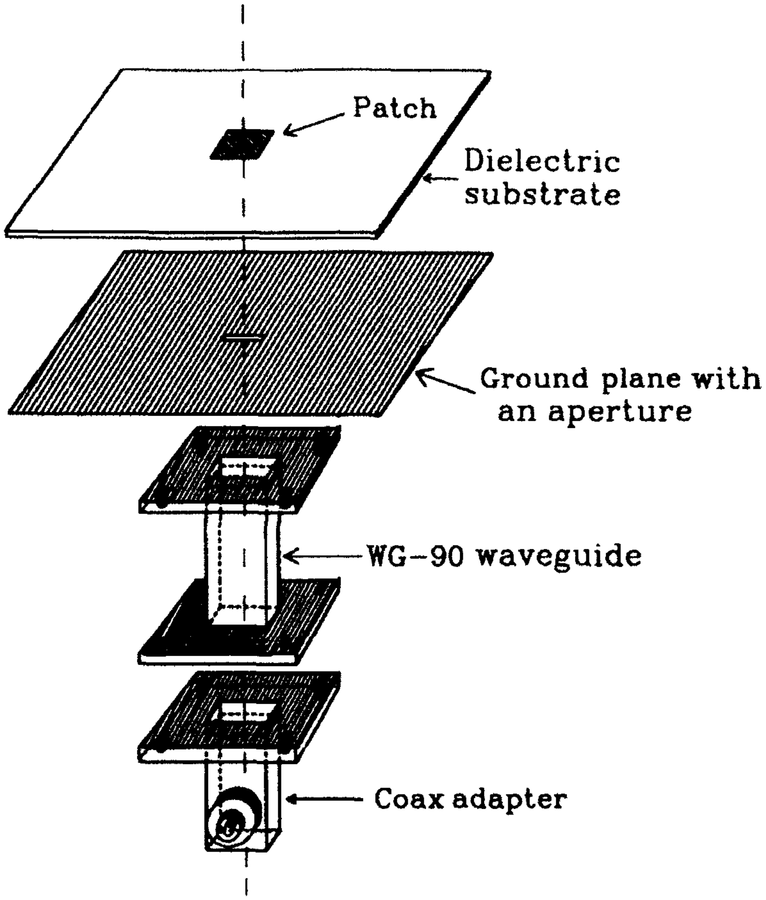

Figure 4: Components of the measured structure.

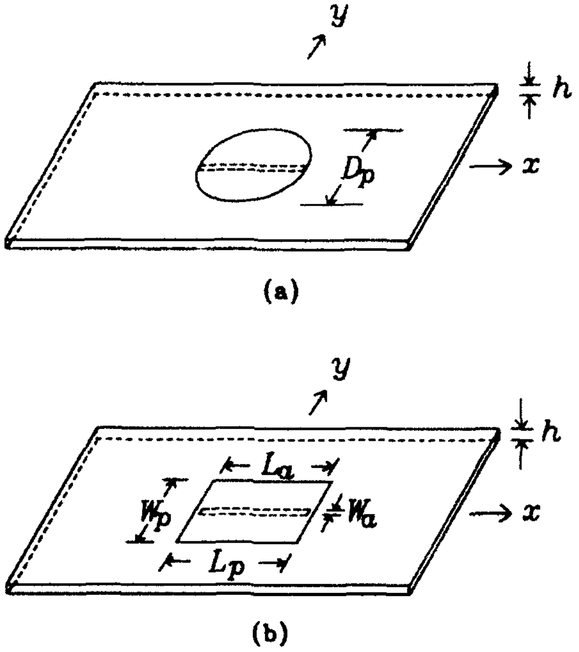

Figure 5: (a) Circular and (b) rectangular microstrip patch antennas used in the measurements. Each antenna is fed through a waveguide-backed concentric rectangular slot in the ground plane.

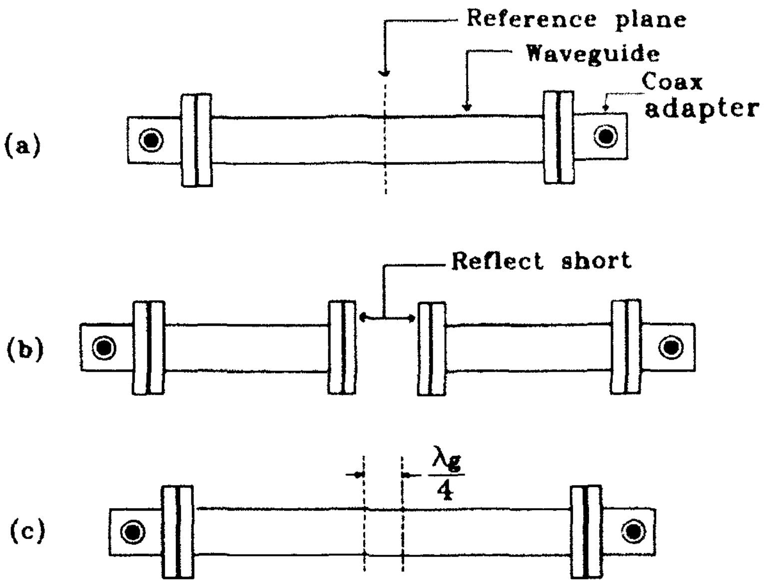

Figure 6: (a) Thru, (b) reflect, and (c) line (delay) standards used in the HP-8510B TRL calibration procedure.

and line (or delay) were taken. The thru, reflect, and line calibration standards were fabricated from four WG-90 waveguide segments, as illustrated in Fig. 6. The thru was arbitrarily selected to be 84.2 mm long (the length of the thru should be at least two guide wavelengths, to reduce the interference between the coax adapters), which resulted in the reflect length of 42.1 mm. A waveguide feed of the same length was used in the actual measurements (see Fig. 4), to ensure that the MRP coincides with the aperture plane. Because no two coax adapters are identical, two reflect standards were fabricated and used in the HP-8510B calibration, as indicated in Fig. 6b. The line (delay) was made 9.9 mm longer than the thru. This 9.9 mm length difference between the thru and the line, which at the center frequency $f_c = 10\,\text{GHz}$ is approximately a quarter of the guide wavelength $\lambda_g = 39.7\,\text{mm}$, results in a time delay of 24.94 ps, and this value was keyed into the HP-8510B network analyzer during the TRL calibration procedure.

The procedure for the far field measurement is rather standard, and is not described here to conserve space.

5 Sample Computed and Measured Results

In this section we present sample computed results obtained using a computer program implementing the procedures developed in Sec. 3. For several antenna configurations, these results are compared with the corresponding measured data obtained by the experimental procedures described in Sec. 4. Although no published results were available for comparison for waveguide-backed microstrip patch antennas, every effort was made to validate at least the most important modules of the developed computer code against independently obtained data. First, the part of the program that deals with an arbitrarily shaped microstrip patch on a grounded substrate (in the absence of the aperture) was extracted and used to compute the scattering characteristics for rectangular patch antennas on both isotropic and uniaxial substrates. The computed RCS results were found to closely agree with those published by Newmann and Forrai [19] and Pozar [20]. Second, the part of the code that deals with the aperture was isolated and used to compute the RCS of a narrow slot in a ground plane. This problem was then related via the B 'binet's principle [21, p. 500] to that of a thin wire scatterer with equivalent radius [22], and the latter was analyze using a commercial code PCAAD [23]. Again, close agreement between the corresponding RCS results was observed. Third, a stripped down version of our program, which did not include the microstrip patch part, was used to analyzed a rectangular waveguide radiating through a centered rectangular slot into a half-space. The computed equivalent magnetic current in the aperture was found to closely agree (both in magnitude and phase) with the corresponding result obtained by Harrington and Mautz [24, Fig. 15a]. Finally, a rectangular waveguide radiating through a centered rectangular aperture covered by a dielectric layer was analyzed. For this problem, in Fig. 7 we compare our aperture admittance results with the computed and measured data obtained by Bodnar and Paris [25]. Although the agreement between the three sets of results is judged to be good, we note that our data are closer to the measured results than the data computed by Bodnar and Paris.

We next present measured and computed results for four waveguide-backed microstrip patch antennas with isotropic substrates, excited through a centered rect-

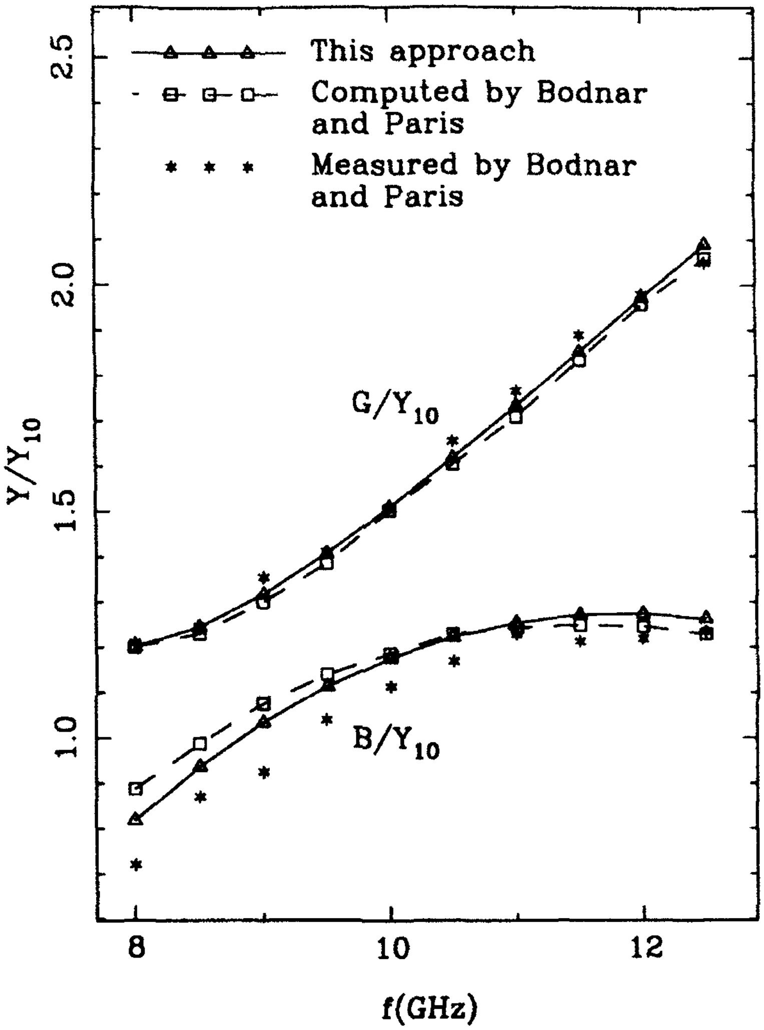

Figure 7: Aperture conductance G and susceptance B normalized to the dominant mode wave admittance of a flanged rectangular waveguide radiating through a centered rectangular aperture covered by a slab with dielectric constant $\epsilon_1 = 2.25$ and thickness $h = 3.201\,\mathrm{mm}$. The waveguide has dimensions $a = 22.86\,\mathrm{mm}$ and $b = 10.16\,\mathrm{mm}$, and the aperture size is $0.7a$-by-$0.8b$.

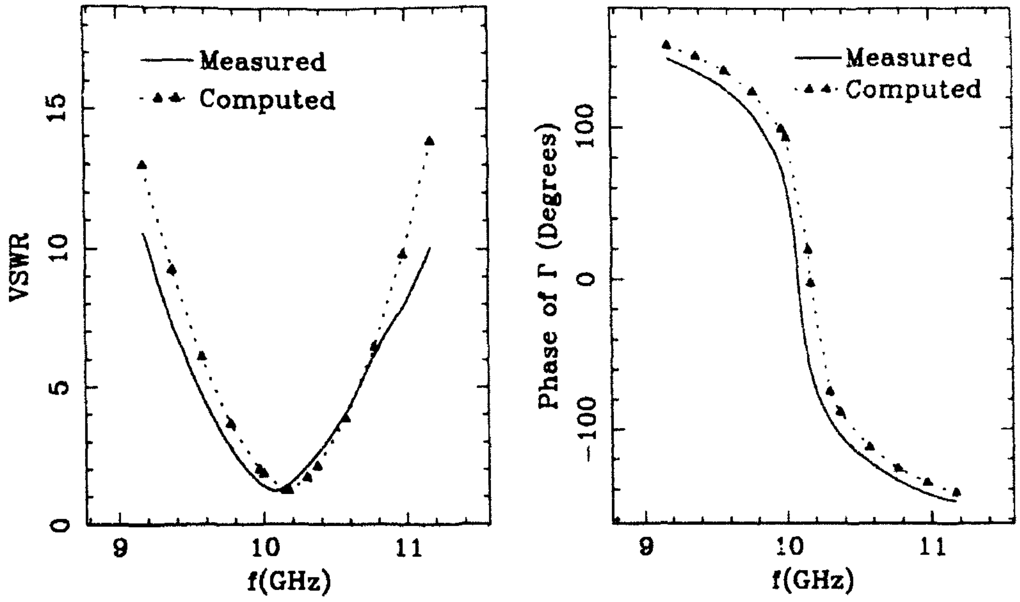

(a) (b)

Figure 8: Plots of (a) VSWR and (b) phase of Γ for a waveguide-excited circular patch antenna without a superstrate (Antenna 1).

angular slot by the dominant (TE_{10}) mode. The parameters of these antennas are collected for easy reference in Table 1. Observe that Antennas 1 and 3 are circular (see Fig. 5a), while Antennas 2 and 4 are rectangular (see Fig. 5b). Also, Antennas 1 and 2 do not have a superstrate, whereas Antennas 3 and 4 are covered by a dielectric slab made of the same material as the substrate. In all cases the same X-band rectangular waveguide (WG-90) is used, with the interior dimensions $a = 22.86$ mm and $b = 10.16$ mm. Referring to Table 1, observe that the largest discrepancy between the computed and measured values of the resonant frequency, where the minimum of the voltage standing wave ratio (VSWR) occurs, is 1%. Note also that the resonant values of VSWR are close to one and, therefore, the antennas are nearly matched at their resonant frequencies. Their bandwidths (BW in Table 1), however, are narrow (which is characteristic of microstrip antennas) and do not exceed 5%.

The computed and measured VSWR and phase of the dominant mode reflection coefficient ($\angle\Gamma$) at the aperture for the four antennas are shown in Figs. 8-11. In

Table 1: Parameters of sample waveguide-fed microstrip patch antennas.

Antenna	1	2	3	4
Relative substrate ϵ	2.2	2.2	2.2	2.2
Substrate thickness h (mm)	3.15	3.15	3.15	3.15
Relative superstrate ϵ	N/A	N/A	2.2	2.2
Superstrate thickness t (mm)	N/A	N/A	1.57	1.57
$\tan\delta$	0.001	0.001	0.001	0.001
Patch dimensions (mm)	$D_p = 14.0$	$L_p = 14.0$ $W_p = 11.7$	$D_p = 13.7$	$L_p = 13.7$ $W_p = 11.4$
Aperture dimensions (mm)	$W_a = 14.0$ $L_a = 0.3$	$W_a = 14.0$ $L_a = 0.3$	$W_a = 13.7$ $L_a = 0.3$	$W_a = 13.7$ $L_a = 0.3$
Measured resonant frequency (GHz)	10.09	10.07	9.95	9.90
Computed resonant frequency (GHz)	10.17	10.17	10.0	10.0
Error in resonant frequency (%)	0.79	0.99	0.5	1.0
Measured gain (dB)	8.63	8.8	7.9	8.2
Measured lowest VSWR	1.22	1.137	1.114	1.013
Calculated lowest VSWR	1.23	1.151	1.075	1.012
Measured BW (%)	4.0	4.24	4.74	4.92
Computed BW (%)	3.8	4.03	4.4	4.52

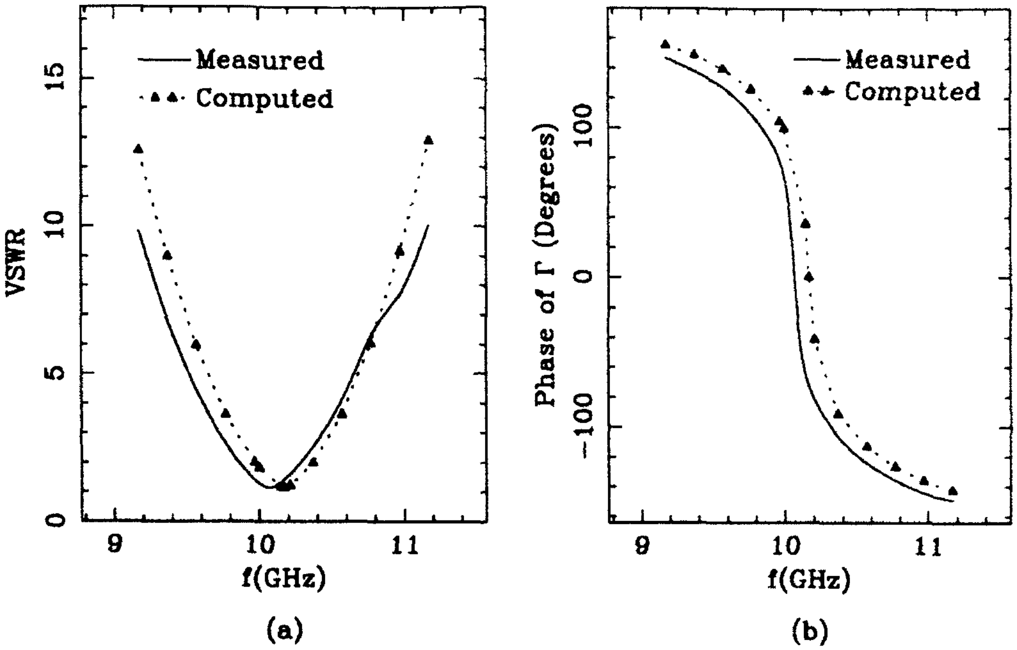

Figure 9: Plots of (a) VSWR and (b) phase of Γ for a waveguide-excited rectangular patch antenna without a superstrate (Antenna 2).

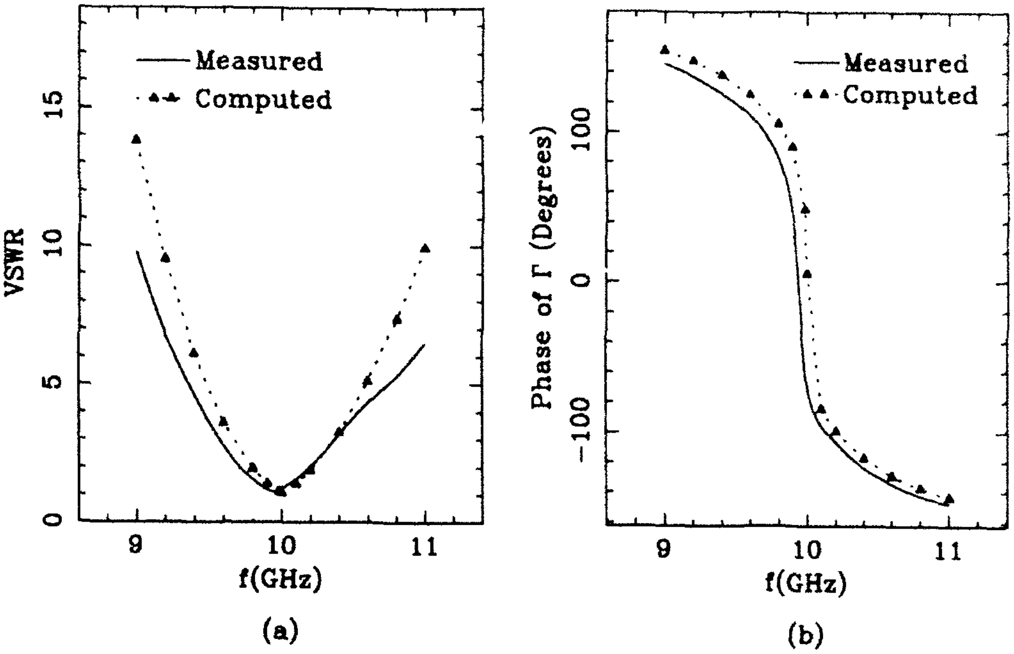

Figure 10: Plots of (a) VSWR and (b) phase of Γ for a waveguide-excited circular patch antenna with a cover layer (Antenna 3).

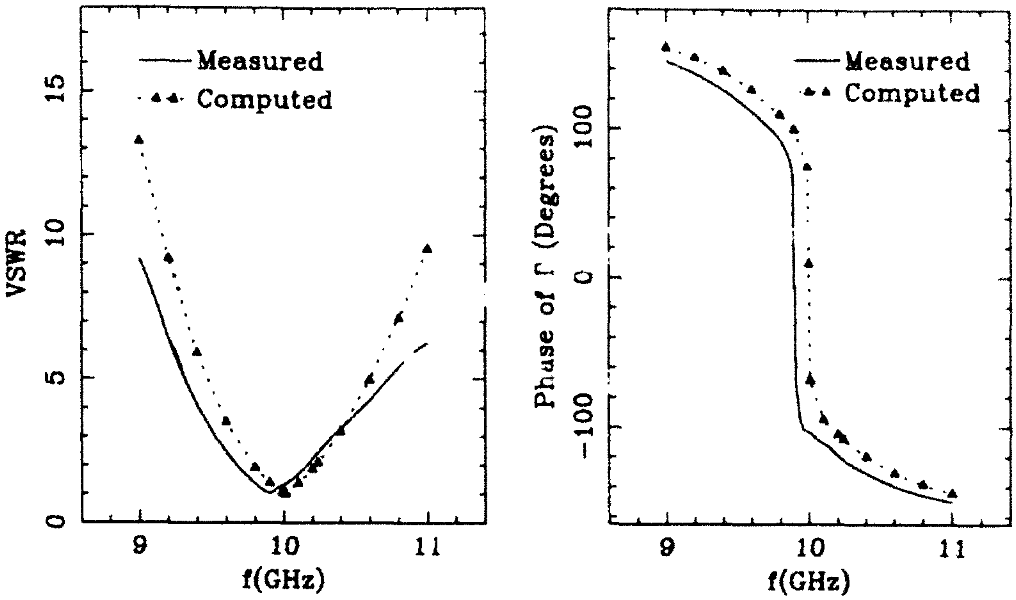

(a) (b)

Figure 11: Plots of (a) VSWR and (b) phase of Γ for a waveguide-excited rectangular patch antenna with a cover layer (Antenna 4).

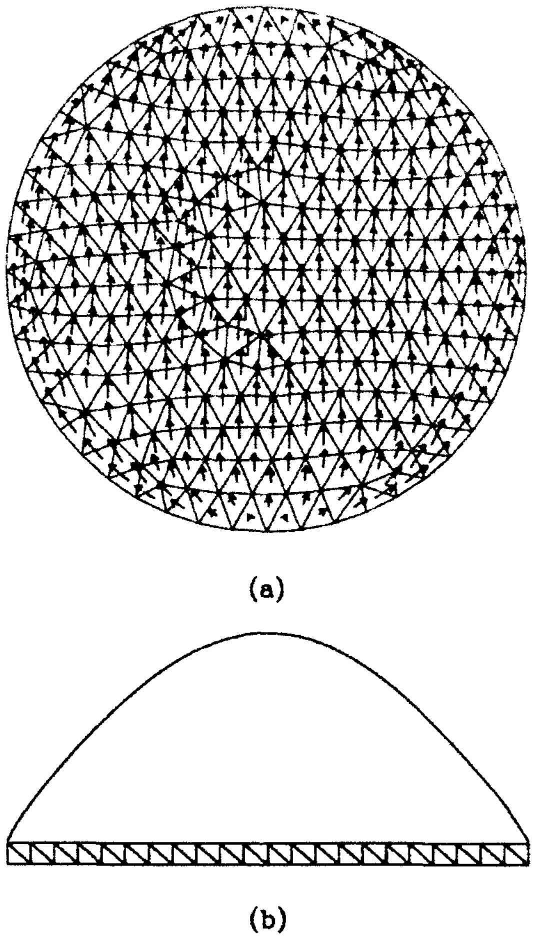

Figure 12: Resonant currents of Antenna 1. (a) Patch electric current (imaginary part). (b) Slot magnetic current (real part of the longitudinal component).

Figs. 12–13 we show plots of the computed patch electric current and the slot magnetic current for Antennas 1 and 2 at their resonant frequencies. Since these currents are in general complex-valued, only the dominant part (real or imaginary, as the case may be) is shown in each case. These figures also illustrate the triangular mesh models used in the analysis. The circular patch of Antenna 1 and the rectangular patch of Antenna 2 were approximated by 394 and 288 triangular elements, respectively. In both cases the slot was modeled by 44 elements. For Antenna 2, this resulted in a 451-by-451 global system matrix in (54), and a computation time of 15 minutes

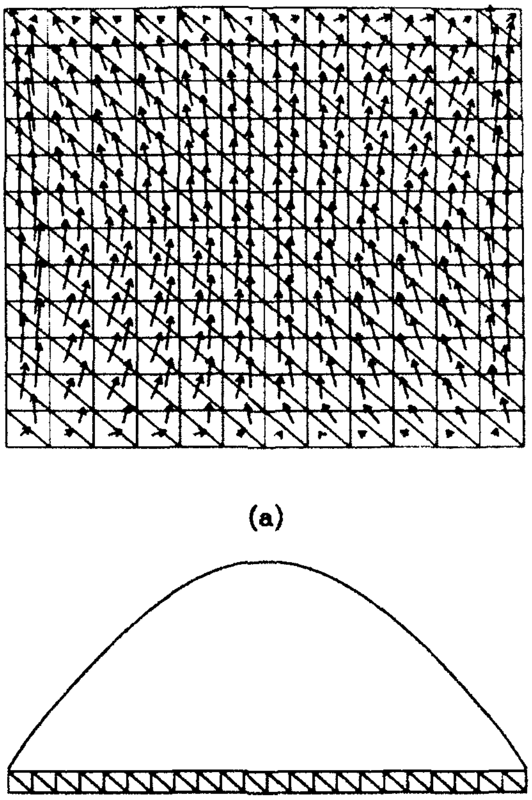

Figure 13: Resonant currents for Antenna 2. (a) Patch electric current (imaginary part). (b) Slot magnetic current (real part of the longitudinal component).

per frequency point on a 12-MIPS computer. In Figs. 14-15, we show the measured and computed far field patterns for the rectangular Antennas 2 and 4. The scallop observed in the measured E-plane patterns is almost certainly caused by the surface wave diffraction at the edges of the finite-size ground plane [26]. This effect is more

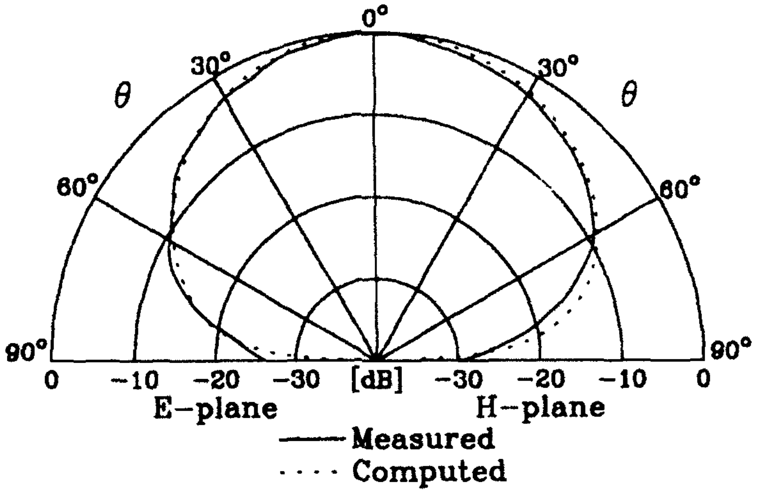

Figure 14: Measured and computed far field patterns for Antenna 2.

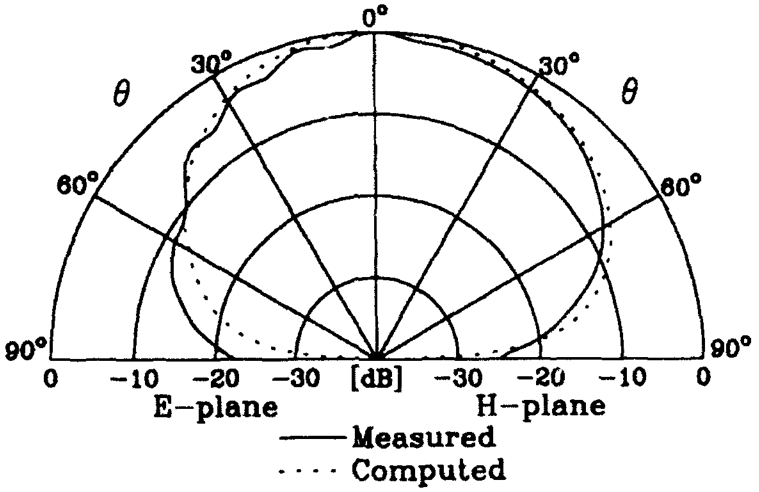

Figure 15: Measured and computed far field patterns for Antenna 4.

pronounced for Antenna 4, because the superstrate increases the intensity of the excited surface wave.

Finally, we present sample results for Antenna 2 under plane wave excitation. In Fig. 16 we plot vs. frequency the magnitude of the dominant mode aperture transmission coefficient T, where the latter is defined in (41). As expected, the peak of transmission occurs at the resonant frequency of the waveguide-driven antenna (see Table 1). In Fig. 17 we plot vs. frequency the monostatic RCS referred to 1 m^2 (the units are dBsm—'decibels above a square meter' [27, p. 160]) for a θ−polarized incident plane wave with $E_\theta^{inc} = 1$ V/m. In addition to the total RCS of the antenna, we also plot the contributions from the microstrip patch and the slot. We note that the first RCS peak is clearly due to the first resonant mode of the patch. At the second peak, which occurs near the resonant frequency of the waveguide-driven antenna, the slot radiation is the dominant effect. We also note that there is an RCS minimum between 10 and 12 GHz, caused by a destructive interference of the patch and slot radiated fields.

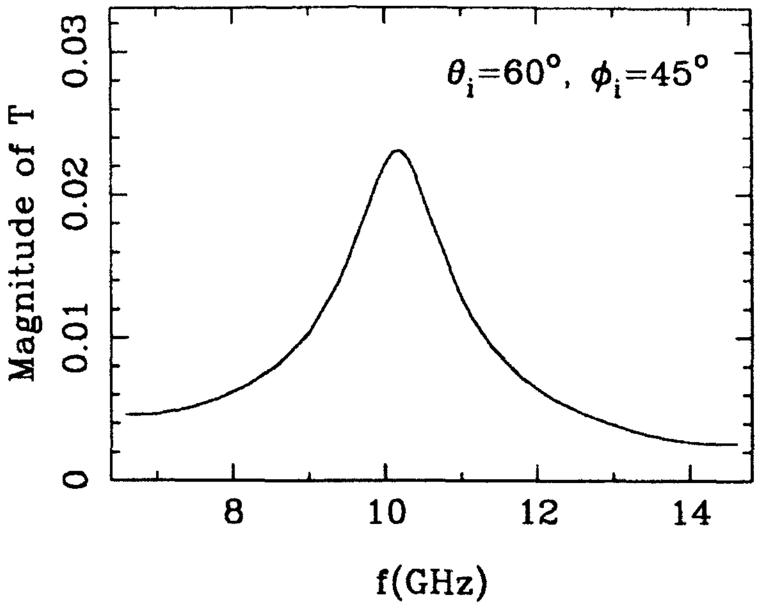

Figure 16: Magnitude of the dominant mode aperture transmission coefficient vs. frequency for Antenna 2.

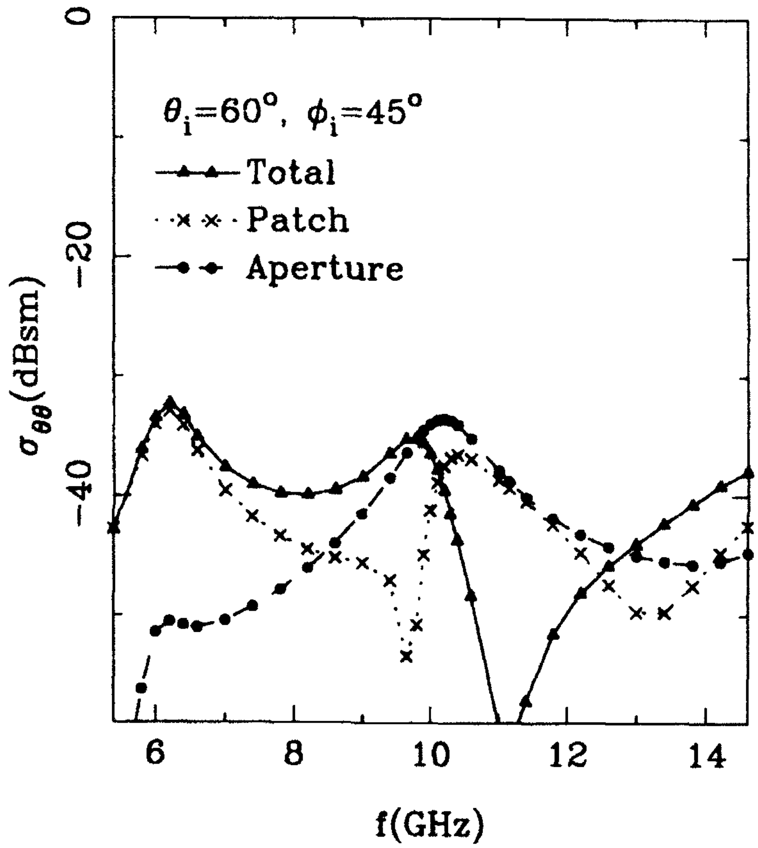

Figure 17: Monostatic RCS of Antenna 2.

6 Summary and Conclusions

We have presented a rigorous integral equation analysis of a microstrip patch antenna excited through an aperture in the mouth of a rectangular waveguide, or illuminated by a plane wave. The substrate and superstrate may comprise any number of isotropic or uniaxial material layers. The patch and the aperture may both be of arbitrary shape. Hence, waveguide-fed microstrip patch antennas of various, possibly irregular shapes, residing in multilayer, possibly uniaxial media, may be analyzed within a single formulation, using the same computer program. The analysis has been validated against experimental and published data. We have also shown that a good impedance match may be achieved in this antenna configuration, but only in a narrow frequency band.

Appendix A

Transmission-Line Analog of Layered Medium

In deriving the integral equations of Sec. 2.1, we have employed a transmission-line network analog of the layered medium, in which each layer is represented by a transmission line section, as illustrated in Fig. 18. This analog comprises two networks,

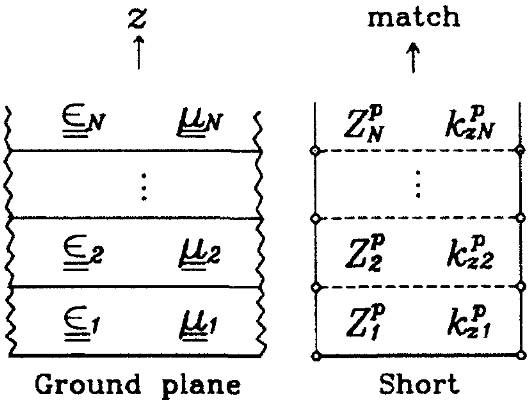

Figure 18: Layered dielectric medium and its transmission-line network analogue.

which arise from the decomposition of the electromagnetic field into two partial fields that are transverse-magnetic (TM) and transverse-electric (TE) to z. The quantities corresponding to these networks are distinguished by the superscripts e and h, respectively. The characteristic impedance and propagation constant of the nth section of the TE and TM transmission lines are given as

$$Z_n^e = \frac{1}{Y_n^e} = \frac{k_o \epsilon_{tn}}{\eta_o k_{zn}^e}, \qquad Z_n^h = \frac{1}{Y_n^h} = \frac{k_{zn}^h}{\mu_{tn} \eta_o k_o} \tag{66}$$

$$k_{zn}^p = \sqrt{k_o^2 \epsilon_{tn} \mu_{tn} - k_\rho^2 / \nu_n^p} \tag{67}$$

Let the network be excited by a 1A shunt current source located at z' in the nth line section of length d_n, as illustrated in Fig. 19a. Then, the voltage $V_i(z \mid z')$ and

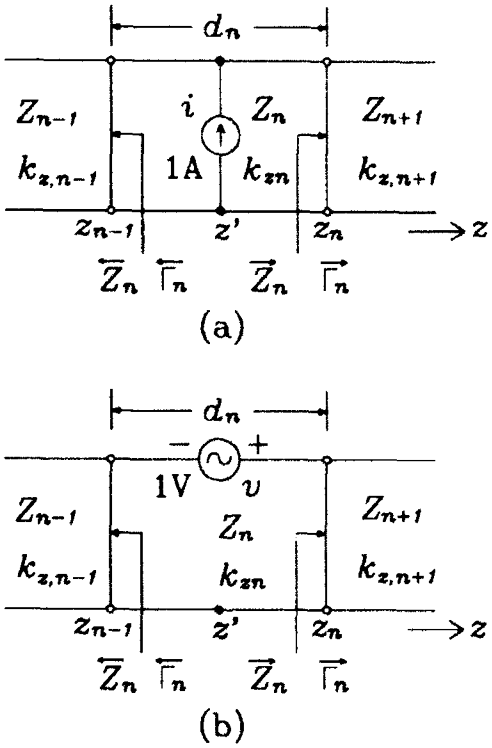

Figure 19: Typical transmission line section with (a) 1A shunt current source and (b) 1V series voltage source.

current $I_i(z\,|\,z')$ at a point z within this line section obey the equations [28, p. 717]

$$\frac{d}{dz}V_i(z\,|\,z') = -jk_{zn}\,Z_n\,I_i(z\,|\,z') \tag{68}$$

$$\frac{d}{dz}I_i(z\,|\,z') = -jk_{zn}\,Y_n\,V_i(z\,|\,z') + \delta(z-z') \tag{69}$$

where δ denotes the delta function. Here and below, we omit the the superscript p for notational simplicity. From (68)–(69), $V_i(z\,|\,z')$ may be expressed in the traveling-wave form

$$\begin{aligned} V_i(z\,|\,z') &= \frac{Z_n\,e^{-jk_{zn}|z-z'|}}{2\left[1-\overleftarrow{\Gamma}_n(z_o)\,\overrightarrow{\Gamma}_n(z_o)\right]} \\ &\quad\cdot\left[1+\overleftarrow{\Gamma}_n(z_o)e^{-j2k_{zn}(z_<-z_o)}\right]\left[1+\overrightarrow{\Gamma}_n(z_o)e^{-j2k_{zn}(z_>-z_o)}\right] \end{aligned} \tag{70}$$

where $z_< \equiv \min(z,z')$, $z_> \equiv \max(z,z')$, and $\overleftarrow{\Gamma}_n(z_o)$ and $\overrightarrow{\Gamma}_n(z_o)$ are the reflection coefficients 'looking to the left' and 'looking to the right,' respectively, at any location z_o within the line section. By means of the translation formula

$$\overset{\rightleftarrows}{\Gamma}_n(z) = \overset{\rightleftarrows}{\Gamma}_n(z_o)\,e^{\pm j2k_{zn}(z-z_o)} \tag{71}$$

where the right and left arrows correspond to the upper and lower signs, respectively, these reflection coefficients can always be expressed in terms of the terminal reflection coefficients, $\overleftarrow{\Gamma}_n$ and $\overrightarrow{\Gamma}_n$, which are related to the corresponding terminal impedances $\overleftarrow{Z}_n$ and $\overrightarrow{Z}_n$ (see Fig. 19) as

$$\overset{\rightleftarrows}{\Gamma}_n = \frac{\overset{\rightleftarrows}{Z}_n - Z_n}{\overset{\rightleftarrows}{Z}_n + Z_n} \tag{72}$$

The voltage $V_v(z\,|\,z')$ and current $I_v(z\,|\,z')$, excited by a 1V series voltage source v in the nth line section (see Fig. 19b), satisfy equations dual to (68)–(69), which are obtained from the latter by making the substitutions: $V_i \rightarrow I_v$, $I_i \rightarrow V_v$, $Z_n \rightarrow Y_n$, and $Y_n \rightarrow Z_n$. Furthermore, it can be shown that the following symmetry and reciprocity relations hold (cf. [28, p. 194])

$$V_i(z\,|\,z') = V_i(z'\,|\,z),\ I_v(z\,|\,z') = I_v(z'\,|\,z),\ V_v(z\,|\,z') = -I_i(z'\,|\,z) \tag{73}$$

As a result, $I_v(z \mid z')$ can be obtained from (70) by replacing in the latter Y_n by Z_n (which also causes the reflection coefficients to change signs). $I_i(z \mid z')$ follows from (68) and (70), and $V_v(z \mid z')$ may then be obtained from the last relation in (73).

The voltage and current on the nth transmission line section that is source-free satisfy the homogeneous form of (68)–(69). From these equations, the voltage at any point z' within the same line section may be found as

$$V(z) = V(z_o)\frac{e^{\mp jk_{zn}(z-z_o)}}{1+\overleftrightarrow{\Gamma}_n(z_o)}\left[1+\overleftrightarrow{\Gamma}_n(z_o)e^{\pm jk_{zn}(z-z_o)}\right] \tag{74}$$

where the upper (lower) sign corresponds to $z > z_o$ ($z < z_o$). In the above, $z_o = z_n$ or $z_o = z_{n+1}$, depending on whether the source is located to left or right, respectively, of the nth line section, and $V(z_o)$ is is the voltage across the line terminals at $z = z_o$. We have omitted the subscript of V in (74), because the latter applies irrespective of the nature of the source, and dropped z' from its argument, because (74) only implicitly depends on the source location, which is outside the line section. The current $I(z)$ corresponding to (74) may be obtained by substituting the latter into (68).

Appendix B

Fourier Transform of a Triangle Shape Function

The Fourier transform of a shape function L_i associated with the nth triangular element is given as

$$\tilde{L}_i = \int_{S_n} L_i\, e^{j\boldsymbol{k}_\rho\cdot\boldsymbol{\rho}}\, dS \tag{75}$$

where $\boldsymbol{k}_\rho = \hat{\boldsymbol{u}}k_\rho$. To evaluate the integral in (75), it is helpful to first convert it to a line integral around the boundary contour, ∂S_n, of S_n (cf. [29], [30], [31]). This is most easily accomplished by noting that

$$e^{j\boldsymbol{k}_\rho\cdot\boldsymbol{\rho}} = \boldsymbol{\nabla}_t \cdot \left(\hat{\boldsymbol{u}}\,\frac{e^{j\boldsymbol{k}_\rho\cdot\boldsymbol{\rho}}}{jk_\rho}\right) \tag{76}$$

and by making use of the divergence theorem. As a result, when $k_\rho \neq 0$, we obtain

$$\tilde{L}_i = \frac{1}{2Ak_\rho^2} \oint_{\partial S_n} (2jk_\rho A L_i + \hat{\boldsymbol{v}} \cdot \boldsymbol{\ell}_i) e^{j\boldsymbol{k}_\rho \cdot \boldsymbol{\rho}} \hat{\boldsymbol{u}} \cdot \hat{\boldsymbol{n}}\, d\ell \tag{77}$$

where $\hat{\boldsymbol{v}} = \hat{\boldsymbol{z}} \times \hat{\boldsymbol{u}}$ and $\hat{\boldsymbol{n}}$ denotes a unit vector normal to ∂S_n at ℓ in the plane and pointing out of S_n. The integral in (77) is easily evaluated in the local coordinateds, if one notes that when ℓ is on edge i, $\hat{\boldsymbol{n}} = \hat{\boldsymbol{n}}_i$, $0 \leq L_k \leq 1$, $L_i = 0$, $L_j = 1 - L_k$, and $d\ell = \ell_i dL_k$ (see Fig. 3). Also, in that case $\boldsymbol{\rho} = \boldsymbol{\rho}_j + \boldsymbol{\varrho}_j$, where $\boldsymbol{\varrho}_j$ is a vector from node j to the point ℓ on edge i of the element. The resulting close-form expression for $\tilde{L}_i$ is given in (65).

Acknowledgments

The authors are grateful to Dr. Chung-I G. Hsu for many valuable discussions and to Fan Lu, Julio Navarro, and Ming-Yi Li for their assistance in the experiment. This work was supported in part by the Office of Naval Research under Contract N00014-90-J-1197.

References

[1] I. J. Bahl and P. Bhartia, *Microstrip Antennas*. Dedham, MA: Artech House, 1980.

[2] J. R. James, P. S. Hall, and C. Wood, *Microstrip Antenna Theory and Design*. London: Peter Peregrinus, 1981.

[3] K. Chang, "Millimeter-wave planar integrated circuits and subsystems," in *Millimeter Components and Techniques, Part V - Infrared and Millimeter Waves* (K. J. Button, ed.), vol. 14, pp. 79–187, New York: Academic Press, 1985.

[4] P. Bhartia, K. V. S. Rao, and R. S. Tomar, *Millimeter-Wave Microstrip and Printed Circuit Antennas*. Norwood, MA: Artech House, 1991.

[5] K. C. Gupta, R. Garg, and R. Chadha, *Computer-Aided Design of Microwave Circuits.* Norwood, MA: Artech House, 1981.

[6] M. Kanda, D. C. Chang, and D. H. Greenlee, "The characteristics of iris-fed millimeter-wave rectangular microstrip patch antennas," *IEEE Trans. Electromagnet. Compat.*, vol. EMC-27, pp. 212–220, Nov. 1985.

[7] R. F. Harrington, *Time-Harmonic Electromagnetic Field.* New York: McGraw-Hill, 1961.

[8] C. M. Butler, Y. Rahmat-Samii, and R. Mittra, "Electromagnetic penetration through apertures in conducting surfaces," *IEEE Trans. Antennas Propagat.*, vol. AP-26, pp. 82–93, Jan. 1978.

[9] K. A. Michalski and D. Zheng, "Integral equation analysis of arbitrarily shaped microstrip structures," Technical Report for ONR, Contract N00014-90-J-1197, Department of Electrical Engineering, Texas A&M University, Apr. 1990.

[10] J. Van Bladel, *Electromagnetic Fields.* New York: Hemisphere, 1985.

[11] L. Lapidus and G. F. Pinder, *Numerical Solution of Partial Differential Equations in Science and Engineering.* New York: Wiley, 1982.

[12] S. M. Rao, D. R. Wilton, and A. W. Glisson, "Electromagnetic scattering by surfaces of arbitrary shape," *IEEE Trans. Antennas Propagat.*, vol. AP-30, pp. 409–418, May 1982.

[13] D. R. Wilton, S. M. Rao, A. W. Glisson, D. H. Schaubert, O. M. Al-Bundak, and C. M. Butler, "Potential integrals for uniform and linear source distributions on polygonal and polyhedral domains," *IEEE Trans. Antennas Propagat.*, vol. AP-32, pp. 276–281, Mar. 1984.

[14] J. R. Mosig, R. C. Hall, and F. E. Gardiol, "Numerical analysis of microstrip patch antennas," in *Handbook of Microstrip Antennas* (J. R. James and P. S. Hall, eds.), pp. 391–453, London: Peter Peregrinus, 1989.

[15] J. R. Mosig and F. E. Gardiol, "A dynamical radiation model for microstrip structures," in *Adv. Electron. Electron Phys.* (P. W. Hawkes, ed.), vol. 59, pp. 139–237, New York: Academic Press, 1982.

[16] W. C. Chew and Q. Liu, "Resonance of the axial-symmetric modes in microstrip disk resonators," *J. Math. Phys.*, vol. 21, pp. 583–591, Mar. 1980.

[17] N. W. Montgomery, *Periodic Structures in Stratified Media – A Mixed Potential Formulation.* PhD thesis, University of Houston, Houston, Texas, May 1991.

[18] "Network analysis–applying the HP 8510B TRL calibration for non-coaxial measurements." HP Product Note 8510-8, Palo Alto, CA, Oct. 1987.

[19] E. H. Newman and D. Forrai, "Scattering from a microstrip patch," *IEEE Trans. Antennas Propagat.*, vol. AP-35, pp. 245–251, Mar. 1987.

[20] D. M. Pozar, "Radiation and scattering from a microstrip patch on a uniaxial substrate," *IEEE Trans. Antennas Propagat.*, vol. AP-35, pp. 613–621, June 1987.

[21] G. T. Ruck, D. E. Barrick, W. D. Stuart, and C. K. Krichbaum, eds., *Radar Cross Section Handbook*, vol. 2. New York: Plenum Press, 1970.

[22] C. M. Bulter, "The equivalent radius of a narrow conducting strip," *IEEE Trans. Antennas Propagat.*, vol. AP–30, pp. 755–758, July 1982.

[23] D. M. Pozar, *Personal Computer Aided Antenna Design.* Antenna Design Associates, Inc., Leverett, MA, Dec. 1991.

[24] R. F. Harrington and J. R. Mautz, "Electromagnetic coupling through apertures by the generalized admittance approach," *Computer Physics Communications*, vol. 68, pp. 19–42, 1990.

[25] D. G. Bodnar and D. T. Paris, "New variational principle in electromagnetics," *IEEE Trans. Antennas Propagat.*, vol. AP-18, pp. 216–223, Mar. 1970.

[26] S. A. Bokhari, J. R. Mosig, and F. E. Gardiol, "Radiation pattern computation of microstrip antennas on finite size ground planes," *IEE Proc., Pt. H*, pp. 278–286, 1992.

[27] E. F. Knott, J. F. Shaeffer, and M. T. Tuley, *Radar Cross Section: Its Prediction, Measurement and Reduction*. Norwood, MA: Artech House, 1985.

[28] L. B. Felsen and N. Marcuvitz, *Radiation and Scattering of Waves*. Englewood Cliffs, N.J.: Prentice Hall, 1973.

[29] B. Houshmand, W. C. Chew, and S. W. Lee, "Fourier transform of a linear distribution with triangular support and its applications in electromagnetics," *IEEE Trans. Antennas Propagat.*, vol. 39, pp. 252–254, Feb. 1991

[30] K. McInturf and P. S. Simon, "The Fourier transform of linearly varying functions with polygonal support," *IEEE Trans. Antennas Propagat.*, vol. 39, pp. 1441–1443, Sept. 1991.

[31] T.-S. Horng, N. G. Alexópoulos, S.-C. Wu, and H.-Y. Yang, "Full-wave spectral-somain analysis for open microstrip discontinuities of arbitrary shape including radiation and surface-wave losses," *Int. J. Microwave Millimeter-Wave Computer-Aided Eng.*, vol. 2, no. 4, pp. 224–240, 1992.

Analysis of Multiconductor Transmission Lines of Arbitrary Cross Section in Multilayered Uniaxial Media[*]

by

Chung-I G. Hsu[†], Roger F. Harrington[†], Krzysztof A. Michalski[‡], and Dalian Zheng[§]

Abstract — A mixed-potential electric field integral equation is formulated and applied in conjunction with the method of moments to analyze a transmission-line system consisting of multiple conducting strips of arbitrary cross section embedded in a stratified medium with or without top and/or bottom ground planes. Each layer of the medium is possibly uniaxially anisotropic, with its optical axis perpendicular to the dielectric interfaces. Computed dispersion curves and modal currents are presented and, when possible, are compared with data available in the literature.

1 Introduction

Recent advances in integrated circuit technology have made microstrips, striplines, coplanar strips, and similar wave-guiding structures attractive not only in microwave and millimeter-wave applications, but also in high-speed digital computers. The conductors used as interconnects between *VLSI* devices may be very close to one another, which necessitates treating them as a single transmission line capable of supporting several modes, rather than several isolated transmission lines. The interconnects in modern microwave and millimeter-wave integrated circuits tend to have trapezoidal cross sections due to etching undercuts or as a result of the epitaxial growth process

---

[*] This work was supported in part by the U.S. Office of Naval Research (ONR) under Contract N00014-90-J-1197.

[†] C. G. Hsu and R. F. Harrington are with the Department of Electrical and Computer Engineering, Syracuse University, Syracuse, NY 13244-1240.

[‡] K. A. Michalski is with the Electromagnetics & Microwave Laboratory, Department of Electrical Engineering, Texas A&M University, College Station, TX 77843-3128.

[§] D. Zheng was with Texas A&M University. He is now with Integrated Engineering Software, Inc., 347-435 Ellice Ave., Winnipeg, Manitoba, Canada, R3B 1Y6.

[1], [2], and cannot always be considered infinitely thin. These interconnects are supported by a dielectric substrate, which often exhibits uniaxial anisotropy, introduced in the manufacturing process [3].

Many numerical procedures have been successfully applied in the past two decades to obtain frequency-dependent characteristics of microstrips and striplines, but most of them are only applicable to (or optimized for) planar conducting strips of zero thickness (cf. [4], [5], [6], [7], [8], [9], [10], [11], [12], [13], [14], [15], [16], [17], to name just a few). Relatively few papers have considered laterally open microstrip structures with conductors of other cross section shapes, such as rectangular [18], trapezoidal [19], [20], circular [21], [22], or rectangular with semi-circular edges [23]. The concept of equivalent width has often been employed to approximately take into account the strip thickness [24]. However, it has recently been demonstrated, using a rigorous mixed-potential integral equation (MPIE) approach [19], that the dispersion curve for a finite-thickness microstrip lies below that of a microstrip with zero thickness, which is opposite to what is observed when the concept of equivalent width is used.

In this paper, we use an MPIE approach, which was originally developed for objects in isotropic media [25], [19], [26], and recently extended to objects in uniaxial media [27], to analyze a transmission-line system composed of multiple conductors of finite thickness and arbitrary cross section, embedded in a medium consisting of an arbitrary number of planar, possibly uniaxially anisotropic, dielectric layers. Computed dispersion curves and modal currents for bound modes are presented and, when possible, are compared with data available in the literature.

2 Formulation

The cross-sectional view of the structure under consideration is shown in Fig. 1. The medium consists of N planar, homogeneous dielectric layers, with the interfaces parallel to the xy plane. Each layer, say the nth, is characterized by permeability μ_{rn} and by transverse and longitudinal permittivities ε_{tn} and ε_{zn}, respectively, all relative to free space. The top layer of the medium may extend to $+\infty$ along the z axis, or be shielded by a ground plane made of a perfect electric conductor (PEC). Similarly, the

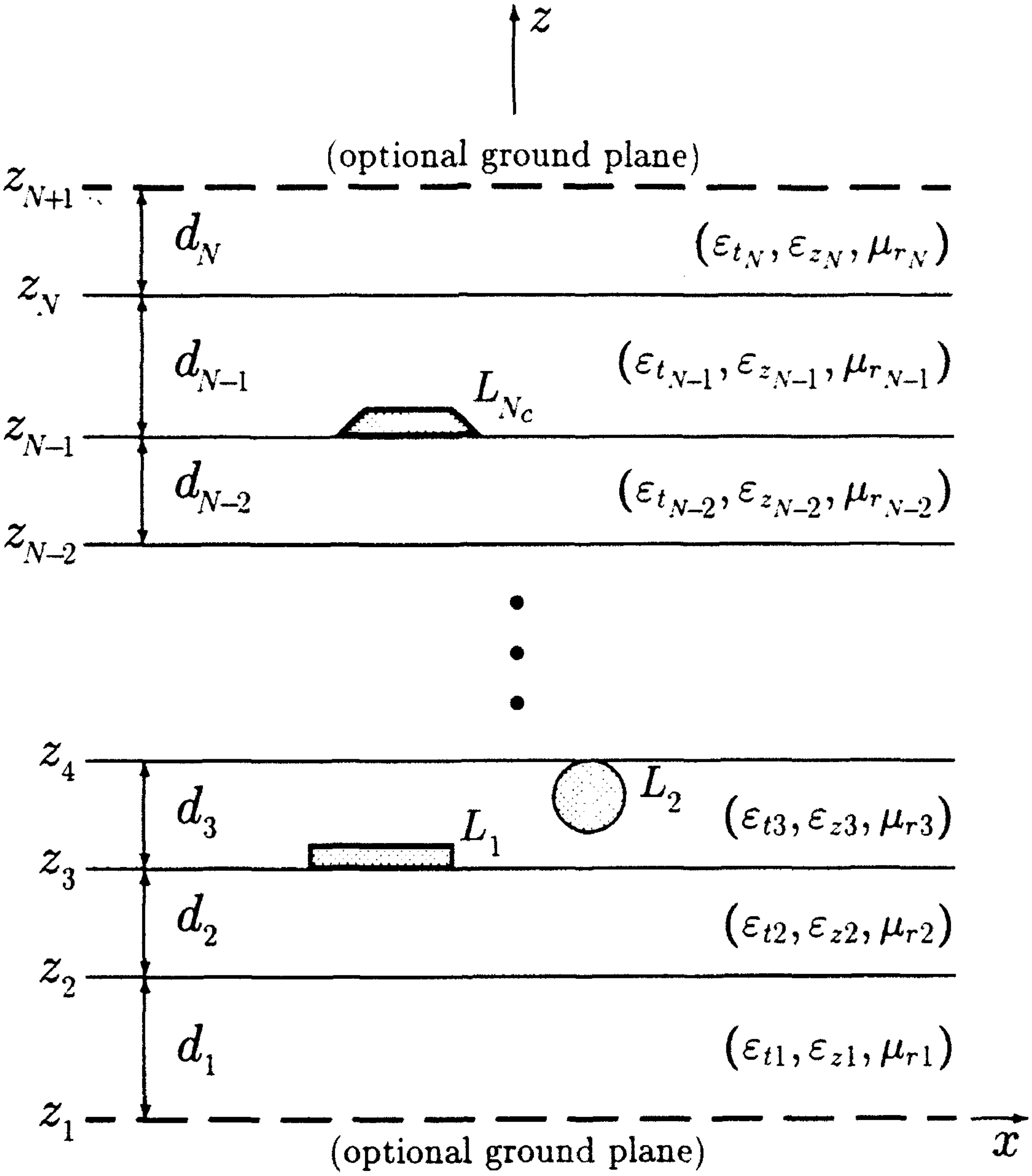

Figure 1: Cross-sectional view of a multiconductor transmission line embedded in a stratified uniaxial medium.

bottom layer may extend to $-\infty$ along the z axis, or be shielded by a PEC ground plane. There are N_c PEC strips embedded in the layered medium, all uniform and of infinite extent along the y axis, but of arbitrary cross section shape. An $e^{j\omega t}$ time dependence is assumed and suppressed throughout.

Since we are interested in modes propagating in the y direction, we may assume that the phase factor $e^{-j\beta y}$ is common to all the fields and currents, where β is the propagation constant to be determined. Hence, we may express the surface current density as

$$\boldsymbol{J}(\boldsymbol{r}) = \boldsymbol{J}(\ell)\, e^{-j\beta y} \tag{1}$$

where ℓ is the arc-length coordinate on the contours of the conductor cross sections. By enforcing the condition that the tangential electric field must vanish at the surface of the conductors, we obtain an electric field integral equation (EFIE) of the form

$$\hat{\boldsymbol{u}}_n \times \sum_{i=1}^{N_c} \int_{L_i} \underline{\underline{\boldsymbol{G}}}^{EJ}(x,z|x',z') \cdot \boldsymbol{J}(\ell')\, d\ell' = 0, \quad \boldsymbol{r} \in L_n,\ n = 1,2,\cdots,N_c \tag{2}$$

where $\underline{\underline{\boldsymbol{G}}}^{EJ}(x,z|x'z')$, with $x \equiv x(\ell)$ and $z \equiv z(\ell)$, is the electric field dyadic Green's function of the layered medium [27], and where $\hat{\boldsymbol{u}}_n$ denotes an outward unit vector normal to the boundary L_n of the nth conductor. In the above and throughout, primed quantities denote source coordinates, unit vectors are distinguished by carets, and dyadics by double underlines.

The severe source-region singularity of the kernel of the EFIE (2) makes it unsuitable for a direct application of the method of moments [28], [29]. Hence, we first transform it into the MPIE form,

$$\hat{\boldsymbol{u}}_n \times \sum_{i=1}^{N_c} \{\boldsymbol{A}_i(x,z) + (\boldsymbol{\nabla}_\ell - \hat{\boldsymbol{y}} j\beta)\Phi_i(x,z)\} = 0, \quad \boldsymbol{r} \in L_n,\ n = 1,2,\cdots,N_c \tag{3}$$

where $\boldsymbol{\nabla}_\ell$ is the transverse (to y) part of the operator nabla, and where

$$\boldsymbol{A}_i(x,z) = \int_{L_i} \underline{\underline{\boldsymbol{K}}}^{A}(x,z|x',z') \cdot \boldsymbol{J}(\ell')\, d\ell' \tag{4}$$

and

$$\Phi_i(x,z) = \int_{L_i} K^{\phi}(x,z|x',z')\,(\boldsymbol{\nabla}'_\ell - \hat{\boldsymbol{y}}\, j\beta) \cdot \boldsymbol{J}(\ell')\, d\ell' \tag{5}$$

are the magnetic vector potential and the electric scalar potential, respectively, due to the surface current on the ith conductor. These potentials are not unique, as discussed in [30], [26], [27]. In the latter reference, two different MPIE formulations, referred to as the "traditional" and the "alternative," are developed for arbitrarily shaped conductors in layered uniaxial media.

The expressions for the dyadic kernel $\underline{\underline{\boldsymbol{K}}}^A$ and the scalar kernel K^Φ comprise improper spectral integrals of the form

$$\mathcal{S}_{\substack{cn\\sn}}\{f(k_x)\} = \frac{1}{\pi}\int_0^\infty f(k_x)\begin{bmatrix}\cos k_x(x-x')\\ \sin k_x(x-x')\end{bmatrix} k_x^n\, dk_x \tag{6}$$

where k_x is the Fourier transform domain counterpart of x, and where the subscripts c and s are associated with the cosine and sine functions, respectively, and n assumes the values 0 or 1. Using this notation, the nonzero elements of $\underline{\underline{\boldsymbol{K}}}^A$ and K^Φ for the traditional MPIE formulation [31], [27] can be expressed as

$$K^A_{xx}(x,z|x',z') = \mathcal{S}_{c0}\left\{V^h_{i,mn}(z|z')\right\} \tag{7}$$

$$K^A_{zx}(x,z|x',z') = -jk_0\eta_0\,\mathcal{S}_{s1}\left\{\frac{\mu_{rm}}{k_\rho^2}\left[I^h_{i,mn}(z|z') - I^e_{i,mn}(z|z')\right]\right\} \tag{8}$$

$$K^A_{zy}(x,z|x',z') = \beta k_0\eta_0\,\mathcal{S}_{c0}\left\{\frac{\mu_{rm}}{k_\rho^2}\left[I^h_{i,mn}(z|z') - I^e_{i,mn}(z|z')\right]\right\} \tag{9}$$

$$K^A_{xz}(x,z|x',z') = -jk_0\eta_0\,\mathcal{S}_{s1}\left\{\frac{\mu_{rn}}{k_\rho^2}\left[V^h_{v,mn}(z|z') - V^e_{v,mn}(z|z')\right]\right\} \tag{10}$$

$$K^A_{yz}(x,z|x',z') = \beta k_0\eta_0\,\mathcal{S}_{c0}\left\{\frac{\mu_{rn}}{k_\rho^2}\left[V^h_{v,mn}(z|z') - V^e_{v,mn}(z|z')\right]\right\} \tag{11}$$

$$\begin{aligned} K^A_{zz}(x,z|x',z') \;=\; \eta_0^2\,\mathcal{S}_{c0}\Bigg\{&\left[\frac{\mu_{rm}}{\varepsilon_{zn}} - \frac{\mu_{rn}}{\varepsilon_{tm}}\left(\frac{k^e_{zm}}{k_\rho}\right)^2\right] I^e_{v,mn}(z|z') \\ &+ \mu_{rm}\mu_{rn}\left(\frac{k_0}{k_\rho}\right)^2 I^h_{v,mn}(z|z')\Bigg\} \end{aligned} \tag{12}$$

$$K^\Phi(x,z|x',z') = \mathcal{S}_{c0}\left\{\frac{1}{k_\rho^2}\left[V^h_{i,mn}(z|z') - V^e_{i,mn}(z|z')\right]\right\} \tag{13}$$

where η_0 and k_0 denote, respectively, the intrinsic impedance and wavenumber of free space, and $k_\rho^2 = k_x^2 + \beta^2$. The subscripts m and n in the above indicate that the observation point (x, z) is in the mth layer, and the source point (x', z') in the nth layer. In deriving (7)–(13), use has been made of the transmission-line network analog of the layered medium [32, Ch. 2], which is illustrated in Fig. 2 for a three-layer geometry. This network actually represents two networks (having identical configurations, but in general different propagation constants and characteristic impedances) that arise from the decomposition of the electromagnetic field into partial fields that are transverse-magnetic (TM) and transverse-electric (TE) to $\hat{\mathbf{z}}$ [32], [33]. The superscript p in Fig. 2 stands for e or h, which designate, respectively, the quantities associated with the TM and TE networks. The propagation constants of the nth transmission line section are found as

$$k_{zn}^e = \sqrt{k_0^2 \varepsilon_{tn} \mu_{rn} - \frac{\varepsilon_{tn}}{\varepsilon_{zn}} k_\rho^2}, \quad k_{zn}^h = \sqrt{k_0^2 \varepsilon_{tn} \mu_{rn} - k_\rho^2} \tag{14}$$

where the branch of the square root is determined by the condition that $\mathrm{Im}\{k_{zn}^p\} < 0$. The corresponding characteristic impedances (and admittances) are given as

$$Z_n^e \equiv \frac{1}{Y_n^e} = \frac{\eta_0 k_{zn}^e}{k_0 \varepsilon_{tn}}, \quad Z_n^h \equiv \frac{1}{Y_n^h} = \frac{k_0 \eta_0 \mu_{rn}}{k_{zn}^h} \tag{15}$$

In (7)–(13), $V_{i,mn}^p(z|z')$ and $I_{i,mn}^p(z|z')$ denote, respectively, the voltage and current at z on the mth transmission line section, due to a 1 A current source at z' on the nth line section. Similarly, $V_{v,mn}^p(z|z')$ and $I_{v,mn}^p(z|z')$ denote, respectively, the voltage and current at z on the mth transmission line section, due to a 1 V voltage source at z' on the nth section. These transmission-line Green's functions are derived in the appendix for a medium with an arbitrary number of layers.

3 Numerical Method

In this section, the method of moments [28], [29] is employed to solve the MPIE (3) for the multiconductor transmission-line problem of Fig. 1. As the first step of the numerical procedure, we approximate the cross section contours of the conductors by

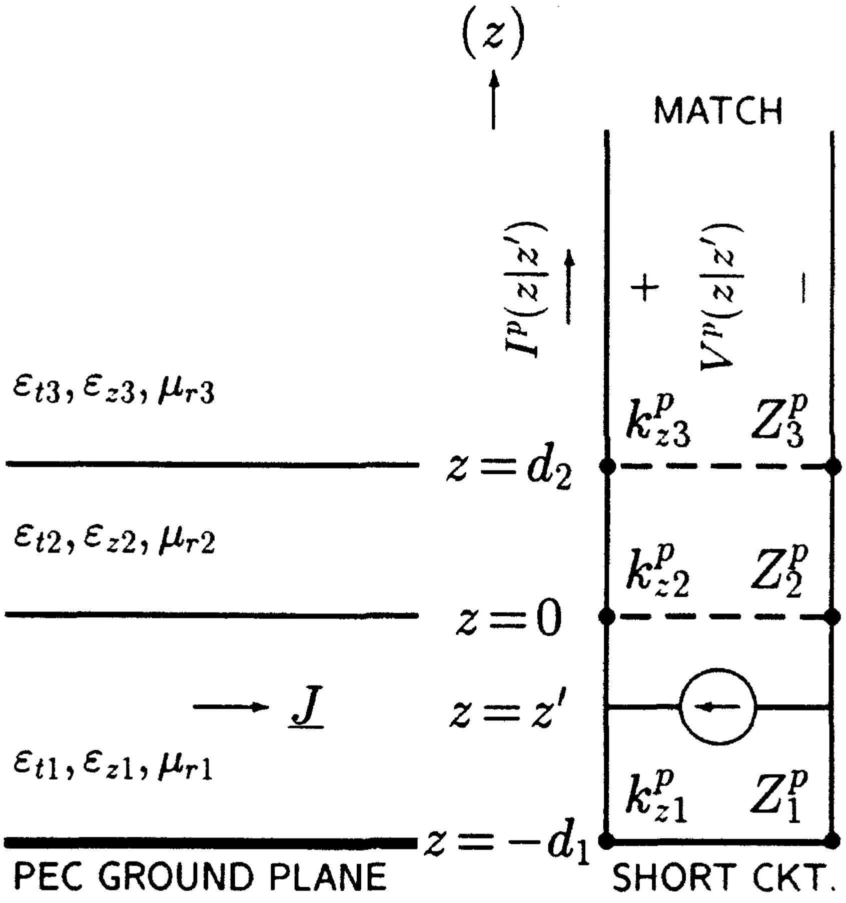

Figure 2: Transmission-line analogue of a layered medium.

piecewise linear segments, as illustrated in Fig. 3. The arc-length coordinate ℓ will now be associated with the approximated contours, instead of the original ones. The method of moments requires that the unknown currents be expanded in terms of a set of known basis functions with unknown coefficients, viz:

$$\boldsymbol{J}_t^p(\ell) = \sum_j I_j^{p,t}\boldsymbol{\Lambda}_j^p(\ell), \quad J_y^p(\ell) = \sum_j I_j^{p,y}\Pi_j^p(\ell), \quad p = 1, 2, \cdots, N \tag{16}$$

where

$$\boldsymbol{\Lambda}_j^p(\ell) = \begin{cases} \hat{\boldsymbol{\ell}}_{j-\frac{1}{2}}^p \dfrac{\ell - \ell_{j-1}^p}{\ell_j^p - \ell_{j-1}^p}, & \ell_{j-1}^p < \ell < \ell_j^p \\ \hat{\boldsymbol{\ell}}_{j+\frac{1}{2}}^p \dfrac{\ell_{j+1}^p - \ell}{\ell_{j+1}^p - \ell_j^p}, & \ell_j^p < \ell < \ell_{j+1}^p \\ 0, & \text{otherwise} \end{cases} \tag{17}$$

with

$$\hat{\boldsymbol{\ell}}_{j+\frac{1}{2}}^p = \frac{\boldsymbol{r}_{j+1}^p - \boldsymbol{r}_j^p}{\Delta_{j+1}^p}, \quad \Delta_{j+1}^p = |\boldsymbol{r}_{j+1}^p - \boldsymbol{r}_j^p| \tag{18}$$

and

$$\Pi_j^p(\ell) = \begin{cases} 1, & \ell_{j-1}^p < \ell < \ell_j^p \\ 0, & \text{otherwise} \end{cases} \tag{19}$$

In the above expressions, the subscript j and the superscript p signify quantities related to the jth expansion function or segment on the pth conductor (the superscript p is omitted in Fig. 3 for simplicity).

The MPIE (3) is next tested with $\hat{\boldsymbol{y}}\Pi_i^p$ and $\boldsymbol{\Lambda}_i^p$. In this process, the transverse nabla operator in (3) is transferred to operate on the testing function by applying Green's first identity, viz:

$$\begin{aligned} \int \boldsymbol{\Lambda}_i^p(\ell)\cdot\boldsymbol{\nabla}_\ell\Phi(x,z)d\ell &= -\int\left[\boldsymbol{\nabla}_\ell\cdot\boldsymbol{\Lambda}_i^p(\ell)\right]\Phi(x,z)d\ell \\ &= -\int\left[\frac{\Pi_i^p(\ell)}{\Delta_i^p} - \frac{\Pi_{i+1}^p(\ell)}{\Delta_{i+1}^p}\right]\Phi(x,z)d\ell \end{aligned} \tag{20}$$

To save computer time, the following approximations are used in the testing procedure:

$$\int \Pi_i^p(\ell)f(\ell)d\ell \approx \Delta_i^p f(\ell_{i-\frac{1}{2}}^p) \tag{21}$$

$$\int \boldsymbol{\Lambda}_i^p(\ell)f(\ell)d\ell \approx \frac{1}{2}\left[\hat{\boldsymbol{\ell}}_{i-\frac{1}{2}}^p\Delta_i^p f(\ell_{i-\frac{1}{2}}^p) + \hat{\boldsymbol{\ell}}_{i+\frac{1}{2}}^p\Delta_{i+1}^p f(\ell_{i+\frac{1}{2}}^p)\right] \tag{22}$$

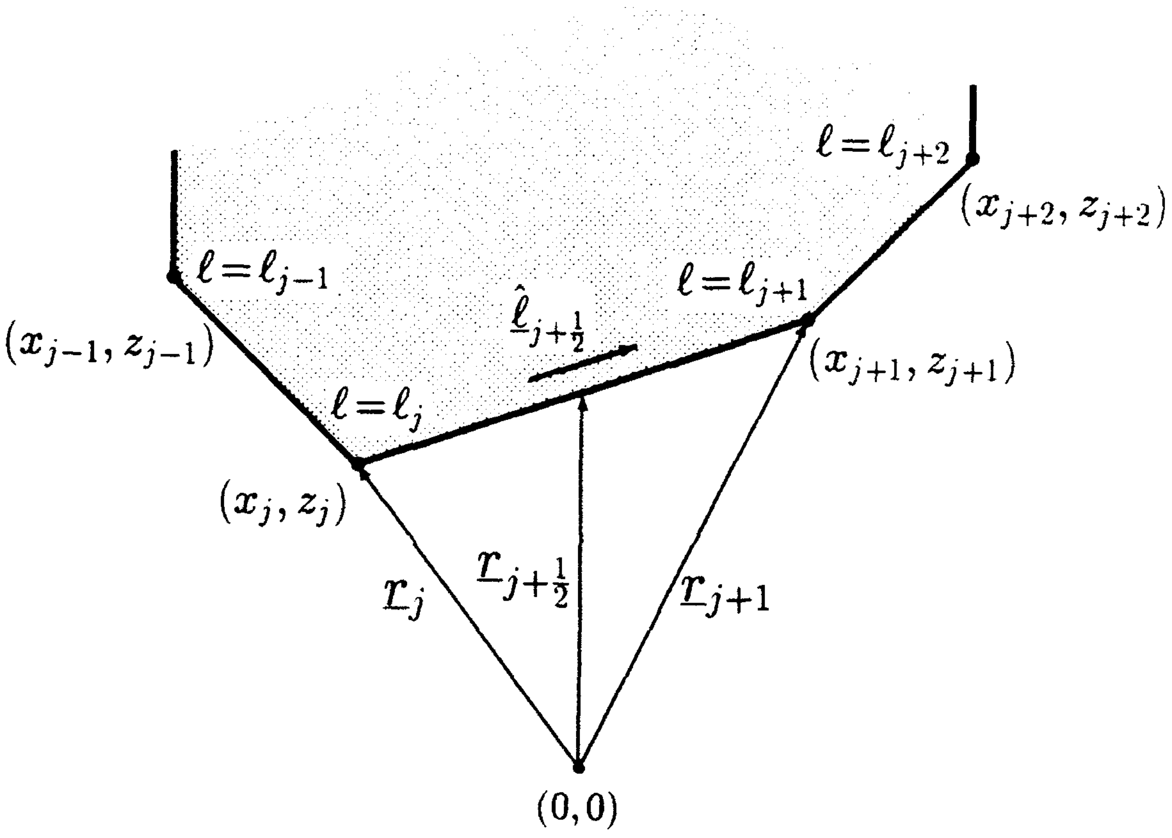

Figure 3: Linear segmentation model of a contour.

where $f(\ell)$ represents the scalar potential $\Phi(x,z)$, or a component of the vector potential $\boldsymbol{A}(x,z)$, and where $\ell^p_{i+\frac{1}{2}}$ is the arc-length coordinate of a point specified by the position vector (cf. Fig. 3)

$$\boldsymbol{r}^p_{i+\frac{1}{2}} = \hat{\boldsymbol{x}}\, x^p_{i+\frac{1}{2}} + \hat{\boldsymbol{z}}\, z^p_{i+\frac{1}{2}} = \frac{\boldsymbol{r}^p_i + \boldsymbol{r}^p_{i+1}}{2} \tag{23}$$

Furthermore, when computing the magnetic vector potential due to $\boldsymbol{A}^p_j$, we approximate the resulting integral as

$$\int \underline{\underline{\boldsymbol{K}}}^A(x,z|x',z')\cdot\boldsymbol{A}^p_j(\ell')d\ell' \approx \frac{1}{2}\int \underline{\underline{\boldsymbol{K}}}^A(x,z|x',z')\cdot\left[\hat{\boldsymbol{\ell}}^p_{j-\frac{1}{2}}\Pi^p_j(\ell') + \hat{\boldsymbol{\ell}}^p_{j+\frac{1}{2}}\Pi^p_{j+1}(\ell')\right] d\ell' \tag{24}$$

As a final step, we substitute the expansions (16) into the tested form of (3) to convert it into a homogeneous matrix equation for the current expansion coefficients. Assuming, for simplicity, that there are only two conductors, this equation has the form

$$\begin{bmatrix} \left[Z^{11,tt}_{ij}\right] & \left[Z^{11,ty}_{ij}\right] & \left[Z^{12,tt}_{ij}\right] & \left[Z^{12,ty}_{ij}\right] \\ \left[Z^{11,yt}_{ij}\right] & \left[Z^{11,yy}_{ij}\right] & \left[Z^{12,yt}_{ij}\right] & \left[Z^{12,yy}_{ij}\right] \\ \left[Z^{21,tt}_{ij}\right] & \left[Z^{21,ty}_{ij}\right] & \left[Z^{22,tt}_{ij}\right] & \left[Z^{22,ty}_{ij}\right] \\ \left[Z^{21,yt}_{ij}\right] & \left[Z^{21,yy}_{ij}\right] & \left[Z^{22,yt}_{ij}\right] & \left[Z^{22,yy}_{ij}\right] \end{bmatrix} \begin{bmatrix} \left[I^{1,t}_j\right] \\ \left[I^{1,y}_j\right] \\ \left[I^{2,t}_j\right] \\ \left[I^{2,y}_j\right] \end{bmatrix} = \begin{bmatrix} [0] \\ [0] \\ [0] \\ [0] \end{bmatrix} \tag{25}$$

with the matrix elements given as

$$\begin{aligned} Z^{pq,tt}_{ij} &= \frac{\Delta^p_i}{4}\left(A^{pq,tt}_{i,j} + A^{pq,tt}_{i,j+1}\right) + \frac{\Delta^p_{i+1}}{4}\left(A^{pq,tt}_{i+1,j} + A^{pq,tt}_{i+1,j+1}\right) \\ &- \frac{1}{\Delta^q_j}\left(\Phi^{pq}_{i,j} - \Phi^{pq}_{i+1,j}\right) + \frac{1}{\Delta^q_{j+1}}\left(\Phi^{pq}_{i,j+1} - \Phi^{pq}_{i+1,j+1}\right) \end{aligned} \tag{26}$$

$$Z^{pq,ty}_{ij} = \frac{\Delta^p_i}{2}A^{pq,ty}_{i,j} + \frac{\Delta^p_{i+1}}{2}A^{pq,ty}_{i+1,j} + j\beta\left(\Phi^{pq}_{i,j} - \Phi^{pq}_{i+1,j}\right) \tag{27}$$

$$Z^{pq,yt}_{ij} = \frac{\Delta^p_i}{2}\left(A^{pq,yt}_{i,j} + A^{pq,yt}_{i,j+1}\right) - j\beta\left(\frac{\Delta^p_i}{\Delta^q_j}\Phi^{pq}_{i,j} - \frac{\Delta^p_i}{\Delta^q_{j+1}}\Phi^{pq}_{i,j+1}\right) \tag{28}$$

$$Z^{pq,yy}_{ij} = \Delta^p_i A^{pq,yy}_{i,j} - \beta^2\Delta^p_i\Phi^{pq}_{i,j} \tag{29}$$

where the index j, when used as a subscript, should not be confused with the imaginary unit. In (26)–(29), we have introduced the notation

$$A^{pq,\tau\eta}_{ij} = \int_{\ell^q_{j-1}}^{\ell^q_j} \hat{\boldsymbol{\tau}}\cdot\underline{\underline{\boldsymbol{K}}}^A(x^p_{i-\frac{1}{2}}, z^p_{i-\frac{1}{2}}|x',z')\cdot\hat{\boldsymbol{\eta}}\, d\ell' \tag{30}$$

$$\Phi_{ij}^{pq} = \int_{\ell_{j-1}^{q}}^{\ell_{j}^{q}} K^{\varphi}(x_{i-\frac{1}{2}}^{p}, z_{i-\frac{1}{2}}^{p} | x', z') d\ell' \tag{31}$$

where $(\tau, \eta) = (t, y)$, and $\hat{\boldsymbol{t}} \equiv \hat{\boldsymbol{t}}(\ell) = \hat{\boldsymbol{\ell}}_{j+\frac{1}{2}}^{p}$ for $\ell_j^p < \ell < \ell_{j+1}^p$. In the general case with N_c conductors, the matrix in (25) comprises $4N_c^2$ blocks of submatrices.

The kernel functions in the above have been defined by the spectral integrals (7)-(13), which are evaluated by a composite Gauss quadrature. To accelerate the convergence of these integrals, we first subtract from the integrands their large argument asymptotic forms. Furthermore, when $|x - x'|$ is larger than $|z - z'|$, we also employ the method of averages [25], [34]. Finally, the closed-form integrals of the asymptotic forms are added back to compensate for the subtracted terms. The former explicitly exhibit their source-region logarithmic singularities, which are integrable and are easily taken care of in evaluating the kernel integrals (30)-(31).

The equation (25) has nontrivial solutions only for those values of β, which make the matrix determinant vanish. These values are found by the Müller method [35], and the corresponding modal current coefficients are then determined from (25).

4 Numerical results

In this section, we present sample numerical results for the propagation constants and modal current distributions for a variety of transmission-line configurations. In all examples considered, the media are assumed lossless and nonmagnetic (i.e., $\mu_{rn} = 1$ for all layers). Some of the structures analyzed comprise both uniaxial and isotropic dielectric layers. If a layer is isotropic, its relative permittivity is denoted by ε_r. Only the proper, bound modes, which propagate unattenuated with a real propagation constant β, are considered. The dispersion curves are given either for β/k_0, or for the effective dielectric constant $\varepsilon_{\text{eff}} = (\beta/k_0)^2$.

In Fig. 4, we present dispersion curves for a circular-wire transmission line embedded in a grounded two-layer isotropic medium with or without a top ground plane. The latter configuration was first analyzed by Faché and De Zutter [21], using an approach especially developed for wire conductors, and their results are shown by

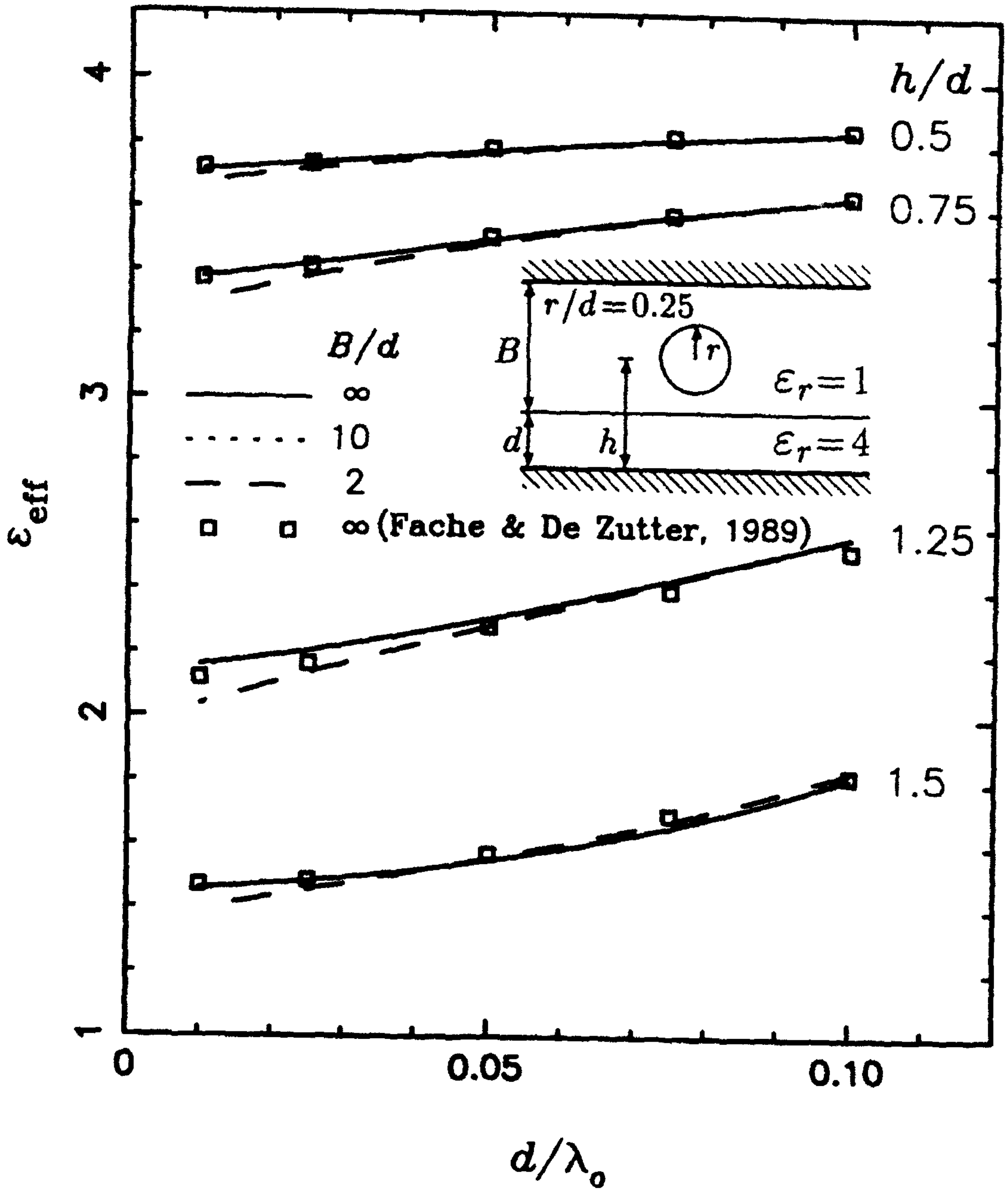

Figure 4: Dispersion curves for a circular-wire transmission line.

square symbols in Fig. 4. In this figure, ε_{eff} is plotted versus the electrical thickness of the substrate, d/λ_0, where λ_0 is the free-space wavelength. The wire is completely embedded in the dielectric slab for $h/d = 0.75$ or 0.5, and in the air region when $h/d = 1.25$ or 1.5. In the analysis, the circular cross section contour of the wire was approximated by sixteen linear segments of equal length. We note that the results for $B/d = \infty$ (unshielded structure) are indistinguishable from those for $B/d = 10$. This is to be expected, since the field of the bound mode is mainly trapped in the substrate and near the conductor. The presence of the top ground plane presents a noticeable disturbance to the bound wave only if it is close to the conductor or to the dielectric interface.

In Fig. 5, we present dispersion curves for a three-conductor microstrip transmission line, which supports three fundamental modes. The dielectric is made of ceramic-impregnated teflon, known as Epsilam 10, which is uniaxial, with $\varepsilon_t = 13$ and $\varepsilon_z = 10.2$. As a check for the computer code, we have further divided the dielectric slab into two layers. Two configurations have been analyzed, one without an air gap ($h/d = 0$), and the other with an air gap ($h/d = 0.04$), and the corresponding results are shown in solid and dashed lines, respectively. These configurations have been previously analyzed by Kitazawa [15], the first one by a full-wave method (square symbols), and the second by a quasi-static approach (dotted lines). It is of interest to note that a small air gap between the ground plane and the dielectric slab results in big changes in the dispersion curves. The longitudinal (transverse) current distributions for modes 1, 2, and 3 are found to be even (odd), odd (even), and even (odd), respectively.

In Fig. 6, we present dispersion curves for a three-wire transmission line embedded in a grounded dielectric slab, which supports three fundamental modes. The solid lines represent the results computed by Faché et al. [22] for the case of an isotropic substrate ($\varepsilon_r = 4$), whereas our results for the same substrate are illustrated by the dotted lines. Note that a logarithmic scale is used for the frequency. Our results for a uniaxial substrate, where $\varepsilon_t = 3.9$ and $\varepsilon_z = 4.1$, are indicated by three different symbols. As can be seen from the figure, even this slight anisotropy has a noticeable effect on the dispersion curves. In the isotropic case, all three modes remain in the

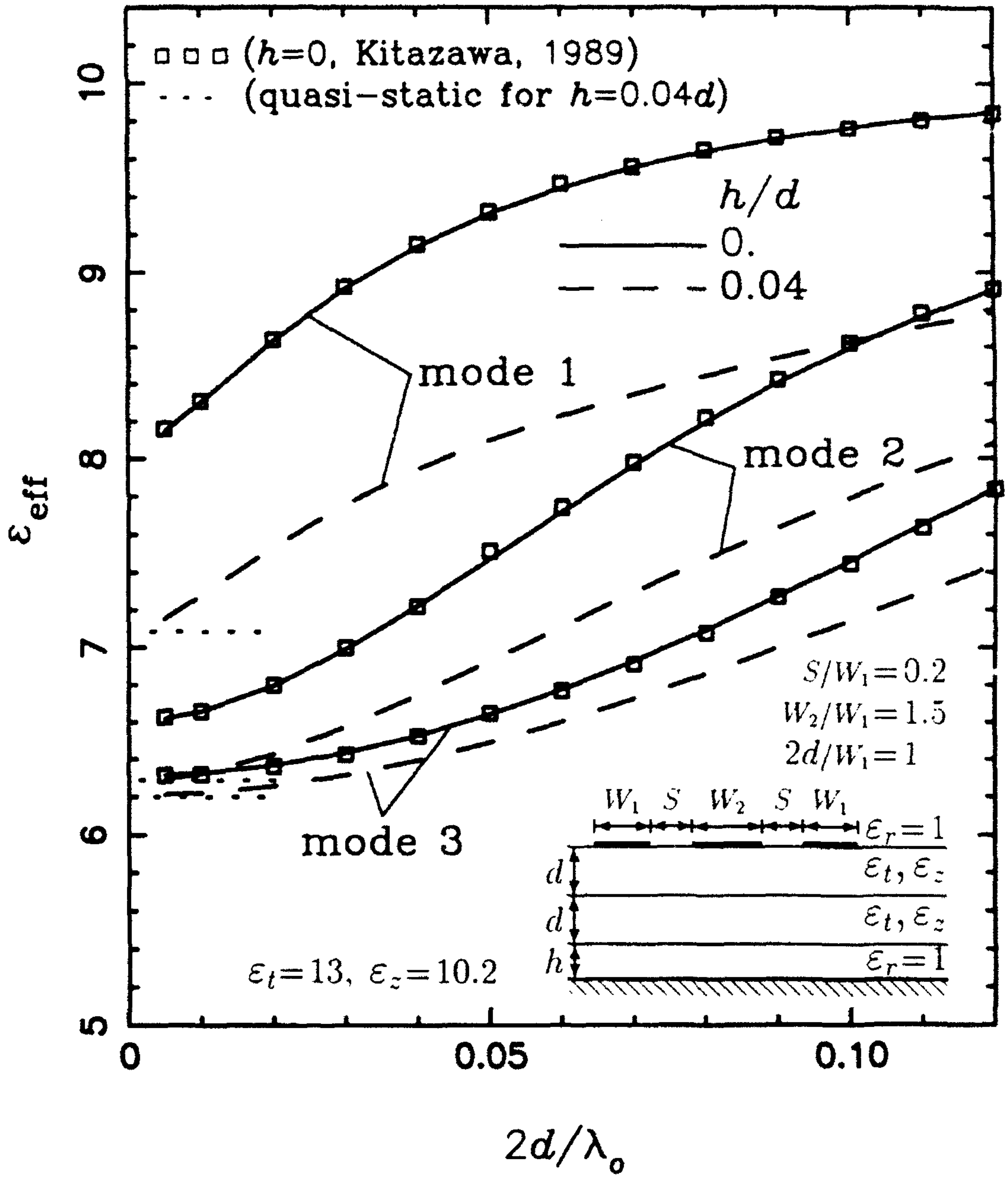

Figure 5: Dispersion curves for a three-strip microstrip transmission line.

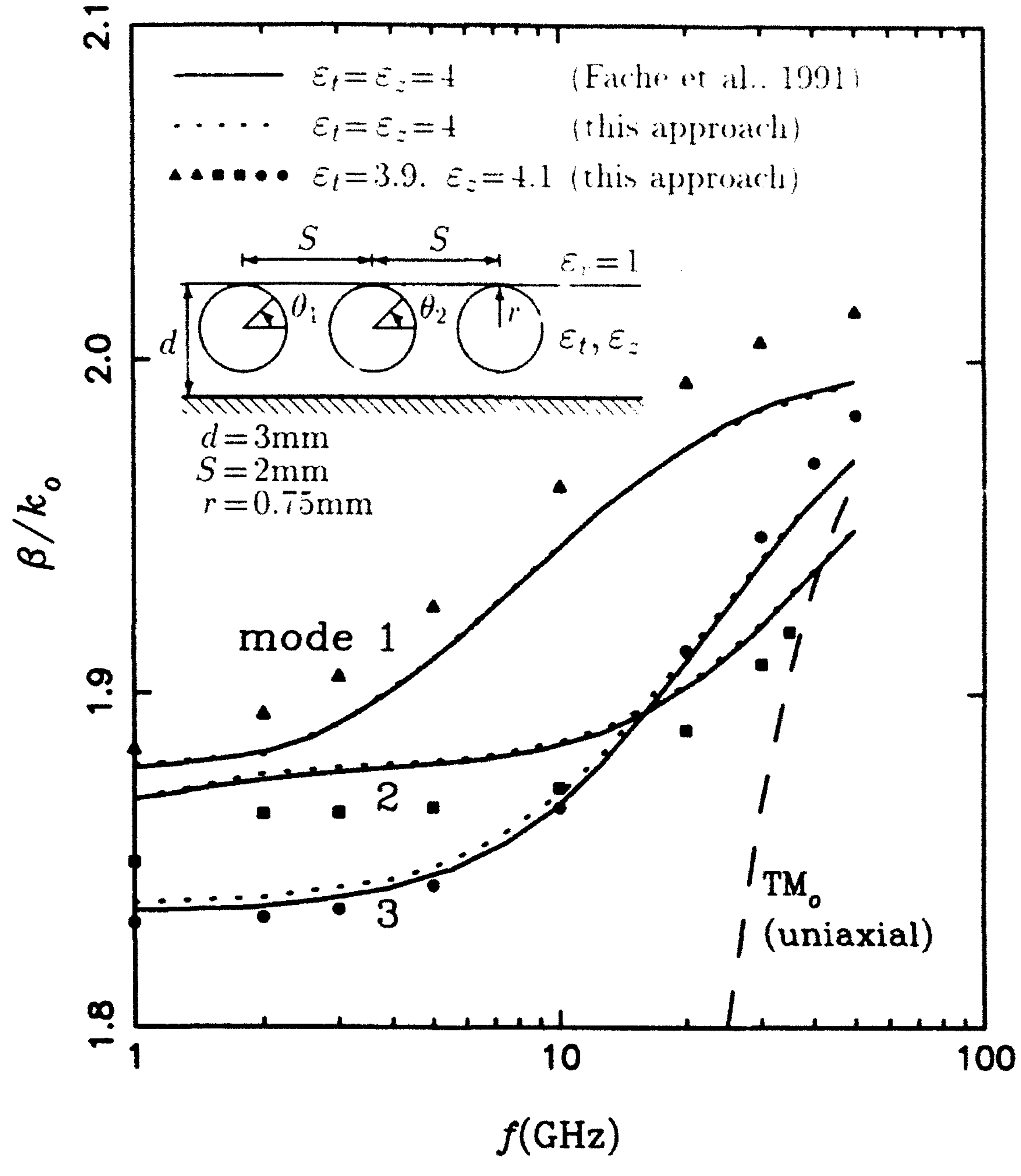

Figure 6: Dispersion curves for a three-wire transmission line.

bound regime in the frequency range considered. In the uniaxial case, mode 2 enters the leaky regime [36] at a frequency between 30 to 40 GHz, above which the dominant slab mode, indicated as TM_0 in Fig. 6, is excited. The dispersion curve of the latter is obtained by finding the zero of (34) (see the appendix). The longitudinal and transverse modal current distributions at $f = 10$ GHz are shown in Fig. 7. For modes 1, 2, and 3, the longitudinal (transverse) currents are even (odd), even (odd), and odd (even), respectively. Because of this symmetry property, we only plot the currents on the left and center conductors. We note that the longitudinal and transverse currents are in phase quadrature, which is characteristic of bound modes on lossless transmission lines.

We next consider three transmission line structures, which differ in the cross section shape of the conductors, as illustrated in Fig. 8. The cross sections of the conductors are (*a*) trapezoidal (which may arise as a result of an epitaxial growth process), (*b*) rectangular (the ideal case), and (*c*) inverted trapezoidal (which may be due to etching undercuts). The dispersion curves for the three fundamental modes that each of the three transmission lines may support are plotted in Fig. 9. The longitudinal (transverse) current distributions for modes 1, 2, and 3 are found to be even (odd), odd (even), and even (odd), respectively. In Fig. 9, we also show the quasi-static results obtained by Schroeder and Wolff [2] for the same transmission lines, but having a finite-width substrate. We observe that the dispersion curves for configurations (*a*) and (*b*) differ less than those for (*b*) and (*c*). This is expected, since in the former two geometries the conductor widths adjacent to the dielectric slab (where there is a highly concentrated field) are the same. We also note that the quasi-static results of [2] are very close to the low-frequency limits of mode 3 of our results. However, it is not clear from [2] to which mode these quasi-static values correspond.

In Fig. 10, we present dispersion curves for a two-strip transmission line in an unshielded medium comprising both uniaxial and isotropic layers (see the inset). Since there are only two conductors and there are no ground planes in this structure, we expect it to have only one non-cutoff fundamental mode (called mode 1 in Fig. 10). Nevertheless, an additional non-cutoff mode (called mode 2) has been found. In

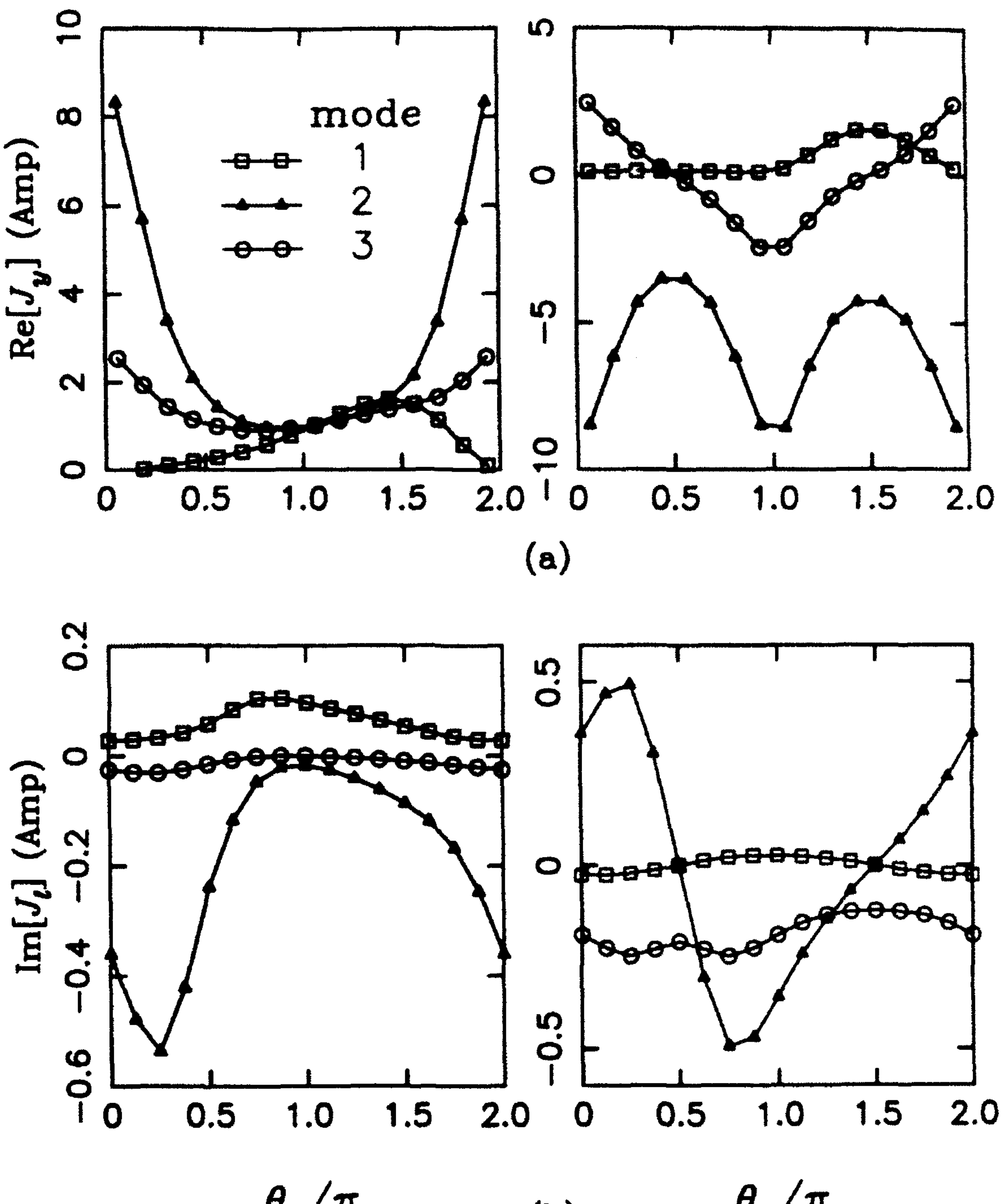

Figure 7: (a) Longitudinal and (b) transverse current distributions at f = 10GHz for the three-wire transmission line in the configuration of Fig. 6, with $\varepsilon_t = 3.9$ and $\varepsilon_z = 4.1$.

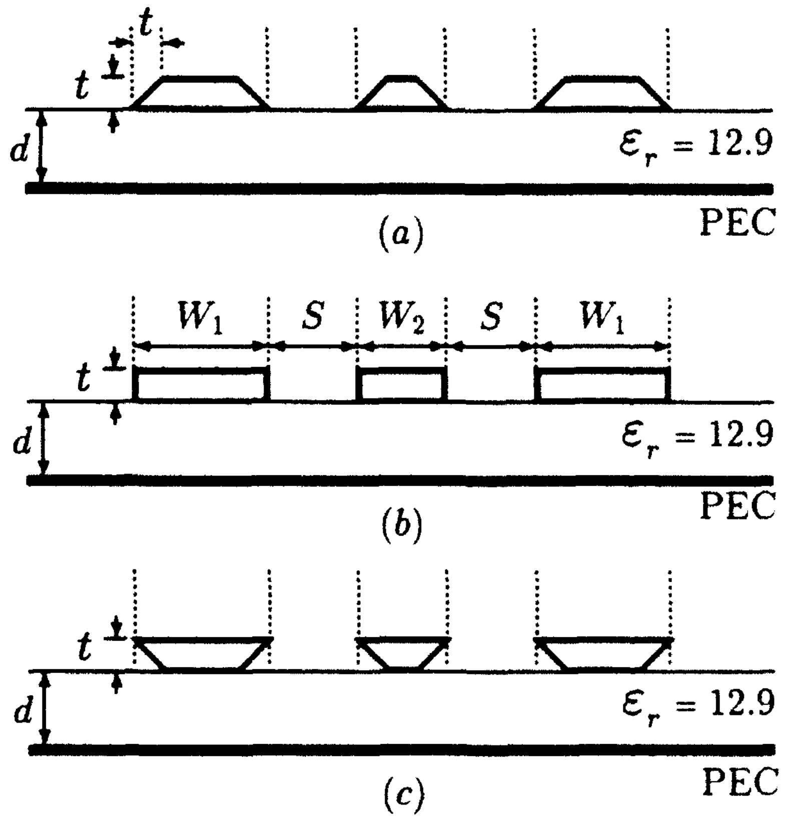

Figure 8: Geometry of three transmission line configurations with conductors of (a) trapezoidal, (b) rectangular, and (c) inverted trapezoidal cross section. The dimensions are $d = 120\,\mu\text{m}$, $W_1 = 15\,\mu\text{m}$, $W_2 = S = 10\,\mu\text{m}$, and $t = 3\,\mu\text{m}$.

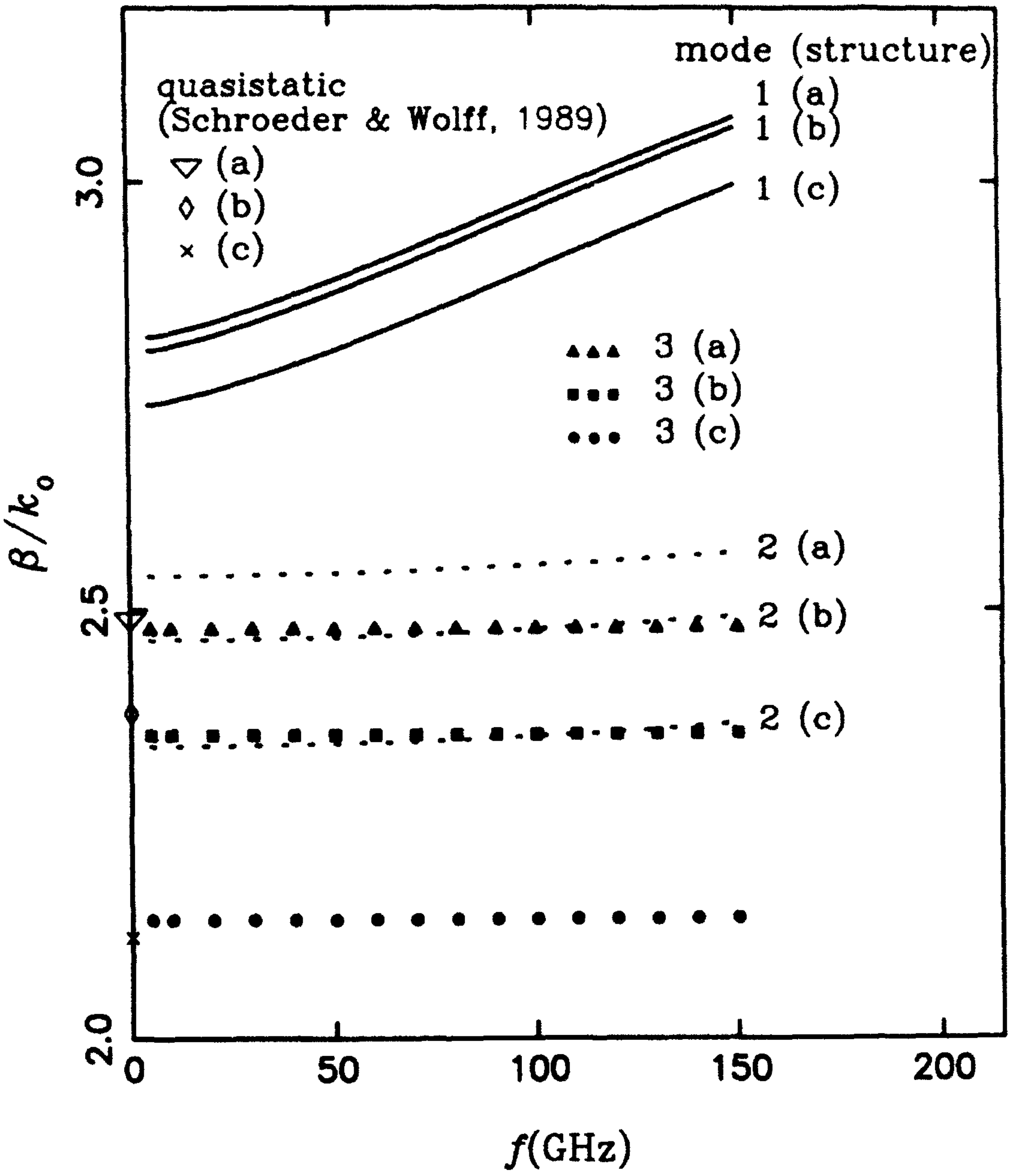

Figure 9: Dispersion curves of modes 1, 2, and 3 for the transmission line configurations (a), (b), and (c) of Fig. 8. The quasi-static results of Schroeder and Wolff are for a structure with a substrate of a finite width of 130 μm.

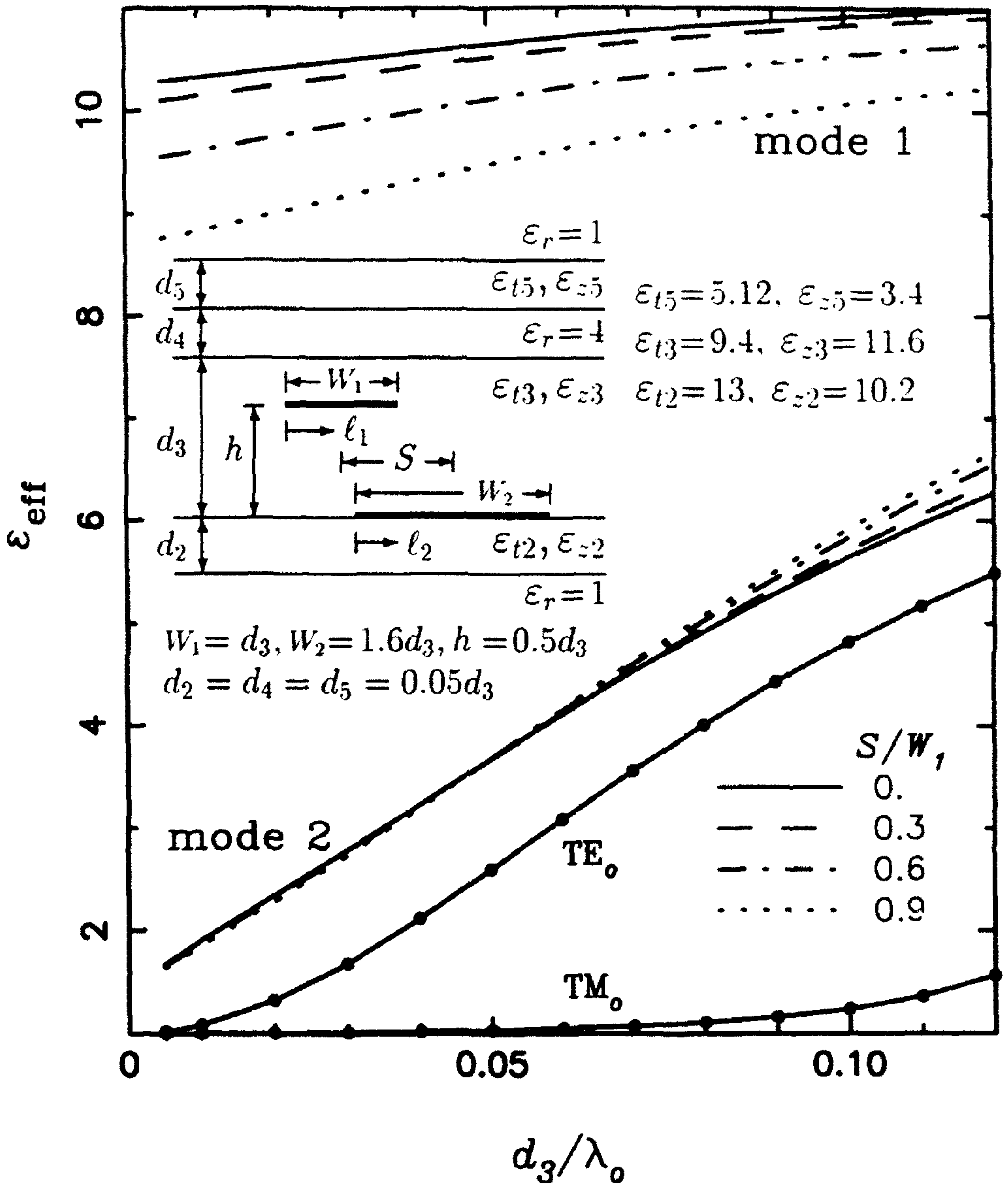

Figure 10: Dispersion curves for a two-strip transmission line in an unshielded layered medium.

addition to the dispersion curves of these two modes, we also plot in Fig. 10 the dispersion curves of the first two slab modes (indicated as TE$_0$ and TM$_0$), computed from (34) of the appendix. The longitudinal currents of mode 1 on the two strips (not shown) are found to be in different directions, whereas those of mode 2 are in the same direction. Hence, mode 2 is similar to the fundamental mode of a coated conducting cylinder, where the surface current on the circumference of the cylinder flows in the same direction, and whose suitability as a single-conductor transmission line was studied by Goubau [37]. A salient feature of this Goubau mode is that its $\varepsilon_{\rm eff}$ is very close at low frequencies to that of free space, and that its field is very loosely bound to the dielectric. In fact, when we replace the two strips in the configuration shown in Fig. 10 by a single strip, we still can find a mode, which behaves similarly to the aforementioned mode 2.

5 Conclusion

A mixed-potential integral equation (MPIE) formulation has been implemented in conjunction with the method of moments to compute the propagation constants and modal currents of a multiconductor transmission line embedded in a laterally open multilayered uniaxial medium. The approach is general and flexible, and can handle both open and shielded structures. It is applicable to conductors of arbitrary cross section, including trapezoidal, which often arises in practice due to underetching or as a result of the epitaxial growth process. Sample numerical results have been presented for several transmission-line configurations and, when possible, compared with available published data, obtained by specialized techniques not easily extendable to conductors of arbitrary cross section.

Appendix

Transmission Line Green's Functions

Consider a transmission-line network analog of the layered medium of Fig. 1, formed by a tandem connection of transmission line sections, each corresponding to a dielectric layer (cf. Fig. 2). Let the network be excited by a 1 A current source located at z' in the nth line section. Then, the voltage and current at z within any line section, say the mth, satisfy the transmission-line equations [32]

$$\left\{ \begin{aligned} \frac{dV_{i,mn}^{p}}{dz} &= -jk_{zm}^{p} Z_{m}^{p} I_{i,mn}^{p} \\ \frac{dI_{i,mn}^{p}}{dz} &= -jk_{zm}^{p} Y_{m}^{p} V_{i,mn}^{p} + \delta(z - z') \end{aligned} \right. \tag{32}$$

where the propagation constant k_{zm}^{p} and characteristic impedance Z_{m}^{p} (and admittance Y_{m}^{p}) have been defined in (14) and (15), respectively. The superscript p, which stands for e or h, as explained in Section 2, will henceforth be left out for brevity.

When $m = n$, i.e., the source and observation points are within the same nth line section, the voltage $V_{i,nn}$ is readily found from (32) as (cf. [32, p. 213], [26])

$$V_{i,nn}(z|z') = Z_n \frac{e^{-jk_{zn}|z-z'|}}{2W_n} \left[1 + \overleftarrow{\Gamma}_n e^{-j2k_{zn}(z_< - z_n)}\right] \left[1 + \overrightarrow{\Gamma}_n e^{-j2k_{zn}(z_{n+1} - z_>)}\right] \tag{33}$$

where

$$W_n = 1 - \overleftarrow{\Gamma}_n \overrightarrow{\Gamma}_n e^{-j2k_{zn}d_n} \tag{34}$$

and $z_< \equiv \min(z, z')$, $z_> \equiv \max(z, z')$. In the above, $\overleftarrow{\Gamma}_n$ and $\overrightarrow{\Gamma}_n$ are the voltage reflection coefficients "looking to the left" and "looking to the right," respectively, at the two interior ends of this line section, as illustrated in Fig. 11. These reflection coefficients can be found as

$$\overleftrightarrow{\Gamma}_n = \frac{\overleftrightarrow{Z}_n - Z_n}{\overleftrightarrow{Z}_n + Z_n} \tag{35}$$

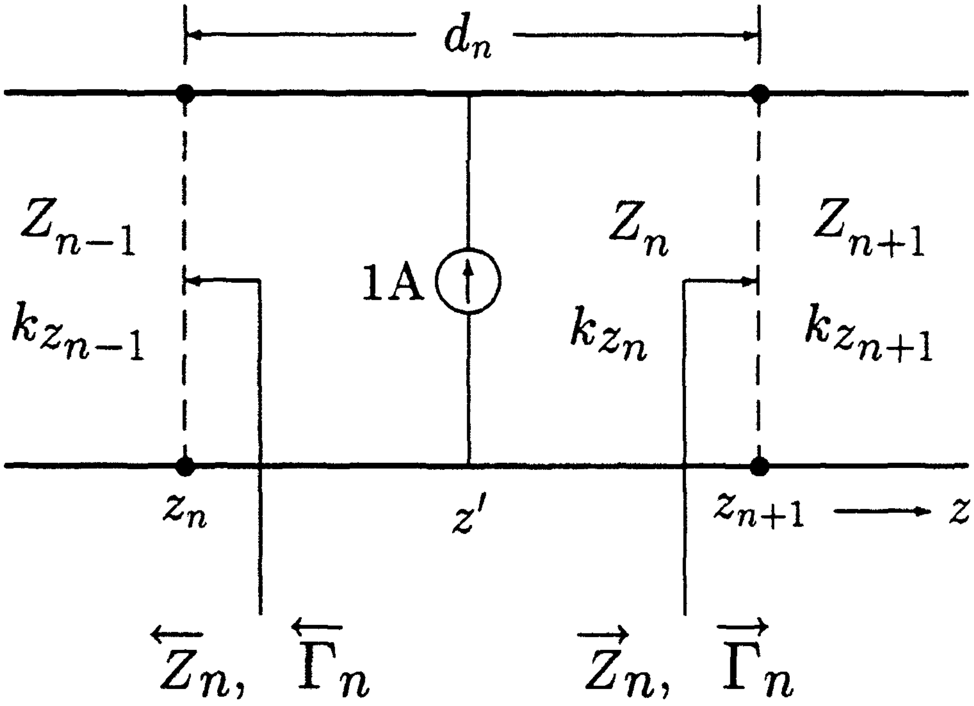

Figure 11: Transmission line section containing a current source.

with the terminal impedances given by the recursive relations

$$\overset{\rightarrow}{\overleftarrow{Z}}_n = Z_{n\pm 1} \frac{\overset{\rightarrow}{\overleftarrow{Z}}_{n\pm 1} + jZ_{n\pm 1} \tan(k_{z,n\pm 1} d_{n\pm 1})}{Z_{n\pm 1} + j\overset{\rightarrow}{\overleftarrow{Z}}_{n\pm 1} \tan(k_{z,n\pm 1} d_{n\pm 1})} \tag{36}$$

where the upper and lower signs correspond to the right and left arrows, respectively.

For $m \neq n$, $V_{i,mn}(z|z')$ is readily found from (32) and (33), by enforcing the continuity of the voltage and current at the interfaces. As a result, we obtain [26]

$$V_{i,mn}(z|z') = \begin{cases} V_{i,nn}(z_{n+1}|z')\,\overrightarrow{T}_{v,mn}(z), & n+1 \leq m \leq N \\ V_{i,nn}(z_n|z')\,\overleftarrow{T}_{v,mn}(z), & 1 \leq m \leq n-1 \end{cases} \tag{37}$$

where

$$\overrightarrow{T}_{v,mn}(z) = \frac{e^{-jk_{zm}(z-z_m)}}{1+\overrightarrow{\Gamma}_m e^{-j2k_{zm}d_m}} \left[1+\overrightarrow{\Gamma}_m e^{-j2k_{zm}(z_{m+1}-z)}\right] \prod_{i=n+1}^{m-1} \frac{\left(1+\overrightarrow{\Gamma}_i\right) e^{-jk_{zi}d_i}}{1+\overrightarrow{\Gamma}_i e^{-j2k_{zi}d_i}} \tag{38}$$

$$\overleftarrow{T}_{v,mn}(z) = \frac{e^{-jk_{zm}(z_{m+1}-z)}}{1+\overleftarrow{\Gamma}_m e^{-j2k_{zm}d_m}} \left[1+\overleftarrow{\Gamma}_m e^{-j2k_{zm}(z-z_m)}\right] \prod_{i=m+1}^{n-1} \frac{\left(1+\overleftarrow{\Gamma}_i\right) e^{-jk_{zi}d_i}}{1+\overleftarrow{\Gamma}_i e^{-j2k_{zi}d_i}} \tag{39}$$

It is understood in the above that the product terms are equal to one if the lower limits exceed the upper limits.

The transmission-line Green's functions can be efficiently implemented into a computer program, as explained below. First, we recognized that (33) may be written as

$$V_{i,nn}(z|z') = Z_n f_1\left(n; z; z'; \overleftarrow{\Gamma}_n; \overrightarrow{\Gamma}_n\right) \tag{40}$$

which serves to define the function f_1. The corresponding current can then easily be found from the first of (32) as

$$I_{i,nn}(z|z') = \pm f_2\left(n; z; z'; \pm\overleftarrow{\Gamma}_n; \pm\overrightarrow{\Gamma}_n\right), \quad z \gtrless z' \tag{41}$$

which defines the function f_2. In a like manner, we may write (37) as

$$V_{i,mn}(z|z') = Z_n \begin{cases} f_1\left(n; z_{n+1}; z'; \overleftarrow{\Gamma}_n; \overrightarrow{\Gamma}_n\right) \cdot f_3\left[m; n; z; \overrightarrow{\Gamma}_j|_{(n<j\leq m)}\right], & m > n \\ f_1\left(n; z_n, z'; \overleftarrow{\Gamma}_n; \overrightarrow{\Gamma}_n\right) \cdot f_4\left[m; n; z; \overleftarrow{\Gamma}_j|_{(m\leq j<n)}\right], & m < n \end{cases} \tag{42}$$

which defines the functions f_3 and f_4. The corresponding current can again be found from the first of (32) as

$$I_{i,mn}(z|z') = \begin{cases} f_2\left(n; z_{n+1}; z'; \overleftarrow{\Gamma}_n; \overrightarrow{\Gamma}_n\right) \cdot f_3\left[m; n; z; -\overrightarrow{\Gamma}_j|_{(n<j\leq m)}\right], & m > n \\ -f_2\left(n; z_n; z'; -\overleftarrow{\Gamma}_n; -\overrightarrow{\Gamma}_n\right) \cdot f_4\left[m; n; z; -\overleftarrow{\Gamma}_j|_{(m\leq j<n)}\right], & m < n \end{cases} \tag{43}$$

The current $I_{v,mn}$ and voltage $V_{v,mn}$, due to a unit-strength voltage source in the nth line section, satisfy a set of equations dual to (32). Hence, we may obtain these voltage and current transmission-line Green's functions from (40)–(43) by making the substitutions $V \longrightarrow I$, $I \longrightarrow V$, and $Z \longrightarrow Y$. Note that the last substitution causes all reflection coefficients to change signs. We observe that only four subroutines, corresponding to the functions f_1 through f_4, are required to implement all the transmission-line Green's functions in the computer code.

References

[1] F. E. Gardiol, "Design and layout of microstrip structures," *IEE Proc.*, vol. 135, Pt. H, pp. 145–157, June 1988.

[2] W. Schroeder and I. Wolff, "A new hybrid mode boundary integral method for analysis of MMIC waveguides with complicated cross-section," in *Digest IEEE MTT-S Int. Symp.*, (Long Beach, C.A.), pp. 711–714, 1989.

[3] N. Alexópoulos, "Integrated–circuit structures on anisotropic substrates," *IEEE Trans. Microwave Theory Tech.*, vol. MTT–33, pp. 847–881, Oct. 1985.

[4] E. J. Denlinger, "A frequency dependent solution for microstrip transmission lines," *IEEE Trans. Microwave Theory Tech.*, vol. MTT–19, pp. 30–39, Jan. 1971.

[5] T. Itoh and R. Mittra, "Spectral–domain approach for calculating the dispersion characteristics of microstrip lines," *IEEE Trans. Microwave Theory Tech.*, vol. MTT–21, pp. 496–499, July 1973.

[6] G. Kowalski and R. Pregla, "Dispersion characteristics of single and coupled microstrips," *Arch. Elek. Übertragung.*, vol. 26, no. 6, pp. 276–280, 1972.

[7] G. Kowalski and R. Pregla, "Dispersion characteristics of single and coupled microstrips with double-layer substrates," *Arch. Elek. Übertragung.*, vol. 27, no. 3, pp. 125-130, 1973.

[8] Y. Hayashi and T. Kitazawa, "Analysis of microstrip transmission line on a sapphire substrate," *J. Inst. Electron. Commun. Eng. Jap.*, vol. 62-B, no. 6, pp. 64–71, 1979.

[9] A. M. A. El-Sherbiny, "Hybrid mode analysis of microstrip lines on anisotropic substrates," *IEEE Trans. Microwave Theory Tech.*, vol. MTT-29, pp. 1261–1266, Dec. 1981.

[10] T. Kitazawa and Y. Hayashi, "Propagation characteristics of striplines with multilayered anisotropic media," *IEEE Trans. Microwave Theory Tech.*, vol. MTT-31, pp. 429–433, June 1983.

[11] F. Medina and M. Horno, "Determination of Green's function matrix for multiconductor and anisotropic multidielectric planar transmission lines: A variational approach," *IEEE Trans. Microwave Theory Tech.*, vol. MTT-33, pp. 933–940, Oct. 1985.

[12] B. E. Kretch and R. E. Collin, "Microstrip dispersion including anisotropic substrates," *IEEE Trans. Microwave Theory Tech.*, vol. MTT-35, pp. 710–718, Aug. 1987.

[13] N. Faché and D. De Zutter, "Rigorous full-wave space-domain solution for dispersive microstrip lines," *IEEE Trans. Microwave Theory Tech.*, vol. 36, pp. 731–737, Apr. 1988.

[14] N. Faché, J. Van Hese, and D. De Zutter, "Generalized space domain Green's dyadic for multilayered media with special application to microwave interconnections," *J. Electromagn. Waves Appl.*, vol. 3, pp. 651–669, July 1989.

[15] T. Kitazawa, "Variational method for multiconductor coupled striplines with stratified anisotropic media," *IEEE Trans. Microwave Theory Tech.*, vol. 37, pp. 484–491, Mar. 1989.

[16] Y. Yuan and D. P. Nyquist, "Full-wave perturbation theory based upon electric field integral equations for coupled microstrip transmission lines," *IEEE Trans. Microwave Theory Tech.*, vol. 38, pp. 1576–1584, Nov. 1990.

[17] K. A. Michalski and D. Zheng, "A spectral-domain method for the analysis of the fundamental-mode leakage effect in microstrip lines on uniaxial substrate," *Microwave & Opt. Technol. Lett.*, vol. 4, no. 4, pp. 158–161, 1991.

[18] J. F. Kiang, "Integral equation solution to the skin effect problem in conductor strips of finite thickness," *IEEE Trans. Microwave Theory Tech.*, vol. 39, pp. 452–460, Mar. 1991.

[19] K. A. Michalski and D. Zheng, "Rigorous analysis of open microstrip lines of arbitrary cross section in bound and leaky regimes," *IEEE Trans. Microwave Theory Tech.*, vol. 37, pp. 2005–2010, Dec. 1989.

[20] C. F. Railton and J. P. McGeehan, "An analysis of microstrip with rectangular and trapezoidal conductor cross sections," *IEEE Trans. Microwave Theory Tech.*, vol. 38, pp. 1017–1022, Aug. 1990.

[21] N. Faché and D. De Zutter, "Full-wave analysis of a perfectly conducting wire transmission line in a double-layered conductor-backed medium," *IEEE Trans. Microwave Theory Tech.*, vol. 37, pp. 512–518, Mar. 1989.

[22] N. Faché, F. Olyslager, and D. De Zutter, "Full-wave analysis of coupled perfectly conducting wires in a multilayered medium," *IEEE Trans. Microwave Theory Tech.*, vol. 39, pp. 673–680, Apr. 1991.

[23] M. Chryssomallis and J. N. Sahalos, "An analytic method to study open thick microstrips," *Arch. Elektrotech.*, vol. 72, no. 4, pp. 283–291, 1989.

[24] K. C. Gupta, R. Garg, and I. J. Bahl, *Microstrip Lines and Slotlines*. Dedham, MA: Artech House, 1979.

[25] J. R. Mosig and F. E. Gardiol, "A dynamical radiation model for microstrip structures," in *Adv. Electron. Electron Phys.* (P. W. Hawkes, ed.), vol. 59, pp. 139–237. New York: Academic Press, 1982.

[26] K. A. Michalski and D. Zheng, "Electromagnetic scattering and radiation by surfaces of arbitrary shape in layered media, Part I: Theory," *IEEE Trans. Antennas Propagat.*, vol. 38, pp. 335–344, Mar. 1990.

[27] K. A. Michalski, "Formulation of mixed-potential integral equations for arbitrarily shaped microstrip structures," *J. Electromagn. Waves Appl.*, to appear.

[28] R. F. Harrington, *Field Computation by Moment Methods*. New York: Macmillan, 1968. Reprinted by Krieger Publishing Co., Melbourne, FL, 1982.

[29] A. W. Glisson and D. R. Wilton, "Simple and efficient numerical methods for problems of electromagnetic radiation and scattering from surfaces," *IEEE Trans. Antennas Propagat.*, vol. AP–28, pp. 593–603, Sept. 1980.

[30] K. A. Michalski, "On the scalar potential of a point charge associated with a time-harmonic dipole in a layered medium," *IEEE Trans. Antennas Propagat.*, vol. AP–35, pp. 1299–1301, Nov. 1987.

[31] K. A. Michalski, "The mixed-potential electric field integral equation for objects in layered media," *Arch. Elek. Übertragung.*, vol. 39, pp. 317–322, Sept.–Oct. 1985.

[32] L. B. Felsen and N. Marcuvitz, *Radiation and Scattering of Waves*. Englewood Cliffs, N.J.: Prentice Hall, 1973.

[33] N. K. Das and D. M. Pozar, "A generalized spectral-domain Green's function for multilayer dielectric substrates with application to multilayer transmission lines," *IEEE Trans. Microwave Theory Tech.*, vol. MTT–35, pp. 326–335, Mar. 1987.

[34] J. R. Mosig and F. E. Gardiol, "Analytic and numerical techniques in the Green's function treatment of microstrip antennas and scatterers," *IEE Proc.*, vol. 130, Pt. H, pp. 175–182, Mar. 1983.

[35] S. D. Conte and C. de Boor, *Elementary Numerical Analysis: An Algorithmic Approach*. New York: McGraw–Hill, 1980.

[36] H. Shigesawa, M. Tsuji, and A. A. Oliner, "Dominant mode power leakage from printed-circuit waveguides," *Radio Sci.*, vol. 26, no. 2, pp. 559–564, 1991.

[37] G. Goubau, "Single–conductor surface–wave transmission lines," *Proc. IRE*, vol. 39, pp. 619–624, June 1951.